



HAL
open science

Development of chelating materials for localized metal extraction in neurodegenerative diseases

Juan Felipe Salazar Ariza

► **To cite this version:**

Juan Felipe Salazar Ariza. Development of chelating materials for localized metal extraction in neurodegenerative diseases. Chimie. Université Claude Bernard - Lyon I, 2024. Français. NNT : 2024LYO10293 . tel-04866046

HAL Id: tel-04866046

<https://theses.hal.science/tel-04866046v1>

Submitted on 6 Jan 2025

HAL is a multi-disciplinary open access archive for the deposit and dissemination of scientific research documents, whether they are published or not. The documents may come from teaching and research institutions in France or abroad, or from public or private research centers.

L'archive ouverte pluridisciplinaire **HAL**, est destinée au dépôt et à la diffusion de documents scientifiques de niveau recherche, publiés ou non, émanant des établissements d'enseignement et de recherche français ou étrangers, des laboratoires publics ou privés.

**THESE de DOCTORAT DE
L'UNIVERSITE CLAUDE BERNARD LYON 1**

**Ecole Doctorale N° 206
Nom complet Ecole Doctorale**

Discipline : Chimie

Soutenue publiquement le 05/12/2024, par :
Juan Felipe Salazar Ariza

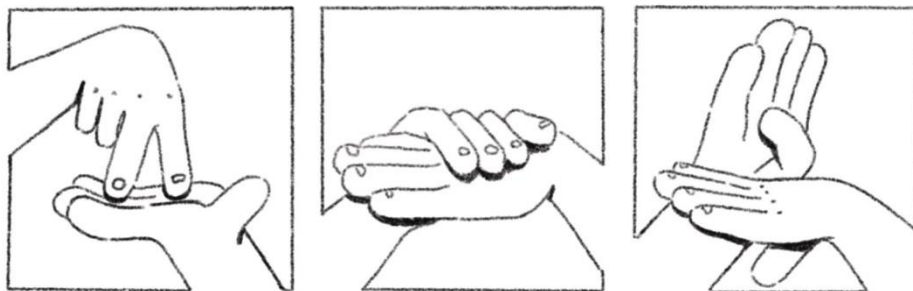
**Development of chelating materials for
localized metal extraction in
neurodegenerative diseases**

Devant le jury composé de :

Osorio-Madrazo, Anayancy	Professeure, Université d'Iéna	Rapportrice
Roux, Stéphane	Professeur, Université de Franche-Comté	Rapporteur
Faur, Catherine	Professeure, Université de Montpellier	Examinatrice
Trimaille, Thomas	Professeur, Université de Lyon1	Président du Jury
Lux, François	Maître de conférence, Université de Lyon1	Directeur de thèse
David, Laurent	Professeur, Université de Lyon1	Co-directeur de thèse
Montembault, Alexandra	Professeure, Université de Lyon1	Invitée
Tillement, Olivier	Professeur, Université de Lyon1	Invité



Para Tere, Pipito y Mimina



Acknowledgments

Dans un premier temps, je tiens à remercier Anayancy Osorio-Madrazo ainsi que Stéphane Roux d'avoir accepté d'être les rapporteurs de ce travail de thèse. Je remercie également Catherine Faur et Thomas Trimaille de faire partie du jury. Je souhaite aussi exprimer ma gratitude à Philippe Dugourd, directeur de l'Institut Lumière Matière (ILM), et à Jannick Duchet-Rumeau, directrice du Laboratoire d'Ingénierie des Matériaux Polymères (IMP), deux institutions de recherche qui m'ont accueilli pendant mes travaux de thèse.

Je remercie chaleureusement François Lux et Laurent David, mon directeur et codirecteur de thèse, pour ces trois années durant lesquelles vous m'avez aidé à comprendre la science de la chélation métallique ainsi que toutes les propriétés du chitosane. Merci pour votre patience et votre envie de partager vos connaissances. Merci, François, pour nos discussions sur le football ; au final, on peut dire que nous partageons une haine commune envers l'Argentine après la Coupe du monde 2022 et la Copa América 2024. Merci, Laurent, pour ta bonne humeur et tes « buenos días » quotidiens, ainsi de m'avoir permis d'avoir été à l'ESRF, une expérience inoubliable.

Je tiens également à remercier Olivier Tillement, directeur de l'équipe, pour m'avoir accepté en stage de M1, puis en M2, et enfin en thèse au sein du laboratoire. Vos idées m'ont permis d'avancer à plusieurs reprises tout au long de la thèse. J'espère que vous seriez d'accord pour dire que j'ai créé de la valeur durant ces trois années.

Merci, Alexandra, pour ton expertise en rhéologie ainsi que pour m'avoir encouragé face aux nombreux problèmes rencontrés au cours de la thèse. Merci également, Fabrice, pour ton aide et ta disponibilité lors des expériences de sorption.

Je tiens à remercier l'équipe MEX-BRAIN de m'avoir accepté comme un membre à part entière (et de m'avoir permis de participer aux réunions R&D). Merci à Thomas Brichart pour tes conseils très utiles qui m'ont aidé à améliorer mes présentations, ainsi que pour m'avoir permis de survivre à l'été en m'autorisant à rédiger dans les locaux climatisés de MEX-BRAIN (toujours pas de médaille d'or pour la Colombie aux JO). Je souhaite remercier Axel Aigle pour les bons moments passés ensemble, que ce soit en congrès, au bureau ou au labo. J'apprécie beaucoup qu'on a pu s'entendre aussi bien. Merci à Marco Natuzzi pour ton aide tout au long de mon parcours au laboratoire. J'ai beaucoup apprécié travailler avec toi pendant tout ce temps (sauf pendant le stage, puisque tu ne voulais pas être mon maître de stage).

Un grand merci à tous les stagiaires que j'ai pu encadrer pendant cette thèse. Merci, Victor, pour ton travail très sérieux (même si pas toujours bien organisé) qui a contribué à une publication scientifique. Merci, Clara, pour ton aide précieuse, surtout lors des longues et fastidieuses expériences sur les gels. Merci, Sarah, pour ton aide sur les expériences de rhéologie ; au final, une de tes idées a été la clé pour obtenir de bons résultats. Merci, Myriam,

pour ton sérieux et ton aide indispensable ; tu as rendu ma deuxième année de thèse bien plus facile à gérer. Gracias, Marina, por haber sido parte de este viaje. Aprecié mucho tu curiosidad y motivación por la ciencia. Maxence, merci pour ton aide et ta compagnie lors des préparations d'échantillons qu'on a dû refaire encore et encore. Merci aussi d'avoir toujours été volontaire pour aider tes collègues quand elles n'avaient même pas de quoi s'asseoir.

Merci à mes collègues doctorants. Merci, Paul, d'avoir été un excellent maître de stage (le tout premier), pour les séjours à Bastia et tous les fous rires partagés. Au final, j'ai aussi suivi tes pas et je me suis teint les cheveux pour la fin de la thèse les cheveux. Merci, Léna, de m'avoir appris à utiliser la machine à coudre, ainsi que pour tous les bons moments passés ensemble depuis le stage. Merci, Nadjib, pour les entraînements de midi, ton aide, et les soirées qui se prolongeaient jusqu'au lendemain. Merci Thomas pour ton temps et tes conseils sur les gels. I'm so grateful to have shared this PhD journey with you, Jordyn. Thank you for the (free) gym sessions, (free) yoga classes, and especially for being the best partner at the scientific conference in Guadeloupe. Merci, Arthur D., pour ton aide, ta bonne humeur et ta disponibilité, ainsi que pour les quelques parties de basket qu'on a pu faire. Merci, Lise, pour les pauses café, ton aide avec les manips de masse, ainsi que pour tes bonnes adresses de restos. Élise, tu que sabes español aunque nunca me has hablado en él, te agradezco por ser la única que comparte mi pasión por salir a bailar. Leticia, merci d'être l'autre Latino du labo, celle qui me comprend et qui m'aide à mieux vivre la distance avec l'Amérique. Merci, Augustin, pour ta bonne humeur et tes innovations culinaires, comme le tacos aux nouilles. Continue avec cet esprit curieux, il te sera très utile pour la thèse. Merci, Elies, de me suivre dans mes délires ; un de ces jours, on pourra enfin faire les pirates sur les bateaux ! Merci aussi de m'avoir partagé Les classiques de la chimie, un document riche en science. Manon, merci de me supporter, en particulier lors des soirées de rédaction, et de partager tes bonbons Je tiens également à remercier mes collègues de l'IMP, Yun et Yvi, pour votre aide et disponibilité.

Un grand merci à Coralie Grange pour ton soutien lorsque nous devions tous les deux nous battre contre le DFO. Mais surtout, merci pour les débriefs commérages en fin de journée, il n'y a rien de mieux pour conclure une longue journée de travail.

Je remercie l'intégralité de l'équipe FENNEC : Matteo, Yu, Vladimir, Benoît, Arthur M., et Dalila, pour les bons moments, les repas, et autres instants de convivialité qui ont rendu cette thèse plus agréable. Un merci spécial à Fabien, un des piliers du laboratoire, sans qui ce labo et la journée ILM ne seraient pas possibles.

Finalmente, gracias a mi familia y amigos que, a pesar de la distancia, me apoyaron, me soportaron y creyeron en mí. Gracias, Mahe, por el dibujo.

Abstract

Metal homeostasis plays a crucial role in maintaining human health. Current research on neurodegenerative diseases suggests that metal dyshomeostasis actively contributes to the pathogenesis and progression of conditions such as Parkinson's and Alzheimer's diseases. Excess free metals in the brain can have deleterious effects on the body, including oxidative damage through the production of hydroxyl radicals, inflammation, and disruption of biological processes due to altered protein and enzyme conformations.

Systemic metal dyshomeostasis has traditionally been treated with chelation therapy. However, this approach presents several challenges for treating brain metal dyshomeostasis, such as the need for high chelator doses, which can lead to adverse effects, and the non-localized nature of chelation.

Many neurodegenerative diseases currently lack effective cures, and available treatments primarily focus on symptom management. Therefore, the aim of this thesis is to develop a chelating material capable of providing localized and specific metal extraction in particular for iron.

To achieve this goal, multiple chelating polymers were synthesized by functionalization with chelating groups. These polymers were then used to develop various chelating materials, which were thoroughly characterized to assess their mechanical properties and chelating efficacy. Finally, in-vivo applications of these materials were evaluated to explore their potential as novel treatments for localized metal extraction in neurodegenerative diseases.

Résumé

L'homéostasie des métaux joue un rôle crucial dans le maintien de la santé humaine. Les recherches actuelles sur les maladies neurodégénératives suggèrent que la dyshoméostasie des métaux contribue activement à la pathogenèse et à la progression d'affections telles que les maladies de Parkinson et d'Alzheimer. L'excès de métaux libres dans le cerveau peut avoir des effets délétères sur l'organisme, notamment du stress oxydant par la production de radicaux hydroxyles, l'inflammation et la perturbation des processus biologiques en raison de l'altération des conformations des protéines et des enzymes.

La dyshoméostasie systémique des métaux est traditionnellement traitée par la thérapie de chélation. Toutefois, cette approche présente plusieurs difficultés pour le traitement d'une dyshoméostasie des métaux dans le cerveau, notamment la nécessité d'administrer des doses élevées de chélateurs, ce qui peut entraîner des effets indésirables, ainsi qu'une chélation non localisée.

De nombreuses maladies neurodégénératives n'ont pas encore de remède efficace et les seuls traitements disponibles se concentrent principalement sur la gestion des symptômes. L'objectif de cette thèse est donc de développer un matériau chélateur capable de fournir une extraction localisée et spécifique des métaux, en particulier pour le fer.

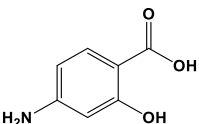
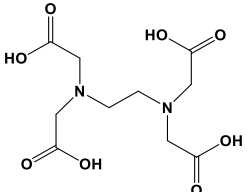
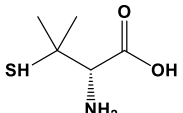
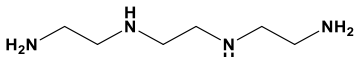
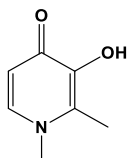
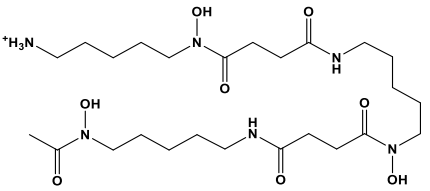
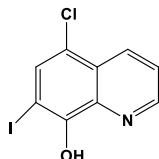
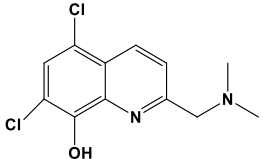
Pour atteindre cet objectif, plusieurs polymères chélatants ont été synthétisés par fonctionnalisation avec des groupes chélateurs. Ces polymères ont ensuite été utilisés pour développer divers matériaux chélatants, qui ont été caractérisés pour évaluer leurs propriétés mécaniques et leur efficacité d'extraction métallique. Enfin, les applications *in vivo* de ces matériaux ont été évaluées afin d'explorer leur potentiel en tant que nouveaux traitements pour l'extraction localisée des métaux dans les maladies neurodégénératives.

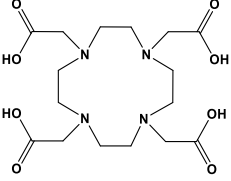
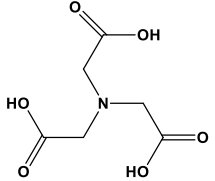
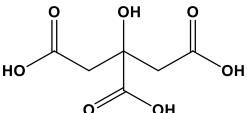
Abbreviations

6-OHDA: Hydroxydopamine	ICP-MS: Inductively coupled plasma mass spectrometry
8-arm-PEG: star-like 8-arm-polyethylene glycol	KED: Kinetic Energy Discrimination
Aβ: amyloid-beta	MALLS: multi-angle laser light scattering
AD: Alzheimer's disease	MPAN: Mitochondrial Membrane-Associated Neurodegeneration
APP: amyloid precursor protein	MRI: Magnetic resonance imaging
BCB: Blood-Cerebrospinal Fluid Barrier	MPTP: 1-methyl-4-phenyl-1,2,3,6-tetrahydropyridine
BBB: Blood-Brain Barrier	mtACP: mitochondrial acyl carrier protein
BPAN: Beta-Propeller-Associated Neurodegeneration	NBIA: neurodegeneration with brain iron accumulation
CNS: central nervous system	NFTs: neurofibrillary tangles
COASY: CoA Synthase-Associated Neurodegeneration	NIHSS: National Institutes of Health Stroke Scale
CrI%: Crystallinity index	nNOS: neuronal nitric oxide synthase
CSF: cerebrospinal fluid	NMDA: N-methyl-D-aspartate
DA: degree of acetylation	NO•: nitric oxide
DBS: Deep brain stimulation	NTA: 2,2',2''-Nitrilotriacetic acid
DFO: Deferoxamine	PAS: Para-aminosalicylic acid
DOTA: 2,2',2'',2'''-(1,4,7,10-Tetraazacyclododecane-1,4,7,10-tetrayl)tetraacetic acid	PD: Parkinson's disease
DOTAGA: 2,2',2''-(10-(2,6-dioxotetrahydro-2H-pyran-3-yl)-1,4,7,10-tetraazacyclododecane-1,4,7-triyl)triacetic acid	PKAN: Pantothenate Kinase-Associated Neurodegeneration
DS: Degree of substitution	PLAN: PLA2G6-Associated Neurodegeneration
DVS: Dynamic Vapor Sorption Analyzer	polyQ: polyglutamine
EDTA: 2,2',2'',2'''-(Ethane-1,2-diyldinitrilo)tetraacetic acid	p-NCS-Bz-DFO: N1-hydroxy-N1-(5-(4-(hydroxy(5-(3-(4-isothiocyanatophenyl)thioureido) pentyl) amino)-4-oxobutanamido) pentyl)-N4-(5-(N-hydroxyacetamido) pentyl) succinimide
FA: Friedreich ataxia	QSM: Quantitative Susceptibility Mapping
FAHN: Fatty Acid 2-Hydroxylase	RNS: reactive nitrogen species
FAD: familial Alzheimer disease	ROS: reactive oxygen species
FARS: Friedreich Ataxia Rating Scale	SN: substantia nigra
HD: Huntington's disease	SNpc: substantia nigra pars compacta
HO•: hydroxyl radical	SR: Swelling ratio
HPLC: high-performance liquid chromatography	TNF-α: tumour necrosis factor alpha
HSH: High-swelling hydrogels	tPA: tissue plasminogen activators
Htt: huntingtin	UPDRS: Unified Parkinson's Disease Rating Scale
ICH: Intracranial haemorrhage	
ICARS: International Cooperative Ataxia Rating Scale	

Chelators

Table 1. Complexation constants of the different chelators mentioned in this work. L corresponds to the ligand.

Chelator	Metal	Complex type	Log β
<p>PAS</p> 	Mn ²⁺	$Mn^{2+} + L^{2-} \rightarrow (MnL_2)^{2-}$	17.2 [1]
<p>EDTA</p> 	Mn ²⁺	$Mn^{2+} + L^{4-} \rightarrow (MnL)^{2-}$	14.0 [2]
	Al ³⁺	$Al^{3+} + L^{4-} \rightarrow (AlL)^{-}$	16.7 [2]
	Fe ³⁺	$Fe^{3+} + L^{4-} \rightarrow (FeL)^{-}$	25.1 [2]
	Cu ²⁺	$Cu^{2+} + L^{4-} \rightarrow (CuL)^{2-}$	18.9 [2]
	Zn ²⁺	$Zn^{2+} + L^{4-} \rightarrow (ZnL)^{2-}$	16.9 [2]
<p>D-penicillamine</p> 	Cu ²⁺	$Cu^{2+} + 2L^{-} \rightarrow (CuL_2)$	16.9 [3]
<p>Trientine</p> 	Cu ²⁺	$Cu^{2+} + L \rightarrow (CuL)^{2+}$	20.3 [4]
<p>Deferiprone</p> 	Fe ³⁺	$Fe^{3+} + 3L^{-} \rightarrow FeL_3$	36.7 [5]
	Cu ²⁺	$Cu^{2+} + 2L^{-} \rightarrow CuL_2$	19.1 [5]
	Zn ²⁺	$Zn^{2+} + 2L^{-} \rightarrow ZnL_2$	13.6 [6]
<p>DFO</p> 	Al ³⁺	$Al^{3+} + LH^{2-} \rightarrow (AlHL)^{+}$	24.1 [7]
	Fe ³⁺	$Fe^{3+} + LH^{2-} \rightarrow (FeHL)^{+}$	41.8 [8]
	Fe ²⁺	$Fe^{2+} + LH^{2-} \rightarrow (FeHL)$	10.0 [9]
	Cu ²⁺	$Cu^{2+} + LH^{2-} \rightarrow (CuHL)$	14.0 [10]
	Zn ²⁺	$Zn^{2+} + LH^{2-} \rightarrow (ZnHL)$	11.1 [10]
<p>Clioquinol</p> 	Cu ²⁺	$Cu^{2+} + 2L^{-} \rightarrow CuL_2$	10.9 [11]
	Zn ²⁺	$Zn^{2+} + 2L^{-} \rightarrow ZnL_2$	7.6 [11]
<p>PBT2</p> 	Cu ²⁺	$Cu^{2+} + 2L^{-} \rightarrow CuL_2$	19.6 [12]

<p style="text-align: center;">DOTA</p> 	Mn^{2+}	$\text{Mn}^{2+} + \text{L}^{4-} \rightarrow (\text{MnL})^{2-}$	20.0 [13]
	Fe^{3+}	$\text{Fe}^{3+} + \text{L}^{4-} \rightarrow (\text{FeL})^{-}$	29.4 [14]
	Cu^{2+}	$\text{Cu}^{2+} + \text{L}^{4-} \rightarrow (\text{CuL})^{2-}$	22.3 [13]
	Zn^{2+}	$\text{Zn}^{2+} + \text{L}^{4-} \rightarrow (\text{ZnL})^{2-}$	20.8 [13]
<p style="text-align: center;">NTA</p> 	Mn^{2+}	$\text{Zn}^{2+} + \text{L}^{3-} \rightarrow (\text{ZnL})^{-}$	7.4 [15]
	Fe^{3+}	$\text{Fe}^{3+} + \text{L}^{3-} \rightarrow \text{FeL}$	15.9 [16]
	Cu^{2+}	$\text{Cu}^{2+} + \text{L}^{3-} \rightarrow (\text{CuL})^{-}$	13.2 [17]
	Zn^{2+}	$\text{Zn}^{2+} + \text{L}^{3-} \rightarrow (\text{ZnL})^{-}$	10.7 [15]
<p style="text-align: center;">Citric acid</p> 	Fe^{3+}	$\text{Fe}^{3+} + 2\text{L}^{3-} \rightarrow (\text{FeL}_2)^{3-}$	15.3 [18]

Contents

Acknowledgments	4
Abstract.....	7
Résumé.....	8
Abbreviations	9
Chelators.....	10
Contents	12
Introduction.....	14
Chapter I: Metal dyshomeostasis and neurodegeneration.....	16
1.1. Toxic Mechanisms of Metals.....	16
1.1.1. Oxidative stress	16
1.1.2. Induction of inflammation.....	18
1.1.3. Interference with enzyme activity.....	18
1.1.4. Neurological effects	19
1.2. Metal overload in the brain.....	21
1.2.1. Neurological disorders directly related to metal dyshomeostasis in the brain	22
1.2.2. Neurological disorders potentially arising from disrupted metal homeostasis within the brain	31
1.3. Chelation therapy mechanisms.....	57
1.3.1. Thermodynamic factors	57
1.3.2. Kinetic factors	60
1.3.3. Chelator Bioavailability for Neurological Applications	61
1.3.4. Local chelation.....	61
Chapter II: Development of chelating polymers.....	64
2.1. DFO functionalised polymer synthesis.....	67
2.1.1. Synthesis of 8-arm-PEG@DFO	67
2.1.2. Chitosan functionalisation with DFO (DA ₄₀ @DFO ₄).....	68
2.1.3. Double-functionalized chitosan (DA ₂₉ @DOTAGA ₉ @DFO ₅)	71
2.2. Polymer characterisations.....	73
2.2.1. Characterization of 8-arm-PEG@DFO	73
2.2.2. Characterization of DA ₄₀ @DFO ₄	77
2.3. Chelation performance assessment	83
2.3.1. Iron (III) chelation in solution proof of concept.....	83

2.3.2. Aluminium (III) chelation in solution proof of concept.....	86
2.4. Conclusion	88
Chapter III: Development of chitosan-based hydrogels.....	90
3.1. Development of iron(III) chelating chitosan based hydrogels, "proof of concept" publication.....	90
3.2. Complementary study of interactions between chitosan metal complexes and salts in solution.....	104
3.2.1. Na ₂ SO ₄ iron (III) mediated release from chitosan based hydrogels previously exposed to an iron (III) citric acid solution at physiological pH.	104
3.2.2. Metal extraction by chitosan based hydrogels, metals being solubilized with EDTA	108
3.3. Effect of grafted chelator on hydrogel properties (publication)	111
3.4. Conclusion	136
Chapter IV: Application for localized chelation for the treatment of brain pathologies	137
4.1. Microdialysis:	137
4.1.1. Microdialysis with 8-arm-PEG@DFO	138
4.1.2. Microdialysis with DA ₂₉ @DOTAGA ₉	141
4.1.3. Conclusion	150
4.2. Hydrogel implants.....	150
4.2.1. Development of chelating biodegradable fibers “proof of concept” publication	150
4.2.2. Synthesis of a chelating fiber for implantation in PD monkey model	177
4.2.3. Swelling of the chosen fiber in physiological saline.....	179
4.2.4. Mechanical properties of the chosen fiber	180
4.3. Conclusion	181
V General conclusion and outlook.....	183
Annexes	185
VI Bibliography:	214

Introduction

The human body is primarily composed of organic elements, namely oxygen, carbon, hydrogen, and nitrogen. These elements represent the majority of body mass, with oxygen accounting for 61.4%, carbon for 22.9%, hydrogen for 10.0%, and nitrogen for the remaining proportion. Additionally, there are seven essential "macro-minerals" crucial for bodily functions: sodium (Na) at 0.1%, potassium (K) at 0.2%, calcium (Ca) at 1.7%, magnesium (Mg) at less than 0.1%, chlorine (Cl) at 0.1%, phosphorus (P) at 1.1%, and sulphur (S) at 0.2% [19].

Moreover, there are nine essential "trace elements" present in the body in low concentrations: iron (Fe), manganese (Mn), copper (Cu), zinc (Zn), selenium (Se), cobalt (Co), nickel (Ni), molybdenum (Mo), and iodine (I). In total, there are 23 essential elements crucial for the proper functioning of the body [20].

There are also non-essential metals present in the body such as Aluminium (Al) Lead (Pb) Cadmium (Cd) strontium (Sr) rubidium (Rb) titanium (Ti) [19]. These elements are referred to as non-essential because they lack any known physiological function in the body. They are typically absorbed due to their similarities with essential minerals [21].

In this work, we focus on metals, hence it is important to evaluate the toxicity of these elements. The toxicity of the elements we study may vary depending on their type, dosage, and frequency of exposure, or lack thereof [19,20]. For instance, the physiological response of essential elements follows the Bertrand diagram depicted in figure 1. When the concentration of these elements aligns with physiological conditions, no toxic effects occur [19,20]. However, when this concentration range is exceeded or decreased, the body can no longer function normally, leading to damages that may result in death [19,20].

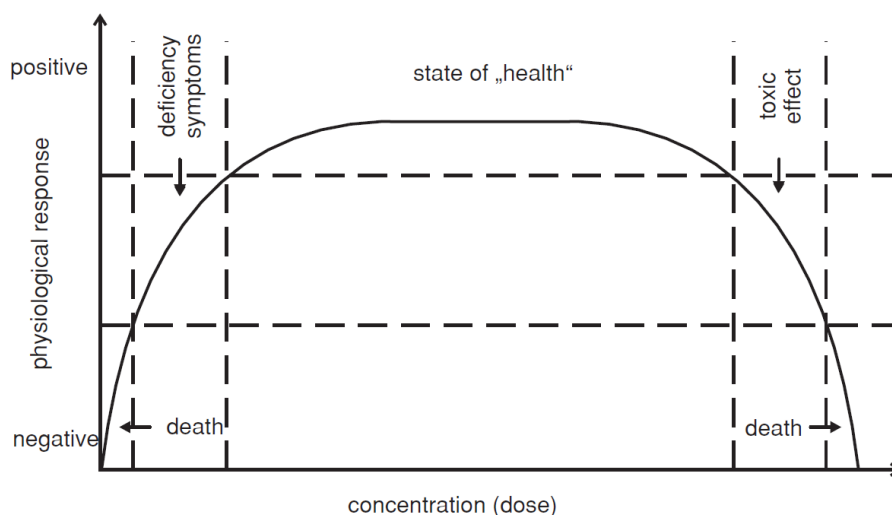


Figure 1. Bertrand diagram, taken from Kaim *et al.*, 2013 [19]

In contrast with essential elements, non-essential elements lack a biological function, thus they don't possess a defined range of healthy concentrations in the body. Even small doses of non-essential elements could be hazardous. Instead, there exists a tolerance concentration threshold where no negative physiological responses are observed [22].

Disruption of the body's homeostasis can lead to several pathologies, such as iron dysregulation in hemochromatosis and copper imbalance in Wilson's disease [23]. In recent years, localized brain dyshomeostasis has been linked to multiple neurodegenerative diseases, including Parkinson's disease, Alzheimer's disease, Friedreich's ataxia, and Huntington's disease [24]. Elevated levels of essential metals, such as copper, manganese, and iron, as well as non-essential metals like aluminium, have been observed in affected regions of the brain [25–29]. The accumulation of these metals is a gradual process, which makes it difficult to establish a direct causal link between metal build up and the progression of neurodegenerative diseases [24].

In these pathologies, the excess metals found in certain brain areas are often loosely bound to proteins or small molecules, unlike healthy metals that are tightly bound to proteins. These loosely bound or “free” metals are believed to play a role in the oxidative damage observed in neurodegeneration [30–34].

Currently, there are no effective treatments to stop or slow the progression of neurodegenerative diseases. As a result, the use of chelators to extract harmful metal cations has emerged as a promising therapeutic avenue. However, traditional chelation therapy is limited in its ability to target metal accumulation in the brain due to the systemic distribution of chelating agents, which has led to mixed results in clinical trials [26,28,35].

To address the limited localized chelation obtained with classic chelation therapy the project ANR-SEMB was established. In this context during my PhD, the use chelating polymers to enhance microdialysis localized metal extraction was proposed as a possible solution. In addition, I developed chelating, biocompatible, and biodegradable materials using chitosan derivatives previously developed by our research team. Moreover, I successfully enhanced the iron (III) chelation properties of these materials by functionalizing them with a more potent and selective iron (III) chelator.

Chapter I: Metal dyshomeostasis and neurodegeneration

1.1. Toxic Mechanisms of Metals

1.1.1. Oxidative stress

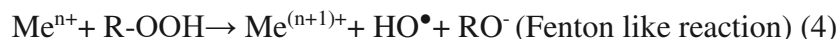
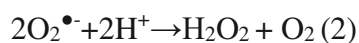
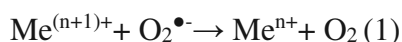
Oxidative stress is defined as a disturbance in the balance between the production of oxidative species and antioxidant defences, which may lead to tissue injury [36]. It is caused by reactive oxygen species (ROS), reactive nitrogen species (RNS), or by the products of lipid peroxidation [37]. Most of these oxidant species are categorized as free radicals. Free radicals are molecules or molecular fragments with one or more unpaired electrons, which gives them considerably high reactivity [30,36]. The most common radicals are the hydroxyl radical (HO^\bullet), superoxide anion ($\text{O}_2^{\bullet-}$), and nitric oxide (NO^\bullet) [36]. The superoxide radical does not directly react with polypeptides, sugars, or nucleic acids. However, it is considered a primary ROS due to its ability to generate secondary ROS, such as hydroxyl radicals. Hydroxyl radicals are among the strongest oxidizing agents and can readily attack most biological molecules [36]. They generally react by hydrogen abstraction, electron transfer and addition reactions [30]. Cellular structures rich in lipids like cell membranes are specially sensible to hydroxyl attacks since they can initiate radical chain reactions, ultimately leading to cellular death [30,36].

Free radicals are produced naturally in the body by various biochemical processes. Additionally, they can be generated in response to electromagnetic radiation from the environment and acquired directly from oxidizing pollutants such as ozone and nitrogen dioxide [36]. Fortunately, the body has mechanisms to protect against free radical damage by producing enzymatic and non-enzymatic antioxidants [30]. One of the most effective classes of antioxidants is thiol compounds, such as glutathione, which protect by trapping radicals and reducing peroxides [36]. Other examples of non-enzymatic antioxidants include vitamin E, which stops the propagation of free radical chain reactions in lipid peroxidation, and vitamin C, which also prevents lipid peroxidation [30,36]. In the category of enzymatic antioxidants, there are enzymes such as peroxidases and catalases, which reduce hydrogen peroxide into water [38].

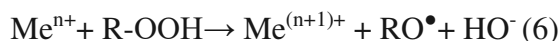
The redox properties that make essential metals beneficial for biological processes can also have detrimental effects [30,39]. For example, redox-active essential metals such as copper(I), iron(II), and manganese(II) can react with naturally produced H_2O_2 via the Fenton reaction (eq 3), generating highly reactive hydroxyl radicals. It's important to note that not only essential elements but also nonessential elements like chromium(III/IV/V) and vanadium(IV) can participate in the Fenton reaction and contribute to the production of radicals (eq 3) [30,33].

For the continuous production of hydroxyl radicals via the Fenton reaction, metals must be reduced. This reduction can occur in the presence of superoxide radicals (eq 1). The combined reaction, known as the Haber-Weiss reaction (eq1-3), involves the metal acting as a catalyst for hydroxyl radical production [30]. Moreover, metals can also be reduced by biological reductants such as ascorbate or thiol compounds [30]. H_2O_2 is not the only reactant capable of producing hydroxyl radicals through metal oxidation. Compounds with the R-OOH structure

can also follow Fenton like reactions, where R is the carbon chain of lipids in the case of lipid peroxidation (eq 4) [30].



The Fenton and Haber-Weiss reactions are not the only chemical reactions involving metals that produce radicals. Metals such as iron(II) and vanadium(IV) can also react with oxygen to generate superoxide radicals (eq 5) [30,32,33]. Additionally, iron(II) can react with R-OOH compounds to form highly reactive alkoxy radicals (eq6) [30].



Redox-inactive metals, such as aluminium(III) and lead(II), can indirectly induce oxidative stress. These metals can bind to the superoxide radical, enhancing its oxidizing capacity [40]. Additionally, aluminium(III) has been shown to facilitate iron-mediated lipid oxidation by binding to phospholipids in cell membranes. This binding alters the membrane structure, making the acyl chains more susceptible to attack by ROS [40]. Another mechanism by which metals can promote a pro-oxidant environment is by strongly binding to antioxidant molecules, rendering them inactive. For example, heavy metals like lead(II) have a high affinity for thiol groups, particularly those present in the antioxidant glutathione [41].

In healthy individuals, essential metals are primarily bound to enzymes and proteins, sterically hindering their interaction with other molecules in the environment and preventing undesirable side reactions [30]. This is especially crucial for iron, the most abundant redox-active transition metal within cells [30]. Approximately 60-80% of iron is bound to haemoglobin (as iron(II)), 10-20% is stored in ferritin (as iron(III)), 3.5% is bound to myoglobin in muscles (as iron(II)), and around 0.1% circulates in the bloodstream as iron(III) bound to transferrin [42,43]. Similarly, in the blood, copper is primarily bound to ceruloplasmin, the main copper transporter, as well as transcuprein and albumin. Within cells, copper is bound to enzymes like superoxide dismutase and cytochrome c oxidase and stored in metallothioneins [31]. In healthy patients, only a small proportion of these essential metals exist as free or labile forms, loosely bound to proteins or small molecules. These free metal ions are more susceptible to producing radicals following the mechanism previously explained [30–34]. Studies have shown that the concentration of free iron, also known as non-transferrin-bound iron (NTBI), is very low in healthy individuals, often below detectable levels (0-1 μM) [30,44]. Similarly, intracellular free copper pools are limited to less than one free copper ion per cell in healthy patients [30]. However, in various neurological pathologies associated with metal dyshomeostasis, the levels of free metals increase, leading to metal overload and overwhelming the previously mentioned regulatory mechanisms. This can result in increased radical production (The specific

neurological pathologies associated with elevated free metal pools will be discussed in detail later in the text) [25–27]. For instance, excess free iron accumulation in cells can induce oxidative stress, leading to ferroptosis, a form of cell death characterized by lipid peroxidation and subsequent plasma membrane rupture [45]. Additionally, non-essential metals like cadmium(II) are believed to indirectly increase radical production by replacing iron and copper in proteins, leading to elevated levels of free metals and, consequently, increased radical generation [30].

1.1.2. Induction of inflammation

Macrophages (microglia in the case of the central nervous system (CNS)) are a major actor in the inflammatory response, displaying remarkable functional diversity, they mostly exist in two distinct phenotypes [32,46–48]. M1 macrophages are often referred to as classically activated macrophages and are closely associated with the initiation of the pro-inflammatory response [46,48]. They play a crucial role in combating invading pathogens by releasing inflammatory mediators [46,47]. On the other hand, M2 macrophages, also known as alternatively activated macrophages are involved in tissue repair and wound healing. They promote the resolution of inflammation [32,46–48].

Pro-inflammatory macrophage activation is triggered by stimuli indicating infection or danger, including cytokines such as tumour necrosis (TNF- α) and interleukins (e.g. IL-1, IL-6, IL8) [46–48]. These pro-inflammatory cytokines suppress the expression of the iron exporter ferroportin, leading to intracellular iron sequestration within the macrophage [46]. This iron accumulation may serve as a host defence mechanism, limiting its availability to invading pathogens [46]. Iron accumulation has been shown to enhance the expression of mitogen-activated protein kinases (MAPKs), leading to the phosphorylation of kinase 2 (MK2) and subsequent TNF- α production promoting the proinflammatory response [46,47]. Iron accumulation within M1 macrophages has been implicated in the development of a persistent proinflammatory state as observed in autoimmune diseases[32]. Furthermore, the production of ROS by physiological process like NADPH oxidase or by metals such as iron, aluminium, lead, cadmium, and nickel can disrupt multiple transcription signalling pathways (e.g., MAPK, NLRP3-ASC-caspase 1, Src family kinases, and NF- κ B) [40,41,47–49]. This disruption can also contribute to an increase in the pro-inflammatory response by the macrophage/ microglia, marked by the production of cytokines like IL-8, IL-6, and TNF- α [32,40,41,47–49]. Additionally, the impairment of antioxidant mechanisms by heavy metals like cadmium and lead can further exacerbate the pro-inflammatory state [41].

1.1.3. Interference with enzyme activity

As previously explained, some non-essential elements have properties similar to those of essential metals. Due to these similarities, non-essential metals can replace essential metals in the body, often in an antagonistic manner. For example, cadmium(II) can replace zinc(II), lead(II) can replace calcium(II), and aluminium(III) can replace iron(III) [19,50].

The replacement of essential metals by non-essential metals can have multiple deleterious consequences, such as inhibiting the proper functioning of enzymes. For example, zinc is a metal found in many proteins and enzymes. zinc(II) is primarily complexed with cysteine and histidine, two amino acids present in these proteins, and serves a structural role [51]. Displacing

zinc alters the protein structure, rendering the enzyme inactive, which affects the proper functioning of the body [52,53]. Cysteine has a unique feature compared to other amino acids: it is one of the four common sulfur-containing amino acids and the only one incorporated into proteins that has a sulfhydryl function [54]. This sulfhydryl group exhibits a higher affinity for heavy metals such as Cd(II) and Pb(II) due to their classification as "softer" acids compared to Zn(II), based on the principles of HSAB theory. Additionally, it demonstrates a comparable affinity for both Cu(II) and Zn(II), as they have similar "hardness" (Table 2) [55,56]. Consequently, zinc finger structures in DNA repair enzymes are sensitive targets, and the displacement of Zn(II) by other transition metals (Cd(II), Cu(II), Ni(II), and Co(II)) results in inhibition [52]. Cadmium, for example, has been found to interfere with at least three DNA repair pathways: base excision repair, nucleotide excision repair, and mismatch repair [53].

The displacement of metals in enzymes is not the only way metals affect enzyme activity. Enzymes, especially their catalytically active subunits, contain sulfhydryl and amine functions. Exposure to non-essential metals (e.g., Cd(II) and Pb(II)) can lead to the binding of these cations to the sulfhydryl group, resulting in enzyme inhibition. This can be observed in Na⁺/K⁺-ATPase and Mg²⁺-ATPase enzymes when exposed to these heavy metals [57]. Moreover, essential metals like Cu(II), Fe(II), and Co(II) can also inhibit enzyme activity by binding to the sulfhydryl function in the enzyme's active site. This inhibition depends on the affinity of the cation for the protein [57].

1.1.4. Neurological effects

For optimal function, the brain requires a stable chemical environment. This high level of sensitivity necessitates multiple mechanisms to safeguard its delicate balance [58]. Two critical barriers play this role: Blood-Brain Barrier (BBB): Separates blood circulation from the brain's interstitial fluid, strictly regulating the passage of molecules and Blood-Cerebrospinal Fluid Barrier (BCB): Separates blood from cerebrospinal fluid (CSF), further protecting the brain from harmful substances (Figure 2) [58].

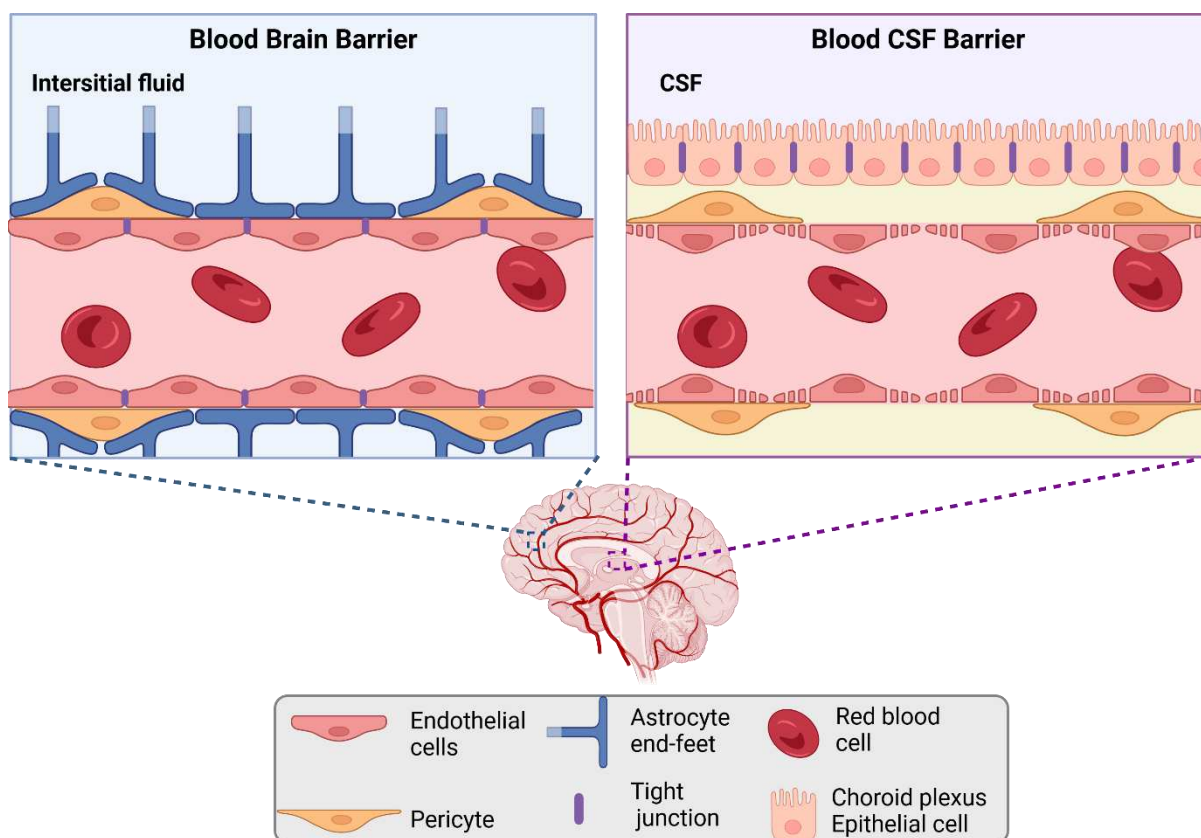


Figure 2. Schematic representation of the blood-brain barrier (BBB) and blood-CSF barrier. Created with BioRender.com.

Breaching the brains defence:

While metals can have diverse effects in the body, here we focus on their potential damage to the brain. These toxic metals can be categorized based on their interaction with the brain barriers in three different categories, general barrier toxicants, selective barrier toxicants and sequestered barrier toxicants [58].

General barrier toxicants are considered the most damaging to barrier structures. Examples of these metal toxicants include lead, cadmium, mercury, arsenic, and aluminium [49,58–60]. They accumulate within the barrier, disrupting its function in several ways [49,58–60]. Reducing membrane fluidity as well as increasing its lipophilicity thus hindering proper functioning of membrane proteins essential for selective transport [40,49,58,59]. They weaken the barriers physical integrity by causing cytoskeletal alterations opening the tight junctions and promoting an enhanced pinocytotic activity allowing more toxins to arrive to the CNS [40,49,58–60].

Unlike general toxicants **selective barrier toxicants** (including manganese and copper, with lead to a lesser extent) don't directly alter barrier permeability [58]. Instead, they selectively interfere with specific regulatory functions of the barriers, leading to neurotoxic consequences [58]. Manganese, while not directly damaging the barrier, it can disrupt its ability to regulate iron homeostasis within the brain [58]. The similar properties of manganese and iron (e.g., ionic radius, electron configuration, high affinity towards transferrin) allow manganese to

compete with Fe transport mechanisms [61]. Studies show that Mn exposure can decrease plasma iron levels while increasing iron concentration in the CSF [58,61]. Similar to manganese, copper itself doesn't damage the barriers. However, its presence can also alter iron transport into the brain, as evidenced by decreased iron influx in rats fed with a high-copper content diet [58].

The last category consists of the **sequestered barrier toxicants**, including iron, zinc, gold, and silver. These metals might be deposited or sequestered in the BBB as a defence mechanism [58]. The sequestration of these metals in the barriers does not provoke any known harmful consequences to the barriers according to the current literature [58]. For instance, when there is an increase in iron concentration, endothelial cells of the blood-brain barrier can accumulate the excess iron. However, when these storage mechanisms are overwhelmed, iron can enter the brain tissue, where it may induce oxidative stress [30,37,58].

Metal overload will affect not only the membranes but also the entire CNS. The brain is particularly vulnerable to oxidative damage due to its high oxygen consumption, low levels of antioxidant defences compared to other cells, and abundance of highly polyunsaturated fatty acids that are sensitive to radicals [49]. Following the same radical formation mechanisms explained earlier, metals such as manganese(II/III), copper(I/II), iron(II/III), aluminium(III), lead(II) and cadmium(II) can increase the production of radicals [30–33,61]. Moreover, the increase in free radicals will activate microglia, inducing a pro-inflammatory response through the release of pro-inflammatory factors. The presence of excess metals will further exacerbate the inflammatory response, causing additional damage [48,49].

Another type of damage caused by metals, which is particularly evident in the CNS, is the disruption of neuronal communication. Heavy metals like Pb(II) can substitute for Ca(II) and enter neurons through calcium-ATPase pumps, disrupting synapse formation, which is essential for brain communication [33,49,62,63]. Cd(II) as well as Pb(II) can disrupt the proper proton gradient across the synaptic vesicle membrane, affecting the correct release of neurotransmitters such as glutamate and GABA [33,64]. Additionally, the accumulation of metals like aluminium(III) can alter the structure of myelin, the fatty sheath that insulates nerve fibers, further disrupting nerve impulses [40].

The diverse mechanisms by which metals exert their toxic effects on the CNS ultimately translate into neuronal injury. This damage manifests as a range of neurocognitive impairments, including learning and memory deficits [40,49]. A compelling example is the established link between blood lead levels and cognitive function in children. Epidemiological studies demonstrate that for each 1 µg/ml increase in blood Pb levels within the range of 5-35 µg/ml, children experience a 2-4 point decrease in IQ scores [40]. Furthermore, growing evidence suggests a potential role for heavy metals in the development of neurodegenerative diseases like Parkinson's (PD) and Alzheimer's disease (AD) [27,30,37].

1.2. Metal overload in the brain

Building upon the discussion of metal toxicity mechanisms in the previous section, we will now explore the specific links between metal overload and various neurodegenerative diseases. This section will delve into how the different mechanisms outlined earlier contribute to the

pathogenesis and progression of diseases where excess free metals play a significant role. These diseases include Manganism, Wilson's disease, Friedreich ataxia (FA), and neurodegeneration with brain iron accumulation (NBIA). Additionally, we will discuss how excess metals could contribute to the progression of diseases where the underlying cause remains unclear, such as PD, AD, Huntington's disease (HD) and strokes. For each disease, we will discuss the origin of the disease, the role of metals in the disease, current available treatments, and exploratory treatments involving metal extraction by chelation therapy

1.2.1. Neurological disorders directly related to metal dyshomeostasis in the brain

1.2.1.1. Manganism

Manganism is a neurological disorder first described by James Couper in Scottish industrial workers who were chronically exposed to manganese oxide dust [29,65]. It is characterized by elevated levels of manganese in specific brain structures, particularly the basal ganglia, including the caudate putamen, globus pallidus, substantia nigra, and subthalamic nuclei [65]. Neuroimaging, particularly MRI, is valuable for diagnosing and assessing tissue damage in Manganism. Due to its highly paramagnetic properties and high magnetic susceptibility manganese deposits exhibit a characteristic MRI signature, displaying symmetrical hyperintensities primarily in the globus pallidus, periaqueductal gray matter, and cerebral peduncles. These abnormalities are less pronounced in the putamen and white matter when viewed on T1-weighted MRI images (Figure 3) [66,67]. While the neurological symptoms of manganism share some similarities with PD, manganism typically presents with milder and less frequent resting tremors, which are often postural or action tremors. It's important to note that there can be significant variability in PD symptoms among patients. [61,68,69]. Additionally, people with manganism may experience a tendency to fall backward, excessive drooling, and frequent dystonia which is often associated with damage to the globus pallidus [61,66,68]. The motor and behavioural effects of manganese toxicity are generally considered irreversible, and there is evidence that these effects can even progress after chronic exposure has ceased [69,70]. The primary route of manganese exposure leading to manganism is inhalation of manganese dust in industrial settings [65,66]. The body typically eliminates excess manganese through the gut and liver. However, inhaled manganese particles bypass these elimination pathways and can directly enter the brain through the olfactory epithelium. Since the brain has limited capacity to remove manganese, it accumulates over time, leading to neuronal damage [68]. Manganese-induced neurotoxicity is thought to involve the generation of ROS within mitochondria. Manganese can be oxidized from Mn(II) to Mn(III) within these organelles. Mn(III) is a potent pro-oxidant, disrupting mitochondrial function and increasing apoptosis [29,70,71]. As mentioned earlier, ROS production triggers an inflammatory response in the brain. Additionally, manganese exposure can activate glial cells to release neurotoxic factors, potentially contributing to the degeneration of dopamine-producing neurons [29,70,71]. Chronic manganese overexposure can also lead to the progressive misfolding of a protein called α -synuclein within neurons. This misfolding further contributes to the inflammatory response and neurodegeneration [68]. Furthermore, manganese exposure can disrupt the brain homeostasis of other metals, such as iron [58,61,70]. This can further increase oxidative stress and contribute to neuronal damage [70].

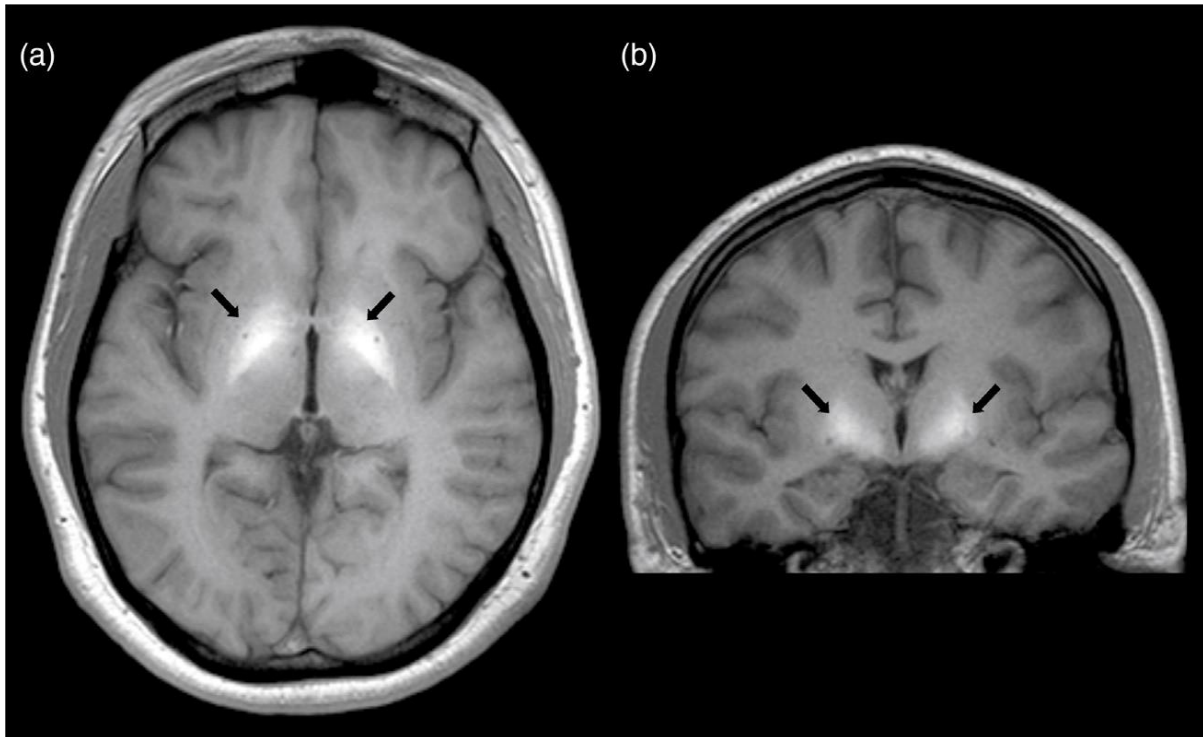


Figure 3. Brain MRI of a patient with manganism. Hyperintensities are shown in globus pallidus in (a) axial and (b) coronal T1-weighted image (black arrows) taken from Dusek and Aaseth, 2016 [66].

The first line of therapy for manganese intoxication is to prevent further exposure by removing the patient from the source [70]. Treatment strategies then aim to lower the overall body burden of manganese in manganism patients. This involves increasing manganese excretion in the urine and decreasing manganese concentrations in the blood [70]. One potential treatment approach is chelation therapy. EDTA (CaNa_2EDTA), an hydrophilic chelator administered intravenously, has been used for manganism [66,69,70,72]. However, it shows limited efficacy in treating both acute and chronic manganese poisoning [42-45]. Even though EDTA may increase urinary manganese excretion, it often fails to improve clinical symptoms [66,69,70,72]. This is likely because its structure makes it insufficiently lipophilic to cross the BBB [70]. Consequently, EDTA likely chelates manganese primarily in the extracellular fluid outside the brain, leaving the manganese accumulated within the brain untouched [70]. Research on alternative chelating molecules has yielded promising results. Para-aminosalicylic acid (PAS) is one such example [70,73]. A case study reported long-term recovery of normal handwriting, significant alleviation of symptoms, and a normal brain magnetic resonance imaging in a female patient with chronic manganese exposure who received PAS treatment [73]. In addition to its chelating properties, PAS possesses anti-inflammatory effects attributed to its salicylate moiety, potentially contributing to its therapeutic benefits [70]. However, PAS is associated with gastrointestinal side effects such as vomiting, nausea, and abdominal discomfort, limiting its tolerability [70]. Furthermore, high doses of PAS-Na ($5000 \mu\text{M}$) have demonstrated toxicity in primary basal ganglia neurons [70].

1.2.1.2. Wilson disease

Wilson disease is an autosomal recessive genetic disorder characterized by a defect in copper metabolism with a prevalence of 1:30000 worldwide [47–51]. This defect arises from mutations in the ATP7B gene, which encodes a copper transporter essential for biliary copper excretion [28,74–76]. The disease leads to a progressive accumulation of copper, primarily in the liver, but also in the brain, cornea, kidneys, and joints [47–51]. The brain is particularly vulnerable to copper overload in Wilson disease. The main areas affected are the basal ganglia, cortex, and brainstem nuclei, all located within the grey matter [75]. Despite being paramagnetic like manganese(II) and iron(III)/(II), copper(II) is less effectively detected by MRI due to its lower magnetic susceptibility. This property results in a weaker MRI signal compared to manganese(II) or iron(III)/(II) [66,67]. Instead, MRI primarily identifies the indirect consequences of metal toxicity on brain tissue. In the case of copper overload, MRI typically reveals nonspecific findings such as hyperintensities in the basal ganglia and white matter on T2-weighted images. These abnormalities are often attributed to tissue oedema, demyelination, and cavitation, which are common features of encephalopathy [66] (Figure 4)

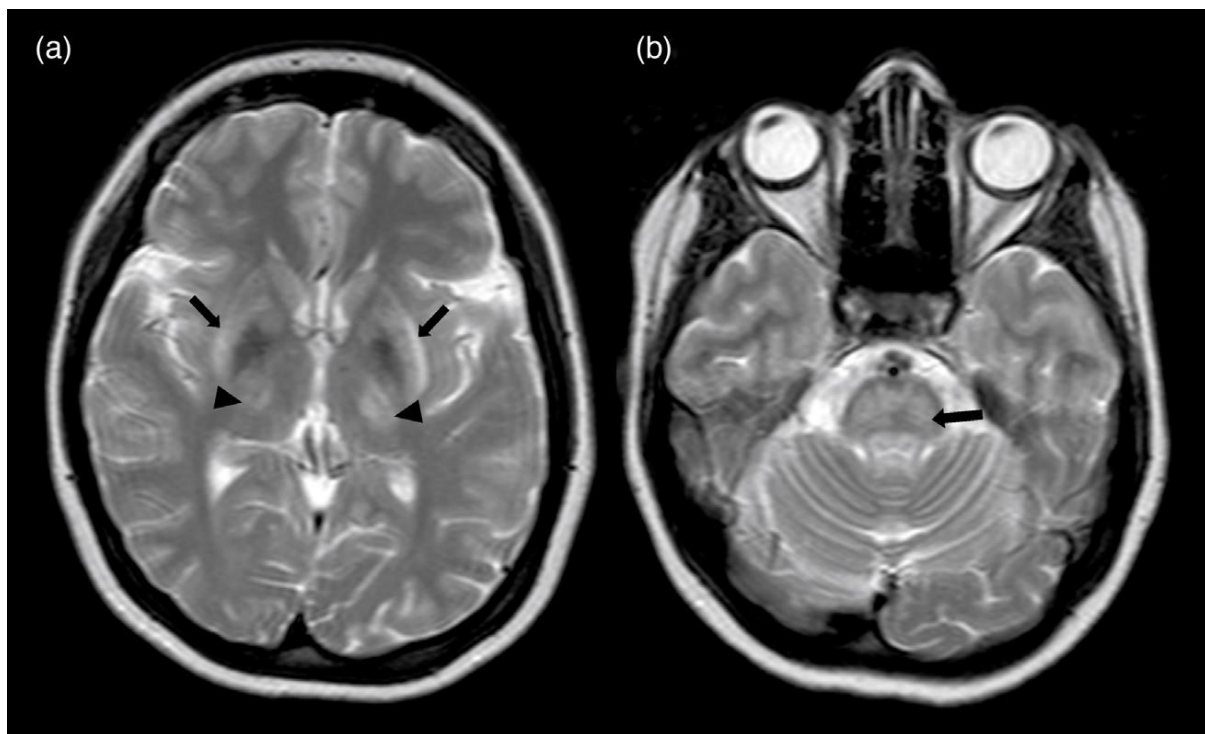


Figure 4. Typical brain MRI findings in Wilson's disease (a) T2-weighted image demonstrating symmetric hyperintensities in the putamen (black arrows) and thalamus (arrowheads), indicative of demyelination, cavitation, and oedema. (b) T2-weighted image showing increased signal in the pontine white matter (black arrow), reflecting demyelination from Dusek and Aaseth, 2016 [66].

The excess copper is primarily "free copper," unbound to carrier proteins like ceruloplasmin [23]. This free copper readily generates ROS, leading to oxidative damage to brain cells. The oxidative nature of the damage supports the link between excess copper and neurodegeneration in Wilson disease [23,28,74]. Restoring copper homeostasis is the cornerstone of Wilson disease treatment. Due to the lifelong nature of the copper accumulation defect, lifelong

medical therapy is essential [23,74]. Ideally, treatment follows a two-phase approach: Initial, acute de-coppering therapy: This phase aims to rapidly reduce excess copper stores in the body [23,74,76]. Maintenance therapy: This long-term phase aims to prevent further copper accumulation and maintain normal copper levels [23,74,76].

Multiple chelating agents have been developed for copper removal in Wilson disease. These include D-penicillamine, trientine, and tetrathiomolybdate [23,28,56,74–76]. Chelating agents bind free copper found in blood and tissues to facilitate its excretion and provide a negative copper balance [23,28,56,74–76].

D-penicillamine (Table 1) is the most common chelating agent used for Wilson disease, acting as the first-line treatment [23,28,74]. It works by chelating copper and promoting its excretion in the urine. While effective in reducing copper overload, D-penicillamine can cause side effects, including neurological worsening, in a significant portion of patients [23,28,74,75]. This may be due to the rapid release of copper from the liver, leading to a temporary increase in blood free-copper levels and higher exposure to the brain [23,74].

Trientine (Table 1), another chelator, also promotes urinary copper excretion but is less potent than D-penicillamine [23,28]. It serves as an alternative for patients who cannot tolerate D-penicillamine or as second-line therapy [23,28,56,74]. Similar to D-penicillamine, trientine can cause neurological worsening in some patients, although the side effects tend to be milder [23,28,74].

Tetrathiomolybdate offers an alternative to traditional chelators [28]. It forms complexes with copper and protein [23,28]. When taken with food, it reduces copper absorption in the gut. Taken between meals, it binds to albumin and free copper for excretion in the bile. This process mobilizes copper from tissues into the bloodstream and increases its excretion [23]. Studies have shown improvement in tremors for patients using tetrathiomolybdate [75].

Zinc salts are used as preventative therapy for neurological complications and as maintenance therapy after chelation therapy [23]. Zinc induces intestinal cells to produce metallothionein, a protein that binds dietary copper, preventing its absorption [23]. While slow-acting, zinc has minimal side effects [23].

Chelation therapy can significantly improve neurological abnormalities in Wilson disease, with positive outcomes like reduced dystonia after copper reduction [23,75]. These improvements can be sustained with long-term compliance to treatment [75]. However, limitations exist due to side effects associated with chelators [23,28,74,75]. Additionally, a partial response to chelation therapy in some patients suggests irreversible brain damage [74].

1.2.1.3. Friedreich's Ataxia (FA)

FA is an inherited neurological disease characterized by degeneration of the spinocerebellar tracts and cardiomyopathy [27,28,77,78]. Inherited as an autosomal recessive disorder, FA is caused by trinucleotide repeat extension in a gene in chromosome 9 leading to frataxin deficiency, a small mitochondrial protein crucial for iron-sulfur cluster synthesis [76,77,79]. Consequently, labile iron accumulates, particularly within the cerebellum's dentate nuclei (Figure 5), promoting oxidative stress and neurodegeneration [27,77–80]. The colocalization

of copper, zinc, and iron in affected brain regions suggests potential combined metal toxicity [77]. However, the exact role of iron in FA remains complex, with its primary or secondary nature in mitochondrial accumulation still under investigation [27,77]. Current therapeutic strategies mainly focus on reducing pathological iron accumulation to prevent free radical damage and mitochondrial dysfunction [27,77].

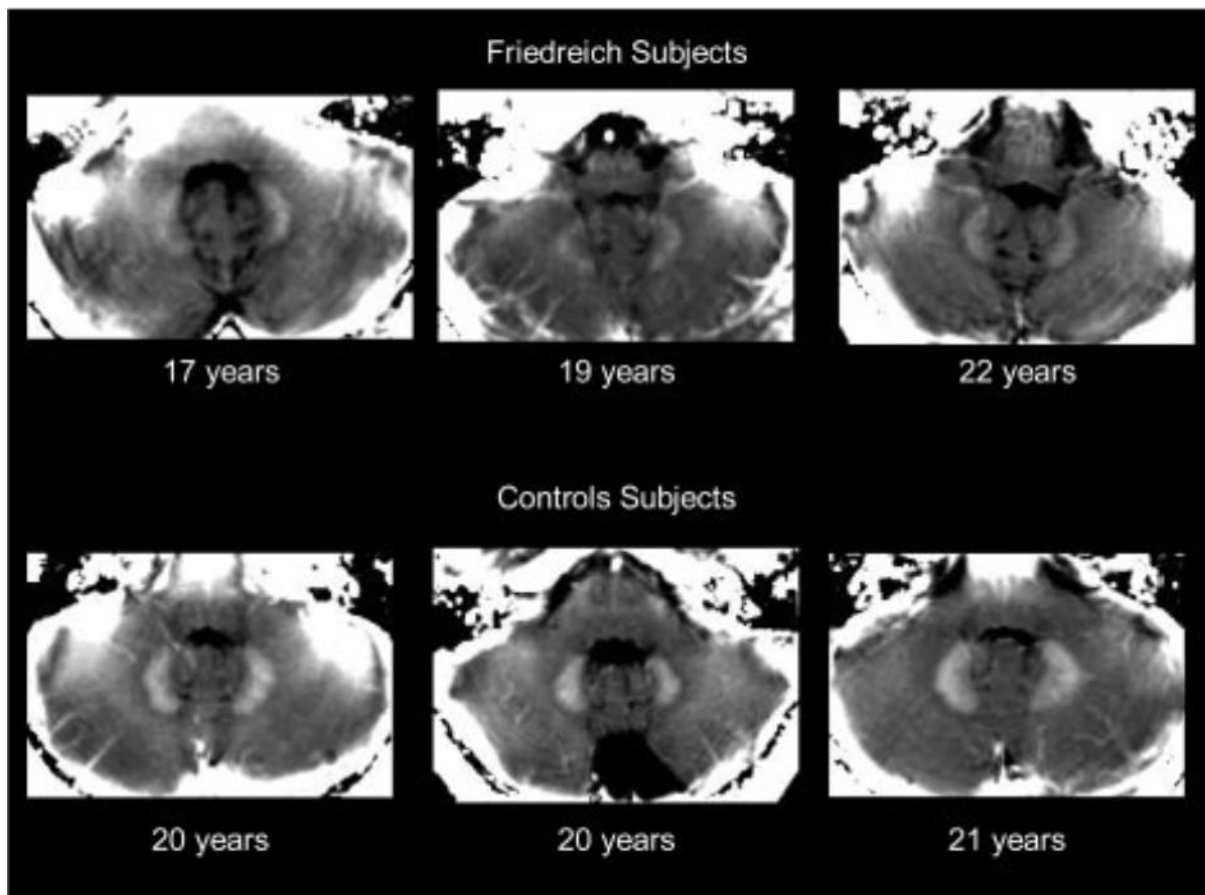


Figure 5. R2* mapping of dentate nuclei in Friedreich's ataxia showing iron accumulation. R2* maps of the posterior fossa using a multi-gradient echo sequence done at 1.5T in three young Friedreich's ataxia patients and three age-matched controls. Dentate nuclei exhibit increased R2* values (brighter signal) in FA patients compared to controls, with smaller, irregularly shaped nuclei. The adjacent cerebellum demonstrates consistent R2* values around 14 s^{-1} , indicating good regional magnetic field homogeneity. Taken from Boddaert *et al.*, 2007 [80]

In order to protect the body from the oxidative stress seen in FA, the use of antioxidants has been explored as a potential therapy [78]. Idebenone, an antioxidant molecule, has been studied with mixed results [77,78]. At low dosage (5mg/kg/day), its therapeutic effect is debated. However, a dose-dependent improvement of the International Cooperative Ataxia Rating Scale (ICARS) was observed in the IONIA study [78]. Conversely, the MICONOS study did not show any neurological improvement measured by the ICARS. Despite the mixed results found for idebenone, it continues to be used as a treatment for FA due to its lack of adverse effects and accessibility [78]. Other antioxidants tested, like coenzyme Q10, A0001, and EPI-743,

present small neurological improvements in the Friedreich Ataxia Rating Scale (FARS), except for coenzyme Q10 where no neurological improvement was observed [78].

Regarding the chelation of excess iron, multiple clinical trials have been conducted using the chelator deferiprone (NCT00224640 and NCT00530127) [80,81]. Deferiprone an oral bidentate chelator with high affinity for iron (III) (Table 1) used in the treatment of iron overload [28,82]. Preclinical studies on the effectiveness of deferiprone have shown reduced ROS damage to mitochondrial proteins in cells [78]. The first study was conducted on nine adolescent patients treated with a low dosage of deferiprone (20-30 mg/kg/day) [80]. Deferiprone administration efficiently and progressively decreased iron accumulation in the dentate nuclei in 8 out of 9 young FA patients, as shown by IRM R2* analysis. Moreover, neurological function slightly improved according to the ICARS, with additional improvements observed in gait and balance, dexterity, and mobility [80]. The second study involved a larger population (72 individuals) and various dosages (20, 40, and 60 mg/kg/day) [81]. Similarly, to the first study, patients treated with low doses of deferiprone (20 mg/kg/day) showed an acceptable safety profile; however, no significant improvement was seen using the FARS. In contrast, higher doses (>40 mg/kg/day) resulted in decreased neurological function, as shown by the ICARS and FARS [78,81]. These results indicate that while iron chelators like deferiprone show potential as a treatment for FA, further investigation is necessary to determine the optimal dosage, which appears to be low to avoid worsening patient outcomes [78,80,81]. In conclusion, no study has successfully achieved its stated endpoint, and results remain inconclusive or conflicting [78].

1.2.1.4. Neurodegeneration with brain iron accumulation (NBIA)

NBIA is a heterogeneous group of progressive neurodegenerative disorders characterized by extrapyramidal movements and the abnormal accumulation of iron in specific brain regions, primarily the basal ganglia [27,83,84]. The concept of NBIA was first proposed by Susan Hayflick in the mid-1990s [27]. Pathologically, NBIA syndromes are characterized by the degeneration of both neurons and astrocytes. Additionally, spheroid bodies, abnormal protein aggregates, are a common feature in many forms of NBIA [83].

Several genetic disorders fall under the NBIA umbrella, including:

- **Pantothenate Kinase-Associated Neurodegeneration (PKAN)**
- **CoA Synthase-Associated Neurodegeneration (COASY)**
- **PLA2G6-Associated Neurodegeneration (PLAN)**
- **Mitochondrial Membrane-Associated Neurodegeneration (MPAN)**
- **Fatty Acid 2-Hydroxylase (FAHN)**
- **Beta-Propeller-Associated Neurodegeneration (BPAN)**
- **Aceruloplasminemia**

PKAN is among the most common forms of NBIA [85]. Due to their prevalence and numerous clinical trials with chelators, this work will focus on this disorder.

PKAN

PKAN is a rare, autosomal recessive genetic disorder caused by mutations in the PANK2 gene located in the chromosome 20. This gene is responsible for producing the enzyme pantothenate kinase-2, which is essential for the production of coenzyme A (CoA) [27,83,85–87]. PKAN is a major subtype of NBIA, accounting for approximately 40% of cases [85]. It has an estimated prevalence of 1-3 cases per million people [87].

Furthermore, a key characteristic of PKAN is the accumulation of iron in the basal ganglia. This is visually represented on neuroimaging as the "eye of the tiger" sign, which consists of a central area of hyperintensity surrounded by a hypointense ring within the globus pallidus on coronal or axial T2-weighted images (Figure 6) [27,84,85,87]. In some cases, additional hypointensities may be observed in the SN, indicating iron deposition in this brain region as well [84,85,87]. It is noteworthy that the neuronal damage in PKAN is primarily confined to the globus pallidus and, occasionally, the SN [86]. The remaining regions of the brain typically appear normal on MRI, without evidence of atrophy, white matter lesions, or increased signal intensity outside of the basal ganglia [85,86].

There are two primary clinical phenotypes of PKAN:

- **Classic PKAN:** This is the most common form representing 75% of PKAN cases, typically presenting in childhood, often before the age of six [87]. Symptoms include gait abnormalities, postural instability, dystonia, rigidity, and speech difficulties. Disease progression is generally rapid [87]. A significant proportion of patients develop pigmentary retinopathy, characterized by night blindness, progressive peripheral vision loss, and eventually potential blindness [85,87]. Additional ocular symptoms include abnormal eye movements, sectoral iris paralysis, and changes in the appearance of the retina [85,87]. The pigmentary retinopathy is believed to occur early in the disease course, and individuals with normal initial eye exams are less likely to develop it later [87].
- **Atypical PKAN:** Onset is later, typically in adolescence or early adulthood with a mean onset on age 14 [87]. Symptoms are often milder and may include speech difficulties, mild gait disturbance, subtle dystonia, or neuropsychiatric features [87]. Disease progression is slower compared to classic PKAN [85,87]. Similarly to classic PKAN patient develop motor features later in their disease course with dystonia being the most common [87].

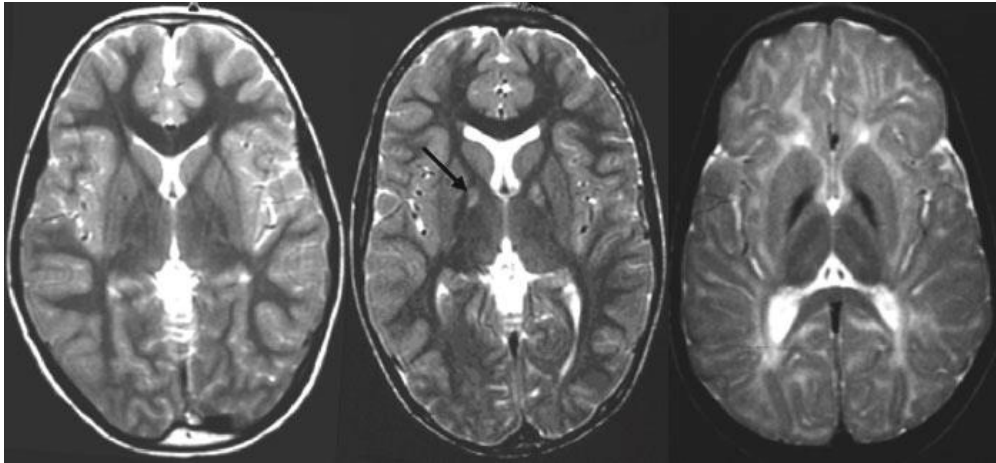


Figure 6. T2-weighted MRI scans comparing brain anatomy in a healthy individual (left), a patient with PKAN exhibiting the classic "eye-of-the-tiger" sign (centre, arrow), and a patient with a non-PKAN form of Neurodegeneration with NBIA displaying hypointensity in the globus pallidus, taken from Texel *et al.* 2012 [27].

PANK2 is one of four pantothenate kinase enzymes responsible for catalysing the conversion of dietary pantothenate to 4'-phosphopantothenate, a crucial intermediate in the biosynthesis of CoA. CoA is a cofactor involved in numerous metabolic pathways [84–87]. Although a decrease in CoA levels is generally associated with PANK2 deficiency, interestingly, normal total CoA levels have been reported in cells lacking functional PANK2. This suggests that other compensatory mechanisms may be involved or that the impact of PANK2 deficiency on CoA levels is more complex than initially thought [85]. PANK2 is primarily localized to the mitochondria and nucleus [85,87]. While the exact mechanisms underlying the pathogenesis of PKAN remain to be fully elucidated, mitochondrial dysfunction is believed to play a central role. One of the key functions of CoA within mitochondria is the activation of mitochondrial acyl carrier protein (mtACP) [84,86].

CoA-derived 4'-phosphopantetheine is essential for the activation of mtACP, which is involved in fatty acid synthesis, iron-sulfur cluster biogenesis, and electron transport [84–86]. Notably, this is one of the few reactions where CoA is consumed rather than recycled [86]. It is hypothesized that PANK2 deficiency leads to a reduction in CoA availability, resulting in impaired activation of mtACP and subsequent disturbances in mitochondrial iron-sulfur cluster biogenesis. This disruption in iron metabolism may contribute to the accumulation of iron [84,85]. *In vitro* studies have demonstrated cytosolic iron accumulation in astrocytes and neurons, suggesting that excitotoxicity or ferroptosis may contribute to the neurodegeneration observed in PKAN [84]. Furthermore, PANK2 dysfunction can lead to the accumulation of its substrates, cysteine and pantetheine. Cysteine has iron-chelating properties, and elevated levels of intracellular cysteine may contribute to secondary iron accumulation [87].

As with other neurodegenerative diseases discussed previously, there is currently no disease-modifying treatment available for PKAN. The primary medications prescribed for PKAN patients aim to manage the symptoms, particularly dystonia, which is often the most disabling

motor impairment. Trihexyphenidyl, clonazepam, and baclofen are commonly used for this purpose [85,87,88]. In recent years, there has been growing interest in novel therapeutic approaches for PKAN. DBS, a technique already used in PD, has shown promise in some cases. Additionally, supplementation with pantothenate has been explored, as anecdotal reports suggest potential benefits for motor function, speech, cognition, and overall well-being in patients with atypical PKAN[87].

Chelation therapy has emerged as a promising therapeutic approach for patients with PKAN. Initial case reports involving the metal chelator deferiprone, demonstrated promising results [89,90]. Both patients were treated with the same dose of 30 mg/kg/day. Both cases showed good tolerability to the treatment and a reduction in brain iron accumulation, as evidenced by MRI (Figure 7). Additionally, improvements in symptoms, such as gait and dyskinesia, were observed [89,90].

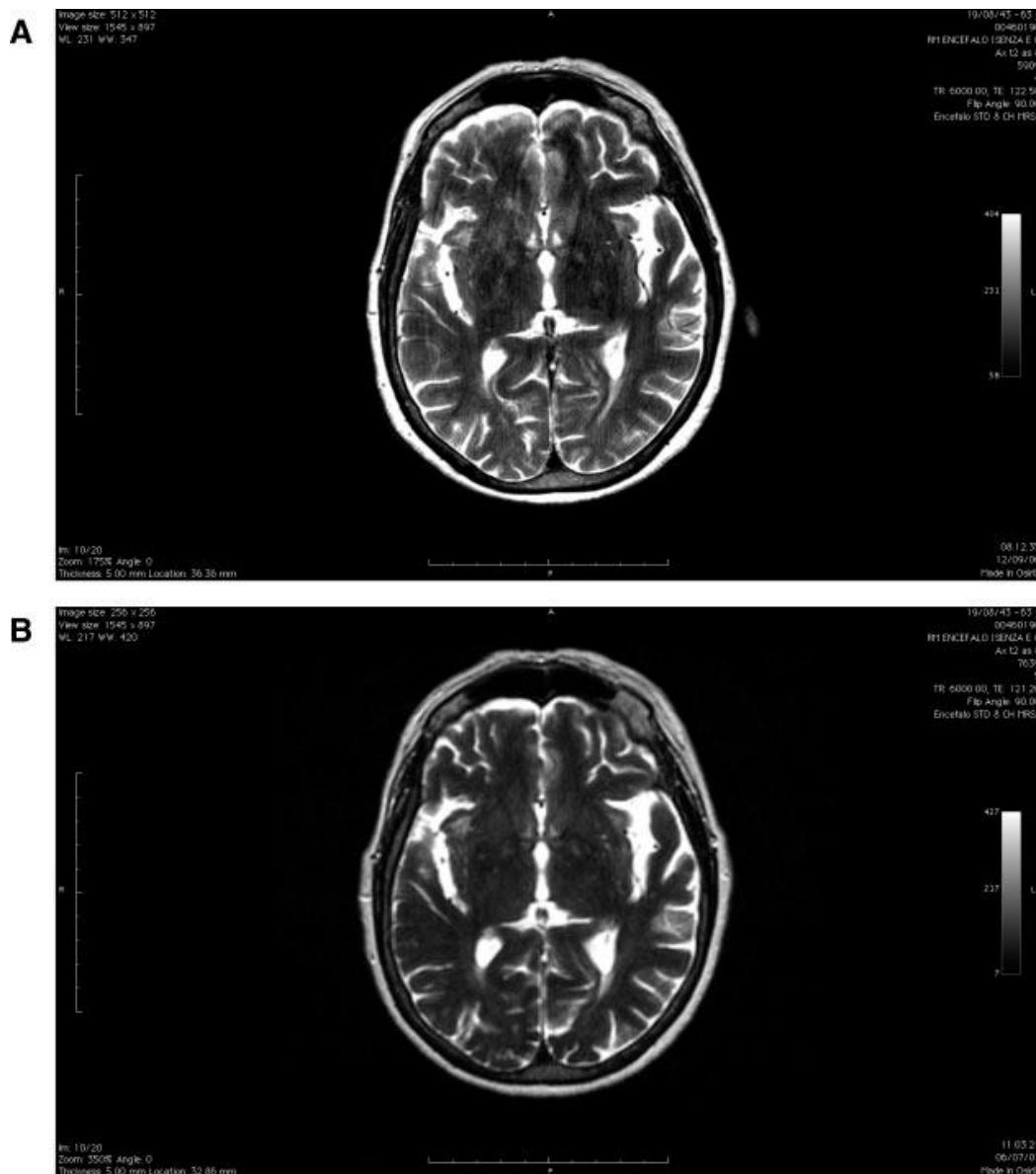


Figure 7. T2-weighted FAST-SE MRI scans of NBIA patient **A)** Despite the presence of uncontrolled head movements, which can compromise image quality, the basal ganglia were observed to be bilaterally hypointense compared to other grey matter structures. A subtle hyperintense rim was also noted surrounding the basal ganglia. Both the hypointensities and the hyperintense rim are indicative of iron overload within these brain regions. **B)** Following 7 months of iron chelation therapy, the MRI abnormalities observed in the basal ganglia were less prominent, suggesting a reduction in iron accumulation, from Forni *et al.* 2008 [89].

The promising findings from initial case reports have prompted the initiation of clinical trials to evaluate the safety and efficacy of deferiprone in the treatment of PKAN. A phase II pilot trial enrolled nine patients who received 25 mg/kg/day of deferiprone for six months. While the treatment was well-tolerated and led to a reduction in iron accumulation in the globus pallidus, as measured by MRI, no significant clinical benefits were observed [91]. A subsequent trial (NCT00907283) included six patients with NBIA, including five with PKAN, who were treated with 30 mg/kg/day of deferiprone for 48 months. Similar to the previous trial, the treatment was well-tolerated, and iron levels in the CNS were reduced. However, no clear clinical improvements were noted [92]. A third trial five PKAN patients treated with the same dosage demonstrated slight motor improvements at 12 months but no sustained benefits at 18 months [93].

A placebo-controlled, double-blind trial (NCT01741532) was conducted to evaluate the efficacy of deferiprone in treating PKAN [94]. The study enrolled 86 gene-confirmed patients and involved an 18-month treatment phase followed by a single-arm open-label extension phase. Participants in the deferiprone group received a daily dose of 30 mg/kg for 18 months. MRI analysis revealed a significant reduction in iron concentration within the globus pallidus in patients treated with deferiprone. Clinically, during the double-blind phase, deferiprone was shown to significantly slow disease progression in patients with atypical PKAN compared to placebo. However, no significant benefit was observed in patients with classical PKAN. During the open-label extension phase, patients who had previously received deferiprone continued to show no change in the rate of disease progression. Interestingly, patients who were switched from placebo to deferiprone during this phase experienced a significant slowing of disease progression [94].

1.2.2. Neurological disorders potentially arising from disrupted metal homeostasis within the brain

Recent studies have implicated metal dyshomeostasis in the pathogenesis of various neurodegenerative diseases. Elevated or reduced levels of certain metals have been observed in biological fluids and tissues of individuals affected by these disorders [24]. Establishing a causal link between metal accumulation and the initiation or augmentation of the neurodegenerative disorder is still controversial, increased metal levels may simple be caused by tissue loss [71]. In the following section, several neurodegenerative disorders involving metal dyshomeostasis will be discussed, with an emphasis on the specific role metals play in these conditions. Additionally, the potential use of chelation therapy as a treatment option will be explored.

1.2.2.1. Parkinson's disease (PD)

PD one of the most common neurodegenerative disease second only to Alzheimer disease (AD) with an estimated 6.1 million people being diagnosed in 2016 [27,95]. PD is a chronic, progressive neurodegenerative disorder primarily affecting the dopamine-producing neurons in the substantia nigra (SN) of the brain. Initially described by James Parkinson in 1817, PD is characterized by motor symptoms such as resting tremor, rigidity, bradykinesia, and postural instability [27,37]. The underlying pathological hallmark of PD is the accumulation and aggregation of α -synuclein protein within neurons, leading to progressive neurodegeneration [96]. This process ultimately results in dopamine depletion in the striatum, disrupting normal brain function [27,37,96]. In the early stages, neuronal loss is predominantly confined to the SN, but as the disease progresses, it becomes more widespread [96].

Dopaminergic neurons, despite constituting less than 1% of total brain neurons, play a critical role in motor behaviour, working memory, mood, addiction, and stress regulation [27]. Their degeneration in PD underlies the characteristic motor impairments [27]. These neurons are believed to be particularly vulnerable to oxidative stress due to their high metabolic rate, limited antioxidant defences, and elevated iron levels [27,96]. Post-mortem studies reveal increased oxidative stress in the substantia nigra pars compacta (SNpc), supporting the role of oxidative damage in nigral cell degeneration [37]. Additionally, the onset of PD is accompanied by the depletion of antioxidant defences, such as glutathione, in the SN, which increases the risk of oxidative damage [37].

The SN exhibits one of the highest iron concentrations in the human body, comparable to that of the liver [27]. Post-mortem studies using iron-sensitive high-field MRI with quantitative T2* mapping have consistently demonstrated increased iron deposition in the SN of PD patients compared to controls (Figure 8) [28,97]. These findings have also been replicated in animal models of PD [97]. Thomas *et al.* 2020 utilized Quantitative Susceptibility Mapping (QSM), an emerging MRI technique that detects local variations in iron content, to study 100 PD patients [98]. They found an excess of iron in brain tissue compared to controls along the cortical ribbon in the prefrontal cortex, the right rostral putamen, the right temporal cortex, and the SN, but no significant increase at the whole-brain level [98]. Using QSM, they also identified a correlation between increased iron in the putamen and poorer motor function. PD is characterized by the loss of dopaminergic projections from the SN to the putamen, and the putamen has a strong relationship with motor function in PD, as observed in post-mortem studies [98].

Moreover, since iron overload is thought to occur early in neurodegeneration, differences in motor ability may be better explained by QSM variations in regions like the putamen rather than the SN, where iron excess is present before a decrease in motor function is observed [98]. This is particularly relevant since SN degeneration starts before the onset of motor symptoms [96].

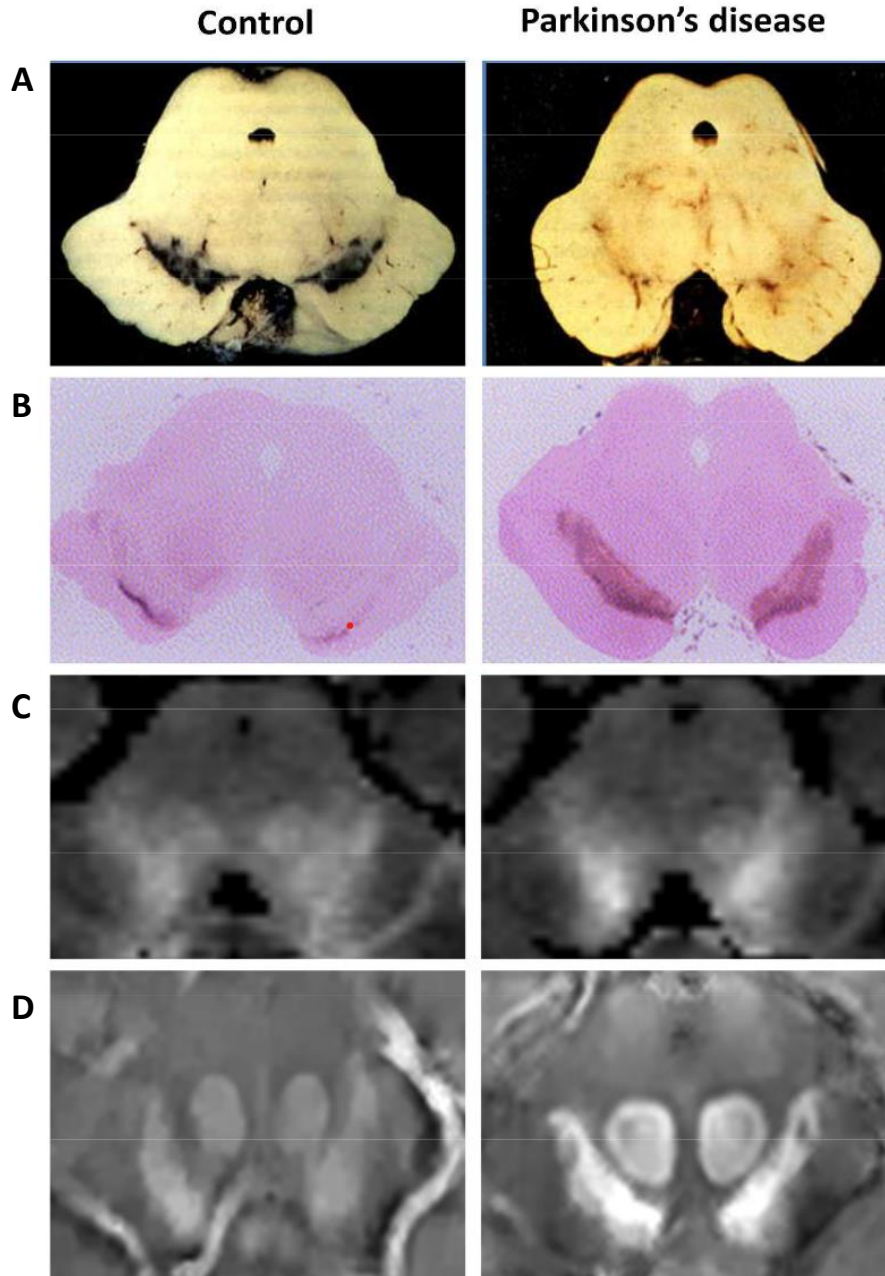


Figure 8. **A:** Post-mortem analysis of the mesencephalon in PD reveals significant neuropathological changes. Dopaminergic neurons, which are naturally stained black due to dopamine auto-oxidation, are markedly depleted in PD. **B:** iron accumulation within the SN is evident upon Perls staining. **C:** QSM allows for the visualization of iron deposits, revealing a hyperintense SN in PD compared to controls. **D:** MRI quantitative T2-weighted imaging demonstrates increased signal intensity in the SN of PD patients, indicative of iron overload. Images taken from Moreau et al., 2018 [97].

Iron is thought to contribute to dopaminergic cell death by catalysing the production of ROS from hydrogen peroxide, a by-product of dopamine catabolism [99]. Despite the low concentration of iron in the SNpc (25% less iron than adjacent SNpc tissue), iron is still considered a factor of oxidative stress due to the colocalization of iron and dopamine.

Additional factors, such as the presence of neuromelanin a pigment that can bind and store iron may exacerbate iron-mediated oxidative damage [25,27,100].

In addition to the increase in iron, certain brain areas of PD patients show alterations in multiple key iron homeostasis proteins, including ferritin, transferrin, iron regulatory protein 2, and divalent metal transporter 1, providing sufficient evidence of dysregulated iron homeostasis [25,100]. This alteration in iron-regulating proteins could explain the accumulation of iron. In PD patients, ferritin in the SN shows a decrease in L-ferritin subunits, which may lead to an increased efflux of iron [25,27]. Another possible source of excess metal could be the release of iron bound to neuromelanin and ferritin by dying neurons [27,76]. Elevated levels of other metal ions, such as manganese, zinc, and aluminium, have also been measured in the SN of PD patients [28,29,48]. Indeed, manganese levels in blood and CSF suggest manganese is a risk factor for the development of PD [29]. Moreover the similarities between manganese and PD further support the neurodegenerative role of metals in PD [61,68,69]. Zinc metabolism also plays a role in the neurodegenerative cascade of PD [48].

Synucleins are a family of redox-active copper-binding proteins. α -Synuclein, in particular, has two copper-binding sites, and the increased formation of α -synuclein aggregates is a direct consequence of the formation of an α -synuclein-copper complex. However, copper levels are decreased in both the serum and SN of PD patients, making the direct implication of copper in the pathogenesis of PD unlikely [24,48,74]. On the other hand, iron (II) and iron (III) can also bind to α -synuclein, but iron (III) in particular can cause α -synuclein aggregation in the form of short, thick fibrils, which differ from the type of fibrils induced by Cu(II) [24,25,27,97,100]. In vitro experiments have shown that iron-induced fibrillation changes the protein structure from an alpha-helical to a beta-sheet conformation, the same structure observed in Lewy bodies [100]. This is not definitive proof, but it supports the hypothesis that increased levels of iron are responsible for the aggregation of α -synuclein present in Lewy bodies in PD patients [27]. Some of the toxic effects of α -synuclein include impaired endoplasmic reticulum to Golgi vesicular trafficking, endoplasmic reticulum stress, sequestration of anti-apoptotic proteins into aggregates, and the formation of pores on cellular membranes [37]. Despite the evidence of excess metals, particularly iron, in the affected areas of PD patients' brains and the proposed mechanisms of these metals in neurodegeneration, whether the increased levels are the cause or a consequence of PD progression is still debated [25,71].

Currently, there is no drug or treatment capable of curing PD [27,28]. Available treatments focus on alleviating the symptoms (both motor and non-motor), but they cannot mitigate the progression of the pathological events underlying PD [28,95]. Treatments for motor symptoms are primarily dopamine-based, either by enhancing dopamine transmission (levodopa) or mimicking the agonist effects of dopamine (dopamine agonists) [27,95]. Initial therapy typically includes levodopa, dopamine agonists, and monoamine oxidase-B inhibitors [28,95]. Levodopa provides better relief for motor symptoms compared to other treatments and generally does not cause serious adverse effects apart from nausea. However, it increases the risk of dyskinesia [95]. Dopamine agonists present more adverse effects; more than 40% of patients using dopamine agonists experience impulse control disorders, and discontinuation of the medication leads to withdrawal symptoms in around 20% of cases [95]. The use of multiple

medications is sometimes necessary to achieve complementary benefits and avoid high dosages of a single medication. For example, monoamine oxidase-B inhibitors block enzymes that degrade dopamine, thereby prolonging the benefits of levodopa [95].

Most medications used to treat non-motor symptoms in PD target neurotransmitters other than dopamine, and the treatments are often the same as those used for non-PD patients with similar symptoms [95]. For dementia, the use of rivastigmine is recommended [95]. Medications used for motor symptoms can also have beneficial effects on non-motor symptoms such as depression and psychosis. If these symptoms persist, more specific medications are often used [95]. A common issue with these drugs is the loss of therapeutic effect after prolonged treatment. This is often due to disease progression rather than medication tolerance or reduced efficacy. Therefore, there is a need for new treatments, particularly those that can limit disease progression rather than just address symptoms [27,95].

There are surgical approaches for treating PD symptoms, primarily used when classical medications lose effectiveness or the patient experiences dyskinesia [95]. Deep brain stimulation (DBS) is a surgical procedure where electrodes are inserted into specific brain regions, such as the subthalamic nucleus, thalamus, and globus pallidus interna in the case of PD [95,101]. This technology is also used to treat other neurological and psychiatric disorders [101]. Despite its effectiveness in reducing motor symptoms, DBS may worsen non-motor symptoms and increase the risk of falls [102]. Additionally, it is not suitable for all PD patients. Ideal candidates include those experiencing severe motor fluctuations or medically unresponsive tremor, without significant cognitive or psychiatric complications [101,102].

Given the possible involvement of metals, particularly iron, in the neurodegeneration seen in PD, and the potential of chelators to decrease metal-induced oxidative stress and α -synuclein aggregation chelation therapy appears to be a promising treatment for PD [28,103]. One of the chelators considered for PD treatment is deferiprone due to its high affinity for ferric iron, ability to scavenge mitochondrial iron, and capacity to cross the BBB [97,104]. Its potential as a PD therapy is supported by promising results in multiple clinical trials for the treatment of Friedreich's ataxia [78,80,81].

Encouraged by preclinical findings, a double-blind, placebo-controlled trial was initiated to evaluate the efficacy of deferiprone in early-stage PD (NCT00943748). Patients were randomized to receive deferiprone (30 mg/kg/day) for 12 months or placebo for 6 months and deferiprone for the other 6 months, followed by a randomized 6-month drug cessation period for all participants. All patients received optimized dopaminergic therapy (levodopa or dopamine agonists) throughout the study [104]. MRI imaging demonstrated a reduction in iron deposition within the SN following several months of daily chelation treatment, without affecting iron levels in unaffected brain regions or causing systemic iron imbalances [104]. Importantly, iron levels rebounded upon treatment cessation, emphasizing the ongoing need for chelation therapy to maintain its beneficial effects. [104]. Motor function, assessed by the Unified Parkinson's Disease Rating Scale (UPDRS), demonstrated improvement following six months of treatment, which persisted at the 18-month mark. However, this improvement gradually diminished over time compared to the initial response. Importantly, patients

continuously treated with DFP maintained significantly better motor function than those who discontinued treatment [104].

A separate randomized, double-blind, placebo-controlled trial investigated the effects of deferiprone (30 or 20 mg/kg/day) in early-stage PD patients over a short (6 months) period (NCT01539837) [105]. All participants received standard dopaminergic therapy. Similar to the previous study, deferiprone did not adversely affect cognitive function or overall quality of life. Deferiprone treatment (20 or 30 mg/kg/day) effectively reduced iron accumulation in the dentate and caudate nuclei of Parkinson's disease patients as demonstrated by increased T2* MRI values and no generalised removal of brain iron nor redistribution was evidenced. In contrast to the previous study, iron reduction in the SN was observed in only three patients [105]. This difference might be attributed to the stronger binding of iron to neuromelanin compared to ferritin within the SN, rendering it less susceptible to chelation [105]. Consequently, a longer treatment duration, similar to the initial trial, may be required to achieve significant iron removal from this brain region. Unlike the previous study, this trial did not demonstrate significant motor improvement in the deferiprone group compared to placebo as assessed by the UPDRS. While a trend towards better motor function was observed in patients receiving the 30 mg/kg/day dose compared to the placebo and 20 mg/kg/day groups, this difference did not reach statistical significance. This is likely related to the higher number of patients using a higher dose of deferiprone (30 mg/kg/day) in the first study as well as the difference in the initial UPDRS score and the recruitment difference of patients [105].

While the initial findings are promising, a definitive link between iron chelation and clinical benefit in PD has yet to be established. To address this, another trial following the first presented was initiated focusing on newly diagnosed PD patients without prior exposure to dopaminergic medications (NCT02655315) [106]. Patients received the same dose of total deferiprone as in the previous trial (30 mg/kg/day). While both treatment groups experienced a decline in motor function as assessed by the UPDRS after 36 weeks, the deterioration was more pronounced in the deferiprone group [106]. Contrary to expectations, deferiprone treatment did not halt disease progression but instead correlated with worsening motor and non-motor symptoms. Paradoxically, MRI evaluations revealed a reduction in iron accumulation within the SN despite the clinical decline and no evidence of systemic iron imbalance was observed during treatment [106]. One possible explanation proposed by the authors for the worsening of motor and non-motor symptoms during deferiprone treatment is a direct adverse effect of the drug itself rather than an acceleration of disease progression [106]. This hypothesis suggests that iron chelation reduces tyrosine hydroxylase activity, a key enzyme in dopamine synthesis. Consequently, as dopamine typically inhibits prolactin release, decreased dopamine production leads to increased prolactin levels which is consistent with the evolution of prolactin plasma levels on patients treated with deferiprone [106].

Deferoxamine (DFO), an FDA-approved chelator with a high affinity for ferric iron (Table 1), is the most widely used iron chelator in haematology over the past 30 years [6,56,107,108]. DFO is a potential therapeutic agent for Parkinson's disease (PD) due to its established use in treating iron overload disorders [107,108]. Its mechanism of action involves binding ferric iron and completely occupying its coordination sphere, rendering it metabolically inactive

[107,109]. Additionally, by being an electron donor DFO exhibits antioxidant properties by scavenging free radicals such as hydroxyl radicals and superoxide anions [110]. DFO has demonstrated neuroprotective effects in mice models. When administered intracerebroventricularly, DFO protects against dopamine neuron loss induced by 6-OHDA and prevents neurotoxicity caused by iron and MPTP [28,99]. However, its poor blood-brain barrier penetration [28], low oral bioavailability [28], and rapid degradation (short half-life in plasma, 5–10 min [56]), coupled with significant cerebral and ocular side effects [108], limit its clinical utility.

Chelators like VK28 and M30 are also considered potential therapeutic agents for Parkinson's disease due to their potent iron(III) chelating abilities, comparable to deferoxamine. These compounds have shown promising neuroprotective effects in preliminary studies, along with selective brain distribution [28].

1.2.2.2. Alzheimer's disease (AD)

AD is recognized by the WorldHealth Organization as a global public health priority [111]. It has emerged as the leading neurodegenerative disease worldwide, accounting for approximately 75% of dementia cases. Currently, it is estimated that over 44 million people worldwide are affected by dementia [100,111]. It is primarily a condition of later life, roughly doubling in prevalence every 5 years after age 65 [111]. It is a progressive neurodegenerative disorder characterized by the gradual deterioration of memory, thinking, and behaviour [27,111,112]. While most cases of AD occur sporadically, a small percentage (<0.5%) is inherited as a familial form (FAD) due to mutations in the amyloid precursor protein (APP), presenilin 1, or presenilin 2 genes. Onset of symptoms in FAD typically occurs earlier, often between the ages of 30 and 50 [113]. Unlike FAD, the more common late-onset AD is attributed to a complex interplay of genetic and environmental factors. Genetic predisposition accounts for approximately 70% of AD risk [114].

Histopathologically, AD is characterized by the presence of senile plaques, composed of extracellular amyloid-beta ($A\beta$) protein aggregates (Figure 9), and neurofibrillary tangles (NFTs) formed by hyperphosphorylated tau protein, a highly soluble microtubule-associated protein in normal conditions [37,99,111,112]. The accumulation of $A\beta$ and tau protein aggregates ultimately leads to widespread neurodegeneration, characterized by synaptic loss, neuronal death, subsequent brain atrophy and the development of dementia [27,111]. Additional pathological hallmarks contributing to AD progression include altered metal homeostasis, inflammation, oxidative stress, impaired autophagy and lysosomal function, mitochondrial dysfunction, and glial cell dysfunction [100]. While AD is often considered a primary pathology, it frequently co-occurs with other age-related brain changes. The complex interplay between these pathological processes remains uncertain [111].

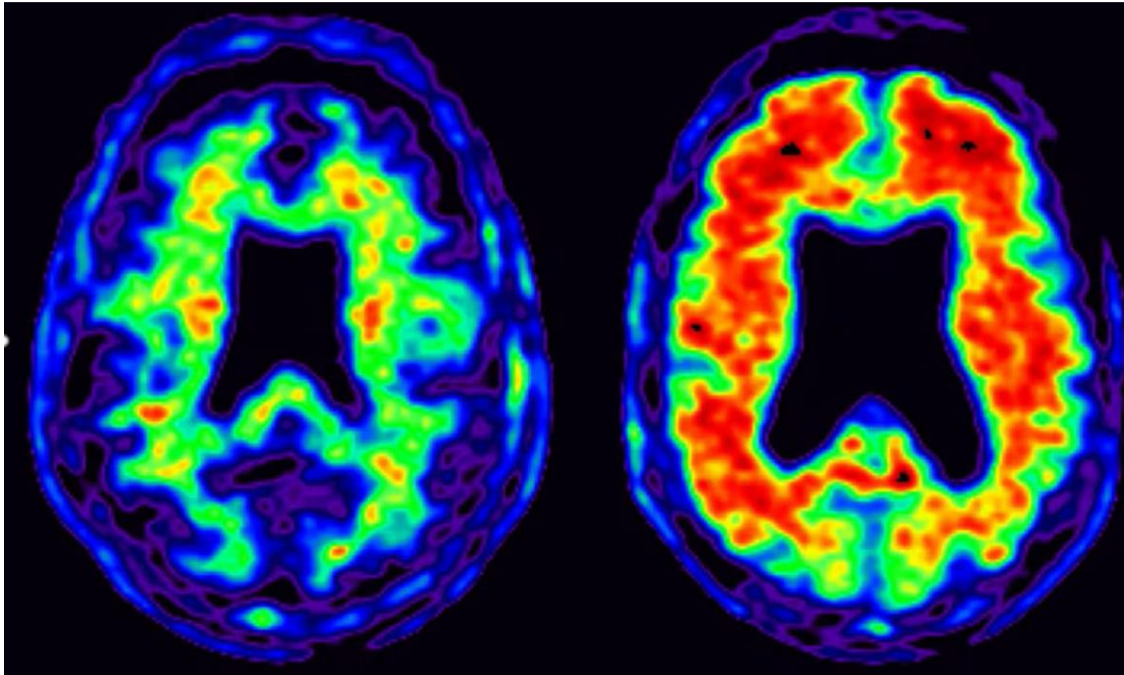


Figure 9. Flortbetapir amyloid PET scans comparing a healthy control (left) and an Alzheimer's disease patient (right). Warmer colours represent higher amyloid accumulation, taken from Lane *et al.* 2018 [111].

Amyloid plaques are extracellular deposits primarily composed of aggregated of misfolded A β peptides with 40 or 42 amino acids (A β ₄₀ and A β ₄₂ respectively), which are derived from the cleavage of the a transmembrane protein APP by secretase enzymes [27,111,115]. While A β ₄₀ is more abundant, A β ₄₂'s higher propensity for fibrillization and hydrophobicity make it the predominant component of plaques [27,111,115]. A β aggregation is a dynamic process involving the rapid formation of higher-order oligomers from smaller assemblies. While A β plaque formation is a hallmark of AD, accumulating evidence suggests that soluble A β oligomers have a higher toxicity [28,111]. It has been suggested that the plaques act as “reservoir” from which amyloid oligomers diffuse [111]. In addition, the accumulation of amyloid plaques is believed to activate microglia, triggering an inflammatory response [115]. A β -induced neuronal damage and dysfunction in AD may be attributed to direct A β toxicity and disruption of axonal transport [115].

Tau, a microtubule-associated protein primarily located in the axons of healthy neurons, plays a critical role in neuronal health by regulating microtubule assembly and stability [115]. In AD tau undergoes abnormal post-translational modifications, leading to hyperphosphorylation and detachment from microtubules. This results in the formation of NFTs, causing the loss of microtubule stabilization, blockage of axonal transport, and even axonal disintegration, ultimately resulting in neuronal death [27,37,111,115]. NFTs initially accumulate in the medial temporal lobe and gradually spread to other brain regions as the disease progresses [111]. While NFTs are closely linked to neuronal loss and clinical symptoms, tau pathology is not exclusive to AD [27,111]. The amyloid cascade hypothesis, which suggest that A β plaques initiate a cascade of events (NFT formation, oxidative stress, inflammation, vascular dysfunction, and ultimately, neurodegeneration) leading to AD, has been challenged due to the presence of A β

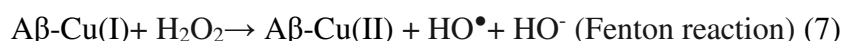
plaques in cognitively normal individuals and the failure of anti-amyloid therapies in clinical trials [37,111,116]. This has led to the exploration of alternative hypotheses, suggesting that A β may be a by-product rather than the primary driver of AD pathology [27,37].

One of the alternative hypotheses that will be discussed in this work is that metals play a significant role in disease progression. Previous studies have reported altered brain metal homeostasis, involving both essential elements and elevated heavy metal concentrations, in AD brains. For instance, higher levels of copper (400 μ M) and zinc (1 mM) have been found in amyloid plaques and AD neuropil regions compared to healthy brains (70 μ M copper and 350 μ M zinc), suggesting a potential link between metal dysregulation and disease pathogenesis [27,35,115–117]. Furthermore, there is a progressive accumulation of metals in the brain as AD progresses from moderate to severe. Notably, this metal accumulation varies at different stages of the disease, primarily in the frontal cortex and hippocampus. Divalent cation accumulation tends to increase in the early stages, while trivalent metal ions accumulate during later stages of AD [35]. Additionally, recent evidences shows a lack of toxicity from A β in the absence of metals, implying that the oxidative damage caused by A β is related to the presence of redox-active metals [37].

Elevated iron levels have been observed in AD-vulnerable brain regions, such as the hippocampus and cerebral cortex, with iron co-localization with A β plaques and NFTs [27]. A β has specific histidine and tyrosine residues capable of binding iron, and iron bound to A β has been shown to promote A β aggregation as well as the production of ROS, most likely by reducing iron (III) [27,37,100,116,117]. While also influencing amyloid precursor protein processing, iron stimulates β -secretase, promoting the amyloidogenic cleavage of APP [100,116]. Furthermore, iron can also bind to tau, promoting its aggregation in iron-rich environments (Figure 10) [100,116,117]. Parallely, iron has been proven to cause tau phosphorylation, which may be attributed to the activation of cyclin-dependent kinase 5 and glycogen synthase kinase 3 β [116,117]. Tau protein accumulation within NFTs induces haem oxygenase-1 expression, potentially exacerbating oxidative stress through iron release from haem catabolism [100]. Elevated ferritin levels in CSF correlate with cognitive decline further supporting the involvement of iron dysregulation in AD [100]. However, AD patients with high pathology but no clinical signs of AD did not show iron accumulation, implying that iron dysregulation occurs concurrently with cognitive impairment. This suggests that iron dysregulation is a concurrent pathological feature rather than the sole driver of AD [116].

Copper, similar to iron, interacts with tau, A β and APP through histidine and tyrosine residues, promoting A β oligomerization and plaque formation [24,37,115–117]. This notion is supported by the ability of copper chelators, such as trientine and D-penicillamine, to redissolve A β from post-mortem AD brain tissue [118]. The complex copper- A β ₄₂ interacts with cell membranes increasing its permeability [116]. Furthermore, Cu(II) increases the neurotoxicity of A β by generating hydroxyl radicals through Fenton's reaction (eq 7) [30,37]. Additionally, the reduction of A β -Cu(II) is believed to be mediated by electrons originating from the C-terminal methionine. While this reaction may initially appear thermodynamically unfavourable, electron transfer between MetS and A β -Cu(II) can be facilitated by the subsequent exergonic deprotonation of MetS \cdot^+ , resulting in the formation of the 4-methylbenzyl radical. This makes

the reaction viable *in vivo* [30,37]. MetS^{•+} may also undergo rapid reactions with superoxide radicals, yielding methionine sulfoxide, which has been found in AD senile plaques (eq 8) [30,37].



Reduction of A β -Cu(II) mediated by external sources of biological reductants like cholesterol, ascorbate, dopamine and fatty acids are also proposed mechanisms [30,37]. High copper concentrations are also linked to tau hyperphosphorylation [116]. While elevated serum copper levels have been observed in AD patients, brain copper levels exhibit a more complex pattern, with both increased and decreased concentrations reported in different brain regions [115–117]. Notably, copper deficiency can lead to Cu(II) accumulation in lipid rafts specially in the binding domain of cell membranes, A β accumulation in these zones create ion channels disrupting calcium homeostasis [116].

Zinc has been a metal of interest in AD due to its highest concentration in the brain compared to other organs and its fundamental role in neurotransmission as an antagonist of glutamate NMDA receptors [115,117]. Like copper and iron, zinc has been colocalized with NFTs and A β aggregates. It has been shown that zinc binds to A β , changing its conformation, promoting its aggregation, and reducing its solubility [24,37,115–117]. However, zinc-induced A β aggregation might be a protective mechanism since zinc is not a redox-active metal; by binding to A β , zinc can compete with harmful redox-active metals, preventing the formation of toxic metal-A β complexes [30,37,116]. Nonetheless, by binding to A β , zinc becomes bio-unavailable, thus contributing to changes in synaptic plasticity and cognitive decline in AD [117]. Zinc also protects against oxidative stress by preventing the oxidation of sulfhydryl groups [116]. Despite zinc's seemingly protective role, excessive zinc release induced by oxidative stress could have deleterious effects, as shown by the flooding of the vesicular pool, causing neuronal network dysfunction due to undue interactions with glutamate and GABA receptors [37,116]. Moreover, zinc also binds to tau, promoting phosphorylation of tau proteins and NFT formation [115,116]. In *in vitro* experiments, zinc has demonstrated a toxic ability to trigger tubulin aggregation, causing neurodegenerative morphological changes; however, this occurs at zinc concentrations much higher than those found under physiological conditions [116].

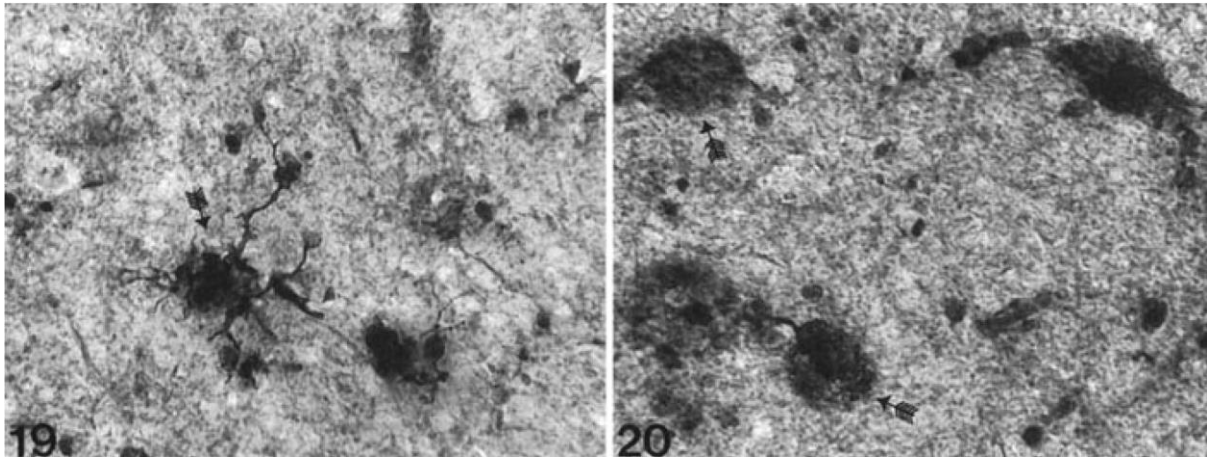


Figure 10. Perls' stain reveals intense iron deposition within cells and processes associated with senile plaques (left panel). Additionally, diffuse iron staining surrounding the plaques is evident (right panel) taken from Texel *et al.*, 2012 [27].

Non-essential metals, particularly aluminium, have also been linked to AD due to their accumulation in the brain (Figure 11) [48,115]. This prolonged retention could potentially lead to toxic NFTs deposits over time [116]. Aluminium exacerbates AD pathology by intensifying amyloid plaque and NFT formation, as aluminium(III) binds strongly to phosphorylated proteins. This is especially true in FAD, where patients exhibit abnormally high extracellular aluminium deposition [115,116]. The implication of aluminium in AD is further supported by studies showing localized neurodegenerative effects that mimic AD in rabbit, rat, cat, dog, and monkey models following the injection of aluminium salts [116]. Despite evidence linking aluminium to increased AD risk, a definitive causal relationship has yet to be established [115,116]. Heavy metals, including lead and cadmium, have been implicated in pathogenesis due to their potential interactions with A β and NFTs, which may influence their production and aggregation [24,48,115,117]. While research suggests a link between heavy metal accumulation and AD risk, the exact role of these metals in disease initiation and progression remains unclear due to conflicting data on their distribution within the brain [24,115,117].

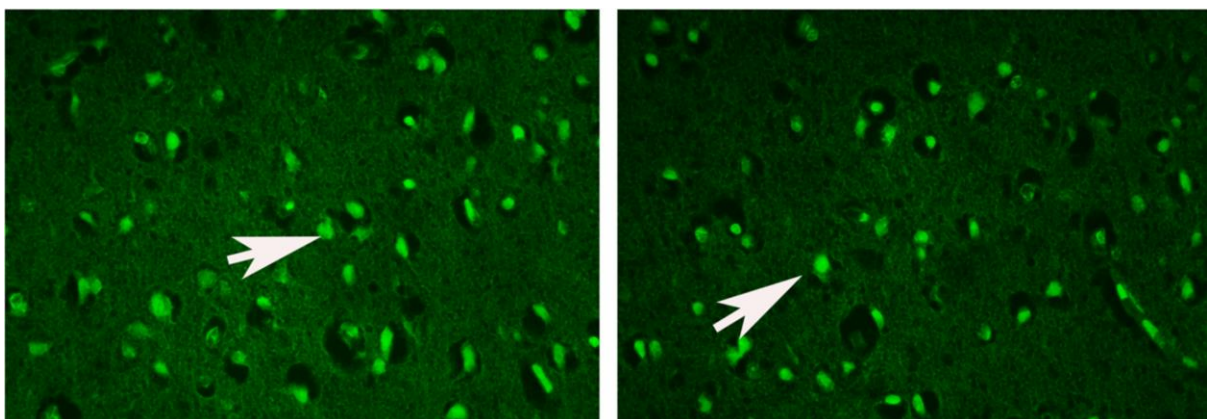


Figure 11. Modified Shaw's staining of sporadic AD brain tissue revealed prominent intracellular aluminium accumulation within cortical neurons, indicated by arrows taken from Das *et al.*, 2021 [116].

Currently, there is no curative treatment for AD, and therapeutic strategies primarily focus on symptom management without altering disease progression [28,111,112,119–121]. Pharmacological treatments for AD could be resumed in two categories cholinesterase inhibitors and N-methyl-D-aspartate (NMDA) receptor antagonist [112,119,120]. Cholinesterase inhibitors constitute the first-line treatment for mild to moderate AD. These drugs elevate acetylcholine levels, a neurotransmitter depleted in AD, by inhibiting its breakdown enzyme, cholinesterase [112,119,120]. While multiple cholinesterase inhibitors exist (donepezil, galantamine, rivastigmine), their efficacy is comparable [112,119,120]. They all present slightly reduced short-term cognitive decline [112,119,120]. Although these drugs provide modest short-term cognitive benefits, they often cause adverse effects such as anorexia, nausea, vomiting, diarrhea, abdominal discomfort, dizziness, fatigue, and muscle cramps, these side effects are mostly dose dependants [112,119,120]. Treatment switching is possible and advisable in cases of intolerance or lack of clinical response [120]. Non-adherence to cholinesterase inhibitor therapy is common in AD patients, influenced by factors such as polypharmacy and medication side effects [119]. Memantine, a non-competitive NMDA glutamate receptor antagonist, reduces excessive glutamatergic activity [112,120]. While beneficial effects on cognition have been observed in moderate to severe AD, memantine has shown limited efficacy in mild AD [112,119,120]. Generally well-tolerated, with infrequent side effects such as dizziness, headache, somnolence, and confusion, memantine is often used in combination with cholinesterase inhibitors [112,112,120].

Given the limited efficacy of current treatments and the absence of disease-modifying therapies, there is a pressing need for novel approaches to AD. Many emerging treatment strategies focus on addressing A β deposition and accumulation [112,119,120]. One strategy is enhancing clearance of A β by active and passive immunization. Passive immunization therapy includes monoclonal humanized antibodies like aducanumab, BAN2401, gantenerumab, with all showing some level of effectiveness reducing the burden of A β plaque in patients with AD [119,120]. Active immunization includes vaccines like AN172 but a phase I clinical trial was prematurely halted due to serious adverse events, including aseptic meningitis, affecting 6% of participants. This adverse immune response was linked to the activation of cytotoxic T cells [120]. Additional therapeutic targets for AD include inflammation, oxidative stress, and mitochondrial dysfunction, although clinical benefits remain elusive. While mitochondrial stabilization was initially promising with latrepirdine (dimebon), phase III trials failed to replicate the positive results from earlier studies [120]

Given the potential involvement of metals in AD pathogenesis through interactions with A β and tau proteins, chelation therapy has emerged as a therapeutic strategy [26,28]. DFO, known for its iron (III) and aluminium (III) chelating properties, was the first chelator tested in an AD clinical trial [122]. This study involved 48 patients with probable AD receiving 250 mg of DFO intramuscularly daily for two years, resulting in a 50% reduction in cognitive decline rate compared to the control group. Despite this positive outcome, the treatment was associated with side effects such as weight loss, loss of appetite, and increased monoamine oxidase metabolite levels [122]. The study's limitations include potential participant selection bias and the possibility that DFO's antioxidant properties, rather than solely its chelation ability,

contributed to the observed benefits [110,122]. No other clinical studies investigating DFO administration has been conducted to date [26,99].

Like for PD, deferiprone has also gain interest in the AD treatment. A phase II clinical trial in prodromal and mild AD patient was conducted (NCT03234686) but no results have been published to date [123].

Copper and zinc chelators, such as clioquinol, have also been investigated for AD treatment due to their ability to bind to these metals and to cross the BBB. Clioquinol, a small lipophilic molecule, forms stable complexes with copper(II) (Table 1) [26]. Promising preclinical results demonstrating reduced A β deposition in animal models led to a phase II clinical trial involving 18 patients with moderately severe AD [26,115,124]. Patients received increasing doses of clioquinol (250-750 mg) for 36 weeks. While clioquinol treatment increased plasma zinc levels, copper levels remained unchanged. Notably, A β ₄₂ levels decreased in the clioquinol group compared to placebo after week 20, accompanied by reduced cognitive decline, especially in more severely affected patients [124]. The mechanism of action of clioquinol is thought to involve the chelation of copper and zinc in A β , facilitating A β disaggregation and clearance from the brain. Unlike other chelators, clioquinol's modest affinity for copper(II) and zinc(II) prevents the depletion of these essential elements in other tissues [124]. Prana Biotechnology, the developer of clioquinol, discontinued its development after identifying unacceptable levels of mutagenic "di-iodo" clioquinol impurities within the manufacturing process [26].

PBT2, a derivative of clioquinol, was evaluated in a phase IIa clinical trial involving 78 AD patients (NCT00471211) [125]. Participants were randomized to placebo, PBT2 50 mg, or PBT2 250 mg daily for 12 weeks. Both PBT2 doses were well-tolerated, with common side effects including headache, dizziness, nasopharyngitis, and fatigue. The higher PBT2 dose significantly reduced CSF A β ₄₂ levels in a dose-dependent manner compared to placebo, suggesting a potential effect on central A β clearance. While executive function improved in the higher-dose group, overall cognitive outcomes were inconsistent. Importantly, PBT2 did not impact serum copper or zinc concentrations, the results concerning copper and zinc levels in CSF were inconclusive [125].

Despite numerous clinical trials and the use of various chelators, no significant therapeutic effect has been observed in AD. While chelation therapy remains a potential therapeutic option, further research is needed to elucidate the roles of different metals in AD pathogenesis and progression to select the most appropriate chelators. For example, divalent chelators like clioquinol or PBT2 might be more suitable for early-stage AD patients, as their use in severe AD cases could potentially deplete essential divalent metal cations. Conversely, trivalent chelators like deferoxamine or deferiprone may be more relevant options for treating severe AD where increasing concentrations of trivalent cations are found [35].

1.2.2.3. Huntington disease (HD)

HD is an autosomal dominant neurodegenerative disorder characterized by a triad of motor, cognitive, and psychiatric symptoms [126]. Chorea, involuntary jerky movements, is a hallmark feature that typically begins with subtle movements and gradually increases in

frequency and amplitude as the disease progresses [126]. The underlying pathology involves the formation of intracellular protein aggregates (inclusion bodies) and neuronal loss primarily within the striatum and cerebral cortex [126,127]. HD has a prevalence of approximately 12.3 per 100,000 individuals [126]. Onset typically occurs in adulthood, around the age of 40, and the disease progresses irreversibly over 15-20 years, with pneumonia being a common cause of death [126,127]. HD is caused by an abnormal expansion of the CAG trinucleotide repeat within exon 1 of the huntingtin (Htt) gene, located on the short arm of chromosome 4. This expansion results in an elongated polyglutamine (polyQ) tract at the N-terminus of the mutant Htt protein [126,127]. In the human population, the number of CAG repeats typically ranges from 7 to 26, with an average of 18 [126]. Individuals with 40 or more CAG repeats in the huntingtin gene are almost certain to develop HD. However, those with 36-39 repeats may experience a delayed onset or may never develop symptoms [126,127]. Interestingly there have been shown a correlation between the CAG repeat length and the disease progression after motor onset [126].

Htt protein is a large protein with an estimated molecular weight of 350 kDa that is mainly expressed in the CNS [126,127]. It has many interaction sites that help it to coordinate to other proteins and cellular functions suggesting it is a scaffolding protein [126]. The N-terminal region is the most active region of the protein and following this domain is where the expansion occurs in HD [127]. The expansion of Htt results in a dysfunctional conformational flexibility of the N-terminal region thus disrupting protein-protein interactions [126,127]. Mutant Htt acquires toxic properties that disrupt cellular processes. These toxic functions include transcriptional dysregulation, impaired calcium homeostasis and metabolism, activation of proteolytic enzymes, and stimulation of microglial and immune responses [126,127]. Mutant Htt increases the sensitivity of neurons to NMDA receptor activation, leading to a surge in intracellular calcium levels [127]. Extra-synaptic NMDA receptor activation triggers neurotoxic pathways, that can sumoylate mutant Htt, potentially reducing its aggregation propensity and increasing the levels of toxic soluble mutant Htt. Mutant Htt is known to associate with mitochondria [127]. This association releases intracellular calcium activating neuronal nitric oxide synthase (nNOS), which binds to NMDA receptors, leading to the production of nitric oxide (NO). NO can directly modify receptor subunits, altering their signalling [127]. Excessive NO can react with superoxides to form peroxynitrite radicals, contributing to oxidative stress. Calcium-activated nNOS binds to the divalent metal transporter 1, facilitating the influx of iron at the plasma membrane and endosomal level. This excessive free iron can facilitate the production of ROS [127].

Multiple studies have found an increase in iron levels specifically in the putamen, pallidum and occipital cortex [128–130]. Parallely with the increased iron signal in the pallidum, caudate, and putamen, there were reported elevations in zinc levels within the pallidum and a reduction in manganese concentrations in the superior frontal region [130]. Copper on the other hand has been seen in elevated levels only in the putamen. These neurochemical alterations correlated with the severity of the disease [130]. As observed in PD and AD, metals such as copper and iron can bind to proteins, altering their conformation and promoting aggregation [24,25,27,37,97,100,115–117]. Similarly, both *in vivo* and *in vitro* studies in HD have demonstrated that iron and copper can interact with the mutant Htt protein and facilitate polyQ

aggregation [128,129]. Moreover, Htt possesses the ability to reduce copper(II) and, to a lesser extent, iron(III), further implicating metals in the pathogenesis of HD [128,130].

Unfortunately, there are currently no effective cures or disease-modifying treatments available for HD. As with other neurodegenerative disorders discussed in this section, the available treatments are primarily symptomatic, aimed at managing the disease's symptoms rather than halting its progression [126,131]. Chorea may not be particularly bothersome for patients and may not necessitate treatment. However, if the involuntary movements significantly impair daily activities, such as manual dexterity or balance, medication should be considered [126]. Chorea in HD is primarily treated with dopamine-depleting agents such as tetrabenazine and deutetrabenazine. While deutetrabenazine offers a more favourable pharmacokinetic profile compared to tetrabenazine, both medications can potentially induce or exacerbate depression [126,131]. Atypical neuroleptics like olanzapine, risperidone, and quetiapine can also be considered for the treatment of chorea in HD [126,131]. These medications are particularly beneficial for patients who exhibit psychiatric comorbidities, including irritability, agitation, and anxiety [126]. Current research efforts aimed at developing treatments for HD are targeting various factors implicated in disease progression. Some of the therapeutic strategies under investigation include mitigating mitochondrial dysfunction, preventing excitotoxicity, addressing transcriptional deregulation, and inhibiting huntingtin protein aggregation [126,131]. Chelation therapy, particularly targeting metal ions involved in protein aggregation, is a promising avenue of research. However, to date, only one chelator (PBT2) has been evaluated in clinical trials for HD [131].

A randomized, double-blind, placebo-controlled phase II clinical trial (NCT01590888) evaluated the safety and efficacy of PBT2 in 109 participants with HD [132]. Two doses of PBT2 (100 mg/day and 250 mg/day) were administered over 26 weeks. PBT2 was found to be safe and generally well-tolerated. Importantly, patients receiving the higher dose (250 mg) demonstrated improvements on the Trail Making Test Part B, a cognitive test assessing set-shifting abilities. However, neither dose of PBT2 showed significant improvements in the composite cognition Z-score, the primary endpoint of the study, when compared to placebo [132].

1.2.2.4. Stroke

Stroke is a leading cause of death and disability worldwide, ranking as the second leading cause of death globally. There are two primary types of stroke: haemorrhagic stroke, caused by bleeding within the brain, and ischemic stroke, resulting from a blood clot blocking a cerebral artery. Haemorrhagic stroke accounts for approximately 15% of all stroke cases, while ischemic stroke comprises the remaining 85% [133–135]. Stroke risk factors can be categorized as modifiable or non-modifiable. Modifiable factors include smoking, hypertension, diabetes, unhealthy diet, and other environmental influences, while non-modifiable factors are primarily genetic [133]. After a stroke, patients can develop a variety of neuropsychiatric disorders, which may negatively impact their social functioning, overall quality of life, and recovery [136]. Post-stroke depression is the most common of these disorders, affecting approximately 35% of stroke survivors. Additionally, it has been reported that nonpsychiatric physicians underdiagnose post-stroke depression in 50%–80% of cases [136].

1.2.2.4.1. Haemorrhagic stroke:

Intracranial haemorrhage (ICH) has a 1 year mortality up to 60% and a high morbidity, with only 20% of patients living independently after 6 months [137]. Risk factors for haemorrhagic stroke include uncontrolled hypertension and the inappropriate use of anticoagulants or antiplatelet agents [99,138]. Haemorrhagic volume is a critical determinant of outcome in ICH. Large hematomas, exceeding 150 mL, often result in fatal cerebral perfusion pressure loss. Conversely, patients with hematomas smaller than 140 mL typically survive the initial event [138]. Multiple imaging modalities, including CT scans and MRI, are employed to assess the extent of brain damage caused by haemorrhage (Figure 12) [139]. Injury following haemorrhage can be categorised into primary injury and secondary injury. Primary injury is sustained during the initial haemorrhage. It is a result from a rapid raise in brain volume and intracranial pressure due to the haematoma formation [133,138,140,141]. Despite initial haemorrhage stabilization in approximately two-thirds of patients, hematoma expansion occurs in roughly one-third of cases. Post-ictus hematoma expansion can lead to rapid neurological decline. While the exact mechanisms driving hematoma growth remain unclear, the majority of rebleeding events occur within the first 24 hours [138]. On the other hand, secondary injury refers to subsequent and long-term damage that develops due to the physical effects of the initial haemorrhage, an inflammatory response to the hematoma, and the release of blood breakdown products. This can result in severe neurological deficits and sometimes delayed fatality [133,138,140,141]. ICH can be classified as primary or secondary. Primary ICH occurs spontaneously, often due to hypertension, while secondary ICH results from an underlying condition such as a brain tumour [141]. Although primarily a brain-based pathology, ICH is significantly influenced by systemic factors, particularly systemic iron levels. Patients with higher iron levels tend to have poorer outcomes [142]. Following ICH, ruptured microvessels release blood components, including erythrocytes, into the brain parenchyma (Figure 13). Erythrocyte lysis occurs rapidly within minutes but can persist for several days post-haemorrhage, contributing to sustained iron release and its deleterious effects on surrounding neurons, astrocytes, and other cells [140,142].

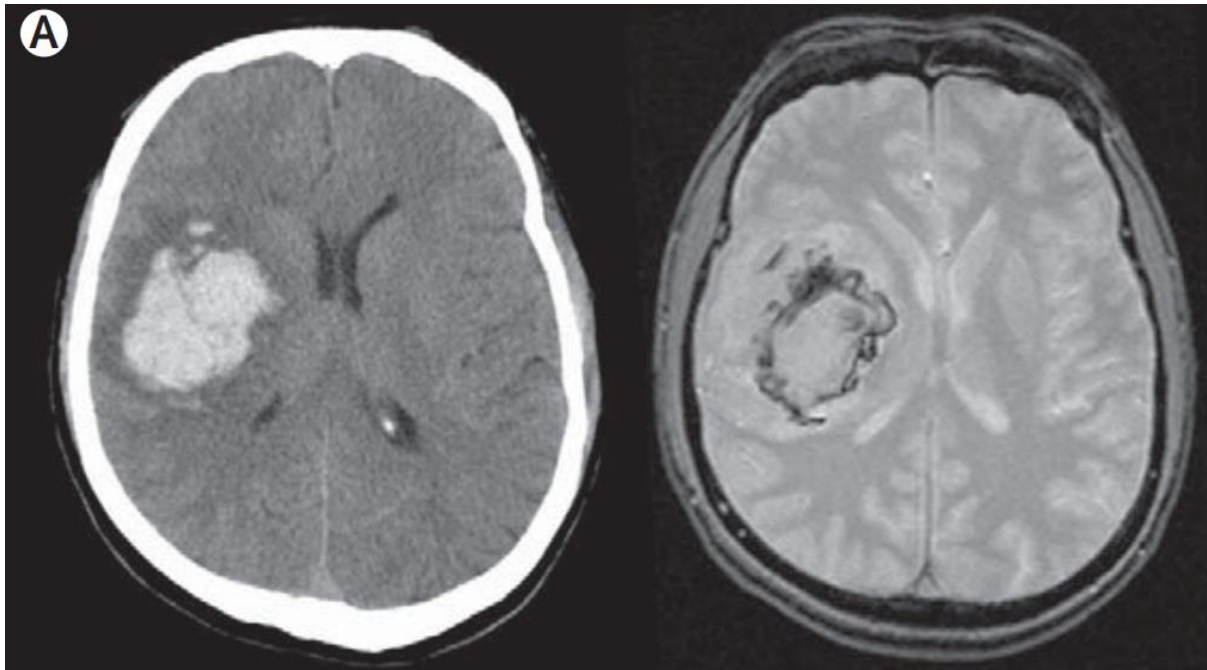


Figure 12. Acute hypertensive hemorrhage appears as a hyperdense lesion on CT scans (left) obtained within 12 hours of symptom onset. MRI, specifically gradient-echo (GRE) sequences (right), reveals a characteristic hypointense rim surrounding the hematoma core, taken from Kidwell and Wintermark, 2008 [139].

Perihematomal oedema develops rapidly within three hours of symptom onset and peaks between 10 and 20 days post-haemorrhage. While its contribution to ICH-induced neurological deficits remains controversial, it is a significant component of secondary brain injury [138,140,141]. Perihematomal oedema occurs in three phases. The initial ionic oedema phase, lasting several hours, is characterized by hydrostatic pressure and clot retraction leading to serum accumulation in the surrounding tissue. This is followed by early vasogenic oedema within the first two days, associated with the coagulation cascade and thrombin generation. Finally, delayed vasogenic oedema occurs, believed to be induced by blood breakdown products [138,140].

Haemoglobin, a released component following erythrocyte lysis, is neurotoxic and contributes to oedema formation by disrupting the BBB [140]. The impairment of BBB function allows increased access to brain of iron carrying molecules (Figure 13) [142]. Haptoglobin rapidly binds to haemoglobin, forming a redox-inactive complex. This complex is subsequently internalized by macrophages and monocytes via the CD163 receptor [140,141]. Contrary to its protective role, recent findings suggest haptoglobin may exacerbate neuronal vulnerability to haemoglobin-mediated iron toxicity. haptoglobin appears to facilitate neuronal uptake of haemoglobin-bound iron via the CD163 receptor [141]. Following endocytosis, the haemoglobin-haptoglobin complex is degraded into haem which is then degraded by haem-oxygenase into carbon monoxide, biliverdin and iron(II). Iron is then stored in ferritin [140–142]. Following intracerebral ICH, ferritin levels increase as a compensatory response to elevated free iron. Although ferritin serves a protective role by sequestering iron, elevated serum ferritin levels have been associated with poorer patient outcomes [143]. Excessive iron

storage leads to ferritin breakdown within lysosomes, resulting in haemosiderin deposition. While haemosiderin is generally considered a relatively stable iron storage form, its potential redox activity cannot be entirely excluded, suggesting a possible role in cellular damage [140,141]. Haemosiderin deposition is also a characteristic feature of the neurodegenerative condition superficial siderosis [144]. Additionally, neurons possess lower ferritin levels compared to glial cells, limiting their capacity to buffer iron released from haemoglobin breakdown [141]. Unbound haemoglobin, following erythrocyte lysis, undergoes degradation, releasing haem. Haem is associated with the production of pro-inflammatory mediators and ROS within the CNS, which are associated with poorer prognosis [141,142]. To protect the brain from haem toxicity, haem is bound by haemopexin, a glycoprotein typically not expressed in the brain but induced after an ICH. The haem-haemopexin complex can then be internalized and metabolized by haem oxygenase as previously explained [141]. Despite multiple iron-regulatory mechanisms in the brain, including haptoglobin and haemopexin, the massive influx of iron and iron-carrying molecules following ICH overwhelms homeostatic capacity [133,140–142]. This iron overload contributes to ROS production as well as the depletion of antioxidant mechanisms like glutathione, exacerbating neuronal damage. The similarities between ferroptosis cell death and neuronal injury following ICH underscore the pivotal role of iron in this pathophysiology [140–142]. Moreover, the release of iron from dying neurons further amplifies the vicious cycle of iron accumulation and oxidative stress (Figure 13) [140–142]. Additionally, in cases of traumatic brain injury, iron deposition has been linked to neurodegeneration, as evidenced by cognitive impairment and an increased risk of developing post-traumatic seizures [140,142].

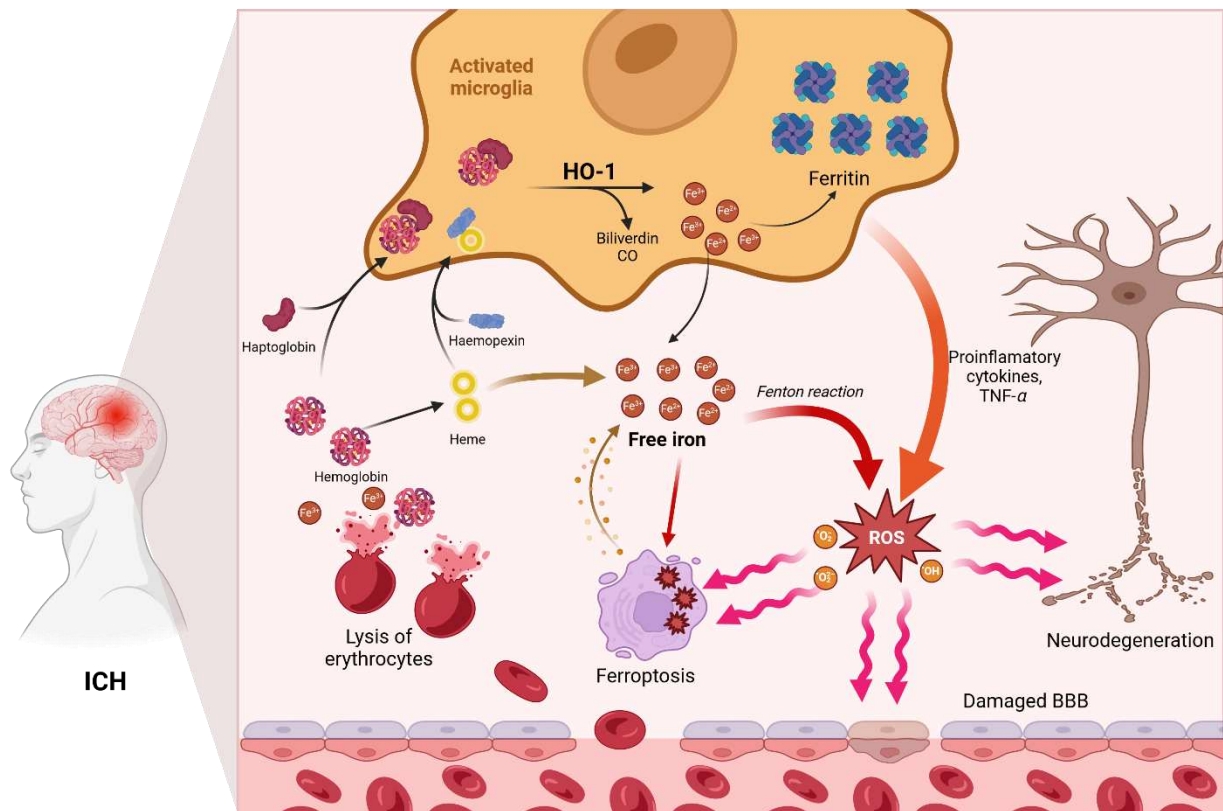


Figure 13. Role of iron as an aggravating factor of oxidative stress in intra cranial haemorrhage. Created with BioRender.com.

Currently there is no gold standard treatment for ICH, multiple strategies focused on management of the haemorrhage [133,137,138,140,141]. Despite compelling evidence linking clot-derived factors to ICH-induced brain injury, clinical trials evaluating surgical clot removal as a therapeutic strategy, such as the STICH trial, where no difference in outcome was seen between optimal medical management versus surgery have yielded inconclusive results [145]. While early clot removal appears intuitively beneficial, the optimal therapeutic window for this intervention remains uncertain [137,138,140]. Surgical interventions, such as craniotomy within four hours of ictus, are associated with increased risk of rebleeding and mortality [137]. Surgical intervention itself can exacerbate brain injury by releasing additional haemoglobin, potentially compromising the efficacy of clot removal procedures [138]. Minimally invasive techniques, such as stereotactic and endoscopic aspiration, have emerged as alternatives to open craniotomy for ICH management. These approaches offer potential advantages including reduced surgical time, blood loss, and the avoidance of general anaesthesia [137]. Other methods investigated for the removal of hematomas include the use of tissue plasminogen activators (tPA). These molecules generate plasmin, which digests the fibrin-containing complex of coagulated proteins in a blood clot, showing promising results. However, tissue plasminogen activators have also been associated with promoting oedema in a mouse model [137,138].

Due to evidences suggesting iron's possible involvement in brain injury following a cerebral haemorrhage, chelation therapy could be a promising option. For instance, the chelator DFO has been shown to reduce oedema and neurological deficits in animal models [146,147]. Based on promising preclinical data, multiple clinical trials have investigated the use of DFO for the management of ICH. A phase I clinical trial (NCT00598572) evaluated the safety, tolerability, and feasibility of daily DFO infusions up to 62 mg/kg/day. This study reported mild blood pressure-lowering effects associated with DFO administration [148]. This positive result lead to a phase II trial (NCT01662895)[149] however, the trial was terminated prematurely due to increased pulmonary toxicity associated with continuous DFO infusion at 62 mg/kg/day for five days [150]. Another double-blind, placebo-controlled phase II trial (NCT02175225) was conducted with a lower dosage of DFO (32 mg/kg/day for 3 days) and a larger number of patients (144 treated with DFO and 147 in the placebo group) [150]. The study provided evidence that an intermediate dosage of DFO at 32 mg/kg/day for 3 days is well-tolerated by ICH patients and does not increase the rates of serious adverse events, major disability, or death. However, the trial showed that treatment with DFO did not significantly reduce the extent of oedema, contrary to findings in animal models, nor did it significantly improve the chances of a good outcome at three months post-ICH. Nonetheless, secondary and exploratory results suggest that DFO might improve outcomes at six months [150].

Zeng *et al.*, 2018 reviewed two clinical studies investigating DFO administration in ICH patients, despite the relatively small sample sizes of 42 and 29 participants, respectively. These studies provided preliminary insights into the potential therapeutic effects of DFO in ICH [151]. The first study involving 42 patients administered intravenous DFO (32 mg/kg/day) for

three days demonstrated reduced oedema and hematoma volume after 15 days. However, no significant improvements in neurological scores were observed at the 15 day nor at the 30-day follow-up [151]. The second study involving 29 patients where the treated group received a lower DFO dose (20 mg/kg/day) for three days. This group exhibited reduced relative oedema volume at days 7 and 14, with improved neurological function compared to controls at these time points. However, no significant differences in neurological function persisted at the 90-day follow-up, consistent with findings from the previous studies [151].

In a non-randomized study of traumatic ICH with a total of 94 participants [152]. Patients in the treated group were administered intravenous DFO (20 mg/kg/day) for 5 days. While oedema volumes were significantly lower in the treatment group on days 3, 7, and 14 compared to the control group, the overall hematoma absorption process was not significantly altered between the two groups over the 14-day study period. Notably, there were no statistically significant differences in outcome between the experimental and control groups [152].

Minocycline, an antibiotic that has been found to have iron chelation properties, has also been of interest in the potential treatment of ICH [153]. In animal models, it has been shown to reduce brain swelling, neurological deficits, and neuronal loss [154–156]. A randomized, open-label pilot study involving 95 acute stroke (ischemic and haemorrhagic stroke) patients evaluated the efficacy of intravenous minocycline (100 mg every 12 hours for five doses) initiated within 24 hours of stroke onset. While minocycline was well-tolerated, no significant therapeutic benefits were observed in terms of clinical outcomes [157].

A randomized controlled trial (NCT01805895) evaluated minocycline in 16 patients with intracerebral haemorrhage [158]. Participants in the experimental group (8 patients) received an initial intravenous dose of 400 mg followed by 4 days of oral minocycline (400 mg daily). While the regimen was safe and achieved neuroprotective serum concentrations, oral administration resulted in delayed drug absorption, limiting its utility in acute settings requiring rapid therapeutic onset [158].

A pilot study involving 20 patients with ICH administered intravenous high doses of minocycline (10 mg/kg/day) within 12 hours of onset and continued for a total of 5 days (NCT03040128) [159]. The study found no difference in functional outcomes or hematoma volumes between the treatment and control groups. However, matrix metalloproteinase-9 (MMP-9) levels were lower in the minocycline group. MMP-9 is suggested to play a role in secondary injury in ICH through remodelling of the extracellular matrix and breakdown of the BBB. Patients tolerated minocycline without adverse events [159].

1.2.2.4.2. Ischemic stroke:

An ischemic stroke occurs when there is a temporary reduction in cerebral blood flow, resulting in a localized depletion of oxygen and glucose [142,160,161]. Similar to haemorrhagic stroke, imaging techniques such as CT and MRI are invaluable tools for diagnosing and assessing the severity of ischemic stroke (Figure. 14) [162,163]. There are two distinct areas affected after an ischemic stroke: the core of the infarction and the surrounding zone known as the ischemic penumbra [161]. In the core area, there is a significant reduction in blood flow, leading to the failure of energy-dependent processes essential for cell survival and disrupting ion

homeostasis, which results in cell death within minutes and ultimately causes neuronal injury [160,161]. Additionally, this leads to the failure of mitochondrial membrane integrity, exacerbating cellular energy depletion [160]. Severe nutrient deprivation within the ischemic core results in irreversible tissue necrosis [160]. In the penumbra, blood flow is also impaired but to a lesser degree compared to the core. Although metabolism and structure are maintained, neurophysiological functions are lost [160,161]. Cells in the ischemic penumbra undergo both apoptosis and autophagy [160]. The blood flow in this area is too low to sustain electrical activity, even though it is sufficient to preserve ion channel activity [161]. The ischemic penumbra can comprise up to 50% of the initial infarct volume. Neurological decline often correlates with the expansion of this vulnerable brain tissue [161]. The energy deficit after the onset of ischemia leads to a drop in pH and depletion of ATP, causing Na⁺/K⁺ pump dysfunction [160,161]. This results in membrane depolarization and activation of calcium channels, which in turn leads to an excessive release of excitatory amino acids, particularly glutamate, into the extracellular space [142,160,161]. This hyperstimulation of glutamate receptors leads to excitotoxic neuronal death [142,161]. Notably, elevated glutamate levels in plasma and CSF correlate with poor outcomes in ischemic stroke patients [135,161]. The receptor disturbance caused by excessive glutamate results in ion homeostasis disruption, leading to a passive influx of water, which causes cell swelling and ultimately oedema. This oedema is a primary factor contributing to neurological deterioration following the initial stages of stroke. [161]. Moreover, the signalling pathways activated during excitotoxicity trigger a proinflammatory response (production of TNF- α and interleukins), as well as migration of macrophages and monocytes to the ischemic penumbra further contributing to ischemic injury [161].

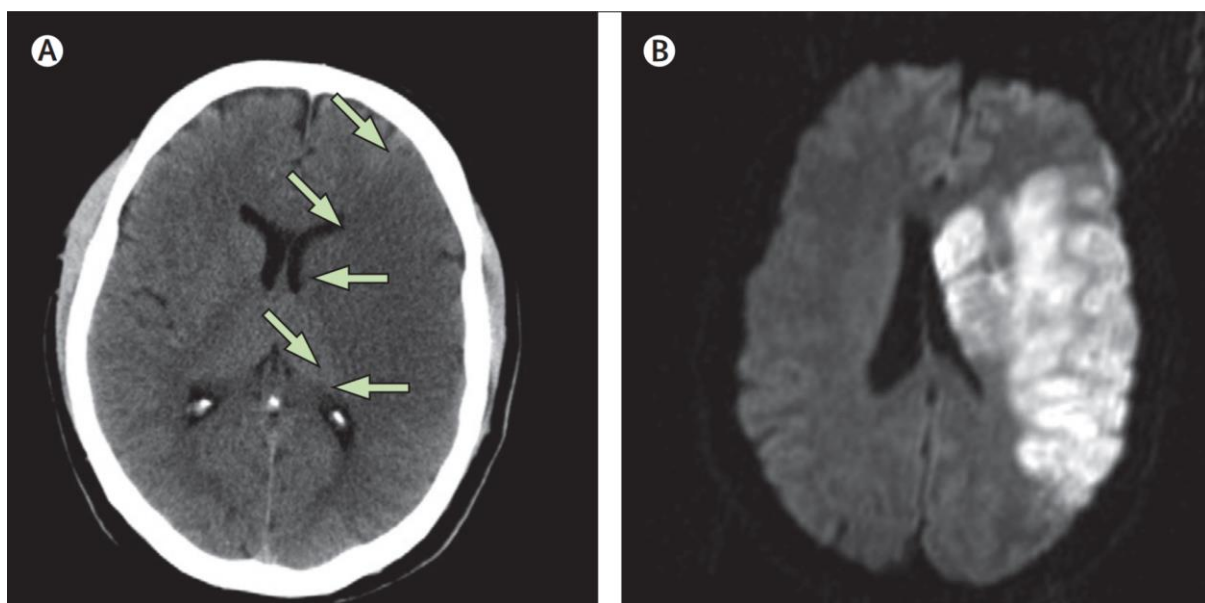


Figure 14. A: Axial cranial CT 7 h after stroke onset. Arrows indicate the margins of the infarction. **B:** Axial diffusion-weighted MRI in the acute phase of malignant middle cerebral artery infarction taken from Huttner and Scwab, 2009 [163].

While the clinical impact of iron-mediated neurotoxicity in ischemic stroke is not fully understood, evidence suggests a potential role for iron in disease pathogenesis. Iron

accumulation and deposition in various brain regions and the correlation between elevated ferritin levels in plasma and cerebrospinal fluid with poor outcomes support this hypothesis [135,142,161]. Due to the reduced blood flow, brain oxygen requirements increase during an ischemic stroke, creating a higher demand for iron transport [135]. An increase in transferrin and transferrin receptor expression has been observed after ischemic stroke; however, its role in either increasing neurodegeneration or providing protection is still controversial [142]. Additionally, the drop in brain tissue pH decreases transferrin's affinity for iron, releasing it and thus increasing the amount of free iron that can produce ROS following the Fenton reaction (Figure 15) [135,141]. Further evidence of iron dyshomeostasis is shown by the upregulation of hepcidin in the blood within the first six hours of ischemic onset. Hepcidin, the main regulator of iron homeostasis, acts by binding to ferroportin, causing its internalization and degradation. This inhibits ferroportin-mediated iron release, preventing a further increase in free iron [142]. Although ferritin is associated with defence mechanisms against oxidative stress by storing iron and reducing its reactivity, thereby protecting cells from iron-mediated oxidative stress, excess ferritin is considered a primary source of free iron in iron-induced oxidative stress [161]. Like in haemorrhagic stroke, ferritin is also upregulated [135,141,142,161]. The mechanisms by which iron is released by ferritin are still unclear; however, it is known that lysosomal activity induces iron release [161]. Additionally, ferritin-bound ferric iron can be released through reduction to ferrous iron, a process facilitated by reactive species such as superoxide, acidosis, catecholamines, and nitric oxide, which are abundant during ischemic conditions [135]. Following artery occlusion, an initial compensatory increase in transport occurs across the intact BBB. Subsequently, a pathological breakdown of the BBB results in increased permeability and leakage (Figure 15). This BBB disruption, characterized by the aberrant exchange of molecules between blood and brain, occurs early in the ischemic cascade, often within the first few hours post-stroke onset, exposing the brain to the systemic labile iron pool [142]. It has been observed in animal models and patients that subjects with systemic iron overload have a poor prognosis during the early phase of ischemic stroke, further suggesting the importance of iron [142,161]. Furthermore, iron overload has been associated with an increased risk of haemorrhagic transformation in animal models [142]. Excitotoxicity, primarily driven by excessive glutamate, is a key mechanism underlying neuronal death in ischemic stroke. Glutamate accumulation depletes antioxidant glutathione, rendering neurons vulnerable to oxidative stress. This oxidative environment, coupled with growing evidence of iron's involvement in oxidative stress, supports the involvement of ferroptosis in ischemic stroke [142,160].

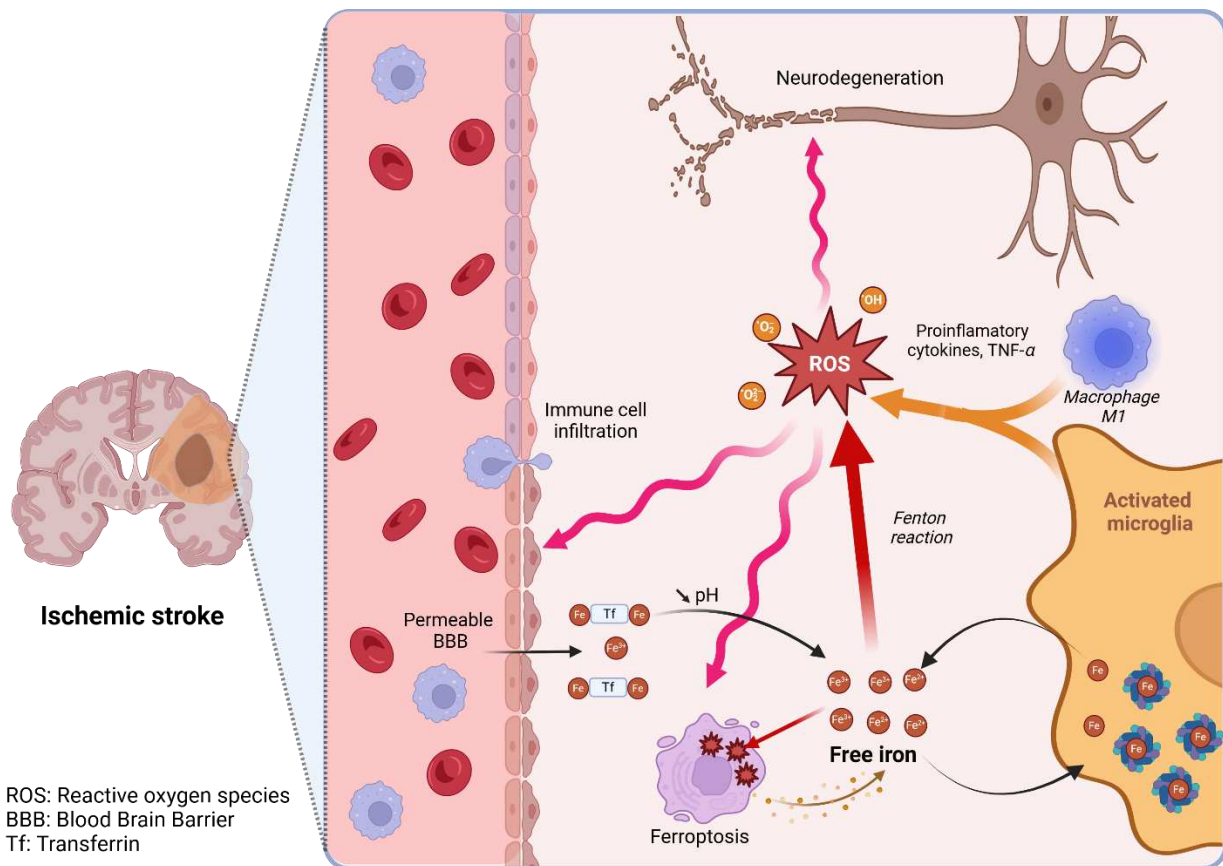


Figure 15. Role of iron in triggering oxidative stress during ischemic stroke. Created with BioRender.com.

Another metal suspected to play a role in ischemic injury is zinc. Zinc accumulation in neurons following ischemic stroke, coupled with a correlation between zinc localization and cell death, further supports the hypothesis that zinc contributes to neuronal demise [164,165]. Accumulating evidence suggests that intracellular zinc stores can be depleted following oxidative stress, releasing zinc into the cytoplasm. Additionally, zinc can be imported from the extracellular environment into cells under these conditions [164]. Zinc overload is thought to be implicated in mitochondrial dysfunction. Normally, zinc is compartmentalized within mitochondria [164]. Sustained accumulation of zinc within mitochondria can induce the production of reactive ROS. This process is believed to occur through the inhibition of complex III in the electron transport chain or by disrupting the function of complex I and α -ketoglutarate dehydrogenase [164]. Synaptic vesicles are considered a primary source of released zinc. It has been shown that zinc is co-released with glutamate from these vesicles. Consequently, excessive glutamate release seen in ischemic stroke is often accompanied by excessive zinc release. This surplus zinc can be subsequently internalized by mitochondria, leading to zinc overload [164,165].

Current therapeutic strategies for ischemic stroke focus on restoring normal blood flow. To date, the only approved treatments are thrombolytic therapy, which dissolves the blood clot, and endovascular mechanical thrombectomy, which physically removes the clot [162,166,167]. Intra-arterial thrombolysis, achieved by positioning a microcatheter near the arterial occlusion, has demonstrated higher recanalization rates compared to intravenous

thrombolysis. Approximately 40% of patients experience complete arterial recanalization, while another 35% achieve partial recanalization [166]. Alteplase, the recombinant form of tPA, has a short half-life of 4-6 minutes due to rapid degradation by plasminogen activator inhibitor [162]. To minimize haemorrhagic risk, alteplase must be administered within 4.5 hours of stroke onset. Successful treatment with alteplase can reduce the likelihood of disability at three months by approximately 30% [162,167]. The composition of the blood clot appears to be a significant factor in determining the efficacy of thrombolytic therapy. For instance, clots that are rich in platelets may be more resistant to thrombolysis, whereas thrombi that are rich in red blood cells tend to have higher sensitivity to alteplase [162].

On the other hand there is mechanical thrombectomy which is becoming the gold standard for ischemic stroke treatment [162]. It is a minimally invasive procedure involving the insertion of a catheter through the groin into the blocked cerebral artery to physically remove the clot, thereby restoring blood flow to the brain. There are primarily two types of mechanical thrombectomy: one using a stent retriever (stentriever) and the other using an aspiration catheter [162]. Mechanical thrombectomy extends the therapeutic window for intervention compared to the window for tPA, with some studies suggesting it can be effective up to 24 hours after stroke onset [162,167]. However, the availability of mechanical thrombectomy services remains limited compared to thrombolytic therapy, which can be administered in most stroke units on a 24/7 basis [162]. The optimal initial treatment for patients with ischemic stroke remains controversial, with ongoing debate regarding the prioritization of thrombolytic therapy or immediate mechanical thrombectomy given the advancements in endovascular procedures [162]. Despite advancements in ischemic stroke management, reperfusion therapy carries the risk of reperfusion injury, potentially worsening outcomes. This injury is attributed to the generation of ROS upon re-establishing blood flow to previously ischemic tissue [167]. Similar to haemorrhagic stroke, severe cerebral oedema following ischemic stroke can elevate intracranial pressure to critical levels, necessitating surgical decompression as a potentially life-saving intervention [166].

Metal dyshomeostasis is a hallmark of ischemic stroke and has prompted investigation into chelation therapy as a potential neuroprotective strategy. Similar to its exploration in haemorrhagic stroke, DFO has been considered for ischemic stroke treatment. To date, only one clinical trial (NCT00777140) has evaluated DFO in this context. This phase II study employed a double-blind, randomized, placebo-controlled design to assess the safety and tolerability of intravenous DFO in a total of 62 ischemic stroke patients receiving intravenous tPA [168]. Participants received either placebo or a single 10 mg/kg bolus of DFO followed by a 72-hour continuous infusion of escalating DFO doses (20, 40, and 60 mg/kg/day). Treatment initiation coincided with tPA infusion. Iron saturation of transferrin decreased in DFO-treated groups compared to controls, except for those receiving the lowest dose. In the highest dose group, this reduction became evident after 24 hours, indicating a decrease in systemic iron levels. Intriguingly, a subgroup analysis of patients with moderate to severe ischemic stroke revealed a trend towards improved neurological function at 90 days in patients treated with higher DFO doses (40 and 60 mg/kg/day). Additionally, the proportion of patients with favourable outcomes increased with DFO dose at both 7 and 90 days [168].

In addition to its investigation as a neuroprotective agent for haemorrhagic stroke, minocycline has also been studied for its potential benefits in ischemic stroke. A study involving 152 patients with acute ischemic stroke evaluated the efficacy of 200 mg/day minocycline initiated within an average of 12.64 hours post-stroke onset. Minocycline was administered for a total of 5 days. The minocycline group demonstrated improved National Institutes of Health Stroke Scale (NIHSS) scores at day 90 compared to baseline, with these differences evident as early as day 3. These findings suggest a potential benefit of early minocycline administration in acute stroke [169].

A subsequent study (NCT0063039) evaluated minocycline safety, tolerability, and pharmacokinetics in a dose-escalation trial involving acute ischemic stroke patients [170]. Intravenous minocycline administration at doses ranging from 3 to 10 mg/kg daily for three days was well-tolerated and achieved serum concentrations known to exert neuroprotective effects in preclinical models [170].

Given the potential implication of zinc toxicity in ischemic stroke, clinical trials involving zinc chelators have been initiated. For instance, the lipophilic chelator DP-b99 underwent multiple phase I and II trials demonstrating favourable safety profiles [171,172]. Although a phase IIb study did not reveal significant differences in NIHSS scores at 90 days, secondary endpoints indicated a substantial improvement in the 90-day recovery rate when compared to placebo [171]. These findings prompted a phase III trial (NCT00893867) to assess the therapeutic efficacy of DP-b99 in ischemic stroke [173]. A total of 446 patients with acute ischemic stroke participated in a randomized, double-blind, placebo-controlled trial. Intravenous DP-b99 (1 mg/kg/day) was administered within nine hours of symptom onset for four consecutive days. Patients did not receive alteplase. Treatment was well-tolerated, but the study failed to demonstrate any clinical benefit of DP-b99 [173].

1.2.2.5. Superficial siderosis

Superficial siderosis of the CNS is a rare disease typically caused by chronic or intermittent bleeding into the subarachnoid space. Common underlying causes include recent or previously resected CNS tumours, CSF cavitory lesions (meningocoele, pseudomeningocoele), vascular malformations, CNS trauma, subarachnoid haemorrhage, intracranial or spinal surgery, and brachial plexus or nerve root injury [144,174–176]. However, in approximately one-third of cases, the source of bleeding remains unidentified [176]. The most common clinical manifestations of superficial siderosis are deafness and cerebellar ataxia, which occur in approximately 90% of patients [144]. A hallmark of this condition is the deposition of haemosiderin, which is visualized on MRI as a hypointense rim surrounding the surface of the brainstem, cerebellum, and sometimes cortical fissures (Figure 16) [144,174–176].



Figure 16. T2 weighted MRI scans showing hemosiderin deposition (arrows) along cerebellar folia, brainstem, cerebral surfaces (a) and cervical spinal cord (b) from Nanda *et al.*, 2010 [176]

Iron is implicated in neurodegeneration, particularly in conditions characterized by axon degradation. This correlation is supported by the observation of preserved neural tissue at the core of the spinal cord, where iron accumulation is less pronounced [174]. The mechanism underlying iron overload in these conditions is thought to be similar to that seen in haemorrhagic stroke. Chronic bleeding leads to the release of erythrocytes, which, upon lysis, release their contents, including haem and iron [174]. Haem is degraded by haem oxygenase, generating carbon monoxide, biliverdin, and iron(II), which is subsequently stored in ferritin. As a protective response to iron overload, ferritin expression is upregulated in the brain [174]. Continuous free iron exposure leads to an increase in ferritin L subunits production. L subunits allows the long-term storage of iron as hemosiderin deposits [176]. However, it is hypothesized that hemosiderin may release stored iron, increasing the pool of free iron within the brain and contributing to oxidative stress [174,176].

The current treatment for superficial siderosis primarily focuses on addressing the underlying cause of bleeding [144,175]. Once the source of bleeding has been identified, surgical intervention is often considered. This may involve closing dural defects using sutures, patches, collagen sponge, fibrin glue, or muscle/fat grafting. However, despite surgical intervention disease may progress, especially in cases of longstanding superficial siderosis, where irreversible neural tissue damage may limit the potential benefits of surgery [175].

Chelation therapy, particularly using deferiprone, has been investigated as a potential treatment for superficial siderosis. However, the majority of clinical experience with deferiprone in this context is based on relatively small patient populations. A common dosage regimen is 30 mg/kg/day, which was established following a pilot safety trial involving 10 patients. This

dosage has been shown to be safe and effective in reducing hemosiderin deposition, as demonstrated by MRI studies [177].

Several studies have reported similar findings, with patients receiving 30 mg/kg/day of deferiprone showing reductions in hemosiderin deposition and neurological stabilization. In some cases, slight clinical improvements have been observed [178–180]. The largest study to date, involving 38 patients, has also reported positive outcomes [181]. One study (NTC00907283) involving 5 patients suggested that early initiation of deferiprone treatment, before the development of severe symptoms and advanced neurodegeneration, may be associated with better clinical outcomes [178]. However, it is important to note that another study involving 10 patients reported poor tolerability to the medication, with 40% of patients discontinuing treatment due to neutropenic sepsis. Furthermore, no significant clinical or radiological benefits were observed in this study [182].

1.3. Chelation therapy mechanisms

Having explored the diverse toxicity mechanisms of metals and their contribution to various health problems, particularly their impact on brain health, we now turn our attention to potential therapeutic interventions. Chelation therapy has emerged as a promising approach for removing excess metals from the body [20]. We will discuss its mechanisms of action as well as the factors that determine its effectiveness for removing metals in the case of metal dyshomeostasis.

Chelation therapy has a historical origin, with the development of BAL a dithiol compound as an antidote for the war gas dichlorovinyl arsine during World War II, it competes with protein sulfhydryl groups for arsenic compounds forming a stable complex with arsenic (III) [20,183]. Chelation therapy operates on the principle of using small molecules to bind and remove toxic metals from the body. These molecules reduce metal toxicity by either converting the metals into less harmful compounds or relocating them from the sites where they exert their toxic effects to areas where they cannot cause harm, without disrupting the balance of essential metals [12,20,28]. In the context of neurodegenerative diseases, the principle of preserving essential elements becomes even more critical. The goal is to selectively extract labile essential ions, which are believed to contribute to the deleterious effects associated with these diseases [12,28,35]. In the following section the different requirements for an effective a chelator in the context of neurodegenerative diseases are discussed in detail.

1.3.1. Thermodynamic factors

1.3.1.1. Stability

One of the most critical parameters for an effective chelator is its stability [56,107,184]. This stability is defined by the formation constant (β) of the metal-chelator complex (equation 10). The formation constant reflects the equilibrium between free metal ions and the bound complex (equation 9) [56]. A higher formation constant (β) indicates a greater affinity of the chelator for a specific metal ion [56]. For example, a complex denoted as $\text{Me}_p\text{L}_q\text{H}_r$ (where Me is the metal, L is the ligand in its full deprotonated state, p, q, and r represent the stoichiometric coefficients) [56].

Complex formation equation: $p\text{Me} + q\text{L} + r\text{H} \rightarrow \text{Me}_p\text{L}_q\text{H}_r$ (9) (charges omitted for simplicity)

$$\beta = \frac{[Me_p L_q H_r]}{[Me]^p [L]^q [H]^r} \quad (10)$$

The protonation constants of the chelating agent significantly influences complex formation. This is because protons compete with metal ions for binding sites on the ligand [56]. Additionally, the environmental pH plays a crucial role. For instance, human body pH varies considerably: extracellular pH is around 7.4, intracellular pH is about 6.8, and the gastrointestinal tract ranges from pH 1 to 6 [56]. Furthermore, the affinity of a chelator for a specific metal depends on both the nature of the metal cation and the coordinating groups within the chelator molecule [56,184]. This relationship is governed by the HSAB theory, which dictates that "hard" acids prefer to bind to "hard" bases, and vice versa[55,56]. Chelators with oxygen-containing coordinating groups will have a higher affinity for "hard" metal ions like iron (III) or aluminium (III) compared to chelators with sulfhydryl groups, which favour "softer" cations like cadmium (II) or lead (II) (Table 2) [55,56]. Chelators can be classified based on their denticity, which refers to the number of donor atoms in the molecule that can bind to the target metal ion [56]. For instance, bidentate chelators possess two donor groups that can simultaneously bind a metal ion [56,185]. As a general rule, chelators with higher denticity form more stable complexes with metal ions compared to those with lower denticity [107,185,186]. This enhanced stability is attributed to the chelate effect [185].

As previously discussed in the different presented pathologies, iron (III), copper (II), manganese (II), and aluminium (III) are the primary metals suspected of contributing to disease progression. Chelators like deferiprone, deferoxamine, and, to a lesser extent, DOTA and EDTA, exhibit high denticity and affinity for iron (III) (Table 1). For softer metals such as copper (II) and manganese (II), penicillamine, trientine, DOTA, EDTA, and PAS appear to be more suitable chelator options based on their complexation constants (Table 1).

Table 2. Categorization of metal ion and coordination group according to the HSAB principle taken from Crisponi and Nurchi 2016 [56].

Metal ions			Coordinating groups		
Hard	Intermediate	Soft	Hard	Intermediate	Soft
Li ⁺ , Na ⁺ , K ⁺ , Be ²⁺ , Mg ²⁺ , Ca ²⁺ , Sr ²⁺ , Mn ²⁺ , Al ³⁺ , Ga ³⁺ , Cr ³⁺ , Fe ³⁺ , Sn ⁴⁺ , (CH ₃) ₂ Sn ²⁺ , UO ₂ ²⁺ , VO ₂ ⁺	Fe ²⁺ , Co ²⁺ , Ni ²⁺ , Cu ²⁺ , Zn ²⁺ , Pb ²⁺ , Sn ²⁺ , Sb ³⁺ , Bi ³⁺	Cu ⁺ , Ag ⁺ , Au ⁺ , Hg ⁺ , Pd ²⁺ , Cd ²⁺ , Pt ²⁺ , Hg ²⁺ , CH ₃ Hg ⁺ , Pt ⁴⁺	H ₂ O, OH ⁻ , F ⁻ , RCOO ⁻ , Cl ⁻ , RO ⁻ , NH ₃ , RNH ₂	RNH ₂	R ₂ S, RSH, RS ⁻

While chelator complexation with a metal ion is a desired outcome, it may not entirely prevent unintended interactions [56,107,109]. For example, iron complexed with chelators like EDTA

or citrate can still coordinate with H_2O_2 if present, leading to its participation in Fenton's reaction and the generation of free radicals [107,187]. To minimize unwanted interactions with biological molecules, an ideal chelator should strive to fully saturate the coordination sphere of the target metal ion while avoiding ligand exchange with other molecules in the environment. Unlike EDTA-iron (III), where a seventh coordination site is occupied by water, this water molecule is capable of exchanging with oxygen or H_2O_2 specially at high H_2O_2 concentrations (100 H_2O_2 per iron ion), leading to redox activity [56,107,109,187].

Excess metals in the body are rarely found free. Instead, they are often bound to small proteins like albumin or small molecules like citrate, as seen in patients with iron overload [32]. Therefore, for a chelator to effectively extract metals from the body, the chelator's affinity for the metal ion must be greater than the affinity of the metal ion for these biological molecules [20].

1.3.1.2. Selectivity

The selectivity of a chelator is critical for its effectiveness in medical applications [28]. Selectivity determines whether the complex formed with the targeted toxic metal ion is sufficiently stable compared to complexes formed with other essential metal ions naturally present in the body [28,56,186]. Since these essential metals are often found at much higher concentrations than the targeted toxic metal, a good chelator must efficiently bind the toxic metal without significantly interfering with other cations to avoid disrupting metal homeostasis [56,186].

The selectivity of a chelator also relies on thermodynamic parameters, as discussed previously regarding the stability of complexes [56,184]. For a chelator to exhibit high selectivity for a specific metal, its complexation constant with the target metal should be several orders of magnitude greater than those for other ions [184]. This ensures that the chelator preferentially binds the toxic metal, minimizing interactions with essential metals and thereby maintaining the body's metal balance [184]. For example, both DFO and deferiprone exhibit iron (III) complexation constants that are several orders of magnitude higher than their respective complexation constants for other essential metals, such as copper (II) or zinc (II) (Table 1), making them highly selective iron (III) chelators.

Chelation therapy for essential elements present in excess, like iron overload in hemochromatosis and potentially in some neurodegenerative diseases, presents a unique challenge in terms of selectivity. The ideal chelator must be effective at extracting enough of the excess element to achieve a therapeutic effect, yet minimally disruptive to avoid causing a deficiency [28]. This delicate balance is crucial because strong metal chelators, while effective at competing with metal-binding proteins in the body, can lead to unintended consequences. These consequences include altered metal distribution, where excess chelator removes essential metals from their intended locations. Additionally, chelation can inhibit essential metal-containing enzymes by removing their metal cofactors, disrupting critical biological processes [28,186]. These drawbacks are all the more present in neurovegetative diseases where the excess metal is found in specific brain parts, thus making systemic chelation therapy not a suitable option.

1.3.2. Kinetic factors

Other important aspect to consider for the choice of a good chelator for chelation therapy is the kinetics, three kinetic factors have been identified. First the pharmacokinetic behaviour of the chelating agent, the kinetic behaviour of the toxic metal and the rate of interaction between the chelating agent and the metal-ion [56].

1.3.2.1. Pharmacokinetic properties

Pharmacokinetic properties, significantly impact the frequency and route of chelator administration [56]. Ideally, a chelator would possess a prolonged half-life within the body to maintain its activity for an extended duration [56]. However, in reality, chelators undergo metabolic processes that render them inactive [56]. Examples of these processes include disulfide bond formation in thiol-containing chelators, N-acetylation of amines, and glucuronidation of hydroxypyridinones [56]. A common strategy to address chelator inactivation is to administer a dose exceeding the stoichiometric amount required for metal complexation [186]. This approach aims to compensate for the loss of chelator activity due to metabolism [186]. However, excessive chelator concentrations within the body can disrupt normal physiological functions [6,186,188]. In the case of a local metal overload by targeting chelator delivery to the affected region, the circulating time during which the chelator can be metabolized and rendered inactive is reduced, enhancing its effectiveness in chelating the target metal. The different strategies to achieve a local or targeted administration of chelator are discussed in detail at the end of the chapter in the section local chelation.

Another factor influencing the circulation time of chelators is their ease of excretion by the body. Classical chelators like DFO (5-10 min half-life in blood) often have a short half-life within the body due to their low molecular weight (<45 kDa), which facilitates rapid renal elimination [56,189]. To extend their half-life, recent strategies have focused on increasing their molecular weight by grafting chelators to macromolecules such as proteins, polymers, or nanoparticles. This approach can prolong the circulation time of the chelator, potentially reducing the required number of doses and mitigating potential side effects [109,189,190].

1.3.2.2. Kinetics of the toxic metal

The kinetic behaviour of the toxic metal in the body plays a critical role in determining the success of chelation therapy [56]. This behaviour is governed by the metal's biodistribution, which encompasses the processes of absorption, circulation throughout the body, and ultimately, accumulation in specific organs [56]. In classical chelation therapy, the chelator primarily reaches its peak concentration within the blood [56,190]. Consequently, the rate of metal clearance from blood becomes a crucial factor [56]. If metal removal from plasma is too rapid, the chelator's effectiveness can be diminished due to a limited window of action [56]. Ideally, a chelator should not only effectively remove the metal from blood but also exhibit the ability to follow the metal ion into target tissues and promote chelation at those sites [56]. Therefore, in the case of neurodegenerative diseases, toxic metal biodistribution appears to be confined to the CNS. Therefore, effective chelation therapy requires the chelating agent to reach peak concentrations and be specifically targeted to the CNS.

1.3.2.3. Exchange rate between chelating agent and metal ion

The rate of interaction between a chelating agent and a metal ion, regardless of whether the metal is free or bound to transport proteins in the blood, is a critical factor for effective chelation therapy [56]. The metal extraction by the chelator from the biological molecule has to be faster than the rate of chelator and/or the metal disappearance from the bloodstream [56]. Even if thermodynamic parameters favour complexation with the chelating agent, slow interaction kinetics can hinder chelation from occurring [56]. Due to their redox-active nature and loose binding to proteins and small molecules, the targeted metals in the studied pathologies are more labile and prone to ligand exchange. To prevent complex dissociation and avoid the redistribution of toxic metals, the chelating agent should form a kinetically inert complex. Chelating agents with higher denticity and cyclic structures tend to be less labile than those with lower denticity and linear structures. For example, bidentate hydroxamates are more labile compared to hexadentate chelating agents like DFO [56,107].

1.3.3. Chelator Bioavailability for Neurological Applications

For a chelating agent to effectively treat neurological disorders, it must reach its target, the metal ions within the brain at sufficient concentrations [28]. This necessitates good bioavailability, which translates to the chelator's ability to cross various biological membranes, particularly the BBB [28,56,107]. Three key parameters significantly influence a compound's ability to permeate a lipid membrane like the BBB:

Lipophilicity: Highly lipophilic chelators like hydroxypyridinones readily cross the BBB [28,56,107]. However, they can also cross other critical barriers such as the placental barrier leading to enhancing potential toxic side effects [107].

Ionization State: Neutral molecules generally penetrate cell membranes more efficiently than charged molecules [107]. In the context of chelator design, a neutral chelator might be preferable for enhanced BBB permeability [28]. Furthermore, excretion is also favoured for neutral molecules [56]. Therefore, a neutral chelator-metal complex is generally preferable for efficient elimination from the body [56,107].

Molecular Size: As mentioned earlier, increasing a chelator's molecular weight can improve its half-life in the body [109,190]. However, for oral bioavailability, there's a size limitation. Chelators with a molecular weight exceeding 500 Da typically exhibit poor oral absorption [56,107].

1.3.4. Local chelation

Unlike other metal overload diseases like hemochromatosis or Wilson's disease, neurodegenerative diseases often exhibit localized metal overload confined to the brain or even specific brain regions. Traditional chelation therapy is designed for systemic metal chelation. To address neurodegenerative diseases, novel strategies and properties are required for targeted brain metal chelation without interfering with systemic metal homeostasis. The following section will explore various strategies aimed at increasing the uptake of chelators by the brain.

One strategy to enhance the delivery of chelators to the brain is to increase their lipophilicity, thereby facilitating their ability to cross the BBB. This can be achieved by grafting hydrophilic compounds like isopentyl groups or acetoxymethyl moieties [191].

Leveraging the brain's high nutrient demands, it's possible to enhance the uptake of chelators into the brain. For example, by functionalizing glucose with chelating moieties, the brain's natural glucose transport mechanisms can facilitate the delivery of chelators across the BBB. Furthermore, masking the chelating groups with glucose moieties can prevent premature metal binding until enzymatic cleavage of the sugar occurs, ensuring that chelation takes place within the brain [191].

Grafting chelators with neutral amino acids that are naturally transported into the brain can enhance their uptake. For example, functionalization with L-DOPA or alanine amino acids has been explored for this purpose [191,192]. To achieve more targeted delivery, functionalizing neuropeptides with metal-chelating groups is a viable option. The peptide NAP, composed of eight amino acids (Asn-Ala-Pro-Val-Ser-Ile-Pro-Gln), can cross the blood-brain barrier and exhibits neuroprotective properties. This peptide could be functionalized with chelating groups. A similar strategy could involve functionalizing brain receptor-specific peptides with chelating groups to target the brain [191].

The use of prochelators can also provide localized chelation. Prochelators are molecules that lack intrinsic metal-chelating properties but acquire these properties upon exposure to an external stimulus. Ideally, this stimulus should be present only in the brain to ensure localized chelation within that region. One approach involves using photoreactive groups like ortho-nitrobenzyl, which inhibit chelating properties until activated by UVA light [191]. However, this method requires brain irradiation with UVA light, which can be challenging, especially in deep brain regions. Alternative prochelators can be activated by oxidative stress. For example, BSIH, a molecule without intrinsic chelating properties, can release a boric ester upon reaction with H_2O_2 . This transformation yields SIH, which exhibits iron-chelating properties. Moreover, by reacting with H_2O_2 , BSIH can also protect tissues from oxidative stress (Figure 17) [191].

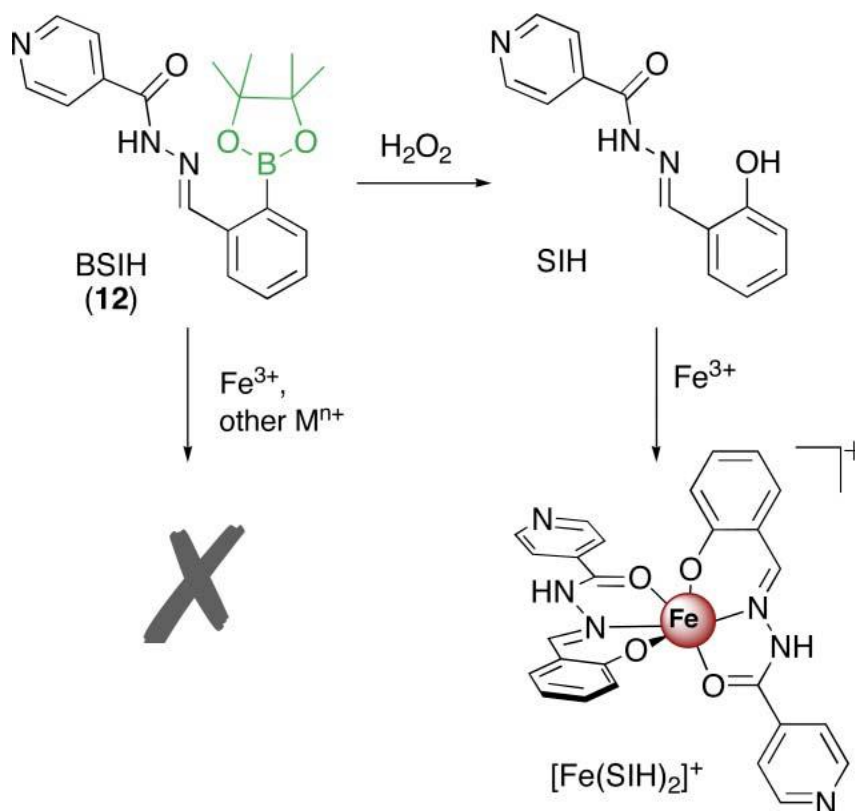


Figure 17. BSIH, a prochelator, exhibits no chelating properties in its original form. However, upon reaction with hydrogen peroxide, it transforms into SIH, which possesses iron-chelating properties. Taken from L.R. Perez and K.J. Franz, 2009 [191].

Nanoparticles ranging in size from 10-1000 nm have been shown to cross the BBB via receptor-mediated transport systems. Grafting chelators onto nanoparticles can reduce their toxicity and enable the use of hydrophilic chelators that would otherwise be unable to penetrate the BBB [191,193]. Additionally, nanoparticles offer the advantage of allowing for multiple targeting strategies. For example, functionalizing nanoparticles with brain-targeting peptides can enhance their delivery to the brain [194].

Another strategy for localized chelation involves the use of chelating hydrogels. These hydrogels, loaded with chelating molecules, offer the advantage of sustained drug release [195,196]. Alternatively, direct functionalization of the hydrogel with chelating groups can confer chelating properties to the material itself. Due to their slow degradation, these hydrogels can provide long-lasting localized chelation [197]. For brain chelation, this approach necessitates direct deposition of the hydrogel within the brain tissue. This strategy will be discussed in detail in the following chapters.

Chapter II: Development of chelating polymers

To overcome the limitations of small-molecule chelating agents for treating brain pathologies, the use of biopolymers has been explored. These polymers serve as an initial matrix that can be functionalized with chelators, creating chelating polymers [190,198–201]. This approach increases the overall molecular weight of the chelator, potentially extending its half-life in the body after direct administration [190]. Furthermore, the utilization of polymers presents the opportunity to develop materials specifically tailored for the desired application. For instance, natural polymers like chitosan, alginate, and hyaluronic acid, as well as synthetic polymers such as polyacrylamide and poly(ethylene glycol) dimethacrylate, are commonly employed as building blocks for hydrogels [202–204]. By grafting chelators onto these polymers, the resulting chelating material can provide localized chelation, which is particularly advantageous for treating neurodegenerative diseases where metal dyshomeostasis occurs in specific areas of the body. Furthermore, depending on the size of the final polymer, it could also be employed in dialysis or microdialysis. A notable example is the MEXBRAIN start-up, which combines these two technologies for the treatment of systemic metal overload through haemodialysis (Figure 18). This innovative technology is currently undergoing two clinical trials, the first being MEXWILLS (NCT05917327) which aims to evaluate the medical device (a soluble chitosan functionalised with DOTAGA) safety and capacity to extract free copper from blood in patients with Wilson disease. The second clinical trial (MexACLF NCT06340269) evaluates the safety and capacity to extract free iron from patients with acute on chronic liver failure. The treatment is based on the principle that the large chelating polymer located in the dialysate is unable to permeate the dialysis membrane due to the higher molecular weight compared to the cut-off of the dialysis membrane. While, metal ions bound to small molecules and proteins, can pass from the blood to the dialysate. These metal ions are subsequently captured by the chelating polymer, resulting in a concentration of metal ions within the dialysate and enhancing metal extraction compared to simple diffusion [198]. It's important to note that the MEXBRAIN technology, designed for haemodialysis, chelates metals in a non-localized manner. However, when combined with brain microdialysis, chelation can be targeted specifically to CSF surrounding the brain, avoiding systemic chelation and minimizing the risk of systemic metal depletion.

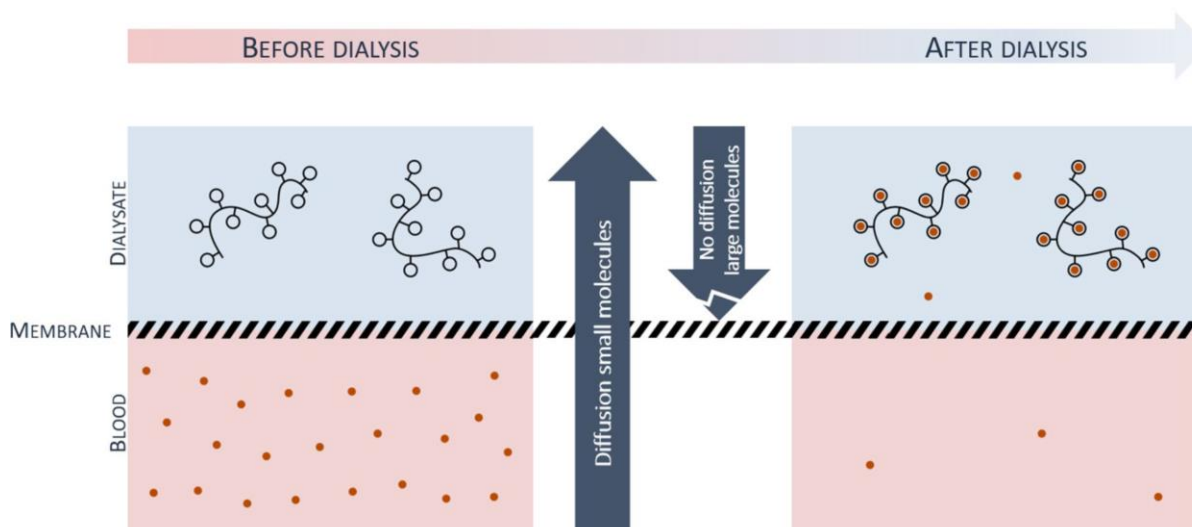


Figure 18. Schematic representation of the chelating polymer-dialysis system developed by MEXBRAIN. The red dots symbolize the targeted loosely bound metal ions.

The first polymer chosen to be functionalized is a polyethylene glycol (PEG) derivative called star-like 8-arm-polyethylene glycol (8-arm-PEG) with terminal amine functions in each arm (Figure 19). PEG is approved by the FDA as a pharmaceutical polymer material, and it has been used in many products due to its properties of increasing the biocompatibility and the solubility of multiple compounds [205–207]. Additionally, PEG and PEG derivatives are available with a diverse range of terminal functional groups, including amine, alcohol, carboxylic acid, azide, and thiol, which facilitates their conjugation with various molecules [206].

Star-like PEG derivatives are characterized by having at least three linear arms connected to a central core. These arms are equivalent in size and structure. There are primarily two synthesis strategies for producing multi-arm PEG. The most common approach is the "core-first" strategy, where glycerol, pentaerythritol, or D-sorbitol cores are used as initiators to promote the polymerization of each arm. In contrast, the "arm-first" strategy involves crosslinking linear PEG chains with a multi-functional core to create the star-shaped polymer. [206,208]. Compared to linear PEG with a similar molecular weight, multi-armed PEG offers several advantages, including lower solution viscosity due to reduced arm entanglement [208]. However, the most significant benefit in this context is the increased number of terminal functional groups available for conjugation, which enhances the drug loading or functional capacity per polymer molecule [206,208].

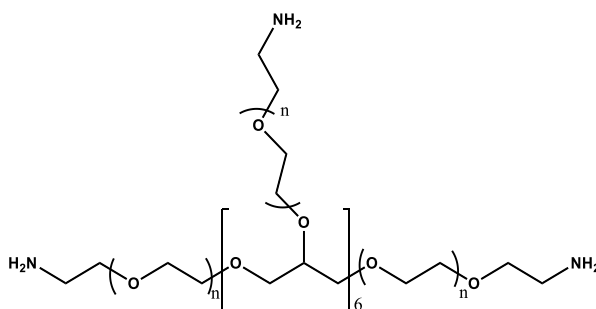


Figure 19. Chemical structure of 8-arm-PEG.

The second polymer chosen for functionalisation is chitosan (Figure 20). Chitosans are a family of linear copolymers composed D-glucosamine linked to N-acetyl-D-glucosamine through a β -(1 \rightarrow 4) bond. The fraction of N-acetyl-glucosamine units is called the degree of acetylation (DA) [209–213]. Chitosans are derived from chitin, through alkaline deacetylation of chitin [209,212,213]. Chitin is a natural polymer found in crustaceans shells, insect's cuticles, and fungi cell walls. However, natural chitosan can be derived from fungal sources [213]. Industrially, the primary source of chitosan is crustacean shells, which makes it a cheap and readily available source [211,213].

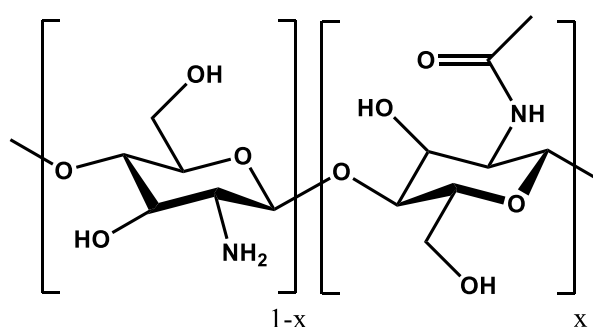


Figure 20. Chemical Structure of Chitosan polymer family (x =DA i.e. degree of acetylation).

Chitosans are versatile polymers with multiple properties valuable in the medical field. Chitosan's biocompatibility is attributed to its macromolecular structure, which resembles extracellular matrix glycosaminoglycans [210]. Additionally, its biodegradability is facilitated by enzymes, which catalyse the hydrolysis of beta (1 \rightarrow 4) linkages between the different residues. Vertebrates are believed to primarily degrade chitosan using lysozyme and bacterial enzymes found in the colon [214]. Additionally chitosan has been found to have antibacterial and antifungal properties, making it a promising polymer for biomedical applications [210,214]. The DA and molecular weight distributions of chitosan are two key factors that influence its properties. However, this work will focus on the impact of DA, while the effect of molecular weight will not be fully addressed. Increasing the DA enhances chitosan's hydrophilicity and solubility in the deprotonated state [213,215]. Biodegradability is also influenced by DA, with higher DAs leading to faster degradation rates [213,214]. Protonated chitosan with a low DA exhibits a high density of protonated amine groups, which brings hydrophilicity, solubility and facilitates interactions with cell membranes and enhances muco-adhesion. Increasing the molecular weight further increases these interactions per polymer chain, further promoting muco-adhesion [213]. Like the selected 8-arm-PEG (Figure 19), chitosan possesses amine groups (in N-glucosamine) (Figure 20) enabling further chemical modifications to tailor its characteristics for specific applications [216,217]. At low pH, the amine groups of chitosan become protonated, rendering it a water-soluble cationic polyelectrolyte. As the pH increases, deprotonation of the amine groups occurs, resulting in chitosan insolubility for $DA < 40\%$. This transition between soluble and insoluble chitosan occurs at the pKa of its amine groups, which is typically in the range of 6.2 to 6.5 [213,218].

Neutralization of concentrated chitosan solutions induces hydrogen bonding and hydrophobic interactions, resulting in the formation of a physical hydrogel without requiring additional crosslinkers [219]. Neutralized chitosan exhibits chelating abilities for metallic cations such as Cu^{2+} , Zn^{2+} , Fe^{2+} , Fe^{3+} ... [220,221]. However, unmodified chitosan metal complexes have unsaturated metal coordination spheres [221]. This can lead to redox reactions and non-specific transmetallation due to similar complexation constants for various metal cations, limiting its effectiveness for *specific* iron chelation in therapeutic contexts [222–224].

Iron is a primary target for chelation therapy in neurodegenerative diseases due to its frequent association to disease pathogenesis as seen in the previous chapter. Consequently, a strong iron-specific chelator is desirable. A previous collaboration between ILM, IMP, and the start-up MEXBRAIN successfully grafted a chelator onto chitosan by using a DOTA derivative (DOTAGA anhydride). A low DA chitosan (6%) achieved a grafting rate of ~17% DOTAGA, while a reacylated chitosan (DA~30%) had a lower grafting rate of ~7% DOTAGA [198,225]. DOTA can chelate iron (III), as evidenced by its complexation constant (Table 1).

However there are chelators who have higher complexations constants with iron(III) such as deferiprone or DFO (Table 1). Moreover, both chelators are commonly used to treat iron overload and have been previously evaluated in clinical trials for neurodegenerative diseases, as discussed in the preceding chapter, whereas DOTA isn't.

Additionally, the difference in complexation constants between iron (III) and copper (II) or iron (III) and zinc (II) is more pronounced for DFO and deferiprone than for DOTA (see Table 1) rendering deferiprone and DFO specific iron chelators. However DFO complexes iron (III) with a 1:1 iron-to-chelator stoichiometry whereas deferiprone chelates iron (III) in a 3:1 ratio [5,8]. This implies that a DFO-functionalized polymer will exhibit greater iron binding capacity per functionalized group compared to its deferiprone counterpart. Therefore, for functionalization of polymers for iron (III) extraction, the chosen chelator was DFO.

2.1. DFO functionalised polymer synthesis

To graft DFO onto the polymer via its amine group, the DFO derivative p-NCS-Bz-DFO (N1-hydroxy-N1-(5-(4-(hydroxy(5-(3-(4-isothiocyanatophenyl) thioureido) pentyl) amino)-4-oxobutanamido) pentyl)-N4-(5-(N-hydroxyacetamido) pentyl) succinimide (provided by Chematech) was selected. The isothiocyanate moiety of p-NCS-Bz-DFO reacts with the polymer's amine group, forming an isothiurea bond between the chelator and the polymer backbone [226]. Nevertheless, p-NCS-Bz-DFO is a hydrophilic compound soluble exclusively in DMSO, thus, the reaction medium will need to be optimized.

2.1.1. Synthesis of 8-arm-PEG@DFO

Eight-arm polyethylene glycol (8-arm-PEG) is solubilized in DMSO at a concentration of 0.9%(w/w) (0.25 mM) at 40°C. After complete dissolution, NCS-Bz-DFO powder is added with stirring to achieve a final concentration of 0.069 %(w/w) (0.92 mM). The mixture is stirred continuously at 40°C for four hours. The reaction mixture is subsequently diluted tenfold with water and purified through tangential filtration (membranes with cut-off 40kDa) using a volume of water fifteen times that of the initial reaction mixture. The purified product is then lyophilized.

2.1.2. Chitosan functionalisation with DFO (DA₄₀@DFO₄)

The coupling reaction between an amine and an isothiocyanate moiety is more efficient at higher pH values, however, low DA chitosan is not soluble in this range of pH [226]. Therefore, a first step of reacetylation of chitosan is necessary in order to extend the solubility range of chitosan, in particular to obtain a chitosan soluble at neutral pH. The synthesis is then performed in two steps (Figure 21).

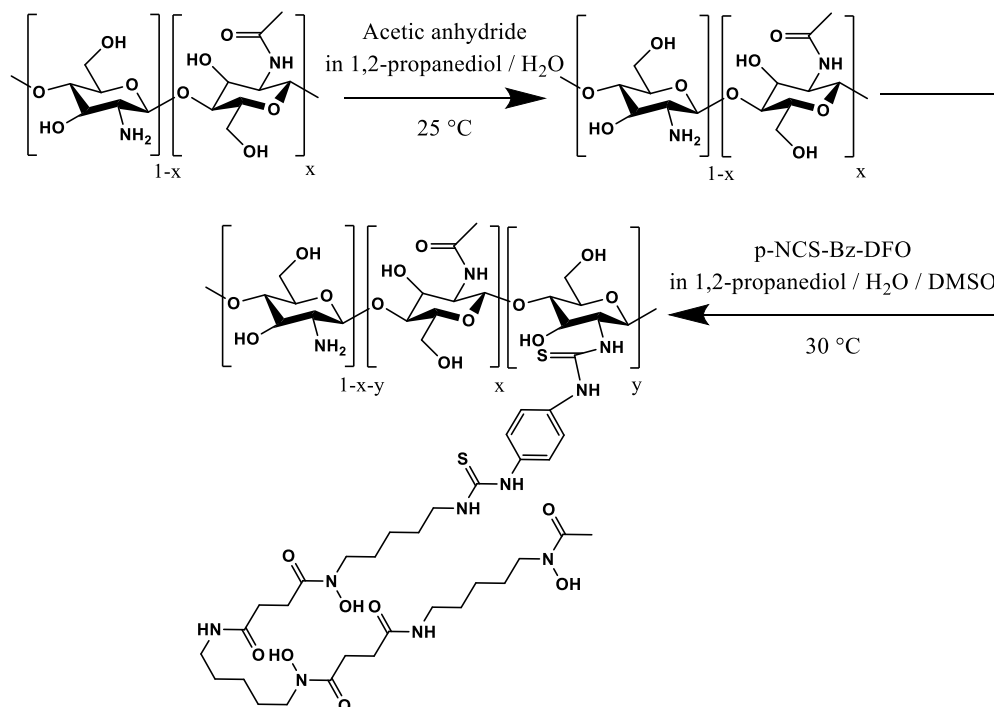


Figure 21. Synthesis pathway of DA₄₀@DFO₄ from chitosan, x corresponds to degree of acetylation (DA), y is the grafting ratio (substitution degree) of p-NCS-Bz-DFO.

Reacetylation step:

Chitosan reacetylation was performed using acetic anhydride as the reagent in a water/1,2-propanediol mixture (Figure 21). Detailed procedures can be found in the "Materials and Methods" section of Chapter III in the paper "Chitosan-based hydrogel for iron (III) chelation in biological conditions". Briefly, a 1.5% (w/w) low DA chitosan solution was prepared in 1% acetic acid. To achieve a chitosan concentration of 1.25% (w/w), 1,2-propanediol was added. 1,2-propanediol limited water content, thereby reducing acetic anhydride hydrolysis risk. Acetic anhydride, diluted to 3% (v/v) (0.32M) in 1,2-propanediol, was added under stirring until the chitosan concentration reached 1% (w/w). For DA determination, the mixture was purified through tangential filtration using a volume of ultrapure water fifteen times the initial reaction mixture volume, followed by lyophilization.

DA was determined according to Hirai's method by calculating the ratio between the peak area corresponding to the CH₃ protons of the acetyl moiety and the peak area corresponding to the six protons of chitosan (excluding the anomeric protons) (Figure 22) [227]. x is equivalent to

the DA, in this case the DA of the reacetylated chitosan is equal to $40 \pm 0.5\%$. In the following, the reacetylated chitosan with DA of 40% will be referred to as DA₄₀.

$$\frac{Area_{3.00-4.55 \text{ ppm}}}{Area_{2.45 \text{ ppm}}} = \frac{6}{3x} = \frac{2}{x}$$

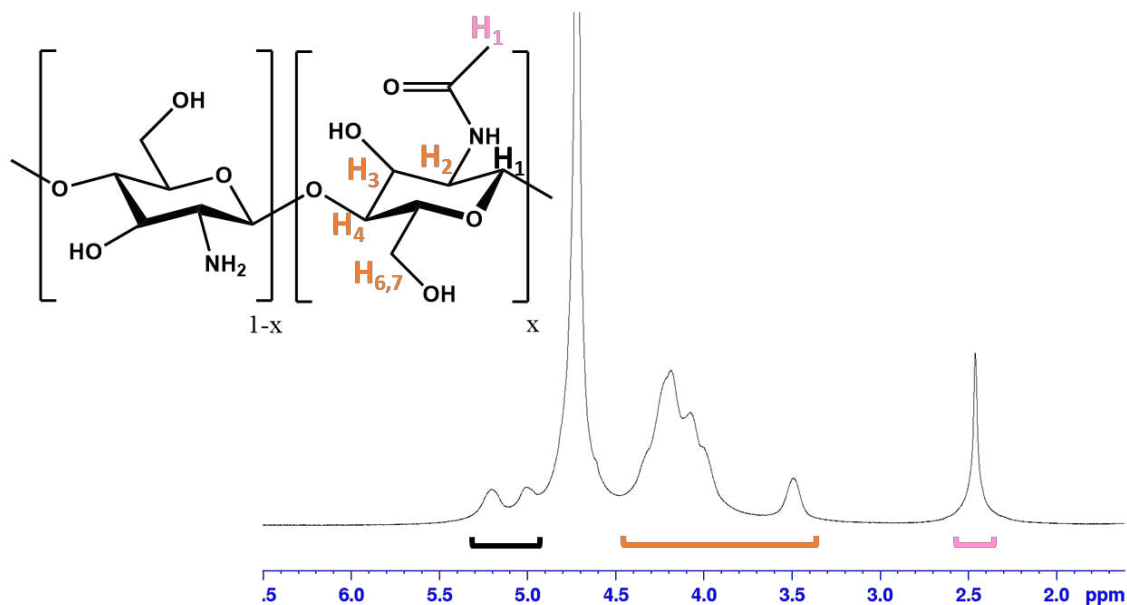


Figure 22. Representation and ¹H RMN spectrum of reacetylated chitosan DA₄₀. Analysis performed at 0.5% (w/w) in D₂O at 70°C at the NMR platform in Axel'One Campus.

Functionalisation step:

Chitosan, unlike PEG, is not soluble in organic solvents whereas p-NCS-Bz-DFO is insoluble in water therefore it is necessary to find a common reaction solvent. Multiple synthesis tests were done in order to find proper solubility conditions (Table 3).

Ideally, the acetylation and functionalization steps should be conducted in a single one-pot reaction. The initial reaction medium will then consist of a mixture of water, 1,2-propanediol and DMSO since p-NCS-Bz-DFO is only soluble in DMSO. Following the acetylation step, the reaction mixture contains 1% (w/w) chitosan in 30% (v/v) 1,2-propanediol. For all synthesis experiments, the final concentrations are maintained at 0.5% (w/w) polymer thus there will always be a minimum of 15% (v/v) 1,2-propanediol. Similar to its role in the acetylation step, 1,2-propanediol helps to reduce the water content of the reaction mixture, minimizing the risk of isothiocyanate hydrolysis. The reaction between amines and isothiocyanates is favoured when the amine is deprotonated, so the pH of the reaction mixture should be maintained, if not above the pK_a of chitosan's amine groups (6.2-6.5), close to it in order to have available free amines for coupling [218,226]. The solvent proportions for each synthesis test can be found in Table 3.

In the first synthesis experiment, p-NCS-Bz-DFO was solubilized in DMSO at a concentration of 1% (w/w) and added dropwise to the reaction mixture. The solution became

cloudy after approximately 27% of the total volume of p-NCS-Bz-DFO was added (Figure 23 #1).

For the second experiment, the same protocol was followed, but the reaction mixture was heated to 30°C. Cloudiness was observed after the addition of approximately 36% of the total p-NCS-Bz-DFO solution (Figure 23 #2). In both experiments, the water fraction was still too high to ensure complete solubility of p-NCS-Bz-DFO.

Therefore, in experiment 3, the proportion of DMSO was increased from 11% (v/v) to 25% (v/v) by diluting the initial p-NCS-Bz-DFO solution 2.3-fold with DMSO. Under these conditions, the entire volume of p-NCS-Bz-DFO solution could be added without cloudiness. However, the solution became cloudy approximately 30 minutes after the addition of p-NCS-Bz-DFO (Figure 23 #3).

In experiment 4, instead of diluting the p-NCS-Bz-DFO solution, extra DMSO was added directly to the reaction mixture prior to the addition of the 1% (w/w) p-NCS-Bz-DFO solution. The resulting solution was largely transparent, with only small suspended residues visible after one hour. The presence of DMSO in the reaction mixture prior to the addition of DFO ensures a higher concentration of DMSO within the reaction media when p-NCS-Bz-DFO is added compared to simply diluting the p-NCS-Bz-DFO solution (as in experiment 3). This elevated DMSO concentration enhances the solubility of p-NCS-Bz-DFO (Figure 23 #4).

In the 5th experiment, the same protocol as used in the fourth experiment was followed, with the exception of adjusting the pH of the solution to 6.5 prior to the addition of p-NCS-Bz-DFO. This modification did not alter the final outcome compared to the fourth experiment (Figure 23 #5). It was observed that maintaining a pH closer to 7 resulted in the precipitation of DA₄₀ even before the addition of the 1% (w/w) p-NCS-Bz-DFO solution. Therefore, the reaction should be conducted at a pH below 7 to prevent chitosan precipitation in this mixture of water/1,2-propanediol/DMSO.

For synthesis experiments 6 and 7, the amount of 1,2-propanediol was doubled while other parameters were maintained constant. Synthesis 6 was conducted at pH 5.5, while synthesis 7 was performed at pH 6.5. Synthesis 6 resulted in a transparent solution (Figure 23 #6), whereas synthesis 7 yielded a slightly cloudy and viscous solution (Figure 23 #7). It is hypothesized that the higher pH in synthesis 7 decreased the solubility of DA₄₀ in the reaction medium. While reducing the DMSO concentration could potentially improve DA₄₀ solubility, the final DMSO proportion should be maintained above 11% to avoid the solubility issues encountered in previous experiments.

Therefore, in the final synthesis test, the DMSO concentration was reduced to 18% instead of 25%. This modification resulted in a transparent solution that is purified through tangential filtration against 7.5 volumes of 0.1 M acetic acid, followed by 7.5 volumes of ultrapure water. (Figure 23 #8). The resulting polymer will be designated as DA₄₀@DFO₄. While this polymer is soluble in water at physiological pH, it precipitates under isotonic conditions, rendering it unsuitable for direct administration as a solution. However, DA₄₀@DFO₄ can be utilized in the development of chelating hydrogels, as further explored in Chapter III presented as an article entitled "Chitosan-based hydrogel for iron (III) chelation in biological conditions".

Table 3. Summary of each synthesis test conditions showing the synthesis pH, temperature, variations in 1,2-propanediol and DMSO proportions in the reaction mixture.

Number	pH	Theoretical DFO grafting rate %	T°	Final DMSO % (v/v)	Final 1,2-propanediol % (v/v)
#1	5,5	5	Room temperature	11,1	15
#2	5,5	5	30°C	11,1	15
#3	5,5	5	30°C	25	15
#4	5,5	5	30°C	25	15
#5	6,5	5	30°C	25	15
#6	5,5	5	30°C	25	30
#7	6,5	5	30°C	25	30
#8	6,5	5	30°C	18	30

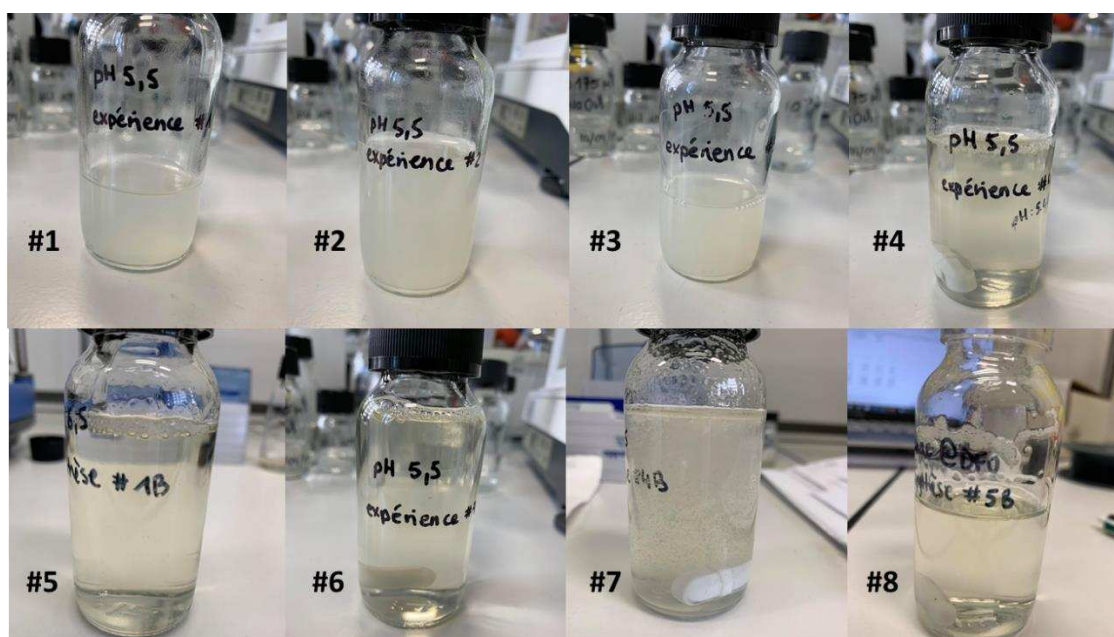


Figure 23. Images of the synthesis experiments in different solvent ratios (Water/1,2-propanediol /DMSO), the experiment number correspond to table 3.

2.1.3. Double-functionalized chitosan (DA₂₉@DOTAGA₉@DFO₅)

To create a chelating polymer with both high physiological solubility and iron specificity, DFO was grafted onto chitosan derivative with a DA of 29% and grafted DOTAGA (DA₂₉@DOTAGA₉) (Figure 23). Due to the hydrophilic nature of DOTAGA, the DA₂₉@DOTAGA₉ polymer exhibits excellent solubility at physiological pH and remains soluble in a solution containing 18% (v/v) DMSO, 30% (v/v) 1,2-propanediol, and 52% (v/v) water at pH 6.0±0.5 at a concentration of 0.5% (w/w). These conditions are identical to those used for the synthesis of DA₄₀@DFO₄. Unlike chitosan with a DA of 29% (DA₂₉) without

DOTAGA, which precipitates under these conditions. The grafting of DOTAGA onto chitosan enhances its solubility, enabling the subsequent functionalization of DA₂₉@DOTAGA₉ with p-NCS-Bz-DFO, even at lower degrees of acetylation than 40%. The synthesis of this double-grafted polymer involves three main steps, as previously described by Grange *et al.*, 2023 (Figure 24) [199].

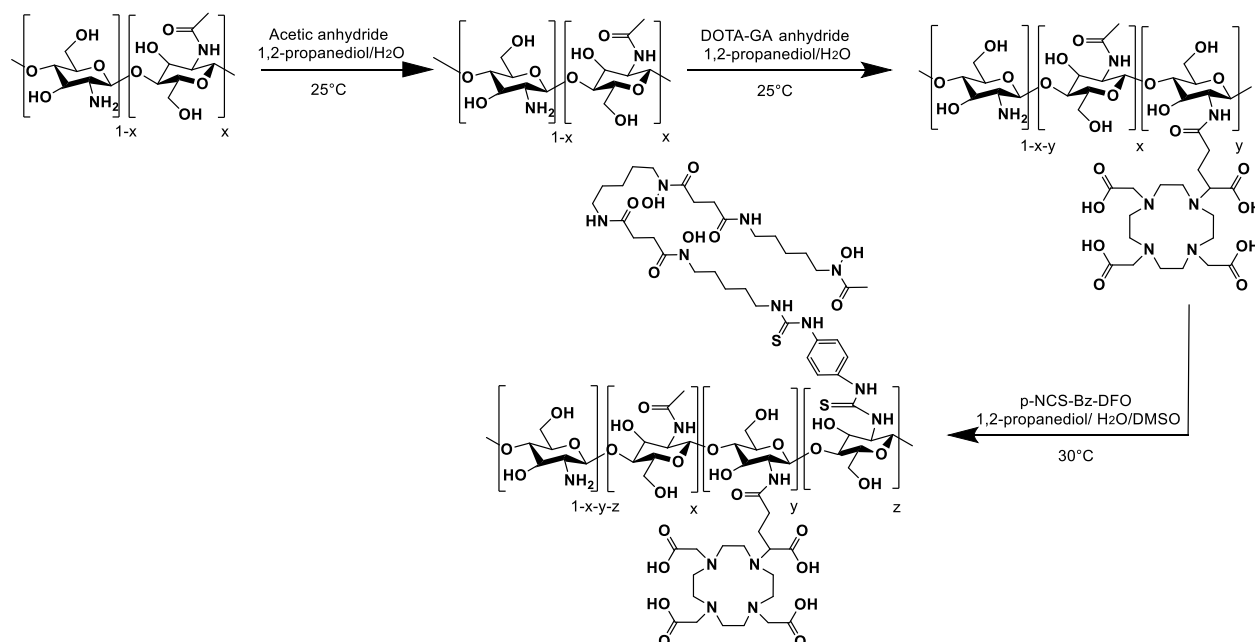


Figure 24. Synthesis pathway of DA₂₉@DOTAGA₉@DFO₅ from chitosan, x corresponds to degree of acetylation (DA), y is the grafting ratio (substitution degree) of DOTAGA and z the grafting ration of p-NCS-Bz-DFO.

1. Reacetylation: Starting with low DA chitosan, a reacetylation step is performed using the same parameters as those employed for the synthesis of DA₄₀, with the exception of acetic anhydride concentration, which is diluted to 2.4% (v/v) (0.24 M) in 1,2-propanediol.
2. DOTAGA Grafting: The reaction mixture is diluted with 1,2-propanediol to achieve a final concentration of 50% (v/v) to minimize hydrolysis. DOTAGA anhydride is then added to a final concentration in the reactor of 6% (w/w). The product is purified by tangential filtration against a volume of acetic acid 0.1M 7.5 half times the volume of the reactional mixture, and then against 7.5 half times the volume of the reactional mixture of ultrapure water.
3. p-NCS-Bz-DFO Grafting: The purified DA₂₉@DOTAGA₉ polymer is dissolved in ultrapure water at a concentration of 1% (w/w). The subsequent grafting of p-NCS-Bz-DFO is performed under the same conditions as those used for the synthesis of DA₄₀@DFO₄ being pH 6.0±0.5 and 52%/30%/18% the proportions of solvent (water, 1,2-propanediol, DMSO respectively) after addition of the p-NCS-Bz-DFO 1%(w/w) DMSO solution.

Further details on the synthesis can be found in the *material & methods* of the article draft “Development of chitosan-based hydrogels with tailored hydrophilicity and swelling characteristics” in chapter III.

Unlike DA₄₀@DFO₄, DA₂₉@DOTAGA₉@DFO₅ is able to stay soluble at pH 7.4 in isotonic conditions (0.7% (w/w) NaCl) without precipitation at a concentration of 0.5% (w/w). This property makes it suitable for applications where the polymer must be in solution, such as dialysis fluids [199]. The observed difference in behaviour between these two DFO-grafted polymers can be attributed to their distinct hydrophobicity/hydrophilicity balances. While p-NCS-Bz-DFO itself is a hydrophobic molecule, increasing its grafting ratio on the polymer can enhance its overall hydrophobicity. In contrast, increasing the DA or grafting with DOTAGA can improve hydrophilicity in the deprotonated state. However, the addition of DOTAGA appears to have a more pronounced effect on hydrophilicity, likely due to the introduction of several negative charges from each DOTAGA moiety due to its multiple carboxylic acid functions (pK_{a1}:2.4, pK_{a2}:4.3, pK_{a3}:4.6, pK_{a4}:9.7 and pK_{a5}:11.9 [13]), whereas acetylation only promotes hydrophilicity in the deprotonated state. This results in a higher solubility of the double grafted DA₂₉@DOTAGA₉@DFO₅ polymer compared to DA₄₀@DFO₄'s solubility.

2.2. Polymer characterisations

Characterizing the physico-chemical properties of the polymers was essential for understanding their behaviour. The article entitled "Chitosan-based hydrogel for iron (III) chelation in biological conditions", we briefly discuss some of these techniques for DA₄₀@DFO₄. However, given the primary focus of the article on chelating hydrogel development, these techniques will be described in more detail in this section.

2.2.1. Characterization of 8-arm-PEG@DFO

¹H NMR

The comparison of the NMR spectra of the initial 8-arm-PEG (Figure 25) and the final DFO-grafted product (Figure 26) reveals that new peaks in the latter correspond to the grafted Bz-DFO moiety. Furthermore, the disappearance of the triplet at 2.8 ppm, attributed to the protons adjacent to the amine function in the original 8-arm-PEG spectrum (Figure 19), provides additional evidence for the successful conjugation of DFO to the polymer *via* amine coupling.

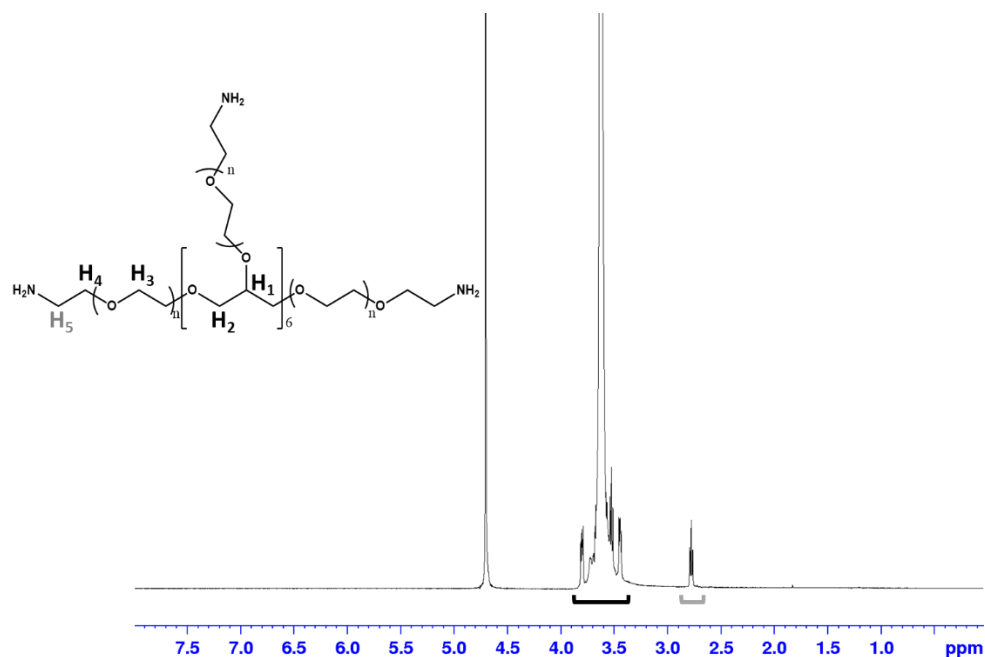


Figure 25. Representation and ^1H RMN spectrum of 8-arm-PEG. Analysis done at 1.5% (w/w) in D_2O 25°C at the NMR platform in Axel'One Campus.

Table 4. Attribution of ^1H RMN signal of 8-arm-PEG in figure 25.

Chemical shift (ppm)	Attribution
3.4-3.9	H ₁ -H ₄ (in black)
2.8	H ₅ (in grey)

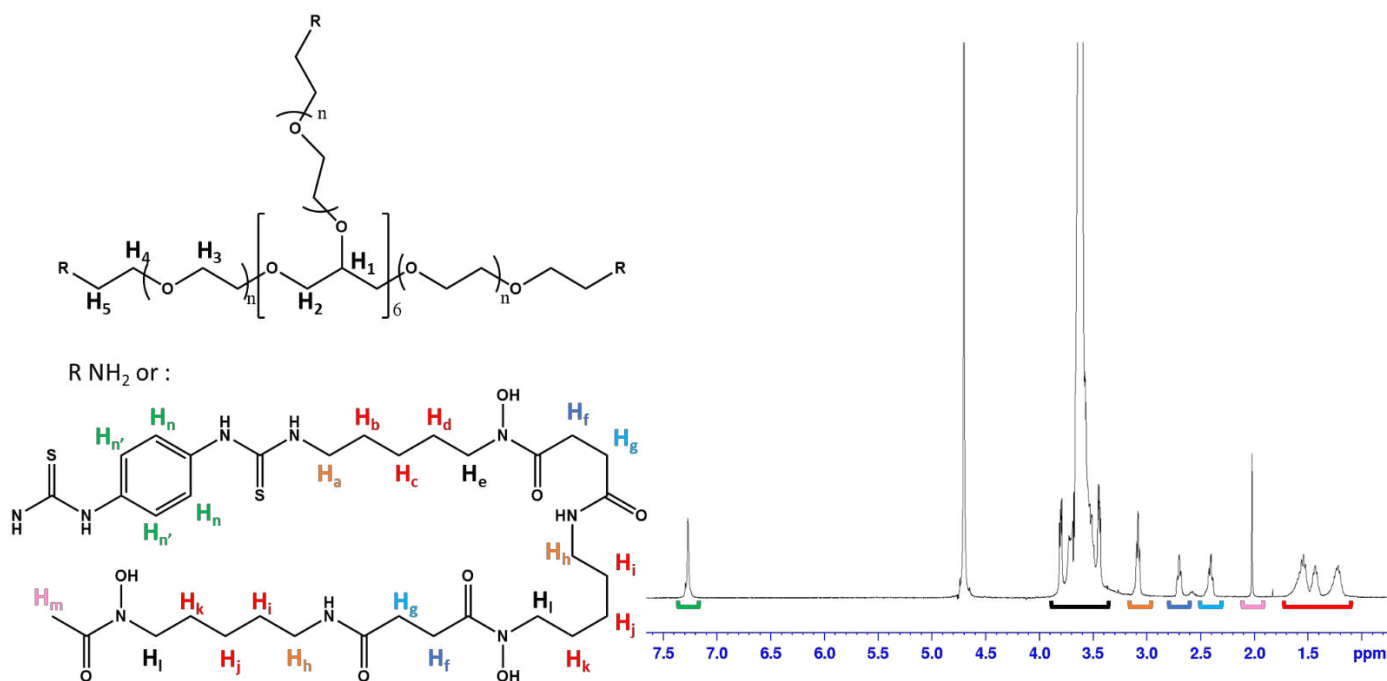


Figure 26. Representation and ^1H RMN spectrum of 8-arm-PEG@DFO. Analysis done at 1.5% (w/w) in D_2O at 25°C at the NMR platform in Axel'One Campus.

Table 5. Attribution of ^1H RMN signal of 8-arm-PEG@DFO in figure 26.

Chemical shift (ppm)	Integration	Attribution
7.3	4	H_n, H_n' (in green)
3.4-3.9	6 +all PEG protons	$\text{H}_e, \text{H}_l, \text{H}_l - \text{H}_5$ (in black)
3.1	6	$\text{H}_a \text{H}_h$ (in orange)
2.7	4	H_f (in blue)
2.4	4	H_g (in cyan)
2.1	3	H_m (in pink)
1.8-1.2	18	$\text{H}_b, \text{H}_c, \text{H}_d, \text{H}_k, \text{H}_i, \text{H}_j$ (in red)

Determination of DFO grafting rate in 8-arm-PEG@DFO by UV/Vis titration

The complex DFO-Fe(III) has a maximum absorption at around 430 nm, DFO alone and iron (III) doesn't not absorb light at that wavelength (figure 27). Therefore, the iron-chelating capacity of the 8-arm-PEG@DFO was evaluated by measuring its iron (III) binding capacity through a UV/Vis dosage of the DFO-iron (III) complex.

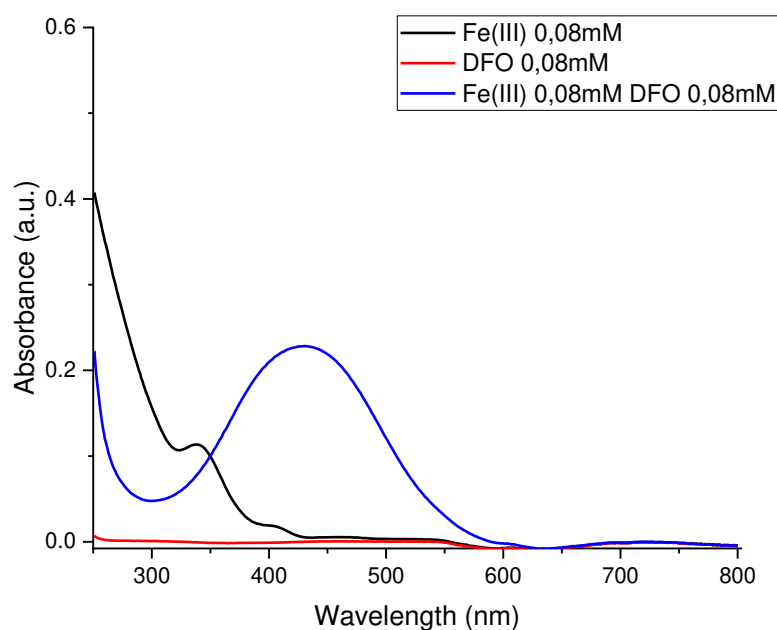


Figure 27. UV-Vis Absorption spectrum of commercial DFO mesylate at 0.08mM (red), iron (III) at 0.08mM (black) and a solution of DFO mesylate and iron (III) both at 0.08mM (blue). All solutions were prepared in a 0.1M AcOH / 0.1M AcONH₄ buffer solution (acetate buffer) to keep the pH stable at 4.5.

Material and methods Multiple solutions of 8-arm-PEG@DFO were prepared at a fixed concentration (0.01 (w/w)) in an acetate buffer solution ammonium acetate (0.1 M)/acetic acid (0.1 M) (pH 4.5), and increasing amounts of iron (III) were added (0-16 μM) and the absorbance measured (figure 28A). As the DFO moieties on the polymer chelate iron (III) ions, a complex is formed, resulting in an increase in absorbance at 430 nm, a characteristic peak for DFO-Fe(III) [228]. After this increase, a plateau effect is observed once all DFO binding sites on the polymer are saturated with iron (III).

Results and discussion A plot of iron concentration (mmol per gram of polymer) versus absorbance at 430 nm for each sample can be used to determine the grafting rate (figure 28B). The crossover between the two linear regimes in this plot corresponds to the transition from unsaturated to saturated DFO binding sites. In this experiment, the grafting rate (C_{DFO}) was determined to be 0.08 mmol of DFO per gram of 8-arm-PEG@DFO. Additionally, the initial slope of the plot provides the molar absorption coefficient of the DFO-Fe(III) complex, which in this case was $\epsilon = 2500 \text{ L}\cdot\text{mol}^{-1}\cdot\text{cm}^{-1}$, consistent with values reported in the literature ($\epsilon = 2300 \text{ mol}^{-1}\cdot\text{cm}^{-1}$) [228].

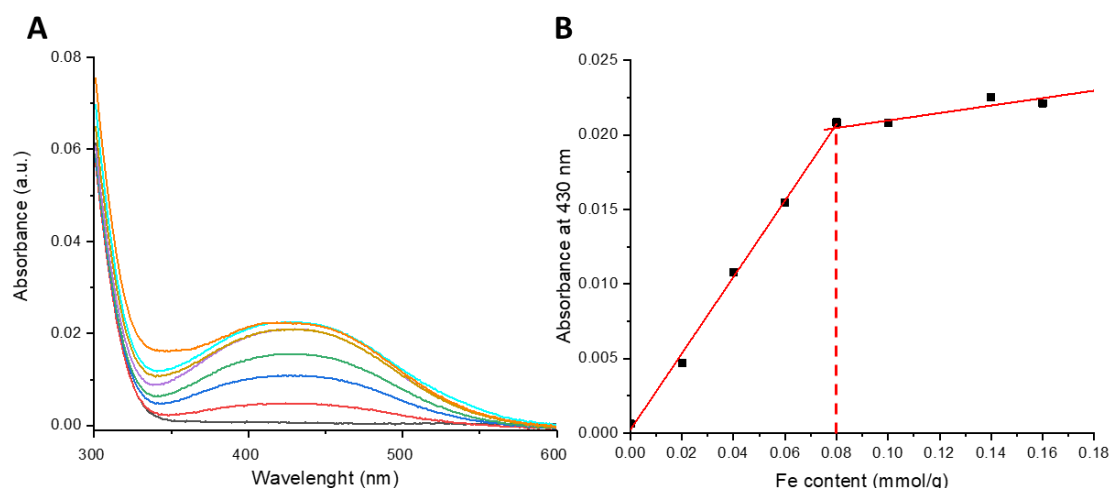


Figure 28. Dosage of a solution of 8-arm-PEG@DFO by Fe (III) in acetate buffer 0.1 M pH 4.5. **A:** UV- Visible spectrum of DA₄₀@DFO₄ at 0.01 (w/w) with increasing iron concentration (0 μM , 2 μM , 4 μM , 6 μM , 8 μM , 10 μM , 14 μM , 16 μM). **B:** Absorbance at 429 nm plotted against mmol of iron per g of 8-arm-PEG@DFO. Red lines correspond to linear regressions. The dotted line represents the crossover concentration corresponding to the saturation of DFO with iron.

In order to determine how many arms are functionalized with DFO

The mass fraction of arms of the 8-arm-PEG@DFO being functionalised correspond to w

$$w = \frac{n_{\text{DFO}} \times M_x}{m_{8\text{-arm-PEG@DFO}}} = \frac{x \times M_x}{x \times M_x + a \times M_a}$$

Where n_{DFO} is the mole number of DFO grafted arms, $m_{8\text{-arm-PEG@DFO}}$ is the mass of PEG. M_x is the molar mass of a PEG arm grafted with DFO, x corresponds to the molar fraction of grafted arms, M_a is the molar mass of an ungrafted PEG arm and a corresponds to the molar fraction of ungrafted arms. Since:

$$a = 1 - x$$

$$w = \frac{x \times M_x}{x \times M_x + (1 - x) \times M_a}$$

$$x = \frac{w \times M_a}{M_x + w(M_a - M_x)}$$

Furthermore

$$C_{DFO} = \frac{n_{DFO}}{m_{8\text{-arm-PEG@DFO}}}$$

Hence

$$x = \frac{C_{DFO} \times M_x \times M_a}{M_x + C_{DFO} \times M_x (M_a - M_x)}$$

$$M_a = 5000 \text{ g.mol}^{-1} \quad M_x = 5752.9 \text{ g.mol}^{-1}$$

This results in $x = 43\%$, or in other words, on average, 3.4 out of the 8 arms are grafted with DFO.

2.2.2. Characterization of DA₄₀@DFO₄

¹H NMR

By comparing the ¹H NMR spectra of DA₄₀ (Figure 22) and DA₄₀@DFO₄ (Figure 29), the characteristic peaks of DFO are clearly seen in the functionalized polymer. Specifically, the phenyl peak at 7.8 ppm corresponds to four protons, and the three broad peaks between 1.6–2.2 ppm correspond to 18 protons from DFO's carbon chain. These peaks can be used to determine the degree of substitution of DFO, referred to as y , by calculating the ratio of one of these specific DFO peaks to the resonances of chitosan in the 3.4–4.5 ppm range, which correspond to six protons from chitosan (excluding anomeric protons) and 12 protons from DFO. This ratio, calculated using either the phenyl peak (equation 2) or the three broad peaks (equation 3), consistently yields a value of $y = 3.8 \pm 0.2\%$. Once y is determined, the same ¹H NMR spectrum can be used to determine the DA using a modified version of Hirai's method. This method accounts for the overlap of signals from the DFO peaks with those of chitosan and the acetyl group. As expected, from equation (4) below, the DA of chitosan remains close to 40% (equation 4).

$$\frac{\text{Area}_{3.7-4.5}}{\text{Area}_{7.8}} = \frac{6+12y}{4y} \quad (2)$$

$$\frac{\text{Area}_{3.7-4.5}}{\text{Area}_{1.6-2.2}} = \frac{6+12y}{18y} \quad (3)$$

$$\frac{\text{Area}_{3.00-4.55 \text{ ppm}}}{\text{Area}_{2.3-2.5}} = \frac{6+12y}{3(y+x)} \quad (4)$$

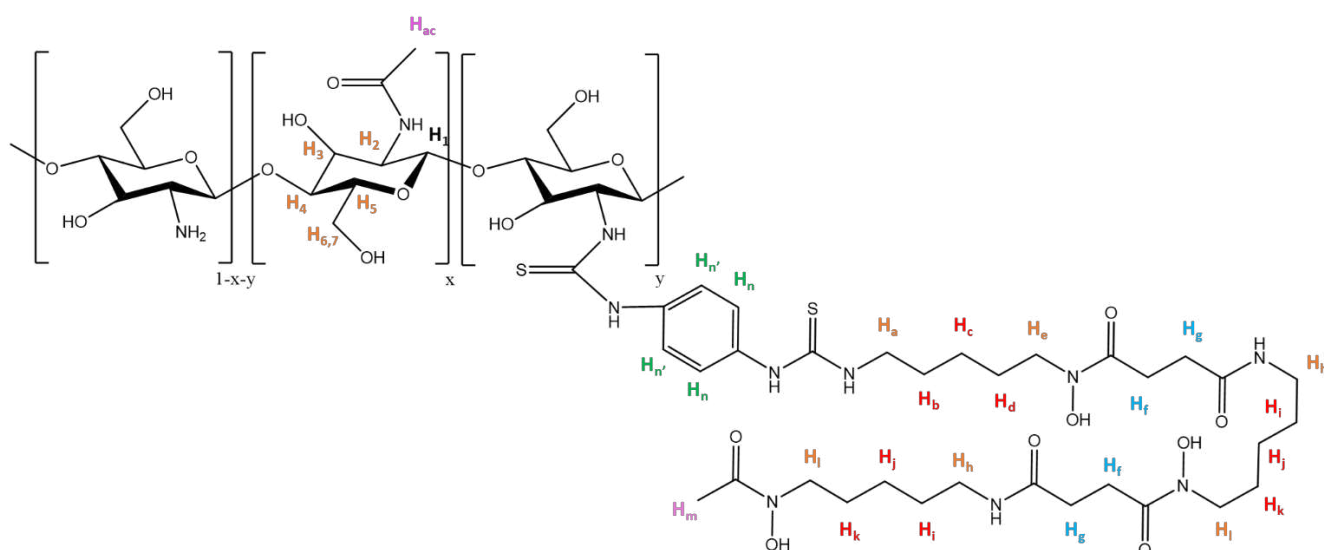
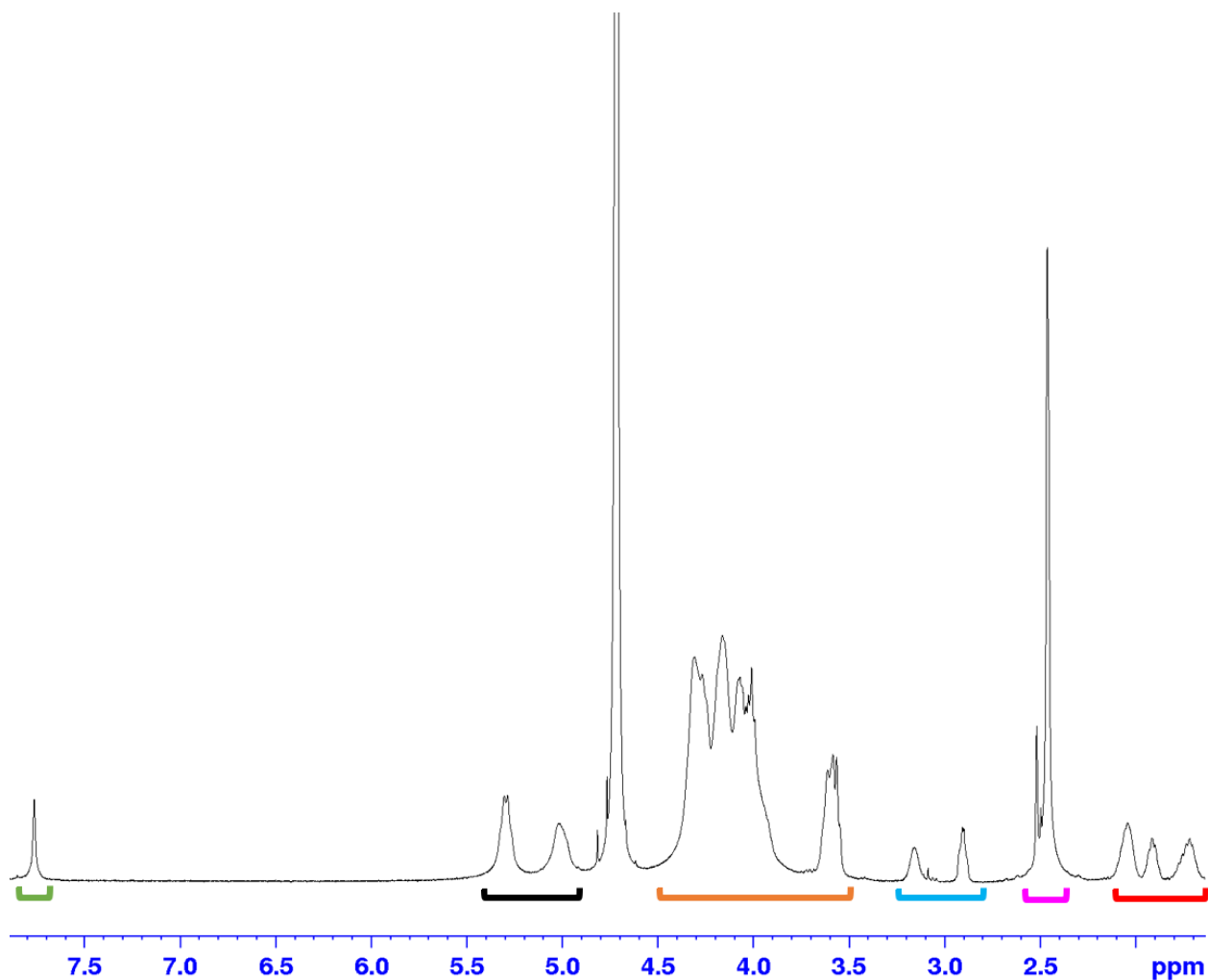


Figure. 29. NMR ^1H spectrum of DA₄₀@DFO₄ in D₂O at 0.5 % w/w at 70°C at the NMR platform in Axel'One Campus and labelling for attribution of ^1H NMR signal of DA₄₀@DFO₄.

Table 6. Attribution of ^1H NMR signals of DA₄₀@DFO₄ (x : acetylation degree, y : DFO grafting) in figure 29.

Chemical shift (ppm)	Integration	Attribution
7.8	4y	H _n et H _{n'} (in green)
4.9-5.5	1	H ₁ (in black)
4.5-3.5	6 + 12y	H ₂ , H ₃ , H ₄ , H ₅ , H _{6,7} , H _a , H _e , H _l , H _h (in orange)
3.2	4y	H _f (in cyan)
2.9	4y	H _g (in cyan)
2.3-2.6	3y + 3x	H _{ac} , H _m (in pink)
1.6-2.2	18y	H _b , H _c , H _d , H _k , H _i , H _j (in red)

Determination of DFO grafting rate in DA₄₀@DFO₄ by UV/Vis titration

Material and methods Similar to 8-arm-PEG@DFO, the iron-chelating capacity of the polymer can be determined using UV/Vis spectroscopy. Multiple solutions of DA₄₀@DFO₄ with a consistent concentration of 0.1% (w/w) are prepared, with increasing iron concentrations up to 150 μM (Figure 30A). By plotting the absorbance of these solutions at 430 nm, which corresponds to the absorption wavelength of the DFO-iron(III) complex, against the iron content (in mmol of iron per gram of polymer), the saturation point of DFO can be identified from the change in slope. For further details on the experimental protocol, please refer to the article entitled “Chitosan based hydrogel for iron (III) chelation in biological conditions” found in the chapter III.

Results and discussion This analysis yields a DFO content (C_{DFO}) of 0.135 mmol per gram of polymer (Figure 30B). The grafting rate can then be determined using the following equations.

The mass fraction of DFO-grafted repeat unit, w , is defined as

$$w = \frac{n_{DFO} \cdot M_y}{m_{Chitosan}} = \frac{y \cdot M_y}{x \cdot M_x + y \cdot M_y + gluc \cdot M_{gluc}}$$

Where n_{DFO} is the mole number of DFO-grafted repeat unit, $m_{Chitosan}$ is the (dry) mass of dissolved DA₄₀@DFO₄ in solution, x is the molar fraction of N-acetyl glucosamine repeat units, $y = n_{DFO}/n_{TOT}$ is the molar fraction of the DFO-grafted repeat units and a is the molar fraction of the glucosamine repeat units. Accordingly, M_x is defined as the molar mass of N-acetyl repeat units, M_y is the molar mass of DFO-grafted repeat units and M_{gluc} the molar mass of glucosamine residue.

Since $gluc = 1 - x - y$ the equation above becomes

$$w = \frac{y \cdot M_y}{x \cdot (M_x - M_{gluc}) + y \cdot (M_y - M_{gluc}) + M_{gluc}}$$

Therefore

$$y = \frac{w \cdot (x \cdot (M_x - M_{gluc}) + M_{gluc})}{M_y - w \cdot (M_y - M_{gluc})}$$

By computation,

$$M_x = M_{gluc-Nac} = 203.19 \text{ g} \cdot \text{mol}^{-1}, M_y = 914.06 \text{ g} \cdot \text{mol}^{-1}, M_{gluc} = 161.16 \text{ g} \cdot \text{mol}^{-1}$$

Using $m_{TOT} = 1 \text{ g}$ of hydrated DA₄₀@DFO₄ dissolved in solution, from the UV titration with Fe (III), we find:

$$\frac{C_{DFO}}{m_{TOT}} = n_{DFO} = 0.14 \text{ mmol}$$

In order to evaluate the mass fraction w , we evaluated a water content of $wc = 8.2\%$ (w/w) in the lyophilized DA₄₀@DFO₄ powder by thermogravimetric analysis, measuring the mass loss between 25 and 200°C under helium flow. Then,

$$w = \frac{n_{DFO} \cdot M_y}{m_{TOT} \cdot (1 - wc)}$$

Hence, the final equation is:

$$y = \frac{C_{DFO} \cdot (x \cdot (M_x - M_{gluc}) + M_{gluc})}{(1 - wc) - C_{DFO} \cdot (M_y - M_{gluc})}$$

From ¹H-NMR, $x = 40\%$

This results in $y = 3\%$

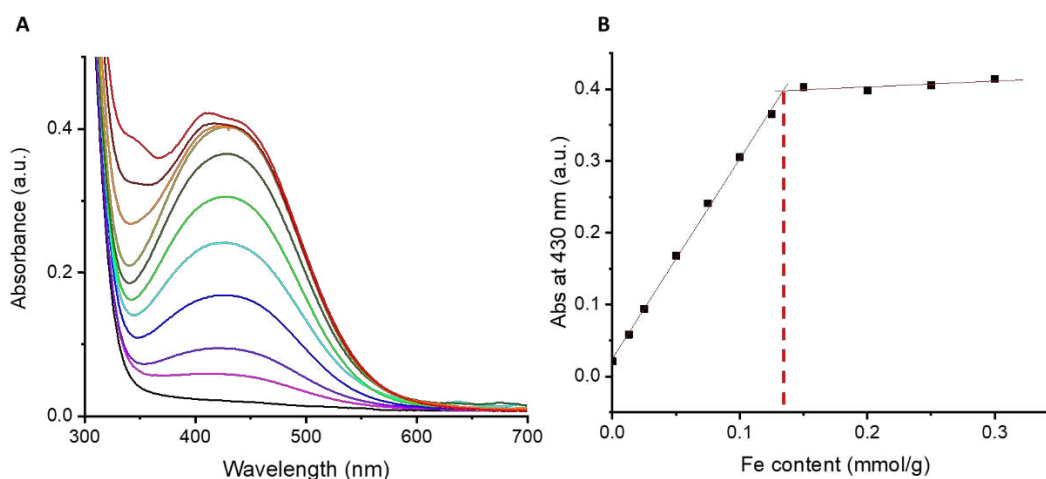


Figure 30. Dosage of a solution of DA₄₀@DFO₄ by Fe (III) in acetate buffer 0.1 M pH 4.5. **A:** UV- Visible spectrum of DA₄₀@DFO₄ at 0.1% w/w with increasing iron concentration (0 μM , 13 μM , 25 μM , 50 μM , 75 μM , 100 μM , 125 μM , 150 μM , 200 μM , 250, μM and 300 μM). **B:** Absorbance at 430 nm plotted against mmol of iron per g of DA₄₀@DFO₄. Red lines correspond to linear regressions. The dotted line represents the crossover concentration corresponding to the saturation of DFO with iron.

HPLC SEC MALLS

To determine the molecular weight of the functionalized chitosan DA₄₀@DFO₄ and compare it to the molecular weight of the initial DA₆ polymer, high-performance liquid chromatography (HPLC) coupled with multi-angle laser light scattering (MALLS) was employed. Analysis were done at the institute Ingénierie des Matériaux Polymères (IMP) by Ms Agnès Crépet.

Materials and methods Chromatographic analysis was performed using a 1260 Infinity Agilent Technologies pump connected to two TSK gel G2500 and G6000 columns (Tosoh Bioscience) in series. A Dawn EOS MALS detector (Wyatt Technology) operating at 664 nm was coupled online to a Wyatt Optilab T-Rex differential refractometer. Sample solutions were prepared at a concentration of 1 mg/mL and eluted in 0.2 M acetic acid/0.15 M ammonium acetate buffer (pH 4.5). Prior to injection, the solutions were filtered through 0.45 µm pore size membranes (Millipore). The eluent flow rate was maintained at 0.5 mL/min.

Results and discussion The molecular weight of chitosan DA₄₀@DFO₄ increases compared to the molecular weight of chitosan DA₆ which confirms the functionalisation of the polymer. Moreover, by calculating the degree of polymerization DP_w for an average chain size of 216 kDa obtained by HPLC-MALLS (Table 7).

$$DP_w = \frac{MW_i}{M_{repeat\ unit}} \approx 1300$$

Where MW_i is the weight-average molecular weight of DA₆ determined by HPLC-MALLS and $M_{repeat\ unit}$ is the average molecular weight of the mean repeat unit of the chitosan polymer considering its DA. The calculation of $M_{repeat\ unit}$ is as follows:

$$M_{repeat\ unit} = x \times M_x + (1 - x) \times M_{gluc} = 163.68\ g.mol^{-1}$$

The theoretical molecular weight of the functionalised DA₄₀@DFO₄ (MW_f) is then calculated as follows:

$$MW_f = [xM_x + yM_y + (1 - x - y)M_{gluc}]N \approx 270\ kDa$$

The experimentally determined molecular weight of 250 kDa for DA₄₀@DFO₄ (Table 7), as measured by HPLC-MALLS, is consistent with the estimated value. Moreover, the hydrodynamic radius (R_w) of 46 nm for DA₆ and 43 nm for DA₄₀@DFO₄ (Table 7), respectively, indicates that the increase in DA from 6% to 40% and the grafting of DFO (4%) have a minimal impact on the polymer conformation.

Table 7. Weight-average molecular weight (MW) and hydrodynamic radius (R_w) of the raw chitosan (DA₆) and the functionalised chitosan (DA₄₀@DFO₄) determined by HPLC-MALLS.

Polymer	MW (kDa)	R_w (nm)
DA ₆	216 ± 2	46 ± 1
DA ₄₀ @DFO ₄	250 ± 2	43 ± 1

2.3. Chelation performance assessment

2.3.1. Iron (III) chelation in solution proof of concept.

The objective of this study is to evaluate the iron extraction performance of the chelating polymers presented in this chapter against the potent iron (III) chelator deferiprone and to compare their extraction performance to that of the first chitosan-based chelating polymer (DA₂₉@DOTAGA₉) developed by the ILM research team [198].

Materials and methods The tested polymers DA₄₀@DFO₄, DA₂₉@DOTAGA₉@DFO₅, DA₂₉@DOTAGA₉, and 8-arm-PEG@DFO were solubilized in ultra-pure water at a concentration of 0.1% (w/w). A stock solution of deferiprone was prepared at 72 μM , and a stock solution of iron (III) at 18 μM in HCl 0.01 was prepared from a standard solution of Fe (III) in 5% HNO₃ (ICP Standard 50090 $\mu\text{g mL}^{-1}$, SCP Science, ref: 140-041-265). Detailed characterisation of DA₂₉@DOTAGA₉@DFO₅ and DA₂₉@DOTAGA₉ can be found of the article draft “Development of chitosan-based hydrogels with tailored hydrophilicity and swelling characteristics” in chapter III.

Using these stock solutions, 20 mL samples were prepared with the following concentrations: 0.001% (w/w) for each polymer (DA₄₀@DFO₄, DA₂₉@DOTAGA₉@DFO₅, DA₂₉@DOTAGA₉), and iron (III) at 0.45 μM . This resulted in a ratio of grafted chelator to the amount of iron (III) of 3:1, 11:1, and 8:1 for DA₄₀@DFO₄, DA₂₉@DOTAGA₉@DFO₅, and DA₂₉@DOTAGA₉, respectively. The concentration of deferiprone was set at either to 1.8 μM or 14.4 μM , resulting in a deferiprone-to-iron(III) ion ratio of 4:1 for the lower concentration and 32:1 for the higher concentration. The deferiprone-iron complex consists of three deferiprone molecules per iron (III) ion. A phosphate buffer (10 mM; Na₂HPO₄ 7.5 mM, KH₂PO₄ 2.5 mM, pH 7.4) was used to maintain the prepared samples at physiological pH. The samples were prepared in the following order to avoid the precipitation of iron (III) at physiological pH: iron (III) was added first, followed by deferiprone, then the phosphate buffer, and finally, the polymer. The samples were stirred at room temperature for 1 hour. 1 mL of each sample was collected for ICP-MS analysis, and the remaining 19 mL was centrifuged in a Vivaspin with a membrane cut-off of 100 kDa until 2 mL remained in the supernatant. During centrifugation, the polymers remained in the supernatant, while small molecules (deferiprone-iron complexes and free deferiprone) passed through the membrane and were found in the undernatant (Figure 31). Moreover, no interaction between the deferiprone-iron complex and the membrane was observed, as confirmed by the minimal difference between the initial iron concentration of the solutions and the iron concentration in the undernatant after centrifugation of the reference samples without polymer (% Recovery in undernatant close to 100%) (Table 8).

For the polymer 8-arm-PEG@DFO and DA₂₉@DOTAGA₉, a similar experiment was conducted with a total sample volume of 100 mL and an iron (III) concentration of 0.18 μM . This resulted in a chelator-to-iron (III) ratio of 5:1 and 19:1 for 8-arm-PEG@DFO and DA₂₉@DOTAGA₉, respectively. Deferiprone concentrations were set at either 1.4 μM or 7.2 μM , yielding deferiprone-to-iron (III) ratios of 3:1 for the lower concentration and 16:1 for the higher concentration. 3 mL of each sample was collected for ICP-MS analysis. The remaining

97 mL was centrifuged using a Vivaspin filter with a membrane cut-off of 30 kDa until 20 mL remained in the supernatant. Reference samples were also prepared, containing only the polymer or the iron (III)-deferiprone complex.

ICP-MS analysis was performed on the supernatant, the undernatant, and the initial solutions of both the samples and the reference samples. The analyses were conducted using a Perkin Elmer NexION 2000 ICP-MS equipped with Syngistix software (Version 2.3), using an ESI SC-FAST sample introduction system in Kinetic Energy Discrimination (KED) mode. KED mode was used in order to avoid the interference between iron most common isotope ^{56}Fe and $^{40}\text{Ar}^{16}\text{O}^+$ formed by the plasma. In KED mode the larger interference ions ($^{40}\text{Ar}^{16}\text{O}^+$) are filtered allowing only the analyte ion (^{56}Fe) to arrive to the detector. The samples were prepared by diluting them in an aqueous solution of 1% (v/v) HNO_3 .

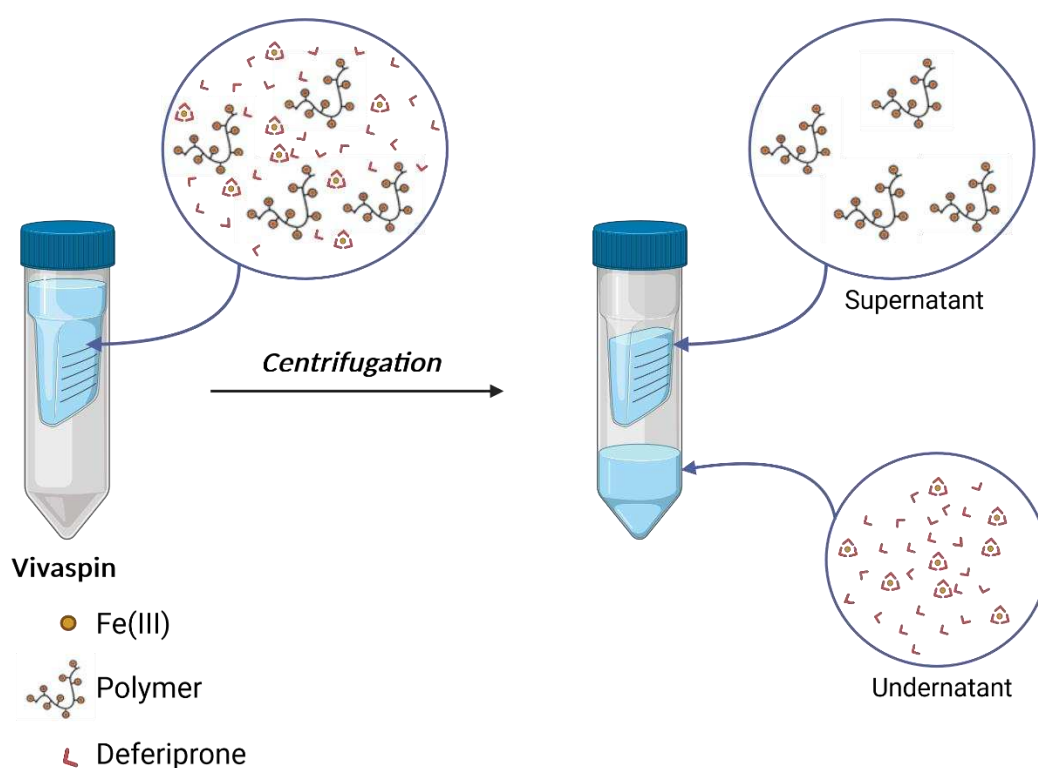


Figure 31. Experimental setup for assessing the iron extraction efficiency of polymers vs deferiprone by Vivaspin®. With a membrane cut-off of 100 kDa for the experiments done with DA₄₀@DFO₄, DA₂₉@DOTAGA₉@DFO₅, DA₂₉@DOTAGA₉ at an iron (III) concentration of 0.45 μM , two deferiprones concentrations 1.8 μM or 14.4 μM , and a membrane cut-off of 30 kDa for the experiments with 8-arm-PEG@DFO and DA₂₉@DOTAGA₉, an iron (III) concentration of 0.18 μM and two deferiprone concentrations 1.4 μM or 7.2 μM .

Table 8. Iron concentrations of the initial solution prior centrifugation and the undernatant after centrifugation measured by ICP-MS in samples without polymer.

Deferiprone (μM)	1.8			14.4			1.4	7.2
Replicates	1	2	3	1	2	3	1	1
[Fe] in initial solution (ppb)	27.95	27.74	25.66	27.41	28.44	27.96	10.9	10.8
[Fe] in undernatant (ppb)	27.81	28.9	30.36	29.8	30.26	29.58	9.9	10.5
% Recovery in undernatant	99.5%	104.2%	118.3%	108.7%	106.4%	105.8%	90.8%	97.2%

Results and discussion. The different polymers tend to adhere to the membrane after centrifugation; therefore, the results presented are based on measuring the amount of iron that passed through the membrane into the undernatant and comparing it to the initial iron concentration. In both iron concentration experiments, and regardless of the deferiprone concentration, the polymers grafted with DFO consistently outperformed the polymers with DOTAGA as the sole chelator (Figure 32), this can be explained by the difference in complexation constants for iron (III) between DFO, Deferiprone and DOTA ($\text{Log}_{\text{DFO}} \beta(\text{FeHL})^+ > \text{Log}_{\text{Deferiprone}} \beta(\text{FeL}_3) > \text{log}_{\text{DOTA}} \beta(\text{FeL})^-$ Table 1). DA₂₉@DOTAGA₉ was unable to extract more than 20% of the iron under any tested condition and even extracted 0% in the experiment with the lowest iron concentration and the highest deferiprone-to-iron ratio (Figure 32B).

In contrast, DA₂₉@DOTAGA₉@DFO₅ extracted nearly all the iron, regardless of the deferiprone concentration ($90.7 \pm 10.1\%$ at the lowest deferiprone concentration and $92.4 \pm 5.0\%$ at the highest). DA₄₀@DFO₄ also demonstrated high iron extraction capacity; however, its efficiency decreased from $87.8 \pm 5.4\%$ in the experiment with 1.8 μM deferiprone (statistically similar to the extraction capacity of DA₂₉@DOTAGA₉@DFO₅) to $70.7 \pm 3.9\%$ in the experiment with a higher deferiprone concentration (14.4 μM) (Figure 32A). This decrease in iron (III) extraction with the increase of deferiprone concentration could be attributed to the lower amount of grafted chelator, specifically DFO, in DA₄₀@DFO₄ (0.14 mmol/g) compared to DA₂₉@DOTAGA₉@DFO₅ (0.33 mmol of DOTAGA per g of polymer and 0.16 mmol of DFO per g of polymer), thus making the increase on deferiprone concentration have a more significant impact on the extraction performance on the low grafted DFO polymer. A similar effect was observed with 8-arm-PEG@DFO (0.08 mmol of DFO/gram), where the polymer's extraction capacity decreased from 77.8% to 38.0% when the deferiprone concentration was increased fivefold (Figure 32B).

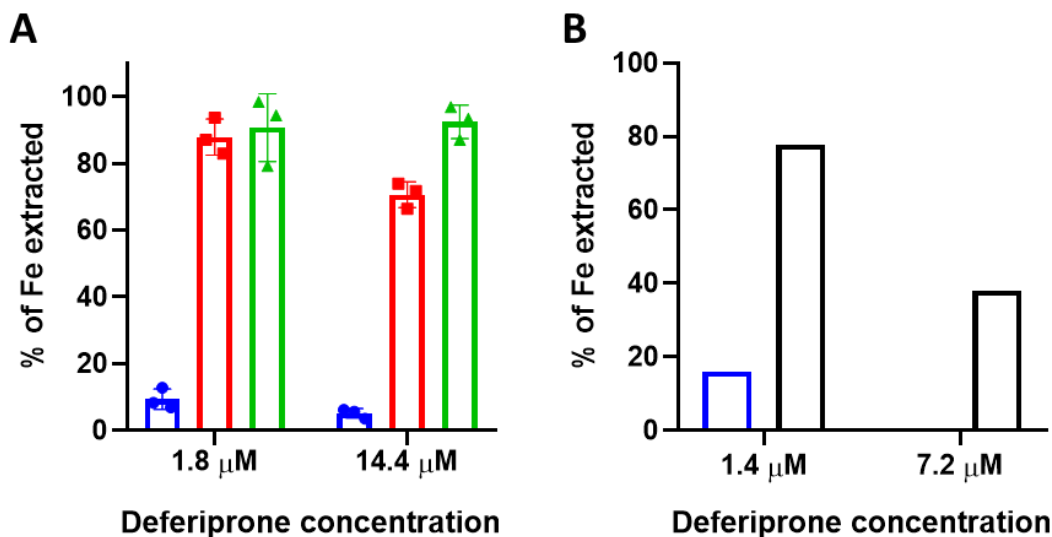


Figure 32. **A:** Percentage of iron extracted by • DA₂₉@DOTAGA₉, ■ DA₄₀@DFO₄, and ▲ DA₂₉@DOTAGA₉@DFO₅ in a solution containing iron (III) (0.45 μM) and deferiprone (1.8 μM or 14.4 μM) in a 10 mM phosphate buffer at pH 7.4. **B:** Percentage of iron extracted by DA₂₉@DOTAGA₉ (blue) and 8-arm-PEG@DFO (black) in a solution containing iron (III) (0.18 μM) and deferiprone (1.8 μM or 14.4 μM) in a 10 mM phosphate buffer at pH 7.4. All results were calculated based on ICP-MS measurements of the supernatant.

2.3.2. Aluminium (III) chelation in solution proof of concept

In addition to essential metals like iron, there are non-essential metals such as aluminium that have been associated with neurodegenerative diseases [115,116]. Consequently, using an aluminium chelator as a potential treatment for these diseases could be promising. DFO is not only a potent iron (III) chelator but also an effective aluminium (III) chelator, with a complexation constant of $\text{Log } \beta(\text{AlHL})^+ = 24.14$ [7]. It has already been successfully used to treat aluminium overload in patients, yielding positive results [229,230]. The efficacy of aluminium (III) extraction by the chelating polymers was assessed by comparing them to EDTA, which has a complexation constant of $\text{Log } \beta(\text{AlL})^- = 16.7$ [2]. Additionally, EDTA played a secondary role in this experiment by preventing the precipitation of aluminium (III) at physiological pH.

Materials and methods. For these experiments, stock solutions of the polymers (DA₂₉@DOTAGA₉, DA₄₀@DFO₄, DA₂₉@DOTAGA₉@DFO₅, and 8-arm-PEG@DFO) were prepared at a concentration of 1% (w/w) in ultra-pure water. A stock solution of EDTA at 52 μM was also prepared in ultrapure water. The aluminium stock solution was prepared at a concentration of 371 μM by diluting a standard Al (III) solution (1000 μg mL⁻¹ in 5% HNO₃, ICP Standard, SCP Science, ref: 140-051-130) with 0.01 M HCl.

Using the stock solutions samples were prepared with the following concentrations: 0.1% (w/w) for each polymer (DA₂₉@DOTAGA₉, DA₄₀@DFO₄ and DA₂₉@DOTAGA₉@DFO₅), and aluminium (III) at 7.4 μM. This resulted in grafted chelator-to-aluminium (III) ratios of

47:1, 67:1, and 18:1 for DA₂₉@DOTAGA₉, DA₄₀@DFO₄ and DA₂₉@DOTAGA₉@DFO₅, respectively. EDTA was used at a concentration of 8.1 μM, resulting in a 1.1:1 ratio of EDTA to aluminium (III). All samples were prepared in Tris-HCl buffer (10 mM, pH 7.4) to maintain physiological pH. As in the experiments with iron, the solutions were added in the following order: aluminium (III), then EDTA, followed by the Tris-HCl buffer, and finally, the polymer. Control samples containing only the polymer, or aluminium (III) with EDTA, were also prepared. All samples were stirred at room temperature for 1 hour before analysis. Samples were analysed at the ILM with a Perkin Elmer NexION 2000 ICP-MS coupled to Perkin - Elmer Flexar LC. Separation was accomplished by a size exclusion column (Polysep 4000) at a flow rate of 0.4 mL/min. A 50 mM ammonium bicarbonate solution (pH 7.4) was used as the eluent. ICP-MS was operated in KED mode for the analysis to avoid interference between ²⁷Al, ¹²C¹⁵N and ¹²C¹⁴NH. The resulting chromatograms are shown in figure 33.

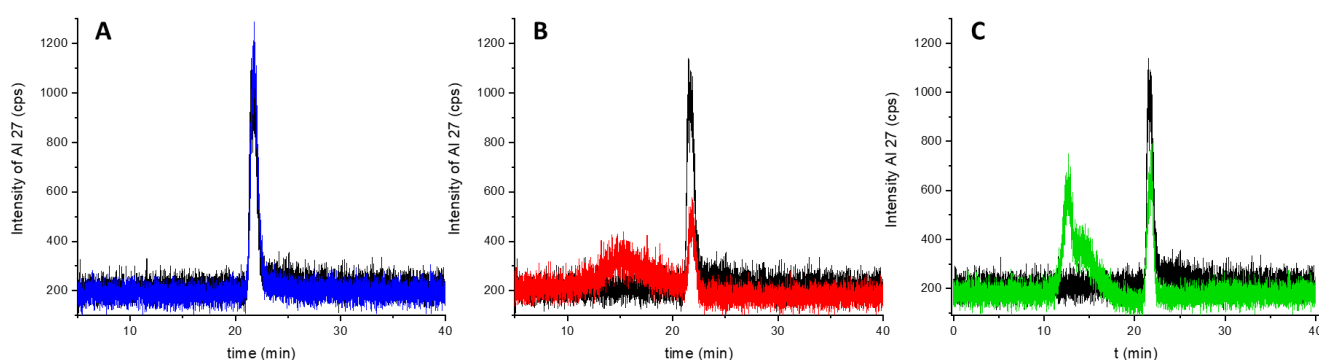


Figure 33. Chromatograms showing the intensity of aluminium (²⁷Al) in counts per second (cps) for the experimental samples (polymer + 7.4 μM aluminium(III) and 8.1 μM EDTA in 10 mM Tris-HCl) compared to the control chromatogram (7.4 μM aluminium(III) and 8.1 μM EDTA in 10 mM Tris-HCl) in black **A**. DA₂₉@DOTAGA₉ in blue **B**. DA₄₀@DFO₄ in red **C**. - DA₂₉@DOTAGA₉@DFO₅ in green.

Results and discussion. The first broad peak, observed between 11 and 19 minutes, corresponds to the polymer, while the second peak at 22 minutes corresponds to the Al(III)-EDTA complex. The high noise-to-signal ratio makes it challenging to precisely determine the exact elution time of the polymer peak. Since the Al(III)-EDTA complex peak is better defined, the analysis focused on measuring the area of this peak. To quantify the amount of aluminium chelated by the polymer, the areas of the Al(III)-EDTA complex peaks were compared between the control sample (Al(III)-EDTA without polymer) and the experimental sample. As shown in figure 33, no polymer peak is visible, and the area of the Al(III)-EDTA complex peak did not decrease in comparison to the control. In contrast, the chromatograms of the samples with DFO-grafted polymers showed a distinct polymer peak and a reduction in the Al(III)-EDTA complex peak, corresponding to 43% and 63% of the total aluminium (III) being extracted by DA₄₀@DFO₄ and DA₂₉@DOTAGA₉@DFO₅, respectively. Comparing the chromatograms clearly indicates that only the DFO-grafted polymers are capable of chelating aluminium(III), which is consistent with the complexation constants of the Al(III)-DFO and Al(III)-EDTA complexes. The apparently superior extraction of aluminium (III) by

DA₂₉@DOTAGA₉@DFO₅ could be attributed to the higher amount of DFO grafted onto this polymer, as observed in its better performance in the iron extraction experiments. However, due to the high noise-to-signal ratio, obtaining precise quantitative results was difficult.

2.4. Conclusion

To utilize chelating agents in a microdialysis setup, it is essential to prevent the chelator from passing through the membrane. For the chelating agent to remain in the dialysate, it must have a larger molecular size than the membrane's cut-off. This necessitates increasing the molecular weight of the chelator. By functionalizing two aminated polymers, 8-arm PEG and chitosan, the molecular weight of the iron (III) chelator DFO was successfully increased.

The DFO derivative p-NCS-Bz-DFO, being hydrophobic and soluble only in DMSO, was employed to functionalize the polymers. 8-arm-PEG, being completely soluble in both water and DMSO, presented no obstacles in the synthesis of the functionalized polymer 8-arm-PEG@DFO in 100% DMSO. The resulting polymer, with, on average, 3.4 out of its 8 arms grafted (0.08 mmol DFO/g), remained soluble in water at physiological conditions, making it suitable for its use in microdialysis applications.

Chitosan, being exclusively soluble in acidic aqueous solutions, presented challenges for grafting the p-NCS-Bz-DFO moiety. To overcome this, the raw chitosan (DA₆) was acetylated to a DA of 40% using acetic anhydride. This modification increased the hydrophilicity of the deprotonated chitosan, making it soluble at near-neutral pH, which is more favourable for the coupling reaction. A mixture of water, 1,2-propanediol, and DMSO (52%/30%/18%, respectively) at pH 6.0±0.5 was used to achieve a common solubility for chitosan and p-NCS-Bz-DFO. Under these conditions, the reaction between p-NCS-Bz-DFO and DA₄₀ resulted in the functionalized chitosan DA₄₀@DFO₄ with a DFO grafting of 0.135 mmol/g. However, unlike 8-arm-PEG@DFO, DA₄₀@DFO₄ is not soluble at physiological conditions making it not suitable for microdialysis applications.

Moreover, grafting the DOTAGA moiety to chitosan also increased its hydrophilicity, leading to the synthesis of the double-grafted chelating polymer DA₂₉@DOTAGA₉@DFO₅. This polymer exhibited higher solubility than DA₄₀@DFO₄ under physiological conditions and had a higher amount of grafted DFO (0.16 mmol/g compared to 0.14 mmol/g for DA₄₀@DFO₄).

The chelation performance of the DFO-functionalized polymers was evaluated by quantifying their ability to extract iron (III) from solution at physiological pH, in competition with the strong iron (III) chelator deferiprone. The results demonstrated that all polymers could extract the majority of iron (III) from the solution, even when an iron (III) chelator (deferiprone) was present in excess relative to the iron (III) concentration. Notably, the polymer DA₂₉@DOTAGA₉@DFO₅ exhibited the best performance.

Furthermore, these experiments revealed that DFO-functionalized polymers outperformed DA₂₉@DOTAGA₉, highlighting that the grafting of DFO significantly enhances iron (III)

extraction capabilities. Additionally, it was shown that among the three tested chitosans (DA₂₉@DOTAGA₉, DA₂₉@DOTAGA₉@DFO₅, and DA₄₀@DFO₄), the DFO grafting enabled the extraction of aluminium from [EDTA-Al(III)]⁻ complexes something that the DOTAGA-functionalized polymer (DA₂₉@DOTAGA₉) alone could not achieve.

Due to the solubility issues exhibited by DA₄₀@DFO₄ in physiological media (neutral pH and isotonic conditions), as well as the gelation properties inherent to chitosan, the next chapter will focus on the development of biomaterials incorporating chelating chitosan derivatives.

Chapter III: Development of chitosan-based hydrogels

A gel is a soft, solid-like material with a significant liquid component relative to the solid components [231]. Gels retain their shape under their own weight. Hydrogels a subcategory of gels, are three-dimensional crosslinked networks of polymers with high water content, typically exceeding 70%. This high water content, resembling natural living tissues, contributes to their excellent biocompatibility [202,203,232,233]. Due to this property, the use of biocompatible polymers in the development of hydrogels has led to their widespread research for medical applications like tissue engineering and drug delivery [204,225,232,234,235]. Hydrogels can be formed through chemical and physical crosslinking. Chemical crosslinking involves creating covalent bonds between functional groups within the polymer using crosslinking agents to form a 3D network [204,232]. In contrast, physical crosslinking relies on physical interactions such as van der Waals forces, electrostatic interactions, or hydrogen bonding to construct the 3D network, resulting in hydrogels with different mechanical properties compared to chemically crosslinked hydrogels [203,204,232,236].

As previously discussed, the amine functional group present in chitosan enables its functionalization with crosslinking agents to form chemical hydrogels. Additionally, chitosan can form physical hydrogels through the deprotonation of its amine groups in concentrated polymer solutions [232,236,237]. While crosslinking agents can be used to create chitosan hydrogels, this approach may have some drawbacks for specific applications. Crosslinking agents can be cytotoxic, react with the functional groups of grafted chelators, and increase the cost of hydrogel synthesis due to the additional reactants involved [202,204,232] and the precautions needed to remove unreacted crosslinkers. For these reasons, the following chapter focuses on the development of physical hydrogels with chelating properties.

Chelating chitosan-based hydrogels have primarily been developed for water purification applications due to chitosan's intrinsic metal-complexing properties [220,221,238]. However, recent advances in functionalizing chitosan with chelators like EDTA or DOTAGA have led to the exploration of these hydrogels for other applications, such as medical applications [225,239].

3.1. Development of iron(III) chelating chitosan based hydrogels, "proof of concept" publication.

The development of chitosan-based chelating polymers led to the publication of the article "Chitosan-based hydrogel for iron (III) chelation in biological conditions" in the journal *Carbohydrate Polymers*. Supplementary information can be found in the annexes.



Chitosan based hydrogel for iron (III) chelation in biological conditions

Juan Felipe Salazar Ariza^{a,b}, François Lux^{a,c}, Fernande Da Cruz-Boisson^b,
Jacqueline Resende de Azevedo^d, Ruben Vera^e, Olivier Tillement^a, Alexandra Montembault^b,
Laurent David^{b,*}

^a Université Claude Bernard Lyon 1, CNRS, Institut Lumière-Matière (ILM), UMR 5306, 2 rue Victor Grignard, F-69622 Villeurbanne Cedex, France

^b Université Claude Bernard Lyon 1, INSA de Lyon, Université Jean Monnet, CNRS, Ingénierie des Matériaux Polymères (IMP), UMR 5223, 15 bd Latarjet, F-69622 Villeurbanne, France

^c Institut Universitaire de France (IUF), 75231 Paris, France

^d Université Claude Bernard Lyon 1, CNRS, Laboratoire d'Automatique, de Génie des Procédés et de Génie Pharmaceutique (LAGEPP), UMR5007, 3, rue Victor Grignard, Bâtiment CPE, F-69100 Villeurbanne Cedex, France

^e Université Claude Bernard Lyon 1, Centre de Diffractionnée Henri Longchambon, 5 rue de La Doua, F-69100 Villeurbanne, France

ARTICLE INFO

Keywords:

Chitosan
Deferoxamine
Gelation
Selective chelation
Iron overload

ABSTRACT

In this study, a chitosan derivative with strong iron (III) chelating capabilities was developed by grafting the Deferoxamine (DFO) chelator to achieve a substitution degree of 3.8 ± 0.2 %. Through blending with ungrafted chitosan of low degree of acetylation (DA), a formulation able to form a physical hydrogels was formed in aqueous media, without the requirement of a cross-linking agent. The functionalization of chitosan with DFO led to xerogels exhibiting superior iron (III) chelation capacity and higher swelling when exposed to aqueous solutions, in comparison with to an unmodified chitosan xerogel. Notably, this material extracts iron (III) even against the strong iron chelator deferiprone. Furthermore, the material demonstrates selectivity for iron (III) chelation even in the presence of competing cations like copper (II) and zinc (II).

1. Introduction

Iron is involved in multiple biological processes necessary to life, from oxygen transportation to enzymatic reactions (Emerit et al., 2001). Despite its physiological importance, iron can be related to different disorders when its homeostasis is compromised, leading to excess of iron loosely bound to proteins and small molecules called non-transferrin-bound iron (NTBI) or catalytic iron (Angoro et al., 2022). Since NTBI is not immobilized, it can participate in redox reactions, producing radicals when reacting with hydrogen peroxide, as observed in the Fenton's reaction ($Fe^{2+} + H_2O_2 \rightarrow Fe^{3+} + OH^- + OH^*$). Furthermore, it serves as a catalyst in the Haber-Weiss reaction ($O_2^{\cdot-} + H_2O_2 \xrightarrow{Fe^{2+}/Fe^{3+}} OH^- + OH^* + O_2$) (Angoro et al., 2022; Emerit et al., 2001; Valko et al., 2005). The resulting radicals are part of the reactive oxygen species (ROS), which are toxic to cells by causing oxidative damage to DNA, lipids and proteins (Emerit et al., 2001). Furthermore, high intracellular iron concentrations have been found to be the main driving force of a distinct form of cell death mechanism known as

ferroptosis (Dixon et al., 2012).

Although excess iron may induce a variety of diseases, the organism has no effective means of eliminating it (Anderson & McLaren, 2012). Iron homeostasis depends only on the regulating proteins (transferrin, ferritin and hepcidin), which are overwhelmed in moments of iron overload crisis (Pietrangolo, 2010). Iron overload and its toxicity manifest in both primary hemochromatosis, a hereditary disorder characterized by excessive iron absorption in the gastrointestinal tract, and secondary hemochromatosis, where iron overload results from recurrent blood transfusions (Valko et al., 2005). Iron overload and its oxidative damage can also be found in other pathologies: for example, the increase of NTBI levels in patients after cardiac surgery and critical illness associated with acute kidney injury (AKI) due to the toxic effects of iron on the kidney (Grange, Lux, et al., 2023; Scindia et al., 2019). Additionally, multiple studies have found that during intra-cranial haemorrhage, iron accumulation shown by ferritin and heme-oxygenase upregulation is associated with more damage to the brain tissue (Chen et al., 2011; Wu et al., 2003; Zhang et al., 2019). Iron is also suspected to play an important role in neurodegenerative pathologies, where it seems to

* Corresponding author.

E-mail address: laurent.david@univ-lyon1.fr (L. David).

<https://doi.org/10.1016/j.carbpol.2024.122670>

Received 12 June 2024; Received in revised form 12 July 2024; Accepted 27 August 2024

Available online 28 August 2024

0144-8617/© 2024 The Author(s). Published by Elsevier Ltd. This is an open access article under the CC BY license (<http://creativecommons.org/licenses/by/4.0/>).

promote protein aggregation and oxidative damage (Apostolakis & Kypraiou, 2017; Moreau et al., 2018). In fact, Thomas et al. (2020) showed a correlation between iron deposition and cognitive decline in Parkinson's disease patients.

Based on the pathologies discussed above, it is clear that regulating iron balance and removing excess NTBI are necessary for the treatment of several conditions. Traditionally, iron overload has been treated by phlebotomy and chelation therapy. However, because the chelator has a limited half-life in the body, patients are repeatedly exposed to high levels of chelators. These elevated concentrations of chelators can in turn lead to undesirable side effects, including removal of other metallic cations or damages to organs like kidneys, ultimately resulting in potential poor compliance with the therapy (Cappellini, 2005; Porter & Huehns, 1989).

The objective of this work is to describe the synthesis of a biocompatible polysaccharide derivative that exhibits strong iron chelation properties. Additionally, it aims to design biomaterials based on this polymer, offering local and long-lasting treatment for some of the multiple pathologies due to iron overload. To achieve these goals, chitosan has been selected as the polymer backbone owing to its distinctive biological features, such as biocompatibility and biodegradability (Kean & Thanou, 2010; Rami et al., 2014; VandeVord et al., 2002). Chitosans constitute a family of copolysaccharides of *N*-glucosamine and *N*-acetylglucosamine, soluble in acidic aqueous media and industrially derived from chitin by alkaline deacetylation (Mogoşanu & Grumezeşcu, 2014). As aminated polysaccharides, chitosans have a macromolecular structure that is comparable to the glycosaminoglycans found in the extra cellular matrices. Meanwhile, the degree of acetylation (DA) has an impact on the physico-chemical and biological properties of chitosans, wherein a higher DA results in accelerated degradation kinetics; this phenomenon can be attributed to the action of lysozyme, which actively participates in chitosan degradation *in vivo* (Chatelet et al., 2001; Rami et al., 2014). In addition, chitosan has been shown to help wound healing and exhibit antifungal and antibacterial properties in particular at low DAs (Kantak & Bharate, 2022; Matica et al., 2019). Chitosan possesses -NH₂ functional groups, allowing for the grafting of the polymer with a wide range of functional moieties, depending on the desired application (Wang et al., 2020).

Chitosans are also known for their ability to chelate metallic cations such as Cu²⁺, Zn²⁺, Fe²⁺, Fe³⁺... (Matica et al., 2019). However, in the case of (unmodified) chitosan-metal complexes, the coordination sphere of the metallic cation is not completely saturated. This allows the metallic cation to undergo redox reactions, resulting in materials with catalytic properties (Chitichigrovsky et al., 2009; Farinelli et al., 2021). Also, enabling unspecific transmetallation due to its similar values in complexation constants for multiple metallic cations, which is a drawback in the context of specific iron chelation for therapeutic goals (Hernández et al., 2007). Several examples of chelators, including DOTAGA, DTPA, EDTA, and DFO, have been grafted onto chitosan to enhance its chelation properties for metal extractions (Ficiară et al., 2024; Howard et al., 2023; Natuzzi et al., 2021; Repo et al., 2010).

A specific property derived from the presence of free amine groups in chitosan is its ability to become a polycation with pH sensitivity (Sorlier et al., 2001). Neutralization of chitosan in solution above a critical concentration, at a pH above 6.5 enables the formation of hydrogen bonds and hydrophobic interactions between chain segments, resulting in the formation of a physical hydrogel without the need for a cross-linking agent (Montebault et al., 2005b). Also, hydrogels based on chitosan derivatives have already been developed for the non-specific extraction of heavy metals in wastewater. For instance, hydrogels prepared with EDTA-functionalized chitosan have shown the capacity to extract heavy metals from water (Repo et al., 2010). In this work, drafting DFO, a specific chelator of iron(III), onto chitosan was performed to obtain a chitosan derivative (i) with significant enhancement its chelation capacity but also (ii) a selectivity for iron(III) compared to bare chitosan, to be incorporated in a formulation maintaining gelation

properties.

In this paper, we show that grafting the FDA (food and drug administration) approved chelator Desferoxamine (DFO) onto chitosan chains, results in a macrochelator that maintains a strong and selective affinity for iron (III), while retaining the gelation properties of chitosan. The synthesis and characterization of DA₄₀@DFO will be described and the formation of gels in aqueous solution is performed, still without the need of crosslinking agents. The chelating properties of this hydrogel material will be evaluated against a strong iron chelator (deferiprone) and the selectivity of iron (III) chelation will be tested in competition against copper (II) and zinc (II) and compared with non-modified chitosan.

2. Material and methods

2.1. Synthesis of DA₄₀@DFO

2.1.1. Chemicals

Medical grade chitosan with low degree of acetylation DA (6 % ± 0.5 %, determined by ¹H NMR spectroscopy using the Hirai method (Hirai et al., 1991)) from Alaska snow crab was purchased from Matexcel (Bohemia, NY, USA, reference number NAT-0030, <http://www.matexcel.com/p/30/medical-grade-chitosan/>). This chitosan was fully characterized. The weight-average and number-average molar masses (respectively $M_w = 216$ kg/mol and $M_n = 130$ kg/mol) were determined by size exclusion chromatography coupled with refractive index and multi-angle laser light scattering measurements (Montebault et al., 2005a). p-NCS-Bz-DFO (N1-hydroxy-N1-(5-(4-(hydroxy(5-(3-(4-isothiocyanatophenyl) thioureido) pentyl) amino)-4-oxobutanamido) pentyl)-N4-(5-(N-hydroxyacetamido) pentyl) succinamide) was obtained from Chematech (Dijon, France). 1,2-propanediol, DMSO and acetic anhydride were purchased from Sigma-Aldrich (Saint-Quentin-Fallavier, France). Glacial acetic acid (AnalR Normapur) grade was furnished by VWR (France).

2.1.2. Reacetylation of low DA chitosan

The *N*-acetylation of chitosan was obtained in a water/1,2-propanediol mixture with acetic anhydride as the reagent (Fig. 1) (Vachoud et al., 1997). Briefly, chitosan solution was prepared at a concentration of 1.5 % (w/w): the polymer was dissolved in deionized water containing 1 % of acetic acid, the mixture was stirred 12 h until complete solubilization of chitosan. Afterwards, 1,2-propanediol was added to obtain a final polymer concentration of 1.25 % (w/w), and the solution was stirred at room temperature for 1 h. Then, acetic anhydride diluted in 1,2-propanediol at 3 % (v/v) (0.32 M) was added dropwise to this hydroalcoholic chitosan solution under strong stirring, the final polymer concentration was then 1 % (w/w). The amount of added acetic anhydride corresponded to the stoichiometric amount necessary to achieve the desired DA of chitosan. The mixture was stirred for 4 h and 5 mL were collected and purified by tangential filtration against water for DA determination. The DA of this reacetylated chitosan (DA₄₀) was determined by ¹H NMR using the Hirai method, close to 40 % (Hirai et al., 1991) without change of the degree of polymerization.

2.1.3. Functionalization of reacetylated chitosan with DFO derivative

The grafting of DFO onto DA₄₀ was achieved in a mixture of water, 1,2-propanediol, and DMSO, using p-NCS-Bz-DFO as the reagent (Fig. 1). The previous DA₄₀ solution directly after reacetylation was diluted with 1,2-propanediol, DMSO, and water to achieve the following concentrations: 34 % (v/v) 1,2-propanediol, 59 % (v/v) water, 7 % (v/v) DMSO, and a polymer concentration of 0.6 % (w/w). The pH of the solution was adjusted to 6.0 ± 0.5 with a NaOH 1 M solution. Subsequently, p-NCS-Bz-DFO, dissolved in DMSO at a concentration of 1 % (w/w), was added to the reaction medium using a peristaltic pump at a flow rate of 100 µL/min under vigorous stirring, maintaining a controlled temperature of 30 °C. This resulted in a final polymer

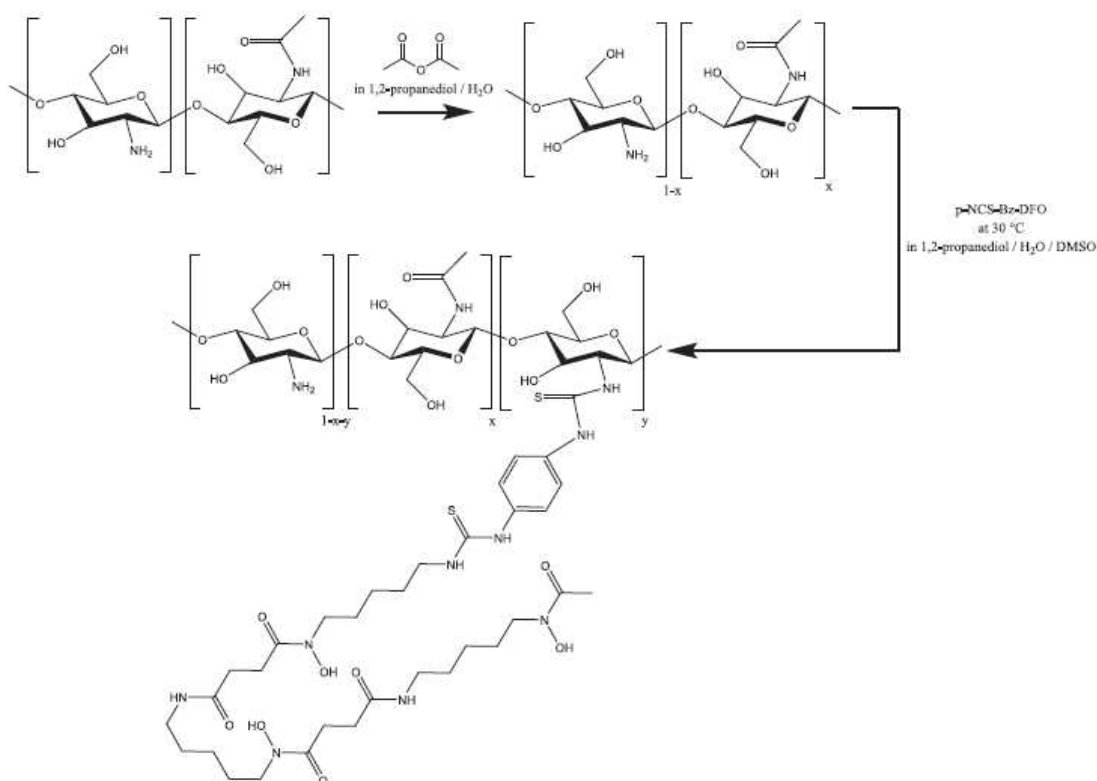


Fig. 1. Synthesis pathway of $DA_x@DFO$ from initial chitosan, x is the degree of acetylation (DA) of the reacylated chitosan, y is the p-NCS-Bz-DFO grafting ratio (substitution degree).

concentration of 0.5 % (w/w). The amount of p-NCS-Bz-DFO added corresponded to the stoichiometric quantity required to achieve a 5 % grafting rate (higher amounts resulted in an insoluble product). The mixture was maintained at 30 °C during the reaction and stirred overnight. After the isothiocyanate groups had reacted with amines to form thioureas, the final product was purified through tangential filtration using a 100 kDa cutoff membrane, first with 0.1 M acetic acid and then with ultra-pure water. For NMR analysis, 5 mL of the final product was purified with 10 mM HCl instead of acetic acid to avoid interferences. Once purified, it was freeze-dried.

2.2. Polymer characterization

2.2.1. Characterization of DFO grafting by UV-Vis titration

The amount of grafted DFO was determined by titration with Fe (III), knowing that the DFO-Fe complex exhibits a distinct orange-red colour (Domínguez-Vera, 2004). The maximum absorption wavelength of the DFO-Fe complex is 430 nm (Imran Ul-haq et al., 2013). The dosage of DFO-Fe complex was thus performed by UV-Visible spectroscopy at this wavelength. The polymer is first dispersed in water at a concentration of 0.5 % w/w. An acetate buffer solution, i.e. ammonium acetate (0.1 M)/acetic acid (0.1 M) is added to the previous suspension to reach a polymer concentration of 0.1 % w/w at a pH of 4.5. Fe (III) was added to this solution at a concentration ranging from 0 to 0.3 mM using a standard iron solution in 5 % HNO_3 provided by SCP-Science (ICP Standard 1000 $\mu g \cdot mL^{-1}$). Absorbance was measured with a Cary 50 Scan UV-visible spectrophotometer using quartz cuvettes with optical path length of 10 mm.

The absorption at 430 nm was then plotted versus the iron content in solution. After linear fitting of the low and high iron concentration regimes of the plot, the iron chelation capacity of $DA_{40}@DFO$ polymer is determined as the concentration at the observed change of slope,

expressed in mmol of iron per gram of polymer.

2.2.2. Characterization of DFO grafting by 1H NMR

1H NMR spectra were performed at the NMR Polymer Center of Institut de Chimie de Lyon (Axel'One Campus) on a 400 MHz Bruker spectrometer and spectra were processed with TopSpin software. Baseline was corrected manually as well as the phase adjustment and integration. Samples were dissolved in D_2O at 0.5 % w/w. Analyses were performed at 70 °C.

2.3. Gel formation

The gels were prepared by following the method by Montembault et al. (2005b) with slight modifications. An illustration of the process can be seen in (Fig. 2). First, $DA_{40}@DFO$ could not be used directly to prepare gels. Indeed, this polymer is soluble only at concentrations ≤ 5 % w/w. And, in this concentration range, neutralization of solutions yielded precipitates. Thus, in order to obtain gellable solutions, we prepared mixed solutions of DA_6 with $DA_{40}@DFO$ and the reference solutions with DA_{40} . Briefly, DA_6 and $DA_{40}@DFO$ powders were dispersed in ultra-pure water following the proportions shown in Table 1 to obtain a total polymer concentration close to 15 % w/w except for the two last formulations which had a total polymer concentration close to 10 % w/w. Acetic acid was added to achieve the stoichiometric protonation of the amine groups. The blend was mechanically stirred until having a homogeneous mixture. The mixtures were then poured into a mould and submerged in a 3 M NaOH aqueous solution to regenerate free amine groups inducing gelation. The hydrogels were then washed with ultra-pure water to eliminate NaOH and acetate salts and then with a phosphate buffer solution 0.1 M (Na_2HPO_4 0.075 M, KH_2PO_4 0.25 M, pH 7.4), to impose a neutral pH to the hydrogel. Phosphate moieties tend to interact with amine groups in chitosan hydrogels (Leduc et al., 2014).

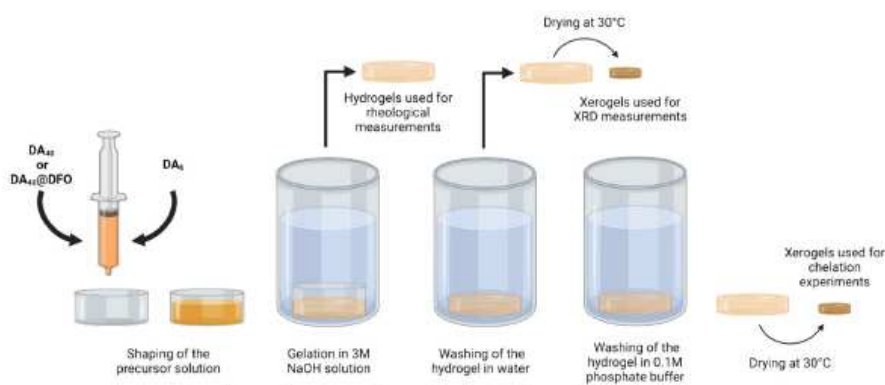


Fig. 2. Steps for the preparation of DA₆/DA₄₀@DFO and DA₆/DA₄₀ physical hydrogels and dried xerogels. (Created with BioRender.com).

Table 1

Description of gel formulations specifying the DFO content per gram of xerogel calculated from the UV dosage of DA₄₀@DFO, its proportion in the precursor solution, and the theoretical extraction capacity per gram of xerogel for each formulation.

Gel formulation	Ratio of DA ₄₀ @DFO/DA ₆ polymer	DFO per g of xerogel (mmol/g)	Theoretical capacity of iron extraction per g of xerogel (mg/g) and (mmol/g) ^a	
14 % DA ₆ 1 % DA ₄₀ @DFO	1/14	0.009	0.503	0.009
13 % DA ₆ 2 % DA ₄₀ @DFO	2/13	0.018	1.005	0.018
10 % DA ₆ 5 % DA ₄₀ @DFO	1/2	0.045	2.513	0.045
14 % DA ₆ 1 % DA ₄₀	0	0	/	/
13 % DA ₆ 2 % DA ₄₀	0	0	/	/
10 % DA ₆ 5 % DA ₄₀	0	0	/	/
15 % DA ₆	0	0	/	/
5 % DA ₆ 5 % DA ₄₀ @DFO	1/1	0.068	3.797	0.068
5 % DA ₆ 5%DA ₄₀	0	0	/	/

^a The theoretical extraction capacity is calculated by considering only the DFO present in each formulation.

Therefore, in the gels and pellets examined in this paper, chitosan may interact with the phosphate anions found in the washing solution. The hydrogels were dried in a humidity chamber (Memmert HCP50) at a constant temperature of 30 °C. The drying cycle proceeded as follows: 1 h at 30 °C and 65 % humidity, followed by a gradual decrease in humidity from 65 % to 35 % over 10 h. Subsequently, the xerogels were maintained at 35 % humidity for 1 h before storage.

Following such procedure, seven DFO-containing gels were prepared with a total polymer concentration of 15 % w/w (Table 1). The first three gels were made using DA₄₀@DFO at concentrations of 1 %, 2 %, and 5 % w/w, together with unmodified chitosan (DA₆) at 14 %, 13 %, and 10 %, respectively. As described above, beyond a concentration of 5 % DA₄₀@DFO, the polymer is not fully soluble. Therefore, the maximum DA₄₀@DFO concentration used to prepare the gel's precursor solutions was 5 % w/w. Additionally, four control gels were prepared without any chelator-grafted polymer, replacing DA₄₀@DFO by DA₄₀ at the same concentrations (i.e. 1 %, 2 % and 5 %), while the last reference was made solely with chitosan DA₆. In this way, gels with different mass ratios of DA₄₀@DFO/DA₆ (0, 1/14, 2/13 and 5/10) were prepared to assess the influence of DA₄₀@DFO on the metal extraction and the gel behaviours.

Moreover, in order to obtain gels and xerogel pellets with a higher fraction of DA₄₀@DFO, two precursor solutions with a lower total polymer concentration of 10 % w/w were prepared. Such second series of chelating hydrogels contained 5 % w/w DA₆ and 5 % w/w DA₄₀@DFO, while the controls were formulated with 5 % w/w DA₆ and 5 % w/w DA₄₀.

2.4. Material characterization

2.4.1. Viscoelastic properties of hydrogels

Dynamic rheological measurements were carried out using an ARES rheometer (TA Instruments) and operating with a plate-plate geometry (diameter of 25 mm) at room temperature (25 °C). The strain amplitude was chosen to ensure that the measurements were carried out within the linear viscoelastic region. Angular frequency sweep measurements were carried out in the range from 100 rad.s⁻¹ down to 0.1 rad.s⁻¹ (with an applied strain amplitude of 0.3 %). Analyses were repeated three times for each type of hydrogel. To produce a hydrogel with flat surfaces, the precursor solution was sandwiched between two plastic sheets and then compressed to achieve the desired thickness of 3 mm before immersing it in the gelation bath. The measurements were done immediately after gelation in the solution of NaOH 3 M at pH > 10.

2.4.2. X ray diffraction analyses

The xerogels utilized for XRD analysis were prepared in the same manner as previously described (part 2.3 gel formation), with the distinction that they were solely washed with ultra-pure water and then dried (Fig. 2). The xerogel crystallinity of formulations derived from the 15 % and 10 % w/w polymer solution were analysed using a Rigaku XtaLAB Synergy-S diffractometer with CuK α (50 kV, 1 mA) at the Henri Longchambon Diffraction Center (Villeurbanne, France). A custom-designed sample holder was used to hold the samples in the beam. The 2 θ scans were achieved between 5 and 70°.

2.4.3. Swelling

Dry pellets of xerogel with a known initial mass W_i were immersed into ultra-pure water at room temperature (25 °C), the pH of the solution after swelling for all samples was 7 ± 0.5 . Samples were taken out of the solution at different time points to measure their swelling index using Eq. (1):

$$(1) \text{ Swelling index} = \frac{W_h - W_d}{W_d} \times 100 \quad (1)$$

Where, W_h is the mass of the rehydrated hydrogel pellet and $W_d = W_i(1 - w_c)$ is the dry mass of the pellet. The residual or bound water fraction w_c in the different xerogels was considered as a constant, independent of the formulation and close to 9.4 ± 0.4 % as measured by

thermogravimetric analysis.

2.5. Metal chelation experiments

2.5.1. Chemicals

Standard iron (III), copper (II) and zinc (II) solutions in 5 % HNO₃ were provided by SCP-Science (ICP Standard 1000 µg.mL⁻¹, reference: 140-051-260, 140-051-290, 140-051-300 for iron (III), copper (II) and zinc (II) respectively) for ICP-MS. Deferiprone (purity 98 %, CAS 30652-11-0), sodium phosphate dibasic (ACS reagent ≥99.0 %, CAS 7558-79-4), potassium phosphate monobasic (Reagent Plus ≥99.0 %, CAS 7778-77-0) HEPES (≥99.5 % CAS 7365-45-9) Na₂SO₄ (ACS reagent, ≥99.0 %, anhydrous, powder, CAS 7757-82-6) were purchased from Sigma-Aldrich.

2.5.2. Single metal chelation

Chelation experiments were carried out with a ferric solution (1000 µg.mL⁻¹ of Fe³⁺) in 5 % HNO₃ as the iron source. A stock solution of deferiprone at 1 g.L⁻¹ was prepared by solubilizing the deferiprone powder in ultra-pure water. Phosphate buffer (10 mM, pH 7.4) was prepared from sodium phosphate dibasic (7.5 mM) and potassium phosphate monobasic (2.5 mM) dissolved in ultra-pure water.

Samples of 20 mL of the metallic cation solution were prepared in 10 mM phosphate buffer with the following concentrations: 3.58 µM of iron (III), 14.3 µM of deferiprone. One pellet of xerogel of known mass was added to each metallic solution (approximately 27 mg for the formulations at 15 % w/w in total polymer and around 18 mg per pellet for the formulation of 10 % w/w in total polymer - for more precise information regarding the dimensions of the pellets used, please refer to Table S2). Samples were stirred at room temperature for 90 h.

2.5.3. Competitive multimetal chelation

For the competitive multimetal ion chelation, the samples were prepared in 10 mM HEPES buffer pH 7.4 and added Na₂SO₄ with the following concentrations: 3.58 µM of iron (III), 3.58 µM of copper (II), 3.58 µM of zinc (II), 12.9 µM of EDTA (1.2 M equivalent/ metal) and 35 mM of Na₂SO₄. The amount of metals extracted by the hydrogel was determined by inductively coupled plasma mass spectrometry (ICPMS) after the hydrogels were mineralized by microwave with 3 mL of HNO₃ 69 %. The analysis was performed using a Perkin Elmer NexION2000 equipped with Syngistix software (Perkin Elmer, Version 2.3) with ESI SC-FAST sample introduction in Kinetic Energy Discrimination (KED) mode. The samples were prepared by dilution in an aqueous solution of HNO₃ 1 % (v/v). The supernatants and the initial metallic solution were also analysed, in the same way as the mineralized (nitric acid-treated) hydrogel pellets.

3. Results and discussion

3.1. Synthesis and characterization of chitosan-DA₄₀@DFO.

3.1.1. Synthesis

The coupling reaction between the NCS function and the amine groups of chitosan is more efficient at alkaline pH (Hermanson, 2008), however low DA chitosan is only soluble in acidic conditions. Thus, we increased the pH range where chitosan stays soluble by increasing its DA through a first reacylation step (Aiba, 1991; Vårum et al., 1994). A chitosan reacylated in homogeneous conditions (hydroalcoholic solution) with a DA of 30 % is soluble at neutral pH (optically clear). However, upon grafting the p-NCS-Bz-DFO, the resulting product precipitated, most likely due to the high hydrophobicity originating from the DFO moiety. To avoid this precipitation, the hydrophilicity was further increased by raising the DA to 40 %. The p-NCS-Bz-DFO compound exhibits pronounced hydrophobicity, thus having minimal solubility in aqueous media. Chitosan, on the other hand, is insoluble in organic solvents such as DMSO. Therefore, a common solubility of

chitosan and p-NCS-Bz-DFO was found in a mix between DMSO and water (volume fraction of DMSO: 18 % v/v); such a reaction medium was used for the functionalization of reacylated chitosan with DFO. Moreover, for DFO functionalization, propanediol was added in the reaction medium to lower the water content and prevent the hydrolysis of the NCS function in water-DMSO mixtures. Such hydrolysis would induce precipitation of NH₂-Bz-DFO (Joseph et al., 1992).

Before the addition of p-NCS-Bz-DFO, the pH of the chitosan DA₄₀ solution in DMSO/water was adjusted to 6.0 ± 0.5 resulting in a significant fraction of non-protonated amines, to allow the reaction between p-NCS-Bz-DFO with the free amines of chitosan (Grange, Aigle, et al., 2023).

3.1.2. Characterization of DA₄₀@DFO

By using the Hirai method on the ¹H NMR spectrum of the intermediate product DA₄₀ (see Supplementary Information, SI), we determined the DA to be equal to 40.0 ± 0.5 %. The ¹H NMR spectrum of the final DA₄₀@DFO product (Fig. 3), allows us to determine the DFO grafting rate y . The resonances used for the DFO were either the singlet at 7.8 ppm from the phenyl equivalent to 4 protons (Eq. (2)) or the peaks between 1.6 and 2.2 ppm corresponding to the DFO's carbon chain equivalent to 18 protons (Eq. (3)). These DFO peak areas were compared to the resonances of chitosan from 3.4 ppm to 4.5 ppm, associated with 6 protons from glucosamine or *N*-acetyl glucosamine and 12 protons from DFO. Both NMR-derived methods yielded the same grafting rate close to 3.8 ± 0.2 %. Moreover the same ¹H NMR spectrum allows us to verify the DA = x by using a method derived from that of Hirai (Hirai et al., 1991) by taking into account the protons from the DFO grafted into chitosan (Eq. (4)). The detailed determination of DFO grafting degree y and acetylation degree x from NMR data can be found in the SI section. As expected, the DA of the final polymer was not impacted by DFO functionalization.

$$\frac{Area_{3.7-4.5}}{Area_{7.8}} = \frac{6 + 12y}{4y} \quad (2)$$

$$\frac{Area_{3.7-4.5}}{Area_{1.6-2.2}} = \frac{6 + 12y}{18y} \quad (3)$$

$$\frac{Area_{3.00-4.55 \text{ ppm}}}{Area_{2.3-2.5}} = \frac{6 + 12y}{3(y + x)} \quad (4)$$

We observe an increase of the absorption at 430 nm with the increase of iron in the samples up to concentration of iron of 150 µM (Fig. 4.A). The first slope is associated with the formation of the complex DFO-Fe (III) and yields a molar extinction coefficient of 2783 M⁻¹.cm⁻¹ which is in agreement with the one found in the literature for the DFO-Fe(III) complex at same wavelength: $\epsilon = 2300 \text{ mol}^{-1}.\text{cm}^{-1}$ (Fig. 4.B) (Imran Ul-haq et al., 2013). This titration showed a DFO content (C_{DFO}) of 0.135 mmol of DFO in 1 g of DA₄₀@DFO polymer which correspond to a grafting rate y given as:

$$y = \frac{C_{DFO} \cdot (x \cdot (M_x - M_{gluc}) + M_{gluc})}{(1 - w_c) - C_{DFO} \cdot (M_y - M_{gluc})} \quad (5)$$

yielding: $y = 3 \%$.

In Eq. (5), w_c is the residual water content (= 8.2 % w/w) of the lyophilized DA₄₀@DFO, $M_x = 203.2 \text{ g/mol}$ is the molar mass of *N*-acetyl glucosamine repeat units, $M_y = 914.06 \text{ g/mol}$ is the molar mass of DFO-grafted repeat units, and $M_{gluc} = 161 \text{ g/mol}$ is the molar mass of glucosamine repeat unit. Finally, $x = DA$ is the degree of acetylation of reacylated chitosan ($x = 40 \pm 0.5 \%$). Detailed information regarding the calculation to determine y from the Fe (III) titration can be found in the SI. The results obtained from the estimation performed via Fe(III) titration with UV-visible spectroscopy are in good agreement with the substitution degree determined by ¹H NMR.

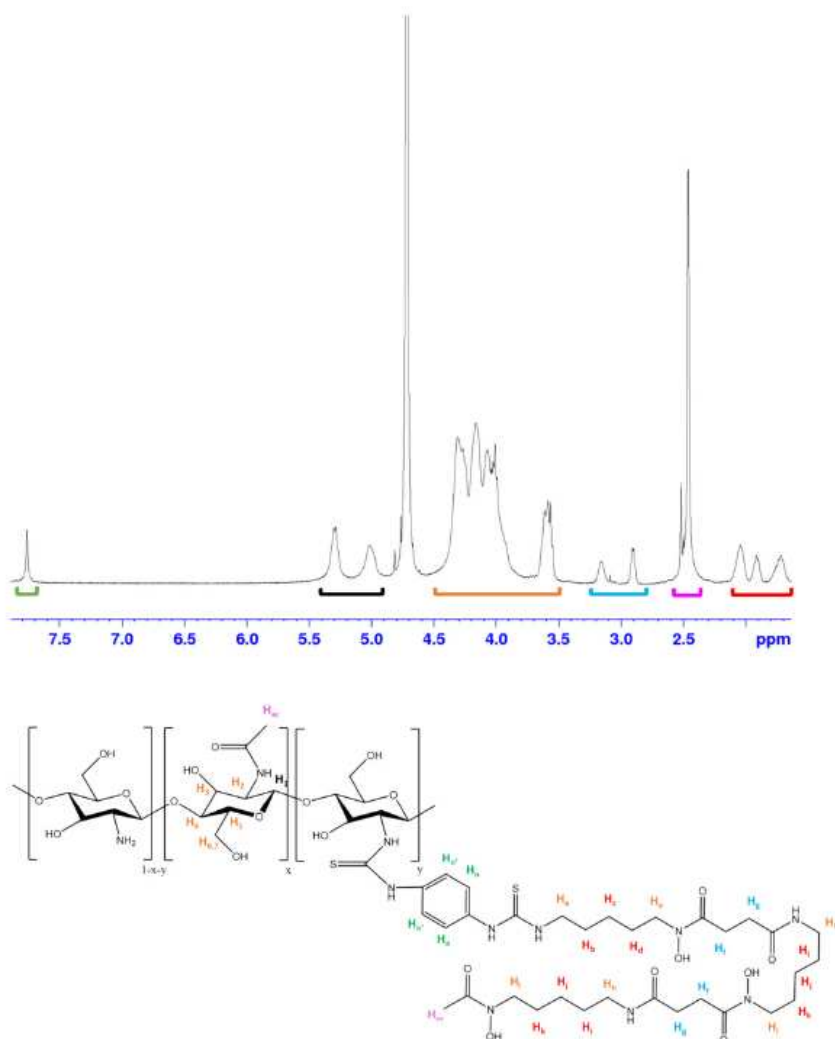


Fig. 3. NMR ¹H spectrum of DA₄₀@DFO in D₂O at 0.5 % w/w at 70 °C and labelling for attribution of ¹H NMR signal of DA₄₀@DFO.

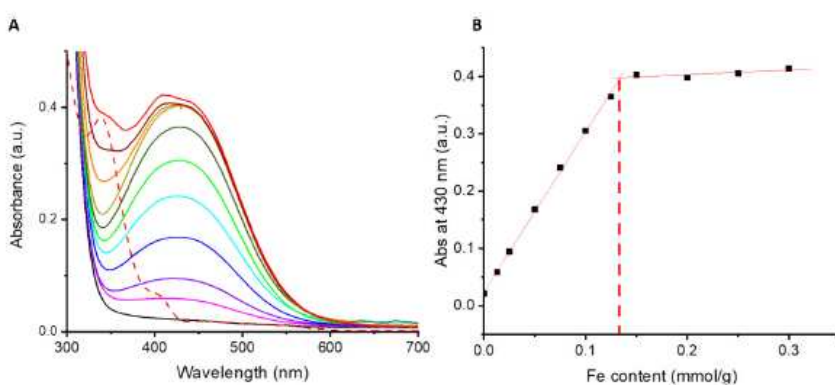


Fig. 4. Dosage of a solution of DA₄₀@DFO by Fe (III) in acetate buffer 0.1 M pH 4.5. A: UV- Visible spectrum of DA₄₀@DFO at 0.1 % w/w with increasing iron concentration (0 μM (black), 13 μM (pink), 25 μM (purple), 50 μM (blue), 75 μM (cyan), 100 μM (green), 125 μM (olive), 150 μM (dark yellow), 200 μM (orange), 250 μM (burgundy red) and 300 μM (red)). Red dotted curve represents the UV/Vis spectrum of a solution of 300 μM Fe (III) in acetate buffer 0.1 M B: Absorbance at 430 nm plotted against mmol of iron per g of Chitosan-DA₄₀@DFO. Red lines correspond to linear regressions. The dotted line represents the crossover concentration corresponding to the saturation of DFO with iron.

3.2. Gel characterization

3.2.1. Rheology

The results in Table 2 and (Fig. S3) display the rheological characterization of hydrogel samples. The G' values were constant over the entire assessable frequency range for all systems (to see an example of the plots of G' and G'' vs frequency for one formulation (Fig. S3.A)). And as shown in (Fig. S3.B), all formulations, after being immersed in the NaOH gelation bath, exhibited G' values in the kPa range, with G''/G' ratios ranging from 0.06 to 0.20. These rheological profiles and G''/G' confirm the formation of soft gels (Fuchs et al., 1998). Changing the proportion of Chitosan-DA₄₀@DFO or Chitosan-DA₄₀ in the ranges studied here did not induce significant differences in the values of G' or $\tan(\delta) = G''/G'$.

The polymer concentration has a more substantial impact on the values of G' of the hydrogels than the DA or the Chitosan-DA₄₀@DFO fraction of chitosan. At higher polymer concentrations, there is a greater likelihood of polymer crystallites and entrapped entanglements, which results in a higher number of junctions per unit volume and consequently in higher values of the elastic modulus (Montebault et al., 2005b).

In this work, the gels were primarily composed of DA₆. Therefore, the rheological properties of the materials are mostly influenced by the major component chitosan DA₆, resulting in similar values of G' for all the gels at the same polymer concentration. Furthermore, for the DA₄₀@DFO chitosan derivative, the grafting rate of DFO ($\gamma = 4\%$) is low, so that the solubility up to 5% w/w of DA₄₀@DFO, gelation ability of the DA₆/DA₄₀DFO mixes and rheological behaviours were preserved after DFO grafting.

3.2.2. Structural characterization by XDR analysis

The influence of Chitosan-DA₄₀ and the grafting of DFO on the crystalline structure of the xerogels were investigated via wide angle X-ray diffraction. Chitosan can be crystallized into hydrated and/or anhydrous polymorphs (Okuyama et al., 1997; Osorio-Madrado et al., 2010). Okuyama et al. (1997) proposed a solved structure for the hydrated polymorph with an orthorhombic unit cell with dimensions $a = 8.95 \text{ \AA}$, $b = 16.97 \text{ \AA}$, and c (chain axis) = 10.34 \AA . For all formulations, a semi crystalline morphology is observable, with reflections at $2\theta = 10.4^\circ$, 20° and 21.9° corresponding to the crystalline reflection of $(020)_h$, $(200)_h$ and $(220)_h$ of the hydrated allomorph (Fig. 5).

The introduction of chitosan DA₄₀ or chitosan DA₄₀@DFO induced a gradual broadening of the $(020)_h$ reflexion peak close to 10.4° , mostly visible in (Fig. 5C and D) where the fractions of reacylated and functionalized chitosan are significant. In all diffractograms, it can be observed that the crystalline contribution of the xerogels containing Chitosan DA₄₀@DFO are lower than their reference formulated with ungrafted chitosan DA₄₀. From these X-ray scattering patterns, a crystallinity index was determined by baseline subtraction and after integration of the diffractograms from $2\theta = 5$ to 34 (Desorme et al., 2013):

$$CrI\% = \frac{Area_{crystal}}{Area_{Total}} \times 100 \quad (7)$$

Where $Area_{Total}$ is the total area of diffraction diagram calculated from $2\theta = 5^\circ$ to $2\theta = 34^\circ$, $Area_{crystal} = Area_{Total} - Area_{amorphous}$ and $Area_{amorphous}$ is the integrated area of the amorphous scattering pattern, estimated as a cubic spline (Osorio-Madrado et al., 2010) (see (Fig. S4) for more details on the estimation on the amorphous and crystalline contributions). The calculated crystallinity indexes are shown in Table 3.

The xerogels prepared with low DA₄₀@DFO or low DA₄₀ chitosan concentrations displayed a crystallinity index close to the pure DA₆ xerogel. As expected from direct observation of the diffractograms, the calculated crystallinity indexes for the reference samples DA₆/DA₄₀ were systematically higher than their corresponding counterparts DA₆/DA₄₀@DFO. The xerogel with higher proportions of DA₄₀@DFO exhibited not only a lower index of crystallinity in comparison with the control gels but also with the gels obtained from solutions at 1% and 2% DA₄₀@DFO. Such behaviour could be ascribed to the steric hindrance of the large DFO group, hindering chitosan crystallization. Even though an increase in the mean DA typically promotes crystallization of chitosan (Facchinatto et al., 2020), in this study, the mixing of DA₄₀ chitosan with low DA₆ chitosan resulted in a slight decrease of crystallinity. Moreover, DFO grafting also contributed to decrease the crystallinity of gels. Such crystallinity could also exist in the precursor hydrogels: indeed, synchrotron X-ray scattering was previously used to show that similar chitosan hydrogels chitosan exhibited a semicrystalline structure (Céline et al., 2013). At the nanoscale, nano-crystallites are believed to act as physical crosslinks of high functionality and contribute to the gel formation and properties. In this study, it was not possible to correlate clearly the crystallinity index of xerogels and the viscoelastic properties of precursor hydrogels (see Tables 2 and 3), possibly because the crystallinity ratio in hydrogels remains lower than in solid forms and a significant crystalline fraction form during the drying step. In conclusion however, in all the xerogels prepared in this study, we evidenced a significant crystallinity fraction, persisting even for high DA₄₀@DFO contents. Such crystallization, triggered by the neutralization process and further enhanced by drying, guaranteed the formation of hydrogels and xerogels that were stable in aqueous and physiological conditions.

3.2.3. Swelling behaviour of xerogels

All dried xerogel pellets are capable of swelling at room temperature (25°C) when placed in water ($\text{pH } 7 \pm 0.5$), reaching their plateau mass after at least 24 h (Fig. 6.A).

Chitosan formulation primarily governs swelling (Fig. 6.A). Notably, the formulation made solely with low DA (DA₆) exhibits the lowest swelling index, and swelling increases with the amount of DA₄₀@DFO or DA₄₀. In the case of the formulations made out of the polymer solutions at 10% w/w, with DA₆/DA₄₀@DFO mass ratio equal to 1, a substantial increase in the swelling index is observed. Moreover, the 5% DA₆ 5% DA₄₀@DFO formulation shows a 49.2 unit increase in % swelling index compared to its reacylated control (5% DA₆ 5% DA₄₀), showing that the presence of DFO increases significantly the swelling of the material. A strong correlation between the swelling index and crystallinity index is observed (Fig. 6.B). Again, these results can be related to the physical crosslinking effect of nanocrystallites, the presence of DA₄₀@DFO, which restricting chitosan crystallization due to the steric hindrance of the large DFO group and/or the introduction of more hydrophilic interactions. Comparing the different DA₆ and DA₆/DA₄₀ reference systems, such experiments also confirmed that low DA neutralized chitosan (DA₆) is the most hydrophobic in the chitosans polymer family (Becerra et al., 2017). However, in the blends prepared in this work, the hydrophobic nature imparted by the DFO-NCS moiety does not seem to significantly impact the swelling or hydrophilicity of the gel. Instead, the more pronounced effect is the impact of the acetylated partner, with

Table 2
 G' plateau value (measured at low frequency) for each hydrogel formulation obtained after neutralization of mixed solutions in a NaOH 3 M gelation bath at $\text{pH} > 10$ and at room temperature (25°C).

Sample	G' (kPa)
14 % DA ₆ 1 % DA ₄₀ @DFO	21.1 ± 3.5
13 % DA ₆ 2 % DA ₄₀ @DFO	14.0 ± 2.0
10 % DA ₆ 5 % DA ₄₀ @DFO	16.2 ± 1.6
14 % DA ₆ 1 % DA ₄₀	17.0 ± 3.3
13 % DA ₆ 2 % DA ₄₀	17.4 ± 1.0
10 % DA ₆ 5 % DA ₄₀	16.2 ± 1.6
15 % DA ₆	16.2 ± 3.1
5 % DA ₆ 5 % DA ₄₀ @DFO	11.4 ± 1.9
5 % DA ₆ 5 % DA ₄₀	11.3 ± 1.7

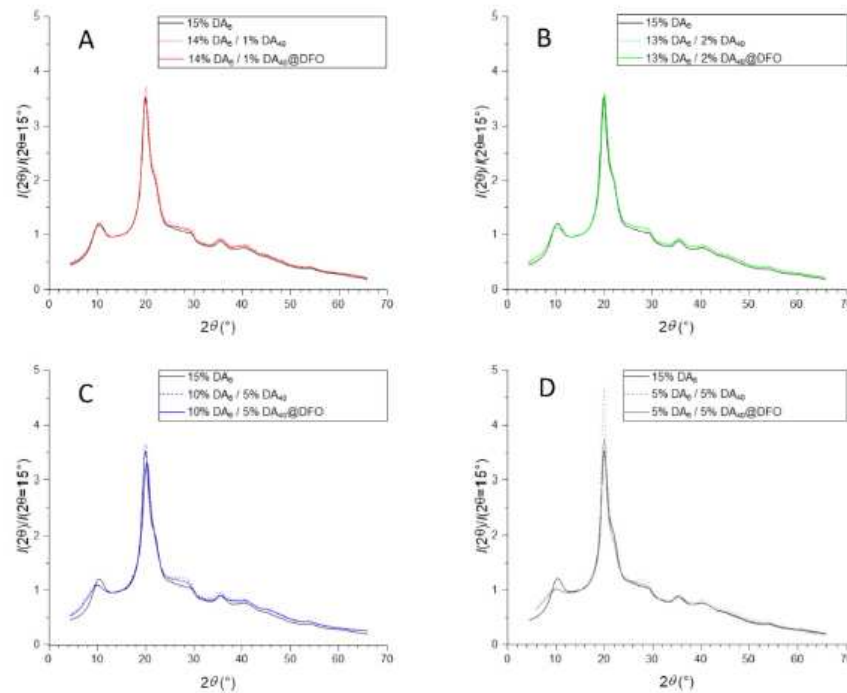


Fig. 5. Diffraction patterns obtained for the xerogels processed from different mother solutions, in comparison with pure low DA chitosan system (– 15 % DA₆). All Diffractograms are normalized with the intensity value measured at $2\theta = 15^\circ$, representative of the amorphous phase. Dashed lines show the reference samples prepared with reacylated chitosans, whereas solid lines display the xerogels functionalized with DFO. (A): Xerogels obtained from processing of chitosan solutions (14 % DA₆/1 % DA₄₀) and (14 % DA₆/1 % DA₄₀@DFO). (B): Xerogels obtained from (13 % DA₆/2 % DA₄₀) and (13 % DA₆/2 % DA₄₀@DFO). (C): Xerogels obtained from (10 % DA₆/5 % DA₄₀) and (10 % DA₆/5 % DA₄₀@DFO). (D): Xerogels obtained from (14 % DA₆/1 % DA₄₀) and (14 % DA₆/1 % DA₄₀@DFO). The crystallinity ratio of chitosan xerogels decreases at high DA₄₀@DFO or DA₄₀ fractions.

Table 3

Crystallinity indexes (CrI%) for each xerogel formulation according to the subtraction of a baseline to the diffractograms. The crystallinity Index is not an exact estimation of the crystallinity ratio, but should vary similarly and help to compare different samples.

Xerogel formulation	CrI (%) ± 0.5 %
14 % DA ₆ /1 % DA ₄₀ @DFO	20.5
13 % DA ₆ /2 % DA ₄₀ @DFO	20.3
10 % DA ₆ /5 % DA ₄₀ @DFO	18.6
14 % DA ₆ /1 % DA ₄₀	21.1
13 % DA ₆ /2 % DA ₄₀	20.6
10 % DA ₆ /5 % DA ₄₀	19.1
15 % DA ₆	21.0
5 % DA ₆ /5 % DA ₄₀ @DFO	17.4
5 % DA ₆ /5 % DA ₄₀	18.5

strong polarity of acetyl moieties, and at high concentration of DA₄₀@DFO, a decrease in crystallinity allowing the gels to exhibit a higher swelling index.

3.3. Chelation experiments

3.3.1. Single metal ion chelation

As discussed previously, the long term objective of DA₆/DA₄₀@DFO materials is to be used *in vivo/in vitro* to chelate NTBI reducing its oxidative danger (Emerit et al., 2001). Thus, the objective of the current study is to establish the proof of concept for a material capable of extracting iron in physiological conditions. In this context, we determined the quantity of extractable iron after contacting the xerogels with aqueous solutions containing iron (III). NTBI in pathological patients is found in the range of 1–10 μmol/L (Angoro et al., 2022). Therefore, the

extraction efficiency of iron (III) using DA₄₀@DFO gels was assessed in samples containing an intermediate iron (III) concentration of 3.6 μmol/L (200 ppb), precomplexed by deferiprone ($\text{Log}(K_{\text{FeDf}}) = 36.7$) (Nurchi et al., 2008), which is an iron chelator used for the treatment of iron overload (Hoffbrand et al., 2003). However, as shown in Table S3, deferiprone has a lower complexation constant towards iron (III) compared to DFO ($\text{Log}(K_{\text{FeDFO}}) = 41.8$) (Toporivska & Gumienna-Kontecka, 2019). Thus, deferiprone plays two roles in this experiment. The first one is to prevent the precipitation of iron (III) at physiological pH. Secondly, given deferiprone established role as an approved chelator for managing iron overload, if our gels are able to remove iron from deferiprone, they should also effectively address iron overload. This is by targeting loosely bound iron in the body.

For this experiment, the metallic solution was prepared with a proportion of 4 deferiprone molecules per iron ion to guarantee that most of iron atoms are complexed by deferiprone. By sampling the supernatant through time and measuring its iron content by ICP-MS, the equilibrium of extraction was attained at least after 70 h (see Fig. S5). After 90 h, the gel pellets of each formulation were removed from the metallic cation solution and both the solution and the gels were analysed by ICP-MS. The metallic extraction was assessed by measuring the amount of metallic ion in the gel and was calculated according to the Eq. (8):

$$\text{Metallic extraction\%} = \frac{M^{n+} \text{gel}_f - M^{n+} \text{gel}_i}{M_i^{n+}} \times 100 \quad (8)$$

where $M^{n+} \text{gel}_f$ is the molar amount of metallic ion found in the pellet (i. e. a xerogel or rehydrated hydrogel), $M^{n+} \text{gel}_i$ is the molar amount of metallic ion measured in the control pellet unexposed to the iron solution and M_i^{n+} is the amount of metallic ion in the starting solution.

Alternatively, studying the molar amount of iron in the supernatant,

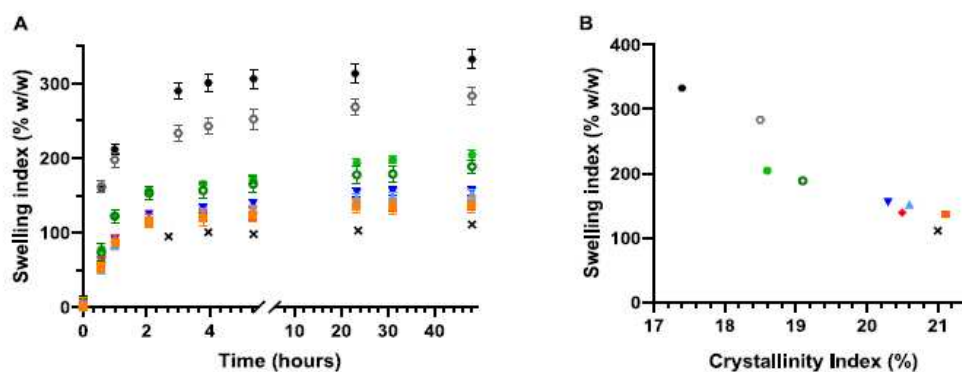


Fig. 6. A: Swelling in water of the different xerogel formulations. ● 5 % DA₆ 5 % DA₄₀@DFO, ○ 5 % DA₆ 5 % DA₄₀, ● 10 % DA₆ 5 % DA₄₀@DFO, ○ 10 % DA₆ 5 % DA₄₀, ▼ 13 % DA₆ 2 % DA₄₀@DFO, ▲ 13 % DA₆ 2 % DA₄₀, ◆ 14 % DA₆ 1 % DA₄₀@DFO, ■ 14 % DA₆ 1 % DA₄₀, × 15 % DA₆. B: Correlation between Swelling index and crystallinity index in xerogels, showing the major role of crystallites in the physical crosslinking of the rehydrated xerogels.

the metallic extraction could also be quantified by the following ratio as defined by Eq. (9):

$$\text{Metallic extraction\%} = \frac{M_i^{2+} - M_f^{2+}}{M_i^{2+}} \times 100 \quad (9)$$

where M_f^{2+} is the molar amount of Fe(III) ions in the solution at the end of the 90 h experiment (in the equilibrium state) and M_i^{2+} is the molar amount of metallic cation in the starting solution.

In this experiment, the quantity of grafted DFO present within the pellet is in excess vs that of iron (III) in the 20 mL initial solution ($3.6 \mu\text{mol/L} \times 20 \cdot 10^{-3} \text{L} = 0.072 \mu\text{mol}$). As an example, xerogels and mother solutions containing DA₄₀@DFO at concentrations of 1 %, 2 %, and 5 %, respectively, have DFO quantities of 0.24 μmol , 0.49 μmol , and 1.22 μmol within xerogel pellets weighing around 24.5 mg of dried polymer (16.3 mg in the case of the formulation 5 % DA₄₀ 5 % DA₄₀@DFO). Consequently, the DFO-to-Fe ratio ranged from about 3.4 to 17.0, resulting in an excess of DFO vs iron species.

Both measurements obtained from Eq. (8) with ICP-MS performed on the xerogels/rehydrated gels or (9) with the supernatant gave similar evaluations of metallic extraction. The results from the analysis of the supernatant using Eq. (9) are presented as mean \pm standard deviation in (Fig. 7.A). ($n = 4$ for the xerogels prepared from polymer solutions at a concentration of 15 % w/w and $n = 3$ for those made with a 10 % w/w

solution). Iron (III) extraction was normalized by the dry mass (mg) of xerogel yielding extraction ratios of $2.4 \pm 0.1 \text{ \%}/\text{mg}$, $2.5 \pm 0.1 \text{ \%}/\text{mg}$ and $3.2 \text{ \%}/\text{mg} \pm 0.3 \text{ \%}$ for the pellets prepared from 1 %, 2 % and 5 % DA₄₀@DFO respectively and for the formulation 5 % DA₆/5 % DA₄₀@DFO it was $4.9 \pm 0.2 \text{ \%}/\text{mg}$. Thus, most of the iron in solution could be complexed as soon as the dry mass of the xerogels exceeded 50 mg. For the control samples, the extraction due to the pellets (without DA₄₀@DFO) is $1.9 \pm 0.1 \text{ \%}$, $1.8 \pm 0.2 \text{ \%}$, $2.2 \pm 0.1 \text{ \%}$, $2.1 \pm 0.2 \text{ \%}$, and $2.6 \pm 0.3 \text{ \%}/\text{mg}$ for the gels with 1 %, 2 %, 5 % DA₄₀, the 15 % DA₆ and 5 % DA₆ 5 % DA₄₀ respectively (for extraction values per pellet see (Fig. S6)), where metallic extraction per pellet were calculated using Eqs. (8) and (9) without normalization of the result by the weight of the xerogel at the start of the complexation experiment). This experiment demonstrates, firstly, that the percentage of DA₄₀ does not influence significantly the extraction of iron from the solution. Meanwhile, we observed a significant extraction of iron from the rehydrated pellets prepared with ungrafted chitosan ($2.0 \pm 0.3 \text{ \%}$ per mg of xerogel in average for all the xerogels made with DA₄₀). The extraction can thus be attributed to an interaction between deferiprone and the deferiprone-Fe (III) complex with chitosan. In particular, partial saturation of the coordination sphere of iron by chitosan becomes a plausible hypothesis, as chitosan is known to form complexes with metallic cations such as iron (III) (Farinelli et al., 2021). In order to further evidence the formation of deferiprone-Fe(III)-chitosan complex, further calculations can be carried

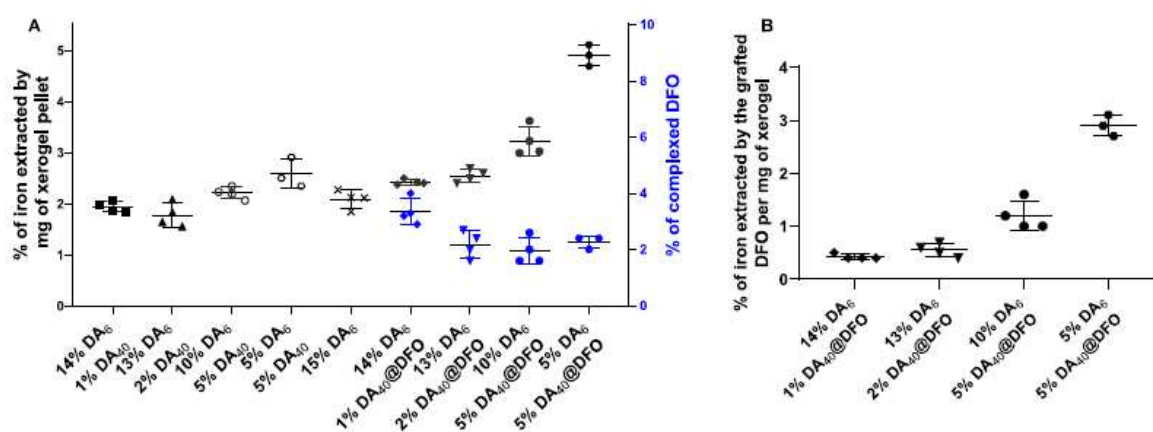


Fig. 7. A: Iron (III) extraction by xerogels after 90 h in 20 mL solution with an initial concentration of $3.58 \mu\text{M}$ of $\text{Fe}(\text{NO}_3)_3$, $14.3 \mu\text{M}$ of deferiprone in phosphate buffer 10 mM (pH 7.4). The measurements were obtained using ICPMS and are given on the black (left) axis as % of iron extracted by mg of xerogel pellet. Blue (right) axis as % of complexed DFO calculated with Eq. (11). B: Net extraction performed by the grafted DFO derivative per mg of xerogel. Results were calculated using Eq. (10).

out. The average iron content within ungrafted chitosan rehydrated pellets made out of 15 % polymer precursor solution ($Iron_{extDA40}$), determined by ICP-MS, was found to be $0.037 \pm 0.002 \mu\text{mol}$. If direct chitosan-Fe(III) complexes could form in competition with deferiprone-Fe(III) complexes, then no change in the deferiprone quantity in the supernatant should be observed ($0.302 \pm 0.002 \mu\text{mol}$). However, upon measuring the absorbance at 280 nm (the maximum absorbance for deferiprone) (Moridani & O'Brien, 2001) and comparing it to a deferiprone calibration curve, it was revealed that, on average, $0.032 \pm 0.002 \mu\text{mol}$ of deferiprone was "missing" from the supernatant (trapped within the rehydrated pellet). Since 3 deferiprone molecules are needed to chelate 1 iron (III) cation, before submerging the chelating xerogel, there are $3 \times 0.037 = 0.111 \mu\text{mol}$ of deferiprone molecules chelating iron (III). The ratio of "missing" deferiprone to complexed deferiprone = $0.032/0.111$ is close to 1/3. Furthermore, the quantities of iron and deferiprone trapped within the rehydrated pellet are remarkably similar, indicating a one-to-one ratio. This suggests that for every Fe atom in the control pellets, there is also one deferiprone molecule inside the pellet. Consequently, the $FeDef_3$ complex, when chitosan is present, it is likely to release two deferiprone molecules, with the iron forming complexes with chitosan, resulting in the formation of the Deferiprone-Fe-Chitosan complex.

Therefore, the net extraction performed by the grafted DFO derivative can be calculated using the following equation:

$$\%Net\ extraction = \%Metallic\ extraction - \%Iron_{Chito} \quad (10)$$

Where $\%Iron_{Chito}$ correspond to the average % of iron extracted by the control hydrogels as explained above, and $\%Metallic\ extraction$ is the total % of iron extracted by the hydrogels. By normalising the net extraction by the weight of dried xerogel we obtained a net extraction of $0.4 \pm 0.1 \%$, $0.5 \pm 0.1 \%$ and $1.2 \pm 0.3 \%$ per mg of xerogel for the systems prepared from the 15 % (w/w) polymer solution having 1 %, 2 % and 5 % $DA_{40}@DFO$ respectively. The same calculation was performed for the formulation 5 % DA_6 5 % $DA_{40}@DFO$ giving a specific DFO extraction DFO of $2.9 \pm 0.2 \%$ of total iron in solution per mg of xerogel as shown in Fig. 7B. Lastly, the complexed DFO fraction with iron, in the formulation containing $DA_{40}@DFO$, was calculated by the following equation:

$$\frac{DFO_{tot} - (Iron_{ext} - Iron_{Chito})}{DFO_{tot}} \times 100 \quad (11)$$

Where DFO_{tot} is the total molar amount of DFO per xerogel pellet, $Iron_{ext}$ is the amount of iron (III) extracted by the xerogel pellet and $Iron_{Chito}$ is the molar amount of iron extracted by the chitosan - deferiprone interaction for the studied xerogel (determined by the molar amount of iron (III) extracted by the control xerogels, without $DA_{40}@DFO$). The fraction of DFO complexed with iron (III) is $3.3 \pm 0.4 \%$, $2.2 \pm 0.5 \%$, $1.9 \pm 0.5 \%$, and $2.3 \pm 0.2 \%$, for the formulations prepared from the 15 % w/w polymer solution having 1 %, 2 %, 5 % $DA_{40}@DFO$ and the 10 % w/w 5 % $DA_{40}@DFO$ formulation respectively. Even though only a small proportion of DFO sites are complexed with iron, materials containing $DA_{40}@DFO$ exhibit a better iron extraction capacity compared to their counterparts without DFO.

Moreover, by plotting the % of iron extracted per mg of xerogel against the amount of grafted DFO, the data display a linear behaviour (see (Fig. S7)). A linear regression yields a correlation coefficient R^2 of 0.874 establishing:

$$\%Iron\ extracted = 39.30 \cdot n_{DFO} + 1.872$$

Where n_{DFO} is the molar amount of DFO per g of xerogel showing a direct proportionality between the number of DFO grafts and iron extraction. In fact, such iron extraction by xerogels functionalized with DFO also reflects the values of complexation constants: since $\text{Log } K_{(FeHDFO)^+}$ is superior to $\text{Log } K_{FeDef_3}$, iron binding results in the formation of Fe(III)-

DFO complexes (see Table S3). Such extraction would not be expected *in vitro* against deferiprone with EDTA-grafted chitosan-based materials. In addition, the association constants used in the simulation of Fe (III) binding with citrate a known low molecular mass ligand present in human blood plasma, (Königsberger et al., 2000) and transferrin (Giri, 2022) show that Chitosan $DA_{40}@DFO$ could also form complexes against the various transport forms of iron *in vivo*. Moreover, in the case of iron overload, the chelator DFO appears to be capable of chelating iron released by ferritin, thus protecting cells from oxidative stress (Lu et al., 2009). It is therefore expected that the materials developed in this paper will have the same protective effect.

3.3.2. Competitive multimetal ion chelation

An important feature of a future chelating material is its ability to target specifically a desired ion (iron (III) in our case) to avoid, as much as possible, to induce a dyshomeostasis of other metallic cations. To this end, the iron binding properties of the materials were evaluated in the presence of other metallic cations such as zinc (II) and copper (II). Such competitor ions were introduced in equimolar concentration of $3.6 \mu\text{mol/L}$, and chelated by EDTA to avoid the precipitation of iron (III) at physiological pH, and to present all metallic cations in the same conditions. It has been observed that metallic complexes with EDTA tend to interact with chitosan through an interaction with amines groups (Tseng et al., 1999) therefore, in this experiment, Na_2SO_4 was added in an excess molar ratio of $n_{Na_2SO_4}/n_{NH_2} = 5$, where n_{NH_2} is the number of mole of amines groups of chitosan, in order to minimise the interactions between M-EDTA complexes and chitosan. Indeed, sulphate ions will competitively interact with the amine groups of chitosan (Hamdine et al., 2005; Vakili et al., 2019) Thus, the only metals extracted by the gel are the ones chelated by the free DFO exclusively. Accordingly, no gel is capable of extracting zinc (II) from the solution but only the gels with $DA_{40}@DFO$ are able to extract copper (II) and iron (III) (Fig. 8). (for extraction values per xerogel pellet see (Fig. S8), Metallic extraction per pellet were calculated using Eqs. (8) and (9)). Concerning iron extraction, the values reported in (Fig. 8) are comparable to the results of the net extraction in single metal chelation experiments for the formulations containing $DA_{40}@DFO$. This confirms that the extracted metals are effectively chelated by DFO in these experimental conditions.

It is clear that Chitosan $@DFO$ exhibits a notable preference for chelating iron (III) over other metals, such as copper (II) and particularly zinc (II) (Fig. 8). However, this chelation is not absolutely specific, since DFO does have the capacity to chelate copper (II) as well (for the values of chelation constant see Table S3), albeit to a lesser extent when compared to its affinity for iron (III) chelation. This observation shows DFO's selective chelation behaviour, with a primary effect on iron (III)

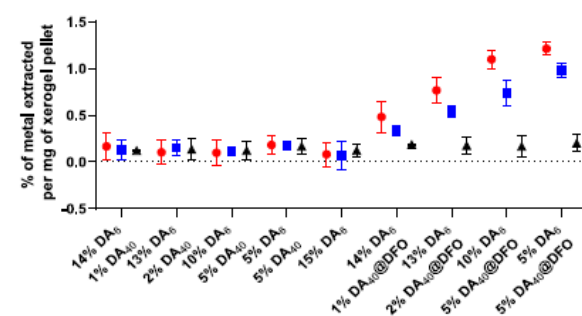


Fig. 8. Extraction of \bullet Iron (III), \blacksquare copper (II) and \blacktriangle zinc (II) by xerogel chitosan pellet after 90 h in 20 mL of a multi metal solution with a concentration of $3.58 \mu\text{mol/L}$ for each metal, $12.9 \mu\text{mol/L}$ of EDTA and 35 mM of Na_2SO_4 in HEPES 10 mM (pH:7.4). The molar fraction EDTA/Metal = 1.2, the molar fraction Na_2SO_4 /amine = 5. The molar fraction DFO/Metal are 1.1, 2.3 and 5.7 for the formulations containing 1 %, 2 %, and 5 % Chitosan- $DA_{40}@DFO$ respectively. The measurements were obtained using ICP-MS.

but still demonstrating some copper (II) chelation. In the case of an iron overload in the body, the major problematic ion will be iron (III) and it will be present in major proportion compared to the other metallic ions like copper (II) or zinc (II). Thus, the utilization of a gel containing DA₄₀@DFO, which primarily chelates iron (III), holds particular significance. Despite the presence of other essential cations like Mg (II) and Ca (II) in biological media, there is no risk of chelating them with DFO. This is because DFO's complexation constants for these cations are very low compared to its $\text{Log } K_{(\text{FeHDFO})^+}$ (Richardson et al., 1989).

4. Conclusion

Due to recent evidence of iron overload in various pathologies and its detrimental effects, such as the production of reactive oxygen species (ROS) and ferroptosis (Angoro et al., 2022; Dixon et al., 2012; Emerit et al., 2001; Valko et al., 2005), extraction of iron (III) from physiological media is a key issue for a broad range of pathologies. This work presents a proof of concept for the synthesis of a bio-material designed for the extraction of metallic cations such as iron (III). Chitosan was chosen as a polymer substrate due to its biodegradability, biocompatibility, and ease of functionalization. We successfully grafted a Desferrioxamine derivative, a strong chelator of iron(III) ($\text{Log}(K_{(\text{FeHDFO})^+})$: 41.8) onto chitosan (Toporivska & Gumienna-Kontecka, 2019), resulting in a macrochelator of iron (III). To achieve a stable product during the grafting reaction, it was necessary to enhance the hydrophilicity of chitosan by re-acetylation up to a DA of 40 %, enabling a DFO grafting rate of 3.8 ± 0.2 %. Furthermore, the gelation properties were obtained by the association of this grafted chitosan with a low DA (ungrafted) chitosan DA₅. We prepared physical hydrogels without the need for crosslinking agents, as confirmed by the rheological studies, with no significant alterations of the viscoelastic properties in comparison with the control gels. By increasing the proportion of DA₄₀@DFO (or reducing the proportion of DA₅), the crystallinity of the xerogels was slightly reduced, due to the steric hindrance caused by the DFO moieties. The resulting dry materials (xerogels) exhibited the ability to swell and rehydrate after drying, thereby allowing iron ions to penetrate the gel and be captured by the DFO grafts present within the rehydrated gel structure. The swelling capacity of the material increased with the amount of DA₄₀ (due to its hydrophilic character compared to low DA chitosan) as well as the amount of DFO. By impeding chitosan crystallization, the grafted DFO contributed to the increased swelling of the xerogels and rehydrated gels.

Chelation experiments demonstrated that materials incorporating grafted DFO exhibited superior iron (III) extraction compared to bare chitosan hydrogels against a strong iron chelator (deferiprone) under physiological conditions. The amount of iron (III) extracted correlated positively with the quantity of DA₄₀@DFO incorporated within the parent gels and their corresponding dried xerogels. To assess the selectivity of the complexation process, we investigated the behaviour of the materials with a mixture of metal ions commonly found in physiological media, including copper (II) and zinc (II). The results confirmed a higher affinity of the DA₄₀@DFO formulations for iron (III), although they also displayed a lower capacity for copper (II) chelation. Our studies further suggest that the apparent chelation capabilities are influenced by the various species present in the solution, including the counterions of the metal salts. Depending on the nature of the cation's counterion or chelate, chitosan can interact with it, potentially impacting the extraction mechanism. Therefore, future chelation studies utilizing chitosan should consider the role of chelates and counterions within the solution, xerogels, and gels.

CRedit authorship contribution statement

Juan Felipe Salazar Ariza: Writing – review & editing, Writing – original draft, Visualization, Validation, Software, Resources, Methodology, Investigation, Formal analysis, Data curation, Conceptualization.

François Lux: Writing – review & editing, Validation, Supervision, Project administration, Methodology, Funding acquisition, Formal analysis, Data curation, Conceptualization. Fernande Da Cruz-Boisson: Investigation, Data curation. Jacqueline Resende de Azevedo: Writing – review & editing, Investigation, Data curation. Ruben Vera: Investigation, Data curation. Olivier Tillement: Validation, Methodology, Conceptualization. Alexandra Montebault: Writing – review & editing, Validation, Methodology, Investigation, Formal analysis, Data curation, Conceptualization. Laurent David: Writing – review & editing, Validation, Supervision, Methodology, Funding acquisition, Data curation, Conceptualization.

Declaration of competing interest

The authors declare the following financial interests/personal relationships which may be considered as potential competing interests: LUX reports financial support was provided by Agence Nationale de la Recherche (ANR). DAVID, SALAZAR ARIZA, MONTEBAULT, LUX, TILLEMENT has patent #FR2110474 pending to MEXBRAIN. DAVID MONTEBAULT, LUX, TILLEMENT has patent #FR2007997 pending to MEXBRAIN. The other authors declare that they have no known competing financial interests or personal relationships that could have appeared to influence the work reported in this paper.

Data availability

Data will be made available on request.

Acknowledgements

We thank the NMR Polymer Center of Institut de Chimie de Lyon, for assistance and access to the NMR facilities. The author wants to thank French Agence Nationale de la Recherche (ANR) for funding of SEMB project (ANR-20-CE19-0011). We extend our gratitude to Thomas Brichart for his assistance with the illustrations.

Appendix A. Supplementary data

Supplementary data to this article can be found online at <https://doi.org/10.1016/j.carbpol.2024.122670>.

References

- Aiba, S. (1991). Studies on chitosan: 3. Evidence for the presence of random and block copolymer structures in partially N-acetylated chitosans. *International Journal of Biological Macromolecules*, 13(1), 40–44. [https://doi.org/10.1016/0141-8130\(91\)90008-1](https://doi.org/10.1016/0141-8130(91)90008-1)
- Anderson, G. J., & McLaren, G. D. (Eds.). (2012). *Iron physiology and pathophysiology in humans*. Humana Press. <https://doi.org/10.1007/978-1-60327-485-2>
- Angoro, B., Motshakeri, M., Hemmaway, C., Svirskis, D., & Sharma, M. (2022). Non-transferrin bound iron. *Clinica Chimica Acta*, 531, 157–167. <https://doi.org/10.1016/j.cca.2022.04.004>
- Apoetolakis, S., & Kypraiou, A.-M. (2017). Iron in neurodegenerative disorders: Being in the wrong place at the wrong time? *Reviews in the Neurosciences*, 20(8), 893–911. <https://doi.org/10.1515/revneuro-2017-0020>
- Becerra, J., Sudre, G., Royaud, I., Monterret, R., Verrier, B., Rochas, C., ... David, L. (2017). Tuning the hydrophilic/hydrophobic balance to control the structure of chitosan films and their protein release behavior. *AAPS PharmSciTech*, 18(4), 1070–1083. <https://doi.org/10.1208/s12249-016-0678-9>
- Cappellini, M. D. (2005). Iron-chelating therapy with the new oral agent ICL670 (Exjade®). *Best Practice & Research Clinical Haematology*, 18(2), 289–298. <https://doi.org/10.1016/j.beha.2004.09.002>
- Céline, P.-B., Antoine, V., Denis, B., Laurent, V., Laurent, D., & Catherine, F. (2013). Development and characterization of composite chitosan/active carbon hydrogels for a medical application. *Journal of Applied Polymer Science*, 128(5), 2945–2953. <https://doi.org/10.1002/app.38414>
- Chatelet, C., Damour, O., & Domard, A. (2001). Influence of the degree of acetylation on some biological properties of chitosan films. *Biomaterials*, 22(3), 261–268. [https://doi.org/10.1016/S0142-9612\(00\)00183-6](https://doi.org/10.1016/S0142-9612(00)00183-6)
- Chen, Z., Gao, C., Hua, Y., Keep, R. F., Muraszko, K., & Xi, G. (2011). Role of Iron in brain injury after intraventricular hemorrhage. *Stroke*, 42(2), 465–470. <https://doi.org/10.1161/STROKEAHA.110.602755>

- Chitichirovsky, M., Primo, A., Gonzalez, P., Molvinger, K., Robitzner, M., Quignard, F., & Taran, F. (2009). Functionalized chitosan as a green, recyclable, biopolymer-supported catalyst for the [3+2] Huisgen cycloaddition. *Angewandte Chemie International Edition*, 48(32), 5916–5920. <https://doi.org/10.1002/anie.200901309>
- Desorme, M., Montembault, A., Lucas, J.-M., Rochas, C., Bouet, T., & David, L. (2013). Spinning of hydroalcoholic chitosan solutions. *Carbohydrate Polymers*, 99(1), 50–63. <https://doi.org/10.1016/j.carbpol.2013.04.070>
- Dixon, S. J., Lemberg, K. M., Lamprecht, M. R., Skouta, R., Zaitsev, E. M., Gleason, C. E., ... Stockwell, B. R. (2012). Ferroptosis: An iron-dependent form of nonapoptotic cell death. *Cell*, 149(5), 1060–1072. <https://doi.org/10.1016/j.cell.2012.03.042>
- Domínguez-Vera, J. M. (2004). Iron(III) complexation of Desferrioxamine B encapsulated in apoferritin. *Journal of Inorganic Biochemistry*, 90(3), 469–472. <https://doi.org/10.1016/j.jinorgbio.2003.12.015>
- Emerit, J., Beaumont, C., & Trivin, F. (2001). Iron metabolism, free radicals, and oxidative injury. *Biomedicine & Pharmacotherapy = Biomedicine & Pharmacotherapie*, 55(6), 333–339. [https://doi.org/10.1016/s0753-3322\(01\)00068-3](https://doi.org/10.1016/s0753-3322(01)00068-3)
- Facchinatto, W. M., dos Santos, D. M., Fiamingo, A., Bernardes-Filho, R., Campana-Filho, S. P., de Azevedo, E. R., & Colnago, L. A. (2020). Evaluation of chitosan crystallinity: A high-resolution solid-state NMR spectroscopy approach. *Carbohydrate Polymers*, 250, Article 116891. <https://doi.org/10.1016/j.carbpol.2020.116891>
- Farinelli, G., Di Luca, A., Kaila, V. R. I., MacLachlan, M. J., & Tiraferri, A. (2021). Fe-chitosan complexes for oxidative degradation of emerging contaminants in water: Structure, activity, and reaction mechanism. *Journal of Hazardous Materials*, 408, Article 124662. <https://doi.org/10.1016/j.jhazmat.2020.124662>
- Ficiară, E., Molinar, C., Gazzin, S., Jayanti, S., Argenziano, M., Nasi, L., ... Cavalli, R. (2024). Developing Iron Nanochelating agents: Preliminary investigation of effectiveness and safety for central nervous system applications. *International Journal of Molecular Sciences*, 25(2), Article 2. <https://doi.org/10.3390/ijms25020729>
- Fuchs, T., Richtering, W., Burchard, W., Kajiwara, K., & Kitamura, S. (1998). Gel point in physical gels: Rheology and light scattering from thermoreversibly gelling schizophyllan. *Polymer Gels and Networks*, 5(6), 541–559. [https://doi.org/10.1016/S0966-7823\(97\)00027-0](https://doi.org/10.1016/S0966-7823(97)00027-0)
- Giri, N. C. (2022). Role of transferrin in iron metabolism. In *Iron metabolism—A double-edged sword*. IntechOpen. <https://doi.org/10.5772/intechopen.100488>
- Grange, C., Aigle, A., Ehrlich, F., Salazar Ariza, J. F., Brichart, T., Da Cruz-Boisson, F., ... Tillement, O. (2023). Design of a water-soluble chitosan-based polymer with antioxidant and chelating properties for labile iron extraction. *Scientific Reports*, 13(1), Article 1. <https://doi.org/10.1038/s41598-023-34251-3>
- Grange, C., Lux, F., Brichart, T., David, L., Couturier, A., Leaf, D. E., ... Tillement, O. (2023). Iron as an emerging therapeutic target in critically ill patients. *Critical Care*, 27(1), 475. <https://doi.org/10.1186/s13054-023-04759-1>
- Hamdine, M., Heuzey, M.-C., & Bégin, A. (2005). Effect of organic and inorganic acids on concentrated chitosan solutions and gels. *International Journal of Biological Macromolecules*, 37(3), 134–142. <https://doi.org/10.1016/j.ijbiomac.2005.09.009>
- Hermanson, G. T. (2008). Chapter 2—The chemistry of reactive groups. In G. T. Hermanson (Ed.), *Biocjugate techniques* (2nd ed., pp. 169–212). Academic Press. <https://doi.org/10.1016/B978-0-12-370501-3.00002-3>
- Hernández, R. B., Yola, O. R., & Mercé, A. L. R. (2007). Chemical equilibrium in the complexation of first transition series divalent cations Cu²⁺, Mn²⁺ and Zn²⁺ with chitosan. *Journal of the Brazilian Chemical Society*, 18, 1388–1396. <https://doi.org/10.1590/S0103-50532007000700015>
- Hirai, A., Odani, H., & Nakajima, A. (1991). Determination of degree of deacetylation of chitosan by ¹H NMR spectroscopy. *Polymer Bulletin*, 26(1), 87–94. <https://doi.org/10.1007/BF00299352>
- Hoffbrand, A. V., Cohen, A., & Hershko, C. (2003). Role of deferoxamine in chelation therapy for transfusional iron overload. *Blood*, 102(1), 17–24. <https://doi.org/10.1182/blood-2002-06-1867>
- Howard, J. A., Kuznetsova, H., Dziubenko, N., Aigle, A., Natuzzi, M., Thomas, E., ... Tillement, O. (2023). Combating lead and calcium exposure with an orally administered chitosan-based chelating polymer. *Scientific Reports*, 13(1), Article 1. <https://doi.org/10.1038/s41598-023-28968-4>
- Imran Ul-haq, M., Hamilton, J. L., Lai, B. F. L., Shenoi, R. A., Horte, S., Constantinescu, I., ... Kizhakkedathu, J. N. (2013). Design of long circulating nontoxic dendritic polymers for the removal of iron in vivo. *ACS Nano*, 7(12), 10704–10716. <https://doi.org/10.1021/nm4035074>
- Joseph, V. B., Satchell, D. P. N., Satchell, R. S., & Waszef, W. N. (1992). Hydrolysis of aryl and alkyl isothiocyanates in aqueous perchloric acid. *Journal of the Chemical Society, Perkin Transactions*, 2(3), 339–341. <https://doi.org/10.1039/P92920000339>
- Kantak, M. N., & Bharate, S. S. (2022). Analysis of clinical trials on biomaterial and therapeutic applications of chitosan: A review. *Carbohydrate Polymers*, 278, Article 118999. <https://doi.org/10.1016/j.carbpol.2021.118999>
- Kean, T., & Thanou, M. (2010). Biodegradation, biodistribution and toxicity of chitosan. *Advanced Drug Delivery Reviews*, 62(1), 3–11. <https://doi.org/10.1016/j.addr.2009.09.004>
- Königsberger, L.-C., Königsberger, E., May, P. M., & Hefter, G. T. (2000). Complexation of iron(III) and iron(II) by citrate. Implications for iron speciation in blood plasma. *Journal of Inorganic Biochemistry*, 79(3), 175–184. [https://doi.org/10.1016/S0162-0134\(99\)00222-6](https://doi.org/10.1016/S0162-0134(99)00222-6)
- Leduc, J.-F., Leduc, R., & Cabana, H. (2014). Phosphate adsorption onto chitosan-based hydrogel microspheres. *Adsorption Science & Technology*, 32(7), 557–569. <https://doi.org/10.1260/0263-6174.32.7.557>
- Lu, Z., Nie, G., Li, Y., Soe-Lin, S., Tao, Y., Cao, Y., ... Zhao, B. (2009). Overexpression of mitochondrial ferritin sensitizes cells to oxidative stress via an iron-mediated mechanism. *Antioxidants & Redox Signaling*, 11(8), 1791–1803. <https://doi.org/10.1089/ars.2008.2306>
- Matica, M. A., Aachmann, F. L., Tøndervik, A., Sletta, H., & Ostafe, V. (2019). Chitosan as a wound dressing starting material: Antimicrobial properties and mode of action. *International Journal of Molecular Sciences*, 20(23), Article 23. <https://doi.org/10.3390/ijms20235889>
- Mogoşanu, G. D., & Grumezescu, A. M. (2014). Natural and synthetic polymers for wounds and burns dressing. *International Journal of Pharmaceutics*, 463(2), 127–136. <https://doi.org/10.1016/j.ijpharm.2013.12.015>
- Montembault, A., Viton, C., & Domard, A. (2005a). Physico-chemical studies of the gelation of chitosan in a hydroalcoholic medium. *Biomaterials*, 26(8), 933–943. <https://doi.org/10.1016/j.biomaterials.2004.03.033>
- Montembault, A., Viton, C., & Domard, A. (2005b). Rheometric study of the gelation of chitosan in aqueous solution without cross-linking agent. *Biomacromolecules*, 6(2), 653–662. <https://doi.org/10.1021/bm049593m>
- Moreau, C., Duce, J. A., Rascol, O., Devedjian, J.-C., Berg, D., Dexter, D., ... FAIRPARK-II study group. (2018). Iron as a therapeutic target for Parkinson's disease. *Movement Disorders: Official Journal of the Movement Disorder Society*, 33(4), 568–574. <https://doi.org/10.1002/mds.27275>
- Moridani, M. Y., & O'Brien, P. J. (2001). Iron complexes of deferoxamine and dietary plant catechols as cytoprotective superoxide radical scavengers. *Biochemical Pharmacology*, 62(12), 1579–1585. [https://doi.org/10.1016/S0006-2952\(01\)00821-8](https://doi.org/10.1016/S0006-2952(01)00821-8)
- Natuzzi, M., Grange, C., Gréa, T., Brichart, T., Aigle, A., Bechet, D., ... Tillement, O. (2021). Feasibility study and direct extraction of endogenous free metallic cations combining hemodialysis and chelating polymer. *Scientific Reports*, 11(1), Article 1. <https://doi.org/10.1038/s41598-021-99462-y>
- Nurchi, V. M., Crisponi, G., Pivetta, T., Donatoni, M., & Remelli, M. (2008). Potentiometric, spectrophotometric and calorimetric study on iron(III) and copper(II) complexes with 1,2-dimethyl-3-hydroxy-4-pyridinone. *Journal of Inorganic Biochemistry*, 102(4), 684–692. <https://doi.org/10.1016/j.jinorgbio.2007.10.012>
- Okuyama, K., Noguchi, K., Miyazawa, T., Yui, T., & Ogawa, K. (1997). Molecular and crystal structure of hydrated chitosan. *Macromolecules*, 30(19), 5849–5855. <https://doi.org/10.1021/ms970509n>
- Ocorio-Madrado, A., David, L., Trombotto, S., Lucas, J.-M., Peniche-Covas, C., & Domard, A. (2010). Kinetics study of the solid-state acid hydrolysis of chitosan: Evolution of the crystallinity and macromolecular structure. *Biomacromolecules*, 11(5), 1376–1386. <https://doi.org/10.1021/bm1001665>
- Pietrangolo, A. (2010). Hereditary hemochromatosis: Pathogenesis, diagnosis, and treatment. *Gastroenterology*, 139(2), 393–408.e2. <https://doi.org/10.1053/j.gastro.2010.06.013>
- Porter, J. B., & Huehns, E. R. (1999). The toxic effects of desferrioxamine. *Baillière's Clinical Haematology*, 2(2), 459–474. [https://doi.org/10.1016/S0950-3536\(99\)00027-7](https://doi.org/10.1016/S0950-3536(99)00027-7)
- Rami, L., Malaise, S., Delmond, S., Fricain, J.-C., Siadou, R., Schlaubitz, S., Laurichesse, E., Amédée, J., Montembault, A., David, L., & Bordenave, L. (2014). Physicochemical modulation of chitosan-based hydrogels induces different biological responses: Interest for tissue engineering. *Journal of Biomedical Materials Research Part A*, 102(10), 3666–3676. <https://doi.org/10.1002/jbm.a.35035>
- Repo, E., Warchol, J. K., Kurniawan, T. A., & Sillanpää, M. E. T. (2010). Adsorption of Co(II) and Ni(II) by EDTA- and/or DTPA-modified chitosan: Kinetic and equilibrium modeling. *Chemical Engineering Journal*, 161(1), 73–82. <https://doi.org/10.1016/j.cej.2010.04.030>
- Richardson, D. R., Hefter, G. T., May, P. M., Webb, J., & Baker, E. (1989). Iron chelators of the pyridoxal isonicotinoyl hydrazone class. *Biology of Metals*, 2(3), 161–167. <https://doi.org/10.1007/BF01142555>
- Scindia, P., Yogesh, Leeds, M., Joseph, Swaminathan, M., & Sundararaman. (2019). Iron homeostasis in healthy kidney and its role in acute kidney injury. *Seminars in Nephrology*, 39(1), 76–84. <https://doi.org/10.1016/j.semnephrol.2018.10.006>
- Sorlier, P., Denuziere, A., Viton, C., & Domard, A. (2001). Relation between the degree of acetylation and the electrostatic properties of chitin and chitosan. *Biomacromolecules*, 2(3), 765–772. <https://doi.org/10.1021/bm015531t>
- Thomas, G. E. C., Leyland, L. A., Schrag, A.-E., Lees, A. J., Acosta-Cabrero, J., & Weil, R. S. (2020). Brain iron deposition is linked with cognitive severity in Parkinson's disease. *Journal of Neurology, Neurosurgery, and Psychiatry*, 91(4), 418–425. <https://doi.org/10.1136/jnnp-2019-322042>
- Toporivela, Y., & Gumienna-Kontecka, E. (2019). The solution thermodynamic stability of desferrioxamine B (DFO) with Zr(IV). *Journal of Inorganic Biochemistry*, 198, Article 110753. <https://doi.org/10.1016/j.jinorgbio.2019.110753>
- Tseng, R.-L., Wu, F.-C., & Juang, R.-S. (1999). Effect of complexing agents on liquid-phase adsorption and desorption of copper(II) using chitosan. *Journal of Chemical Technology & Biotechnology*, 74(6), 533–588. [https://doi.org/10.1002/\(SICI\)1097-4660\(199906\)74:6<533::AID-JCTB79>3.0.CO;2-O](https://doi.org/10.1002/(SICI)1097-4660(199906)74:6<533::AID-JCTB79>3.0.CO;2-O)
- Vachoud, L., Zylowicz, N., & Domard, A. (1997). Formation and characterisation of a physical chitin gel. *Carbohydrate Research*, 302(3), 169–177. [https://doi.org/10.1016/S0008-6215\(97\)00126-2](https://doi.org/10.1016/S0008-6215(97)00126-2)
- Valiki, M., Deng, S., Cagnetta, G., Wang, W., Meng, P., Liu, D., & Yu, G. (2019). Regeneration of chitosan-based adsorbents used in heavy metal adsorption: A review. *Separation and Purification Technology*, 224, 373–387. <https://doi.org/10.1016/j.seppur.2019.05.040>
- Valko, M., Morris, H., & Cronin, M. T. D. (2005). Metals, toxicity and oxidative stress. *Current Medicinal Chemistry*, 12(10), 1161–1206. <https://doi.org/10.2174/0929667053764635>
- Vandevord, P. J., Matthew, H. W. T., DeSilva, S. P., Mayton, L., Wu, B., & Wooley, P. H. (2002). Evaluation of the biocompatibility of a chitosan scaffold in mice. *Journal of Biomedical Materials Research*, 59(3), 585–590. <https://doi.org/10.1002/jbm.b.1270>
- Várnau, K. M., Ottøy, M. H., & Smidsrud, O. (1994). Water-solubility of partially N-acetylated chitosans as a function of pH: Effect of chemical composition and

- depolymerisation. *Carbohydrate Polymers*, 25(2), 65–70. [https://doi.org/10.1016/0144-8617\(94\)90140-6](https://doi.org/10.1016/0144-8617(94)90140-6)
- Wang, W., Meng, Q., Li, Q., Liu, J., Zhou, M., Jin, Z., & Zhao, K. (2020). Chitosan derivatives and their application in biomedicine. *International Journal of Molecular Sciences*, 21(2), Article 2. <https://doi.org/10.3390/ijms21020487>
- Wu, J., Hua, Y., Keep, R. F., Nakamura, T., Hoff, J. T., & Xi, G. (2003). Iron and iron-handling proteins in the brain after intracerebral hemorrhage. *Stroke*, 34(12), 2964–2969. <https://doi.org/10.1161/01.STR.0000103140.52838.45>
- Zhang, M., Li, W., Wang, T., & Zhang, Q. (2019). Association between baseline serum ferritin and short-term outcome of intracerebral hemorrhage: A Meta-analysis. *Journal of Stroke and Cerebrovascular Diseases*, 28(7), 1799–1805. <https://doi.org/10.1016/j.jstrokecerebrovasdis.2019.03.037>

3.2. Complementary study of interactions between chitosan metal complexes and salts in solution.

Non-functionalized chitosan, with its amine and hydroxyl functional groups, exhibits inherent metal complexation properties. Furthermore, chitosan hydrogels are known for their ability to interact with and adsorb a large variety of molecules. These characteristics have led to extensive research on chitosan hydrogels for water purification or drug delivery.

In the previous article, under section 3.3 "Chelation Experiments," it is mentioned that the metal extraction properties of chitosan-based hydrogels (i.e. based on chitosan/chitosan@chelant mixes) are influenced not only by the metal ions but also by all other chemical species present in the solution. Additionally, it is noted that the addition of salts can mitigate some of the interactions between chitosan and metal complexes. In the following section, we will explore in more details how these interactions affect the metal extraction properties of chitosan hydrogels. Furthermore, the mechanisms behind these interactions will be evidenced, categorizing them into two types: direct chelation of the metal ion by chitosan, or indirect chelation via an intermediary chelant. Therefore, to study these interactions, chitosan-based xerogels were submerged in various metal solutions containing different complexing agents, including EDTA, citrate, and deferiprone.

To investigate the role of electrostatic interactions between metal complexes and chitosan, it was necessary to employ a technique that could disrupt these interactions without affecting the chelation process. There are multiple techniques to prevent interactions between molecules in solution and chitosan, known as desorption agents, which are typically used for "washing" chitosan after metal extraction [240,241]. Some of these techniques include acid desorption, basic desorption, chelating agent desorption, and salt desorption. Acid and base desorption were not suitable for our experiments due to the need to maintain physiological pH for accurate evaluation of the chelating materials. Moreover, acidic conditions could lead to the release of metals chelated by the grafted chelator within the hydrogels. Using chelating agents was also not feasible since the added chelating agents can interact with chitosan. Therefore, the technique used here is salt desorption. This method works by weakening the interaction between the adsorbed anion and chitosan through electrostatic interactions [240]. Thus, Na₂SO₄ was chosen due to the higher interaction of SO₄²⁻ with protonated amine groups, compared to other non-interacting salts like NaCl [242].

3.2.1. Na₂SO₄ iron (III) mediated release from chitosan based hydrogels previously exposed to an iron (III) citric acid solution at physiological pH.

Materials and methods A preliminary experiment was conducted by submerging two xerogel pellets, prepared from precursor solutions with the following formulations, in 20 mL of a metallic solution: 15% DA₆, 5% DA₆ 9.5% DA₆@DOTAGA₁₇, 0.5% DA₄₀@DFO, 5% DA₆ 9.2% DA₆@DOTAGA₁₇, 0.8% DA₄₀@DFO, and 5% DA₆ 8% DA₆@DOTAGA₁₇ 2% DA₄₀@DFO. The xerogels were prepared following the same procedure shown in the article "Chitosan-based hydrogel for iron (III) chelation in biological conditions" involving a first acidic precursor solution, followed by a gelation in 3M bath and subsequent washing and drying

The metallic solution contained iron (III) (0.45 mM), citric acid (4.48 mM) to prevent iron precipitation, and HEPES 10 mM (pH 7.4). The solutions were stirred for 24 hours. One pellet from each formulation was extracted from the iron solution and submerged in 20 mL of a second solution containing Na₂SO₄ at 7 mM in HEPES 10 mM (pH 7.4) (Ratio chitosan amines : Na₂SO₄ ~1:0.8). The second pellet of each formulation was also extracted from the iron solution but this time they were submerged in only a HEPES 10 mM (pH 7.4) solution (control samples). Samples were stirred at room temperature for 24 hours after which all hydrogels were extracted from their solution and dissolved in 3 mL of 69% (w/w) HNO₃ by microwave. The resulting samples were diluted to 1% (w/w) HNO₃ and analysed by ICP-MS in kinetic energy discrimination (KED) mode.

Results and discussion By reducing the proportion of DA₆@DOTAGA₁₇ from 9.5% w/w to 8% w/w and increasing the DA₄₀@DFO₄ from 0.5% to 2% in the precursor solution, the total amount of chelator (DOTAGA and DFO) present in the hydrogel decreases. This, in turn, results in a decrease in iron(III) extraction. However, it's important to note that the formulation solely composed of low DA chitosan (15%DA₆) is also capable of extracting iron(III) from the citric acid-iron(III) solution. (Figure 34). This suggests that chitosan, on its own, can interact with iron(III) and/or the metallic complex. This result is coherent with literature where chitosan metal (copper (II)) extraction increases in the presence of citrate-copper (II) complex [243].

Additionally, when hydrogels are submerged in a Na₂SO₄ solution, a portion of the iron within the hydrogel is released back into the solution. This phenomenon highlights the influence of sulphate on metal extraction from chitosan. Specifically, sulphate ions can interact with the amine groups present in chitosan, potentially hindering both direct and indirect iron(III) extraction. The subsequent section will elaborate on how sulphate can impede indirect metal extraction.

To account for this phenomenon, we must first consider the possibility of electrostatic interactions between the citrate-iron (III) complex and chitosan. The iron (III) citrate complex in solution carries a net charge of -3. In order for electrostatic interactions to occur, chitosan must possess protonated functional groups. Although the pKa of chitosan is between 6.2 and 6.5, a physiologically pH of 7.4 still results in a significant number of protonated amines. By applying the following equations considering the pKa of chitosan's amine groups (6.2-6.5), we can calculate the proportion of chitosan amines that are protonated %RNH₃⁺ and that are responsible for the electrostatic interaction between negative charged metal complexes and positively charged chitosan amines.

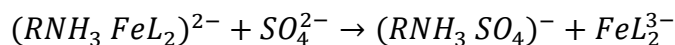
$$pH = pK_{a_{chitosan}} + \log_{10} \left(\frac{[RNH_2]}{[RNH_3^+]} \right)$$

$$\%RNH_3^+ = \frac{[RNH_3^+]}{[RNH_3^+] + [RNH_2]} \times 100$$

Where $[RNH_2]$ is the concentration of deprotonated chitosan amines and $[RNH_3^+]$ the concentration of protonated chitosan amines.

The proportion of protonated amines in the hydrogels ranges from 6% to 11%, making electrostatic interactions between protonated chitosan amines and the citric acid-iron(III) complex plausible. Consequently, when the hydrogels are submerged in Na_2SO_4 solution, the sulphate ions (SO_4^{2-}), being negatively charged like the metallic complex, can interact with the protonated chitosan amines. This interaction may displace the citric acid-iron(III) complex, leading to the observed release of iron(III). Moreover, since the amount of iron(III) released in the presence of the sulphate salt is nearly identical across all formulations (see Table 9), this suggests that the released iron(III) was not chelated by any of the additional chelators present in the formulations with functionalized chitosans. This further supports the idea that sulphate ions are primarily responsible for the displacement and subsequent release of iron from the hydrogels.

However, not all iron (III) cations are released by the formulation made solely of chitosan. One possible explanation is the direct complexation of iron (III) by chitosan itself. Additionally, since the citric acid-iron(III) complex $(FeL_2)^{3-}$ has a higher charge density compared to SO_4^{2-} the electrostatic interaction between the protonated amine of chitosan and the acid-iron(III) complex is favoured. Therefore, to promote the displacement of the iron(III) complex more effectively, higher concentrations of sulphate may be required to shift the balance and enhance the release of the complex.



Where $(FeL_2)^{3-}$ corresponds to the citric acid-iron(III) complex and L is the citric acid ligand.

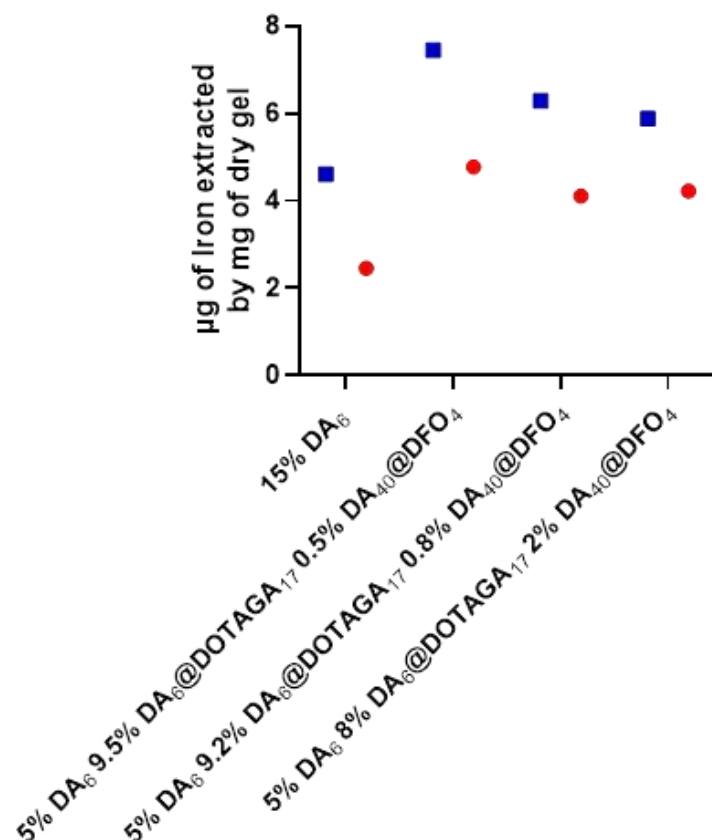


Figure 34. Iron(III) extraction of various chitosan-based xerogels after exposure to 20 mL of metallic solution containing 0.45 mM iron(III), 4.48 mM citric acid, and 10 mM HEPES buffer (pH 7.4) for 24 hours and after being washed for 24 hours ■ in in 20 mL HEPES 10 mM (pH 7.4) or ● in 20 mL Na₂SO₄ at 7 mM in HEPES 10 mM (pH 7.4).

Table 9. µg of iron(III) released by each formulation after exposure to Na₂SO₄ solution at 7 mM.

Gel formulation	µg of iron(III) released by mg of gel
15% DA ₆	2.1
5% DA ₆ 9.5% DA ₆ @DOTAGA ₁₇ 0.5% DA ₄₀ @DFO ₄	2.7
5% DA ₆ 9.2% DA ₆ @DOTAGA ₁₇ 0.8% DA ₄₀ @DFO ₄	2.2
5% DA ₆ 8% DA ₆ @DOTAGA ₁₇ 2% DA ₄₀ @DFO ₄	1.7

3.2.2. Metal extraction by chitosan based hydrogels, metals being solubilized with EDTA

Further, to test the hypothesis of chitosan's indirect chelation via electrostatic interactions with other anionic metal complexes (EDTA-M), where M represents either iron (III) or aluminium (III), a second series of experiments was conducted. Chitosan-based xerogels were first exposed to solutions containing these metal complexes, and the metal extraction efficiency was compared to that of hydrogels exposed to the same concentrations of metal complexes, but with the addition of Na₂SO₄.

Materials and methods An initial experiment was conducted using a HEPES buffer (10 mM, pH 7.4) containing iron(III) at a concentration of 3.6 μM. The same iron standard solution used in previous chelation experiments (Chapter II) was employed. EDTA was also added at a concentration of 4.3 μM (1.2 EDTA molecules per metal ion). One pellet from each formulation was submerged in 20 mL of this metallic/EDTA solution and stirred at room temperature for 90 hours. Interestingly, all formulations, including those without grafted chelators, were capable of extracting nearly all of the iron(III) from the solution (Figure 35 A and B).

A second experiment was conducted using a modified protocol similar to the previous one. In this experiment, aluminium(III) was used as the metal instead of iron(III), at a concentration of 7.4 μM. The EDTA-to-metal ratio was maintained at 1.2:1, resulting in an EDTA concentration of 8.1 μM. Interestingly, as observed in the previous experiment, all formulations were able to deplete the metal from the solution (Figure 36 A and B).

A third experiment was conducted using the same protocol as the second one but adding Na₂SO₄ (35 mM corresponding to five SO₄²⁻ ions per chitosan amine). The amount of extracted metals for each experiment was determined by ICP-MS in KED mode. Samples of the three experiments were prepared by diluting the supernatant in 1% (w/w) aqueous HNO₃.

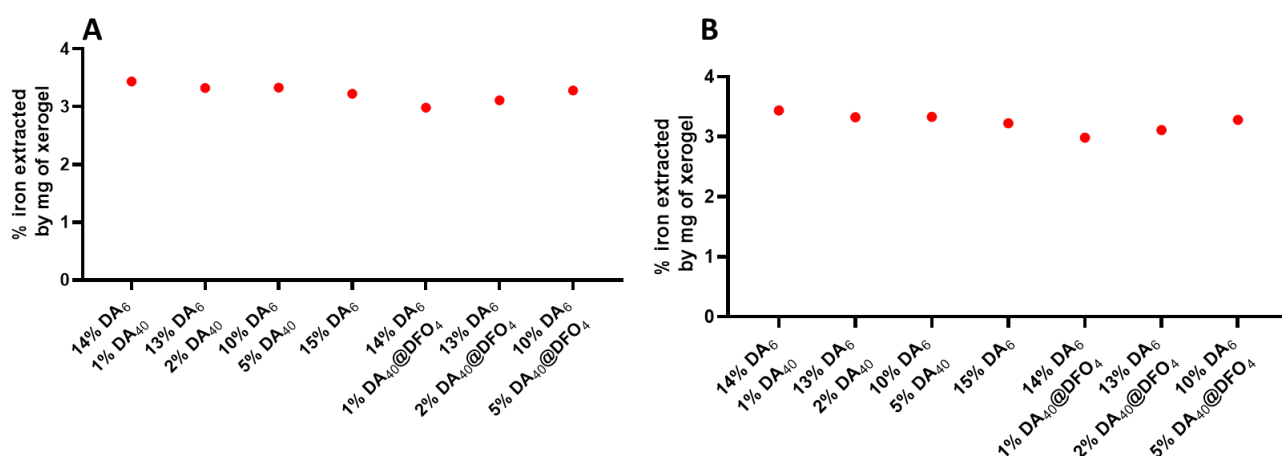


Figure 35. Extraction of ● Iron (III) **A:** by a xerogel chitosan pellet ($m \sim 25$ mg). **B:** mg of xerogel pellet, after 90 hours in 20 ml of an iron (III) solution at 3.6 μM, 4.3 μM of EDTA in

HEPES 10 mM (pH:7.4). The molar fraction EDTA/Metal= 1.2. The molar fraction DFO/Metal are 3.4, 6.9 and 17 for the formulations containing 1%, 2%, and 5% DA₄₀@DFO respectively. The measurements were obtained using ICP-MS.

Results and discussion Similar to previous experiments with citrate-iron (III), all formulations were capable of extracting metals (iron (III) or aluminium (III)). However, the presence of Na₂SO₄ in solution significantly decreased metal extraction capabilities, especially for hydrogels without functionalized chitosan (see Figure 36 C, D and Figure 8 of the article "Chitosan-based hydrogel for iron(III) chelation in biological conditions"). These results indicate that, regardless of the metal in the EDTA-M complex (whether aluminium (III), iron (III), copper (II), or zinc (II)), when the resulting complex carries a negative charge, the addition of Na₂SO₄ masks the electrostatic interactions between chitosan and EDTA-M complexes. As a result, the only metals that can be extracted from the solution are those that undergo direct chelation. This is further confirmed by the fact that, in experiments where Na₂SO₄ was present, only hydrogels with grafted chelators were able to extract any metal (see again Figure 36 C, D and Figure 8 of the article "Chitosan-based Hydrogel for Iron(III) Chelation in Biological Conditions").

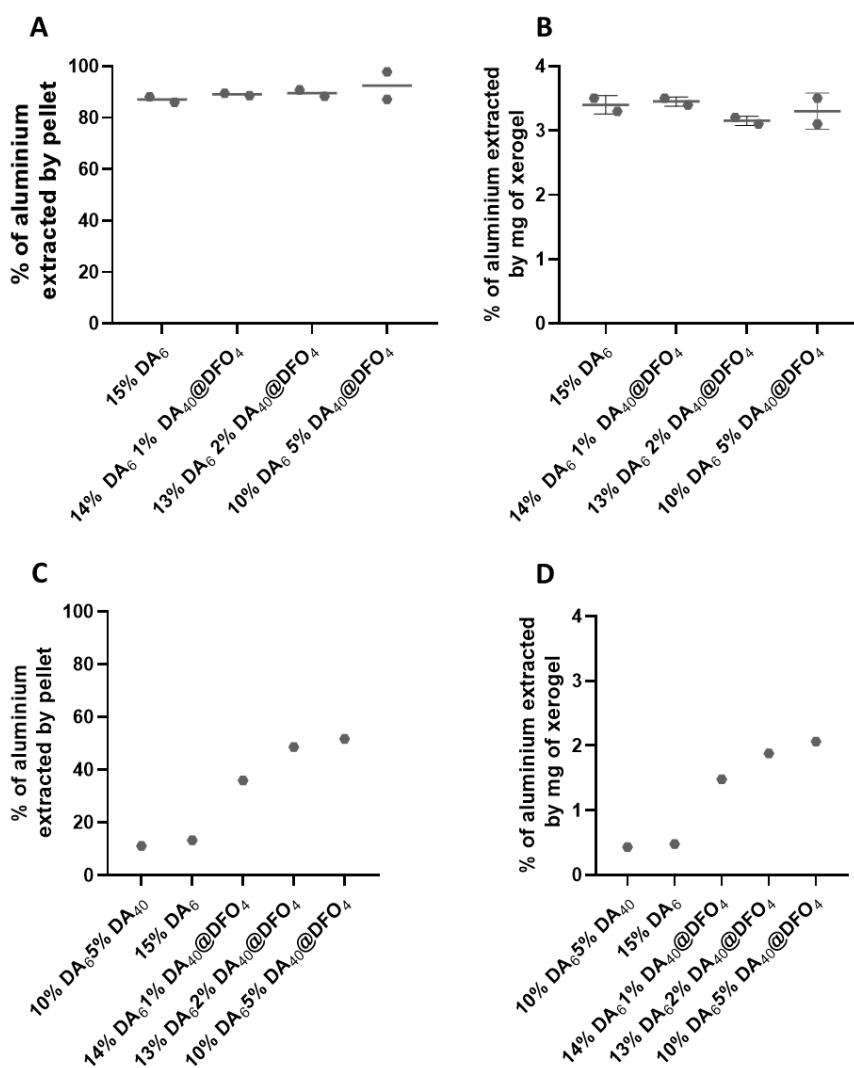


Figure 36. Extraction of ● Aluminium (III) **A:** by xerogel chitosan pellet. **B:** mg of xerogel pellet, after 90 hours in 20 ml of an aluminium(III) solution with a concentration of 7.4 μM , 8.1 μM of EDTA in HEPES 10 mM (pH:7.4). The molar fraction EDTA/Metal= 1.2. Extraction of ● Aluminium (III) **C:** by xerogel chitosan pellet. **D:** by mg of xerogel pellet. These experiments were performed after 90 hours in 20 ml of an aluminium(III) solution with a concentration of 7.4 μM , 8.1 μM of EDTA and 35 mM Na_2SO_4 in HEPES 10 mM (pH:7.4). The molar fraction EDTA/Metal is close to 1.2.

3.2.3. Iron(III) extraction in presence of Na_2SO_4 , Iron solubilization with Deferiprone

In the article "*Chitosan-Based Hydrogel for Iron (III) Chelation in Biological Conditions*", it was observed that when the hydrogels were placed in a solution containing deferiprone and iron (III), the non-functionalized formulations were able to extract iron (III) from the solution. To quantify indirect chelation by electrostatic interactions between the metal complex Fe-deferiprone and chitosan, the following experiment adding Na_2SO_4 was done.

Materials and methods 15% DA_6 pellets were submerged in 20 mL/per pellet of a solution containing iron(III) (3.6 μM) deferiprone (14.3 μM) at a metal-to-deferiprone ratio of 1:4 in a 10 mM phosphate buffer solution (Na_2HPO_4 7.5 mM, KH_2PO_4 2.5 mM, pH 7.4) with 35 mM Na_2SO_4 added (corresponding to five SO_4^{2-} ions per amine group of chitosan). A control solution with the same composition, but without Na_2SO_4 , was also prepared, and pellets were submerged in 20 mL of this control solution. Both the experimental and control samples were stirred at room temperature for 90 hours. Supernatant samples were then collected, diluted in 1% (w/w) HNO_3 , and analysed by ICP-MS in KED mode.

Results and discussion Unlike with EDTA or citrate complexes, the addition of Na_2SO_4 to the deferiprone, iron(III) solution did not significantly decrease the iron (III) extraction efficiency of the non-functionalized chitosan hydrogels (Figure 37). This is because, unlike the studied EDTA or citrate metal complexes, the deferiprone₃-iron(III) complex is neutral at the experimental pH, making electrostatic interactions between the complex and chitosan less likely. These results further support the hypothesis presented in the paper that the iron extracted by the non-functionalized chitosan hydrogels is due to direct chelation through the formation of a deferiprone-iron chitosan complex and not an indirect chelation by electrostatic interactions, as discussed in the section "3.3.1. Single metal ion chelation" of the article "Chitosan-based hydrogel for iron(III) chelation in biological conditions"

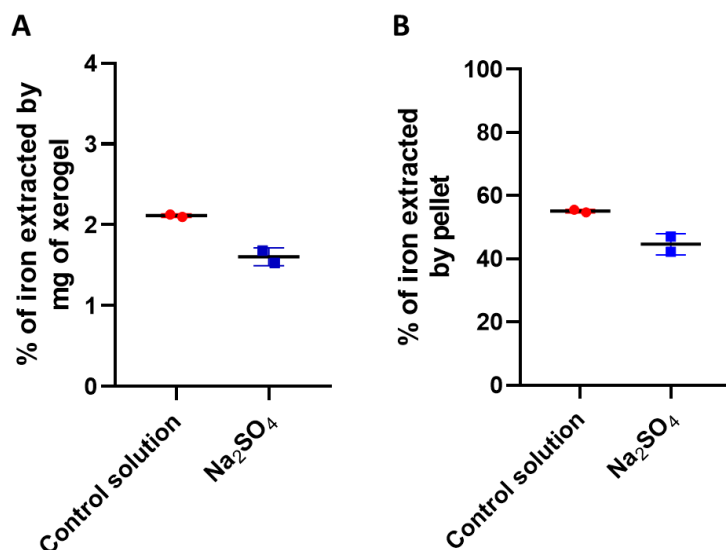


Figure 37. Iron(III) extraction of chitosan (15% DA₆) xerogels **A:** by xerogel chitosan pellet. **B:** mg of xerogel pellet, after exposure to 20 mL of a metallic solution containing 3.6 μM iron(III), 14.3 μM of deferiprone (with a deferiprone : metal ratio of 4:1) in a 10 mM phosphate buffer solution (pH:7.4) ■ with 35 mM Na₂SO₄ and control ● without Na₂SO₄ for 90 hours.

3.3. Effect of grafted chelator on hydrogel properties (publication)

By modifying the chitosan structure through methods such as increasing the DA or grafting chelators like DOTAGA or NCS-Bz-DFO, the resulting polymer's properties, including solubility, hydrophilicity, and crystallinity, are also altered. The impact of these modifications on hydrogel formation and physico-chemical properties is evaluated in the following article “Development of chitosan-based hydrogels with tailored hydrophilicity and swelling characteristics” ready for submission to the journal *Carbohydrate Polymers*. Supplementary information can be found in the annexes.

Development of chitosan-based hydrogels with tailored hydrophilicity and swelling characteristics

Juan Felipe Salazar Ariza,^{1,2} François Lux,^{1,3} Olivier Tillement,¹ Alexandra Montembault,² Fabrice Gouanvé², Laurent David*²

¹ Université Claude Bernard Lyon 1, CNRS, Institut Lumière-Matière (ILM), UMR 5306, 2 rue Victor Grignard, F-69622 Villeurbanne Cedex, France.

² Université Claude Bernard Lyon 1, INSA de Lyon, Université Jean Monnet, CNRS, Ingénierie des Matériaux Polymères (IMP), UMR 5223, 15 bd Latarjet, F-69622 Villeurbanne, France.

³ Institut Universitaire de France (IUF), 75231 Paris, France.

* Correspondence and requests for materials should be addressed to Pr Laurent David (email: laurent.david@univ-lyon1.fr)

Abstract

1. Introduction

Gels are defined by Almdal *et al.* (Almdal *et al.*, 1993) as soft, solid-like materials composed of a liquid present in substantial quantities; the gel can maintain its form under its own weight. Thus, **hydrogels** are a specific type of gels composed of a three-dimensional crosslinked network of polymers with a high entrapped water content (Feng & Wang, 2023; Peers *et al.*, 2020; Pita-López *et al.*, 2021). Due to their high water content, hydrogels possess a physical similarity to natural living tissues, which contributes to their excellent biocompatibility (Feng & Wang, 2023; Li & Mooney, 2016). This biocompatibility has led to the recent development of hydrogels for various biomedical applications, including tissue engineering (Jin & Dijkstra, 2010; Tamo *et al.*, 2022), and drug delivery (Gréa *et al.*, 2024; Peers *et al.*, 2020).

Two main crosslinking methods are used to obtain hydrogels: chemical and physical crosslinking (Peers *et al.*, 2020). Chemical hydrogels are formed by creating covalent bonds between polymer chains, resulting in a 3D network (Jin & Dijkstra, 2010). These covalent bonds can be formed through chemical reactions between functional groups on the polymer chains and added crosslinking agents via mechanisms like Schiff base formation (Budianto *et al.*, 2015; Jin & Dijkstra, 2010), Michael type addition (Jin & Dijkstra, 2010; Metters & Hubbell, 2005), peptide ligation (Jin & Dijkstra, 2010; Jung *et al.*, 2008), click chemistry (Jin & Dijkstra, 2010; Uliniuc *et al.*, 2012) etc. However, some of these crosslinking agents can be cytotoxic, limiting the biomedical applications of these hydrogels (Feng & Wang, 2023; Jin & Dijkstra, 2010; Peers *et al.*, 2020). In contrast, physical hydrogels are formed through weaker interactions like van der Waals forces, hydrophobic interactions, electrostatic interactions or hydrogen bonding (Peers *et al.*, 2020). While these gels often exhibit softer mechanical properties compared to chemically crosslinked hydrogels, physical crosslinking can also lead to faster degradation rates (Peers *et al.*, 2020). One of the interesting properties of hydrogels is their ability to swell. This refers to the capacity of the hydrogel network to weaken, enabling chain extension and absorption of more water within the polymer structure [13]. This swelling behaviour makes hydrogels particularly interesting for drug delivery applications. (Omidian & Park, 2010). Hydrogel swelling is often quantified by the weight-swelling ratio (SR) defined by the following equation where, W_h is the mass of the rehydrated hydrogel and W_d is the dry weight of the hydrogel (Omidian & Park, 2010).

$$SR = \frac{W_h - W_d}{W_d} \times 100 \quad (1) \quad (\text{Omidian \& Park, 2010})$$

As swelling is determined by the interplay between pore size, polymer-water interactions, and the hydrophilicity of the polymer backbone (Becerra *et al.*, 2017; Feng & Wang, 2023; Omidian & Park, 2010), functionalisation of the hydrogel with hydrophilic functional groups such as -OH-, -CONH-, -CONH₂-, and -SO₃H can significantly enhance its swelling capacity. On the other hand, hydrophobic groups and hydrophobic interactions will hinder swelling (Becerra *et al.*, 2017; Feng & Wang, 2023; Laftah *et al.*, 2011; Omidian & Park, 2010). Hydrogels can also

be categorized based on their SR (Feng & Wang, 2023). Shrinkable hydrogels (SH) exhibit an SR below 0%. They find applications in drug delivery and tissue engineering due to their ability to collapse and release loaded substances (Feng & Wang, 2023). Low-swelling hydrogel (LSH) have an SR between 0% and 150%. Their primary applications lie in tissue engineering and bioelectronics due to their mechanical properties (Feng & Wang, 2023). The High-swelling hydrogels (HSH) possess an SR exceeding 150%. They are also valuable for drug delivery and tissue engineering due to their high-water uptake capacity (Feng & Wang, 2023).

Several biopolymers, including polysaccharides like carrageenan, alginate, chitosan, and hyaluronic acid, are commonly used as building blocks for hydrogels (Feng & Wang, 2023; Jin & Dijkstra, 2010; Pita-López et al., 2021). In this work, we focus on chitosan and chitosan derivatives. Chitosans, a family of copolymers derived from chitin through alkaline deacetylation, offers attractive properties for biomedical applications (Mogoşanu & Grumezescu, 2014). Soluble in acidic aqueous media, chitosan possesses excellent biocompatibility and biodegradability (Kean & Thanou, 2010; Rami et al., 2014). Its macromolecular structure resembles glycosaminoglycans found in the extracellular matrix, further enhancing its suitability for tissue engineering (Rami et al., 2014). Additionally, chitosan exhibits antifungal and antibacterial properties, particularly at low degrees of acetylation (DA), making it an ideal candidate for scaffold materials (Kantak & Bharate, 2022; Matica et al., 2019). Notably, the presence of $-NH_2$ functional groups allows for further chemical modification to tailor chitosan's properties for specific applications (Cohen & Poverenov, 2022; Wang et al., 2020). At pH levels below 6.5, the polycationic nature of chitosan facilitates the solubility of chitosan in aqueous solutions, whereas inter-chain hydrophobic interactions may result in a gel upon neutralization if the concentration of the solution and resulting chain entanglements are sufficient to avoid precipitation. This self-assembly process leads to the creation of a physical hydrogels without the need for additional crosslinking agents (Montembault et al., 2005b).

The literature reports various techniques to improve the swelling behaviour of chitosan hydrogels. These techniques include blending chitosan with more hydrophilic polymers and chemical functionalization through phosphorylation, amino acid conjugation, quaternary ammonium formation, and carboxymethylation (Cohen & Poverenov, 2022; de Oliveira Pedro et al., 2016; Jayakumar et al., 2008; Shariatinia, 2018; Tsai et al., 2007). Our research group has previously demonstrated successful grafting of the hydrophilic moiety DOTAGA (up to 17% of substitution degree) onto both low- and high-DA chitosan (up to 30% DA) (Grange et al., 2023; Gréa et al., 2024; Natuzzi et al., 2021). Modifying the DA and the type of grafted moieties on chitosan will significantly influence the hydrophilicity of the resulting hydrogel, thereby impacting its swelling behaviour. Here, the degree of substitution (DS) achieved during grafting will play a crucial role in modulating the balance between hydrophilic and hydrophobic interactions.

This study investigates the impact of different strategies to modulate the hydrophilicity and swelling of chitosan and chitosan-based hydrogels. We will explore the effects of varying DOTAGA degree of substitution, degree of acetylation, also introducing grafting with a more hydrophobic chelant, Bz-DFO.

2. Material and methods

2.1. Polymer synthesis

2.1.1. Chemicals for polymer synthesis

Chitosan Chitoceutical® grade with low degree of acetylation DA ($6\% \pm 0.5\%$, determined by ^1H NMR spectroscopy using the Hirai method (Hirai et al., 1991) from snow crab was purchased from Heppe Medical Chitosan GmbH (reference: 212-160123-01). This chitosan was fully characterized. The weight-average and number-average molar masses (respectively $M_w = 160$ kg/mol and $M_n = 130$ kg/mol) were determined by size exclusion chromatography coupled with refractive index and multi-angle laser light scattering measurements (Montembault et al., 2005a). DOTAGA anhydride and p-NCS-Bz-DFO (N1-hydroxy-N1-(5-(4-(hydroxy(5-(3-(4-isothiocyanatophenyl) thioureido) pentyl) amino)-4-oxobutanamido) pentyl)-N4-(5-(N-hydroxyacetamido) pentyl) succinamide) were furnished by Chematech (Dijon, France). 1,2-propanediol, DMSO and acetic anhydride were purchased from Sigma-Aldrich (Saint-Quentin-Fallavier, France). Glacial acetic acid (AnalR NormaPur) grade was furnished by VWR (France).

2.1.2. DA₆@DOTAGA₁₁

DOTAGA was grafted onto low DA chitosan (DA₆) using DOTAGA anhydride in a mixture of water and 1,2-propanediol (Gréa et al., 2024). Briefly, DA₆ (1.5% w/w) was dissolved in a 1.3% (v/v) acetic acid solution. After complete dissolution, 1,2-propanediol was added to reach a final chitosan concentration of 0.75% (w/w). The solution was stirred for 2 hours at room temperature. Subsequently, DOTAGA anhydride was added to achieve a final concentration of 1.5% (w/w) in DOTAGA and the reaction mixture was stirred overnight. Following the reaction between anhydride groups and amines to form amide bonds, the final product was purified by tangential filtration using a 100 kDa cutoff membrane. Purification involved sequential washings with 0.1 M acetic acid and ultrapure water. Finally, the purified product was freeze-dried.

2.1.3. DA₆@DOTAGA₁₇

The synthesis of DA₆@DOTAGA₁₇ employs the same protocol as DA₆@DOTAGA₁₁, the only difference being a doubled concentration of DOTAGA anhydride added during the reaction. Thus, the final reaction mixture consists of 0.75% (w/w) chitosan, 3% (w/w) DOTAGA anhydride, and a 1:1 (v/v) mixture of water and 1,2-propanediol. The final product was purified by tangential filtration using a 100 kDa cutoff membrane. Purification involved sequential

washes with 0.1 M acetic acid and ultrapure water. Finally, the purified product was freeze-dried.

2.1.4. DA₂₉

The N-acetylation of chitosan was obtained in a water/1,2-propanediol mixture with acetic anhydride as the reagent (Vachoud et al., 1997). Briefly, chitosan solution was prepared at a concentration of 1.5% (w/w): the polymer was dissolved in deionized water containing 1% of acetic acid, the mixture was stirred 12 h until complete solubilization of chitosan. Afterwards, 1,2-propanediol was added to obtain a final polymer concentration of 1.25% (w/w), and the solution was stirred at room temperature for 1 h. Then, acetic anhydride diluted in 1,2-propanediol at 2.4% (v/v) (0.24 M) was added dropwise to this hydroalcoholic chitosan solution under strong stirring, the final polymer concentration was then 1% (w/w) with a ratio 1,2-propanediol /water 30%(v/v). The amount of added acetic anhydride corresponded to a molar ratio $n_{\text{Acetic Anhydride}}/n_{\text{Amine groups}}$ of 1.6 . The mixture was stirred for 4 h and 5 ml were collected and purified by tangential filtration against water for DA determination. The final product was purified by tangential filtration using a 100 kDa cutoff membrane. Purification involved sequential washes with 0.1 M acetic acid and ultrapure water. Finally, the purified product was freeze-dried. The DA of this reacetylated chitosan (DA₂₉) was determined by ¹H NMR, close to 29% (Hirai et al., 1991).

2.1.5. DA₂₉@DOTAGA₉

DA₂₉@DOTAGA₉ was synthesised in two steps: the first one is the reacetylation of low DA (DA₆) chitosan as described above. DOTAGA is then grafted onto reacetylated chitosan (DA₂₉) following a protocol previously developed (Natuzzi et al., 2021). Briefly, after reacetylation, 1,2-propanediol is added in order to obtain a volume ratio of 1,2-propanediol /water of 50% (v/v) and a polymer concentration of 0.7% (w/w). DOTAGA anhydride was added to achieve a final concentration of 6% (w/w) in DOTAGA and the reaction mixture was stirred during 12h. The final product was purified by tangential filtration using a 100 kDa cutoff membrane. Purification involved sequential washings with 0.1 M acetic acid and ultrapure water. Finally, the purified product was freeze-dried.

2.1.6. DA₂₉@DOTAGA₉@DFO₅

The synthesis of DA₂₉@DOTAGA₉@DFO₅ Bz-DFO was achieved in three steps. The first step involves the reacetylation of chitosan using the same protocol as described above. The second step consisted in grafting DOTAGA onto DA₂₉ according to the previously established protocol. Finally, Bz-DFO was grafted onto DA₂₉@DOTAGA₉ following the protocol developed by Grange *et al.* (Grange et al., 2023). Briefly, DA₂₉@DOTAGA₉ is dissolved in ultrapure water at a concentration of 1% (w/w). The pH is adjusted to 6 ± 0.5 using a 1 M NaOH solution. Ultrapure water is then added to achieve a final polymer concentration of 0.96% (w/w). The mixture is stirred at 30 °C. 1,2-Propanediol is added under stirring to reach a final composition of 37% (v/v) 1,2-propanediol and a polymer concentration of 0.61% (w/w). A 1% (w/w) solution of p-NCS-Bz-DFO in DMSO is prepared. DMSO is then added to the mixture to reach

a composition of 10% (v/v) DMSO and a polymer concentration of 0.54% (w/w). The mixture is stirred at 30 °C for 1 hour. The p-NCS-Bz-DFO solution is slowly added to the reactor using a peristaltic pump at a flow rate of 400 $\mu\text{L min}^{-1}$. The reaction is maintained at 30 °C with stirring during 12h. The final reaction mixture has a polymer concentration of 0.49% (w/w) in a solvent mixture of 30% (v/v) 1,2-propanediol and 18% (v/v) DMSO. The resulting mixture was purified by sequential washings with 0.1 M acetic acid and ultrapure water. Finally, the purified product was freeze-dried.

2.2. Polymer characterization

2.2.1. Characterization of DOTAGA and DFO grafting by UV-Vis titration

The amount of grafted DOTAGA was determined by titration with Cu(II) following a method described in previous works (Natuzzi et al., 2021). Briefly, all polymers were first dispersed in water at a concentration of 0.5 % w/w. An acetate buffer solution pH 4.5 (0.1 M ammonium acetate / 0.1 M acetic acid) was added to the previous solutions to achieve a final polymer concentration of 0.075% (w/w) for DA₆@DOTAGA₁₁; 0.05% (w/w) for DA₆@DOTAGA₁₇ and 0.1% (w/w) for DA₂₉@DOTAGA₉. Cu(II) was then added to these solutions at varying concentrations from 0 to 0.5 mM and the use of UV-Vis spectroscopy.

The amount of grafted DFO was determined by titration with Fe(III) following the same method shown by Grange *et al.* (Grange et al., 2023). Briefly DA₂₉@DOTAGA₉@DFO₅ is first dispersed in water at a concentration of 0.5 % w/w. An acetate buffer solution pH 4.5 was added to the previous solutions to achieve a final polymer concentration of 0.1% (w/w) Fe(III) was added to obtain varying concentrations of Fe(III) from 0 to 0.9 mM.

The copper source was a standard solution of Cu(II) in 5% HNO₃ (ICP Standard 50080 $\mu\text{g mL}^{-1}$, SCP Science, ref: 140-041-295), and the iron source was a standard solution of Fe(III) in 5% HNO₃ (ICP Standard 50090 $\mu\text{g mL}^{-1}$, SCP Science, ref: 140-041-265).

Absorption measurements were performed using a Cary 50 Scan UV-visible spectrophotometer with quartz cuvettes having a 10 mm optical path length. The absorbance at 295 nm was plotted against the total copper content per g of polymer. The copper chelation capacity of each polymer was then determined by linear fitting the low and high copper concentration regions of the plot. The chelation capacity is defined as the copper concentration corresponding to the observed change in slope, expressed in mmol of copper per gram of polymer (Fig. 1A-C). The absorbance of the DA₂₉@DOTAGA₉@DFO₅ solutions at 430 nm was plotted against the total iron content per gram of polymer (Fig. 1D). Because DFO has a higher affinity for iron(III) ($\log\beta_{\text{DFO-Fe(III)}}:41.8$ (Toporivska & Gumienna-Kontecka, 2019)) than DOTA ($\log\beta_{\text{DOTA-Fe(III)}}:29.4$ (Clarke & Martell, 1991)), the first inflection point in the curve likely corresponds to the complete complexation of iron with the grafted DFO.

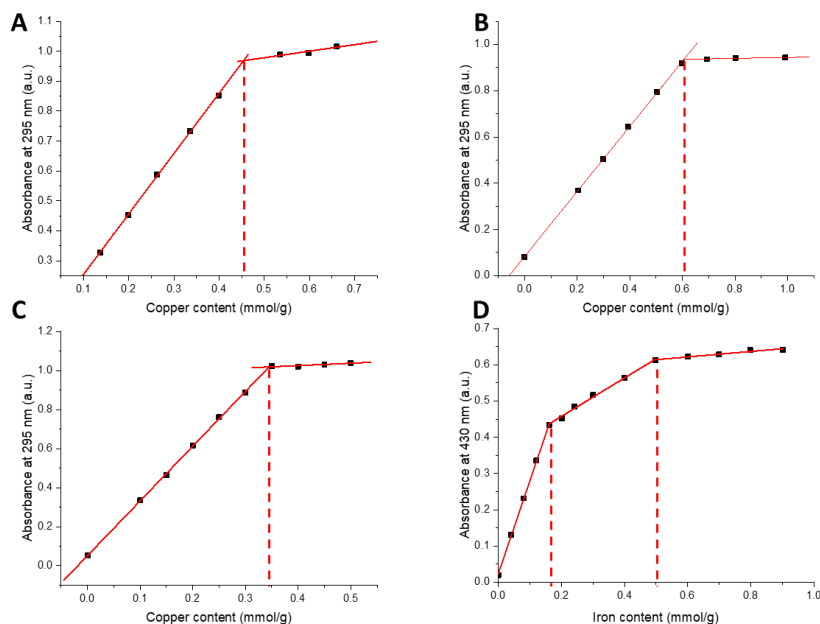


Figure 1: Dosage of all polymers by Cu (II) (A to C) and by Fe (III) (D) (in acetate buffer 0.1 M pH 4.5, red lines correspond to linear regressions. The dotted line represents the crossover concentration corresponding to the saturation of the chelator with copper (II). **A:** Absorbance at 295 nm plotted against mmol of copper (II) per g of DA₆@DOTAGA₁₁ yielding 0.45 mmol of DOTAGA per g of polymer. **B:** Absorbance at 295 nm plotted against mmol of copper (II) per g of DA₆@DOTAGA₁₇ yielding 0.61 mmol of DOTAGA per g of polymer **C:** Absorbance at 295 nm plotted against mmol of copper (II) per g of DA₂₉@DOTAGA₉ yielding 0.35 mmol of DOTAGA per g of polymer. **D** Absorbance at Absorbance at 430 nm plotted against mmol of iron (III) per g of DA₂₉@DOTAGA₉@DFO₅ yielding 0.33 mmol of DOTAGA per g of polymer and 0.16 mmol of DFO per g of polymer.

Knowing the DA of low DA and reacylated chitosans from ¹H NMR, together with the C_{DOTAGA} from the copper chelation capacity of each polymer, we can determine the DOTAGA DS (y) in DA@DOTAGA derivatives using the following equation:

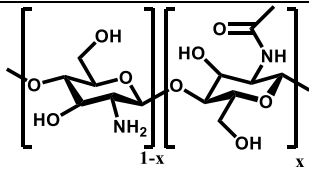
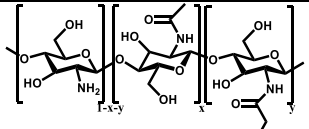
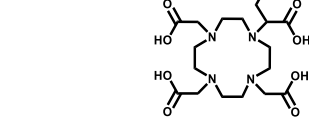
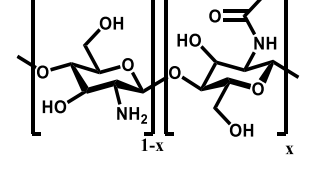
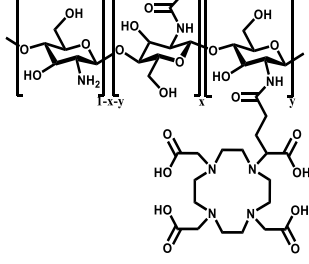
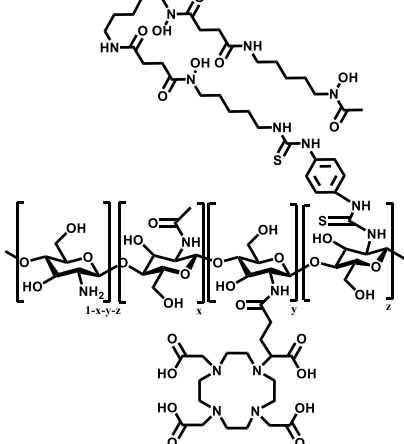
$$y = \frac{C_{\text{DOTAGA}} \cdot (x \cdot (M_x - M_{\text{gluc}}) + M_{\text{gluc}})}{(1 - wc) - C_{\text{DOTAGA}} \cdot (M_y - M_{\text{gluc}})} \quad (2)$$

For DA₂₉@DOTAGA₉@DFO₅, y was determined from the Cu(II) dosage yielding C_{DOTAGA} = 0.37 mmol of DOTAGA per g of polymer (See Fig.S2) Detailed information regarding the calculation to determine y and z from copper and iron UV/Vis dosage can be found in SI section 1.2).

From the first change of slope in (Fig.1 D) we can determine the DFO DS (z) using the following equation:

$$z = \frac{C_{\text{DFO}} \cdot (x \cdot (M_x - M_{\text{gluc}}) + y \cdot (M_y - M_{\text{gluc}}) + M_{\text{gluc}})}{(1 - wc) - C_{\text{DFO}} \cdot (M_z - M_{\text{gluc}})} \quad (3)$$

Table 1: Calculated values of DA, DOTAGA-DS and DFO-DS of the studied polymers.

Analysed polymer	Structure	DA* (±1%)	DOTAGA DS (y) [‡] (±0.5%)	DFO DS (z) [‡] (±0.5%)
DA₆		6	/	/
DA₆@DOTAGA₁₁		6	11.3	
DA₆@DOTAGA₁₇		6	17.3	
DA₂₉		29	/	
DA₂₉@DOTAGA₉		29*	8.6	
DA₂₉@DOTAGA₉@DF O₅		29*	9.3	

*DA determined by $^1\text{H-NMR}$ analysis of non-grafted chitosans, $^{\text{t}}$ DS determined from dosage with Cu(II) or iron(III) with UV-Vis spectroscopy.

2.2.2. Characterization of polymer lyophilizates hydrophilicity by dynamic vapour sorption (DVS)

Polymers were solubilized at 1% (w/w) in 0.01 M HCl, followed by tangential filtration with 0.01 M HCl solution and then with water to remove residual acetic acid. The resulting solutions, with $\text{pH} \approx 5$, were freeze-dried. The resulting lyophilizates were used for dynamic vapor sorption experiments. In such experiments, the studied chitosan lyophilizates were not neutralized.

A Dynamic Vapor Sorption Analyzer (DVS Advantage, Surface Measurement Systems Ltd., London, UK) was used to determine the water sorption isotherms of the polymer lyophilizates. The DVS system employs an ultra-sensitive recording microbalance capable of measuring minute changes in sample mass. This microbalance's exceptional long-term stability makes it ideal for studying vapor sorption phenomena, which can range from minutes to days to reach equilibrium. Vapor partial pressure (p) was controlled by precisely mixing dry and saturated nitrogen using electronic mass flow controllers. Experiments were conducted at 25°C with water vapor activities (a_w) ranging from 0.05 to 0.95. Initial sample weights were between 15 to 50 mg. The samples were pre-dried in the DVS Advantage by exposure to dry nitrogen until constant weight was achieved (m_0). A target water vapor partial pressure was established within the apparatus, and water uptake was monitored as a function of time. Equilibrium mass (m_{eq}) was considered reached when changes in mass with time (dm/dt) were consistently below $4 \times 10^{-4} \text{ mg min}^{-1}$ for 5 consecutive minutes. After reaching equilibrium at one water activity, the partial pressure was automatically increased to the next target value, and the process was repeated using the same dm/dt criterion for determining equilibrium. The equilibrium mass gain (M) defined as $(m_t - m_0)/m_0$ for each water activity (a_w) was used to plot the water sorption isotherm for each sample.

2.3. Hydrogel formation

The gels were prepared by following the method by (Montembault et al., 2005b) with slight modifications. First $\text{DA}_6@ \text{DOTAGA}_{17}$, $\text{DA}_{29}@ \text{DOTAGA}_9$, $\text{DA}_{29}@ \text{DOTAGA}_9@ \text{DFO}_5$ could not be used directly to prepare hydrogels since at a concentration 6.7% w/w neutralization of polymer solution yielded precipitates or total solubilisation of the polymer. Thus, in order to obtain hydrogels, we prepared mixed solutions of DA_6 with grafted ('modified') chitosan. Briefly, lyophilizates of DA_6 and modified chitosan were dispersed in ultrapure water following the proportions shown in Table 2 to obtain a total polymer concentration of 10% w/w. Acetic acid was added to achieve the stoichiometric protonation of the amine groups allowing solubilisation of the polymers. The blend was mechanically stirred until having a homogeneous mixture. The chitosan mixtures were cast into moulds and then immersed in a 3 M NaOH aqueous solution. This immersion process induces the regeneration of free amine groups on the

chitosan, triggering crystallization, interchain hydrophobic interactions and thus physical gelation entrapping chain entanglements (Ladet et al., 2008). In fact, DA₆ plays the role of gelling polymer by allowing interaction between the polymeric chains of both types of chitosan present in solution, which was difficult to achieve by only using the functionalized chitosans. The hydrogels were then washed with ultra-pure water to eliminate NaOH and acetate salts and then with a phosphate buffer solution 10 mM (Na₂HPO₄ 7.5 mM, KH₂PO₄ 2.5 mM, pH 7.4), to impose a neutral pH to the hydrogels. Using such phosphate buffers, phosphate moieties tend to interact with the amine groups chitosan hydrogel (Leduc et al., 2014). In fact anions like phosphates can also be used as electrostatic crosslinking agents (Pierog et al., 2009; Xu et al., 2017). Therefore, in the hydrogels studied in this paper, chitosan might interact with the anions found in the washing solution. After washing of the hydrogels, they were dried in a humidity chamber (Memmert HCP50) at a constant temperature of 30°C. The drying cycle proceeded as follows: 2 hours at 30°C and 65% humidity, followed by a gradual decrease in humidity from 65% to 35% over 10 hours. Subsequently, the xerogels were maintained at 35% humidity for 1 hour before storage.

Six precursor solutions were prepared following the described procedure, each with a total polymer concentration of 10% w/w (Table. 2). The first solution served as the control formulation and consisted solely of DA₆. The remaining five solutions incorporated DA₆ at concentrations of 3.33% w/w and the functionalized polymers at a concentration of 6.67% w/w. Two formulations utilized low-DA chitosan with varying DOTAGA grafting ratios (Gel 2/3 DA₆@DOTAGA₁₁ and Gel 2/3 DA₆@DOTAGA₁₇, respectively in table 2). Three formulations were prepared with high-DA chitosan (29%): one without DOTAGA (Gel 2/3 DA₂₉), one with a DOTAGA grafting ratio of 0.09 (Gel 2/3 DA₂₉@DOTAGA₉), and the last one containing both DOTAGA (grafting ratio 0.1) and the hydrophobic chelant Bz-DFO (Gel 2/3 DA₂₉@DOTAGA₁₀@DFO₅).

Table 2: Description of hydrogel formulations and nomenclature.

Formulation of mother solution	Functionalised polymer used	Hydrogel sample nomenclature	Symbol representing each formulation
10 % DA ₆	/	Gel DA ₆	●
3.33% DA ₆ / 6.67% DA ₆ @DOTAGA ₁₁	DA ₆ @DOTAGA ₁₁	Gel 2/3 DA ₆ @DOTAGA ₁₁	▲
3.33% DA ₆ / 6.67% DA ₆ @DOTAGA ₁₇	DA ₆ @DOTAGA ₁₇	Gel 2/3 DA ₆ @DOTAGA ₁₇	▼
3.33% DA ₆ / 6.67% DA ₂₉	/	Gel 2/3 DA ₂₉	⬢
3.33% DA ₆ / 6.67% DA ₂₉ @DOTAGA ₉	DA ₂₉ @DOTAGA ₉	Gel 2/3 DA ₂₉ @DOTAGA ₉	■

3.33% DA ₆ / 6.67% DA ₂₉ @DOTAGA ₉ @DFO ₅	DA ₂₉ @DOTAGA ₉ @DFO ₅	Gel 2/3 DA ₂₉ @DOTAGA ₉ @ DFO ₅	◆
--	--	--	---

2.4. Material characterization

2.4.1. Viscoelastic properties of hydrogels

Dynamic rheological measurements were carried out on hydrogels using an ARES rheometer (TA Instruments) and operating with a plate-plate geometry (diameter of 25 mm) at room temperature (25°C). The strain amplitude was chosen to ensure that the measurements were carried out within the linear viscoelastic regime. Angular frequency sweep measurements were carried out in the range from 100 rad.s⁻¹ down to 0.1 rad.s⁻¹ (with an applied strain amplitude of 0.2%). In order to understand the effect swelling and composition on the mechanical properties of the hydrogels, measurements were performed at 2 different steps of the hydrogel formation process: a first measurement was done immediately after gelation in the NaOH 3M solution, the second measurement was performed after immersing the hydrogels in ultrapure water for 18 hours (washing solution pH ≈ 10). The mass variation of the different hydrogels was followed at each step of the process.

2.4.2. X ray diffraction analyses

The xerogels utilized for XRD analysis were prepared in the same manner as previously described (part 2.3 gel formation), with the distinction that their corresponding gels were only washed with ultra-pure water until pH 7 and then air-dried. The xerogel crystallinity were analysed using a Rigaku XtaLAB Synergy-S diffractometer with CuK α (50 kV, 1 mA) at the Henri Longchambon Diffraction Center (Villeurbanne, France). A custom-designed sample holder was used to hold the samples in the beam. The 2 θ scans between 5 and 60° were obtained after radial averaging of scattered images.

2.4.3. Swelling

Dry pellets of xerogel with an initial mass W_i were immersed in ultra-pure water at room temperature (25°C) the pH of the solution after swelling for all samples was 7±0.5. Samples were taken out of the solution at different time points to measure their SR using equation 1 and considering that $W_d = W_i(1 - w_c)$, where w_c is residual or bound water fraction in the different xerogels. w_c for each polymer was measured by thermogravimetric analysis (mass loss between 25°C and 200°C, under nitrogen flow), the result for each polymer can be found in SI Table S1.

2.5. Proof of concept for loading and slow release of molecule of interest

Dry pellets of xerogel of each formulation with a known initial mass W_i were immersed in 10 ml of a solution of rhodamine 6G (Dye content ~95 % CAS 989-38-8, Sigma-Aldrich) at a concentration of 25 mg/L for 2 hours. The supernatant of the loading solution was analyzed by fluorescence, but no significant difference was observed between the fluorescence levels of the supernatants from the different loading solutions. To estimate the theoretical amount of rhodamine 6G absorbed by each formulation, the mass increase of each hydrogel was measured by comparing its initial mass to its mass after 2 hours of loading in the rhodamine 6G solution. Assuming the density of the rhodamine solution is 1 g/mL, the theoretical quantity of rhodamine (Q_{th}) absorbed by each hydrogel can be calculated. This approach assumes no interactions between rhodamine 6G and the hydrogel (For details on the volume of the 25 mg/L rhodamine 6G solution absorbed by each gel formulation during the loading phase, please refer to Table S7).

The hydrated pellets loaded with rhodamine 6G were then dried following the same procedure as described in 2.3. Once dried, the loaded xerogels were immersed in 5 ml of ultra-pure water for 139 hours. The supernatant was collected at different time points and the fluorescence was measured, in order to determine the concentration of rhodamine 6G released by the different rehydrated xerogels.

Fluorescence of was measured using a Cary Eclipse Fluorescence Spectrophotometer using plastic cuvettes with an optical path length of 10 mm. The rhodamine 6G excitation wavelength was 530 nm at the emission wavelength was 550 nm. A calibration curve with known concentrations of rhodamine 6G was prepared and use to compared the fluorescence of the supernatants.

The release kinetics were fitted using pseudo first order kinetic model that describe the dissolution profile of the interest molecule. This kinetic model is commonly used to describe the drug dissolution of water-soluble molecules present in porous matrices (Dash et al., 2010). The pseudo first order kinetic model is described by the following equation:

$$Q_t = Q_e(1 - e^{-k_1 t}) \quad (4)$$

Where Q_t is the mass of released rhodamine 6G (μg) per g of xerogel at time t , Q_e is the mass of rhodamine 6G at equilibrium, and k_1 (h^{-1}) the release rate constant.

3. Results and discussion

3.1. Water sorption

DVS experiments were conducted to assess the impact on the hydrophilicity of the system by increasing the degree of acetylation (DA), grafting hydrophilic (DOTAGA) and hydrophobic (Bz-DFO) moieties. The water sorption isotherm curves of the different samples are shown in Fig. 2. All curves exhibit a sigmoid or S-shape, corresponding to the type II in the BET classification. The concave part of the isotherm at low activity is attributed to the sorption of water molecules on specific hydrophilic sites, while the sharp increase in water sorption at high activity is typically explained by the formation of water clusters. As shown in Fig. 2A, increasing the DA leads to greater water sorption, indicating that a higher DA enhances the hydrophilicity of the system by increasing the number of water absorption sites. This result is

expected when the behaviour of chitosan is dominated by neutralized amines (polar acetyl groups bringing more hydrophilicity than neutralized amines). As a result, in the dry polymer material at low water activity, the acid should not be strongly dissociated, although hydrochloric acid is a strong acid in aqueous solutions. In addition, Fig. 2B shows that grafting DOTAGA onto low DA (DA_6) chitosan results in a slightly increased water absorption. This is due to the hydrophilic nature of DOTAGA carrying four dissociated carboxylic absorption sites. However, there is no significant difference between DOTAGA degrees of substitution (DS) of 11% and 17%. A similar trend is observed with chitosans reacylated to a DA of 29%. At high water activity, the dissociation of the hydrochloric acid could be more important and all systems in 2B and 2C converge to the same behaviour. In these conditions, given the inherent hydrophilicity of the systems with resulting protonated amines, DOTAGA grafting does not appear to significantly increase the number of water sorption sites, and the grafting of Bz-DFO, despite being hydrophobic, does not reduce the number of these sites. More experiments are on going for the study of xerogel powders obtained from washed hydrogels, in order to study the polymers in a controlled neutralized state and eliminate the variation of acid dissociation effects. The impact of salt and specific ion interactions (ex: Na_2SO_4) could also be studied by this technique.

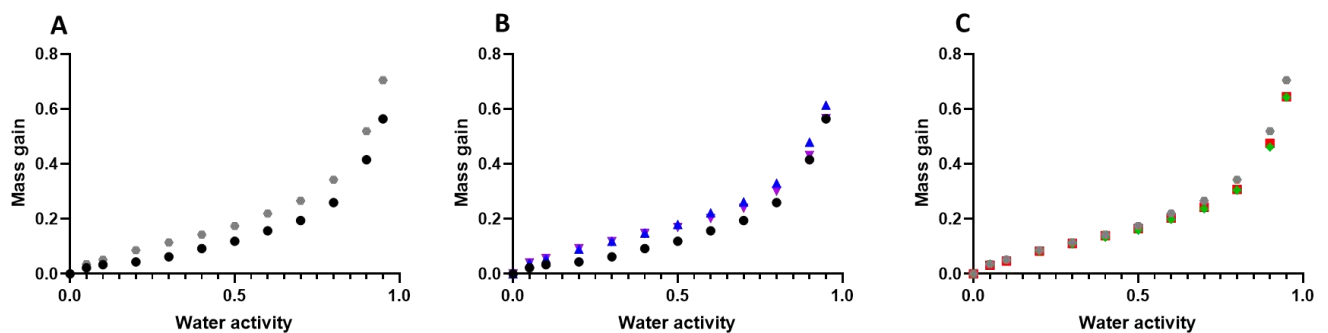


Figure 2. Water vapour isotherms at 25°C of chitosans lyophilizates (A): ● DA_{29} , ● DA_6 , (B): ▲ $DA_6@DOTAGA_{11}$, ▼ $DA_6@DOTAGA_{17}$, ● DA_6 , (C): ● DA_{29} , ■ $DA_{29}@DOTAGA_9$, ◆ $DA_{29}@DOTAGA_9@DFO_5$

3.2. Gel characterization

3.2.1. Rheology

The rheological properties of the hydrogel samples are characterized by both Fig. 3A and Table S3. Notably, all formulations exhibited a constant value of G' across the entire measured frequency range (see Fig. S4 for an example plot of G' and G'' vs. frequency of the hydrogel Gel 2/3 $DA_6@DOTAGA_{17}$ after gelation in a 3M NaOH solution). Furthermore, as shown in Fig. 3A, all formulations displayed G' values in the kPa range after gelation in a 3M NaOH solution and after water washing. Additionally, the G''/G' ratios ranged from 0.04 to 0.26. These combined rheological profiles and low G''/G' ratios confirm the formation of soft gels. (Fuchs et al., 1998).

The measurements performed immediately after gelation in the NaOH solution show no significant differences in G' values between all chitosan hydrogels. This suggests a comparable density of crosslinking points (junctions) in a high ionic force media containing high levels of hydroxide anions. Such hydroxide anions may strongly interact with polysaccharides such as cellulose (Isogai & Atalla, 1998), but chitin (Noishiki et al., 2003) or chitosan (Minh et al., 2017) may also swell in sodium hydroxide solutions. However, after washing, Gel DA₆ and Gel 2/3 DA₂₉ exhibit higher G' values in comparison with the other grafted formulations. This must be attributed to an increase of interactions zones between polymer chains, possibly by nanocrystallite formation. In Gel DA₆ and Gel 2/3 DA₂₉, the absence of a bulky grafted moieties allow for more effective chain crystallization in the gel (Céline et al., 2013), such crystallite acting as crosslinks of high functionality. Following the water bath, hydrogels lacking DOTAGA exhibit shrinkage, with a mass reduction of around -20% for both Gel DA₆ and Gel 2/3 DA₂₉. In contrast, hydrogels containing DOTAGA tended to swell, with Gel 2/3 DA₆@DOTAGA₁₇ evidencing the most significant increase (61% ± 10%, swelling of all gel formulation can be found in Table S4). This variation in mass impacts the rheological properties of the hydrogels. as expected, G' values increase for shrinking hydrogels, while they decrease for swelling hydrogels. To isolate the impact of swelling/shrinkage on G' variations, we normalized G' values by the hydrogel's mass ratio of mass variation between the hydrogel after gelation and after water washing (R_m) using equation (5 and 6).

$$R_m = \frac{M_{water} - M_{NaOH}}{M_{NaOH}} \quad (5)$$

$$G'_{norm} = \frac{G'}{1 - R_m} \quad (6)$$

M_{NaOH} the mass of the hydrogel after gelation in the 3M NaOH bath M_{water} the mass of hydrogel after washing on water. R_m signifies the ratio of mass variation of the hydrogel after the water bath compared to the initial hydrogel

G'_{norm} represents G' without the influence of the expansion of shrinking of the hydrogel network at the measurement time, therefore it is proportional to the number of crosslinks junctions in the hydrogel. G' is the unnormalized storage modulus measured directly on the hydrogel. (refer to table S4 for R_m values).

G'_{norm} gives information of the changes in the network, therefore, it should remain constant after gelation and water washing if no new junctions form or existing ones break. As shown in Fig. 3B, shrinking hydrogels exhibited a significant increase in G'_{norm} . This suggests that shrinkage promotes interactions between polymer chains, potentially leading to the formation of additional crosslinks and a higher junction density. Conversely, the formulations Gel 2/3 DA₆@DOTAGA₁₇, Gel 2/3 DA₂₉@DOTAGA₉, and Gel 2/3 DA₂₉@DOTAGA₉@DFO₅ displayed a decrease in G'_{norm} . Swelling likely separates the polymer chains in these hydrogels, reducing interactions and consequently decreasing the number of junctions in the network. Notably, the only formulation that showed minimal change in G'_{norm} was also the one with the

smallest R_m value. This correlation supports the idea that G'_{norm} normalization helps isolate the impact on junction changes on the rheological behaviour.

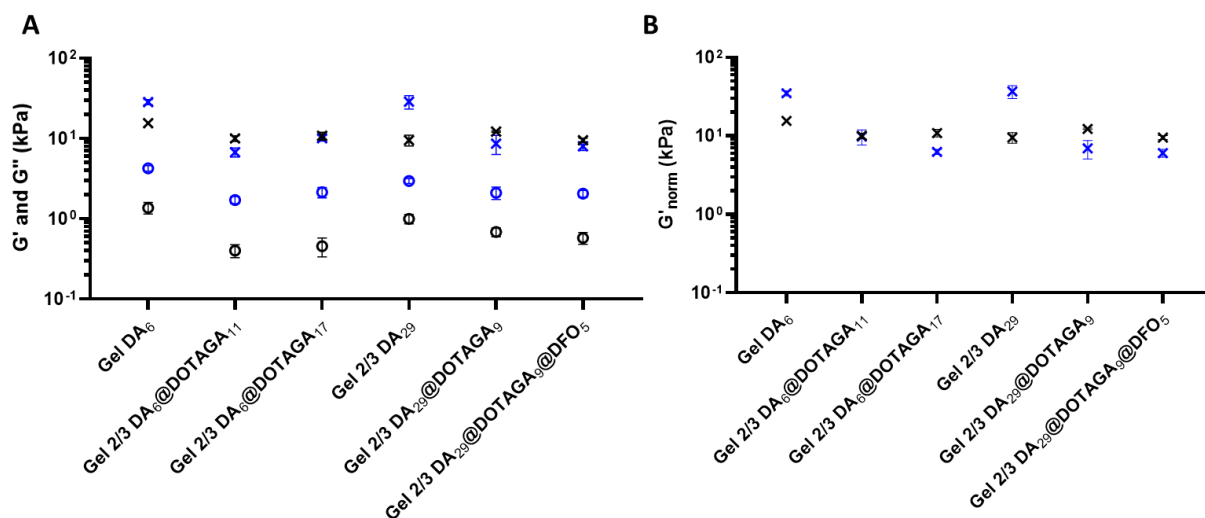


Figure 3. A: (x) G' plateau values measured at a frequency of 0.1 s^{-1} for different hydrogels and (o) G'' values (measured at low frequency) for each hydrogel at each step of the fabrication process. Black symbols for x and o : measurements done after gelation for 2 hours in NaOH 3M. Blue symbols for x and o : measurements done after washing of the hydrogel in water for 18 hours. **B:** G' plateau values (measured at a frequency of 0.1 s^{-1}) for each hydrogel formulation normalized by $(1 - R_m)$.

3.2.2. Crystallinity analysis by Wide angle X-ray Diffraction

The influence of increasing the DA and the grafting ratio of DOTAGA and Bz-DFO on the crystalline structure of the xerogels was investigated by wide-angle X-ray diffraction. Previous studies using synchrotron X-ray scattering have demonstrated a semicrystalline microstructure in (non-grafted) chitosan hydrogels (Céline et al., 2013). Chitosan exhibits two crystalline polymorphs: the hydrated and anhydrous forms. In fig. 4 all formulations displayed a semi-crystalline morphology, with reflections observed at $2\theta = 10.4^\circ$, 20.0° , and 21.9° corresponding to the crystalline reflections of $(020)_h$, $(200)_h$, and $(220)_h$ of the hydrated polymorph, which is consistent with a crystallization process initiated in the hydrogels, in presence of large amounts of water.

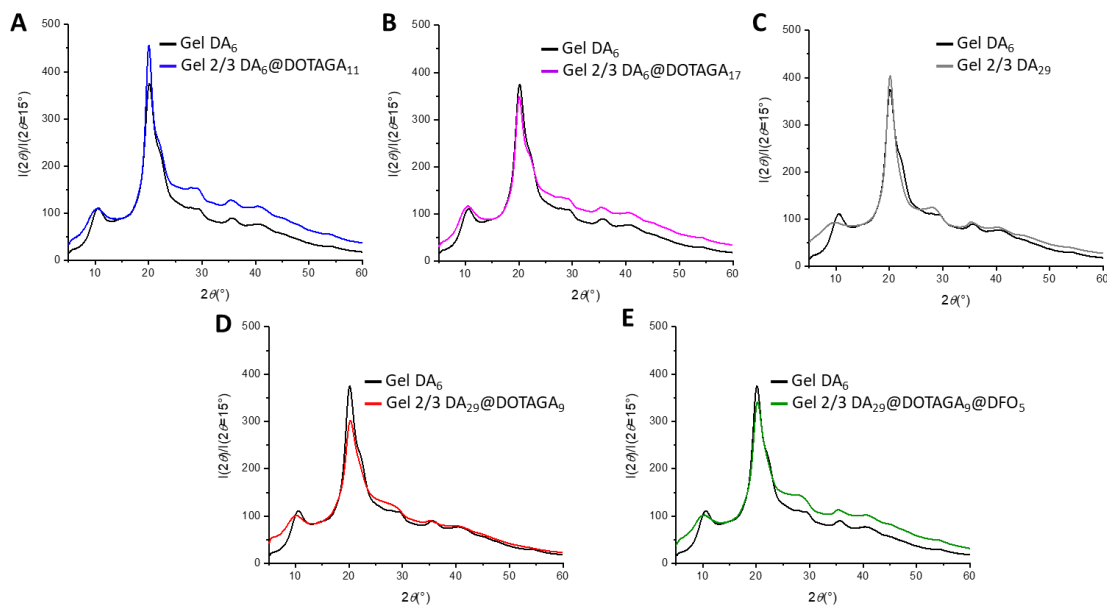


Fig. 4: Diffraction patterns obtained for the xerogels prepared from washed hydrogels. All diffractograms are compared with low DA chitosan xerogel (**—** DA₆). Data are normalized with the intensity value measured at $2\theta = 15^\circ$, representative of the amorphous phase.

The increase of DA and of DOTAGA and Bz-DFO grafting ratios resulted in a gradual broadening of the $(020)_h$ reflection peak near 10.4° . This peak broadening becomes more pronounced in formulations with higher DA and DS (Fig. 3C, D, E). Crystallinity index (CrI%) was determined from these X-ray diffraction patterns using baseline subtraction and integration of the diffractograms between 6° and 34° (Desorme et al., 2013).

$$CrI\% = \frac{Area_{crystal}}{Area_{Total}} \times 100 \quad (7)$$

Where $Area_{Total}$ is the total area of diffraction diagram calculated from $2\theta=6^\circ$ to $2\theta=34^\circ$, $Area_{crystal} = Area_{Total} - Area_{amorphous}$ and $Area_{amorphous}$ is the integrated area of the amorphous scattering pattern, estimated as a cubic spline (Osorio-Madrado et al., 2010) (see (Fig. S5) for more details on the estimation on the amorphous and crystalline contributions). The results of the calculated CrI% for each formulation are shown in Table 3.

Table 3. Crystallinity indexes (CrI%) for each xerogel formulation according to the subtraction of a baseline to the diffractograms. The crystallinity Index is not an exact estimation of the crystallinity ratio, but should vary similarly and help to compare different samples.

Formulation's name	CrI(%) \pm 0.5%
Gel DA ₆	23.3
Gel 2/3 DA ₆ @DOTAGA ₁₁	20.7
Gel 2/3 DA ₆ @DOTAGA ₁₇	18.3

Gel 2/3 DA₂₉	23.4
Gel 2/3 DA₂₉@DOTAGA₉	17.1
Gel 2/3 DA₂₉@DOTAGA₉@DFO₅	16.4

The xerogels prepared from unfunctionalized chitosan (Gel DA₆ and Gel DA₂₉) exhibited the highest crystallinity index (CrI%) values. An increase in the average degree of acetylation (DA) typically promotes chitosan crystallization (Facchinatto et al., 2020). In this study, mixing DA₂₉ with DA₆ did not significantly affect the crystallinity of the xerogels. Interestingly, increasing the DOTAGA grafting ratio in the functionalized polymers resulted in a decrease in CrI%. This trend is observed for both DA₆ and DA₂₉: CrI% (Gel DA₆) > CrI% (Gel 2/3 DA₆@DOTAGA₁₁) > CrI% (Gel 2/3 DA₆@DOTAGA₁₇) and CrI% (Gel DA₂₉) > CrI% (Gel 2/3 DA₂₉@DOTAGA₉) > CrI% (Gel 2/3 DA₂₉@DOTAGA₉@DFO₅). This behaviour was already evidenced for DFO-grafted chitosans (Salazar Ariza et al., 2025) and can likely be attributed to the steric hindrance caused by grafting large molecules like DOTAGA and Bz-DFO, which may disrupt the ordered packing of chitosan chains in the crystalline regions. An interesting deviation from the observed trend is seen when comparing formulations with low-DA and high-DA (0.29) functionalized chitosan. Here, CrI% (Gel 2/3 DA₆@DOTAGA₁₇) is somewhat higher than CrI% (Gel 2/3 DA₂₉@DOTAGA₉), despite the lower grafting ratio in the latter. This suggests that the interplay between DA and DOTAGA grafting ratio on crystallinity might be more complex, possibly in the grafting pattern. In conclusion, all xerogels (and hydrogels) prepared in this work exhibited a significant degree of crystallinity, even at high grafting ratio (DS). This persistent crystallinity, likely initiated by the neutralization process and further promoted by drying, contributes to the stability of the hydrogels and xerogels in aqueous and physiological environments, but also determines swelling (Salazar Ariza et al., 2025).

3.2.3. Swelling of the xerogels

All dried xerogel are capable of swelling at room temperature (25°C) when placed in water (pH 7±0.5), reaching their plateau mass after being immersed for at least 24 hours (Fig. 4A)

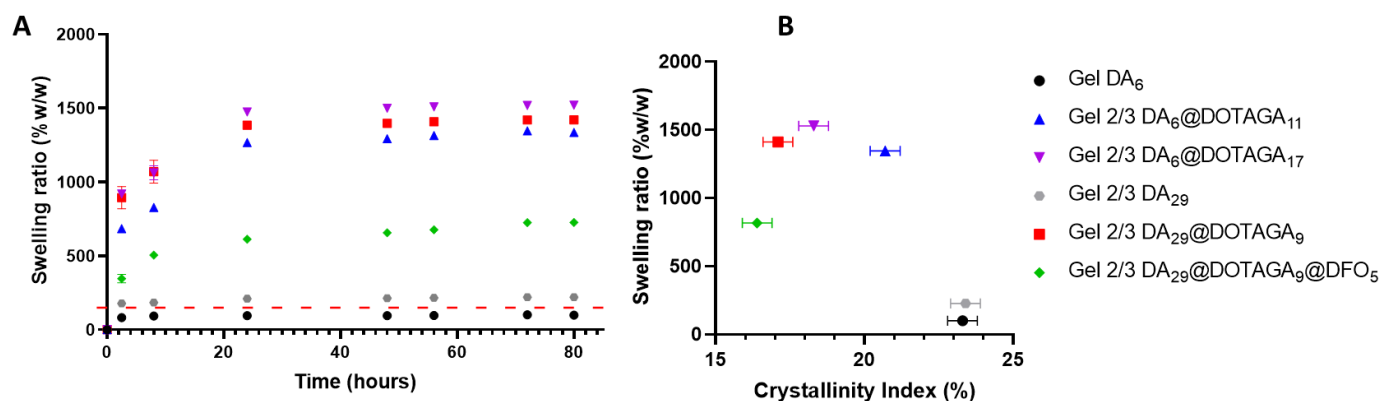


Figure 5: A Swelling in ultrapure water of the different xerogel formulations at 25°C and pH 7±0.5, dotted red line represents the minimal SR to have a high-swelling hydrogel as defined in literature (Feng & Wang, 2023) **B:** Swelling index plotted against crystallinity index.

As previously demonstrated, one approach to increase hydrophilicity (and possible swelling) of neutralized xerogels is raising the degree of acetylation (DA) (Becerra et al., 2017). In this work, increasing the DA from 6% to 29% leads to a higher swelling ratio (SR) (● compare Gel 2/3 DA₂₉ and ● Gel DA₆ in Fig. 5A). Grafting with DOTAGA is another technique to enhance hydrophilicity and decrease crystallinity and consequently, swelling. The hydrogel formulation with the highest DOTAGA content exhibits the highest SR (1528±13%). Although Gel 2/3 DA₆@DOTAGA₁₁ possesses more DOTAGA in comparison with Gel 2/3 DA₂₉@DOTAGA₉, the higher DA (29%) in the latter formulation appears to compensate for the lower DS of DOTAGA, resulting in an SR (Gel 2/3 DA₂₉@DOTAGA₉) > SR (Gel 2/3 DA₆@DOTAGA₁₁). Crystallinity plays a role in swelling, as crystallites can act as crosslinks, hindering swelling (Baskar & Sampath Kumar, 2009). However, even though grafting with a hydrophobic molecule like Bz-DFO further reduces crystallinity, the balance between hydrophobicity and hydrophilicity has a more significant impact on hydrogel swelling, as evidenced by the lack of correlation between CrI% and SR (Fig. 5B). Such behaviour could be due to the formation of DFO-DFO hydrophobic interactions.

Consistent with the observed swelling behaviour (Fig. 5A), only the formulation prepared with low-DA chitosan does not meet the criteria for an HSH due to its SR below 150%. This finding aligns with literature reports, where HSHs based on chitosan are typically either functionalized chitosan or blends of low-DA chitosan with other, more hydrophilic polymers. Additionally, most HSHs are injectable hydrogels that gel *in situ* (Feng & Wang, 2023; Gréa et al., 2024). Notably, this work presents an implantable HSH with superior swelling capacities compared to previously reported chitosan-based HSHs (Feng & Wang, 2023).

It's important to highlight the significant differences in water sorption results between the polymers and the hydrogels, as well as the greater impact of the grafted moiety on hydrogel water uptake when submerged in water compared to water vapor sorption experiments. These differences can be attributed to multiple factors including the neutralization states of the systems and the water uptake mechanisms. Further experiments are necessary to compare the swelling and water sorption behaviours of the same neutralized xerogel systems.

Indeed, the chitosan lyophilizates used in the DVS experiments are not neutralized, which makes them inherently hydrophilic with a variable degree of protonation. This effect could superimpose to the effect of grafting either hydrophilic or hydrophobic moieties on the overall hydrophilicity of the system. Additionally, hydrogels submerged in water absorb significantly more water in the form of bulk water compared to the water amount adsorbed by the lyophilizates during DVS at low water activity (Gámiz-González et al., 2015). A direct comparison was not possible at water activity of 1, since the lyophilizates may dissolve in aqueous solutions due to their acidic reserve.

3.2.4. Proof of concept of slow release

The colour changes of the xerogels from their original state to pink after immersion in the rhodamine 6G solution confirms that all formulations can be loaded with the dye (Fig. 6 B). All formulations exhibited a R^2 value close to 1 for the pseudo-first-order kinetic model (Fig. 6 A and Table 4).

Swelling capacity is a crucial factor for hydrogel applications in drug delivery. In this study, higher Q_{e1} values correspond to formulations with greater SR, as observed in Gel DA₆, Gel 2/3 DA₆@DOTAGA₁₇, and Gel 2/3 DA₆@DOTAGA₁₁, which all exhibit similar Q_{e1} values. In contrast, formulations such as Gel 2/3 DA₂₉@DOTAGA₁₀@DFO₄, and even more notably the formulation without DOTAGA, display lower Q_{e1} values (Fig. 6 A and Table 4).

When analysing the ratio Q_{e1}/Q_{th} , we find that Gel DA₆ is the only formulation with a Q_{e1}/Q_{th} ratio close to 1, indicating nearly complete release of rhodamine 6G. In the other formulations, however, Q_{e1}/Q_{th} is greater than 1, suggesting that only a fraction of the rhodamine 6G is released from the hydrogel (Table 4). This implies that interactions between the hydrogel matrix and rhodamine hinder its release. The lower the Q_{e1}/Q_{th} ratio, the stronger the interactions appear to be. For instance, in non-functionalized hydrogels, Q_{e1}/Q_{th} decreases with increased acetylation, suggesting that rhodamine may interact with acetyl groups, thereby reducing its release despite higher swelling ratios compared to non-acetylated formulations.

Interestingly, Q_{e1}/Q_{th} also decreases as the amount of DOTAGA in the formulation increases. Given that DOTAGA is negatively charged, it likely interacts with the positively charged rhodamine 6G, which may impede its release. Notably, the formulation containing DFO exhibits a higher Q_{e1}/Q_{th} ratio compared to its counterpart without DFO (Gel 2/3 DA₂₉@DOTAGA₉). This can be attributed to DFO introducing steric hindrance, which potentially reduces interactions between DOTAGA and rhodamine 6G, thereby facilitating greater release.

Additionally, the release kinetics are slower in the DOTAGA-functionalized hydrogels, further supporting the hypothesis of interactions between DOTAGA and rhodamine 6G that impede the release process.

Table 4. Parameters for each formulation for the pseudo first-order model and pseudo second-order model. k_1 represents the pseudo-first order rate constant, and Q_{e1} is the theoretical maximum mass of rhodamine released according to the pseudo-first order kinetic model.

Pseudo first order kinetic model					
Formulation's name	R^2	$k_1 \times 10^{-2} \text{ (h}^{-1}\text{)}$	$Q_{e1} \text{ (}\mu\text{g/g)}$	$Q_{th} \text{ (}\mu\text{g/g)}$	Q_{e1}/Q_{th}
Gel DA₆	0.942	18.2 ± 3.9	18.7 ± 0.7	17.4 ± 1.2	1.07

Gel 2/3 DA₆@DOTAGA₁₁	0.979	1.9 ± 0.3	54.0 ± 3.7	249.1 ± 20.8	0.22
Gel 2/3 DA₆@DOTAGA₁₇	0.993	2.5 ± 0.2	59.7 ± 1.8	293.1 ± 6.2	0.20
Gel 2/3 DA₂₉	0.913	33.2 ± 6.2	10.1 ± 0.4	42.9 ± 1.1	0.24
Gel 2/3 DA₂₉@DOTAGA₉	0.984	1.5 ± 0.2	65.1 ± 5.0	236.4 ± 13.9	0.26
Gel 2/3 DA₂₉@DOTAGA₉@DFO₅	0.983	1.5 ± 0.2	36.6 ± 2.9	91.3 ± 2.6	0.40

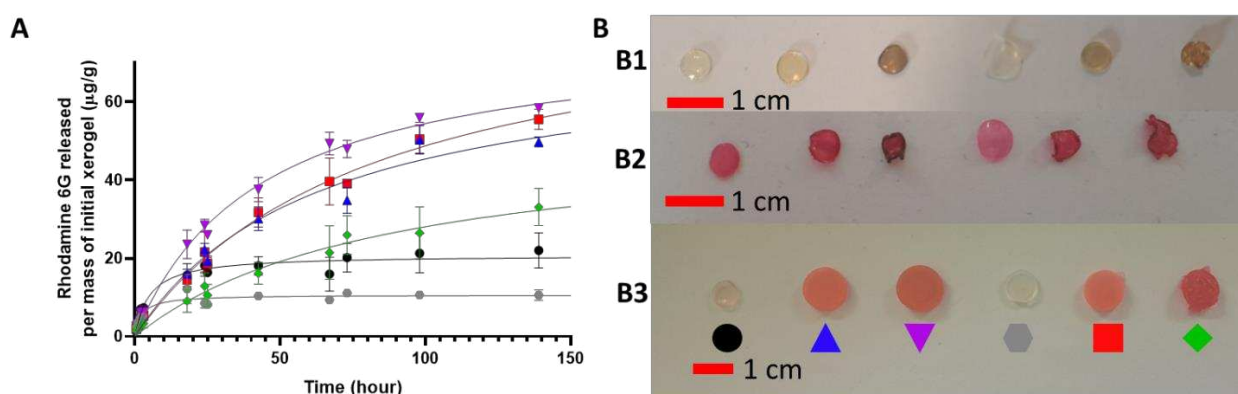


Figure 6: **A** Follow-up of Rhodamine 6G release from different Gel formulations continuous lines represent the pseudo second-order modelling of each formulation. **B1:** Xerogels before loading of rhodamine 6G. **B2:** Xerogels dried after loading in 10 ml of rhodamine 6G solution at 25mg/L for 2 hours. **B3:** hydrogels after the release of rhodamine 6G in 5 ml of ultra-pure water for 139 hours. For the correspondence between symbols and the different systems, please refer to Table 2.

4. Conclusions

In this work, we increased the hydrophilicity of chitosan materials in the neutralized state by increasing its DA from 6% to 29% and by grafting DOTAGA, a chelatant macrocycle. Grafting a hydrophobic chelatant (Bz-DFO) consistently reduced hydrophilicity. Furthermore, gels were obtained by the association of this grafted chitosans with a low DA (ungrafted) chitosan DA₆. We prepared physical hydrogels without the need for crosslinking agents, as confirmed by the rheological studies, with no drastic alterations of the viscoelastic properties after gelation compared to the hydrogel made solely with DA₆. However, the grafting of DOTAGA prevented syneresis of the hydrogels when washed with water compared to the unfunctionalized hydrogels. Moreover, it allowed the corresponding xerogels to swell, which translates into an increase of hydrophilicity and decrease in crosslinks (crystallites) per unit of volume due to the steric hindrance of the grafts.

The xerogels of this work were all able to swell in water. In fact, all gels resulting from grafting of bulky molecules (DOTAGA and Bz-DFO) could be considered High Swelling Hydrogels (HSH), except the one made with only DA₆. The swelling capacity increased with the amount of DOTAGA and DA, however, the presence of Bz-DFO decreased their swelling abilities. This demonstrates that we can tune the swelling of the different hydrogels by playing with these three structural parameters (DA, DOTAGA DS, and Bz-DFO DS). Since swelling is an essential property for drug loading and drug delivery, we showed a proof-of-concept for drug delivery using these HSHs with the rhodamine 6G fluorophore. Hydrogels functionalized with DOTAGA exhibited lower rhodamine 6G release (Q_{e1}) than the theoretical amount (Q_{th}), likely due to electrostatic interactions between the anionic DOTAGA moiety and the cationic rhodamine 6G. The grafting of bulky molecules, such as Bz-DFO, can reduce this interaction through steric hindrance, resulting in a release amount closer to the expected value. Additionally, these interactions between the hydrogel and rhodamine led to a slower release compared to non-functionalized hydrogels.

Despite these interactions, hydrogels with higher swelling capacity still released larger amounts of rhodamine, demonstrating the benefit of high-swelling hydrogels (HSHs) for drug delivery applications.

5. References

- Almdal, K., Dyre, J., Hvidt, S., & Kramer, O. (1993). Towards a phenomenological definition of the term 'gel'. *Polymer Gels and Networks*, 1(1), 5–17. [https://doi.org/10.1016/0966-7822\(93\)90020-I](https://doi.org/10.1016/0966-7822(93)90020-I)
- Baskar, D., & Sampath Kumar, T. S. (2009). Effect of deacetylation time on the preparation, properties and swelling behavior of chitosan films. *Carbohydrate Polymers*, 78(4), 767–772. <https://doi.org/10.1016/j.carbpol.2009.06.013>
- Becerra, J., Sudre, G., Royaud, I., Montserret, R., Verrier, B., Rochas, C., Delair, T., & David, L. (2017). Tuning the Hydrophilic/Hydrophobic Balance to Control the Structure of Chitosan Films and Their Protein Release Behavior. *AAPS PharmSciTech*, 18(4), 1070–1083. <https://doi.org/10.1208/s12249-016-0678-9>
- Budianto, E., Muthoharoh, S., & Nizado, N. M. (2015). Effect of Crosslinking Agents, pH and Temperature on Swelling Behavior of Cross-linked Chitosan Hydrogel. *Asian Journal of Applied Sciences*, 03, 581–588.
- Céline, P.-B., Antoine, V., Denis, B., Laurent, V., Laurent, D., & Catherine, F. (2013). Development and characterization of composite chitosan/active carbon hydrogels for a medical application. *Journal of Applied Polymer Science*, 128(5), 2945–2953. <https://doi.org/10.1002/app.38414>
- Clarke, E. T., & Martell, A. E. (1991). Stabilities of trivalent metal ion complexes of the tetraacetate derivatives of 12-, 13- and 14-membered tetraazamacrocycles. *Inorganica Chimica Acta*, 190(1), 37–46. [https://doi.org/10.1016/S0020-1693\(00\)80229-7](https://doi.org/10.1016/S0020-1693(00)80229-7)
- Cohen, E., & Poverenov, E. (2022). Hydrophilic Chitosan Derivatives: Synthesis and Applications. *Chemistry – A European Journal*, 28(67), e202202156. <https://doi.org/10.1002/chem.202202156>

- Dash, S., Murthy, P. N., Nath, L., & Chowdhury, P. (2010). Kinetic modeling on drug release from controlled drug delivery systems. *Acta Poloniae Pharmaceutica*, *67*(3), 217–223.
- de Oliveira Pedro, R., Schmitt, C. C., & Neumann, M. G. (2016). Syntheses and characterization of amphiphilic quaternary ammonium chitosan derivatives. *Carbohydrate Polymers*, *147*, 97–103. <https://doi.org/10.1016/j.carbpol.2016.03.083>
- Desorme, M., Montembault, A., Lucas, J.-M., Rochas, C., Bouet, T., & David, L. (2013). Spinning of hydroalcoholic chitosan solutions. *Carbohydrate Polymers*, *98*(1), 50–63. <https://doi.org/10.1016/j.carbpol.2013.04.070>
- Facchinatto, W. M., Santos, D. M. dos, Fiamingo, A., Bernardes-Filho, R., Campana-Filho, S. P., Azevedo, E. R. de, & Colnago, L. A. (2020). Evaluation of chitosan crystallinity: A high-resolution solid-state NMR spectroscopy approach. *Carbohydrate Polymers*, *250*, 116891. <https://doi.org/10.1016/j.carbpol.2020.116891>
- Feng, W., & Wang, Z. (2023). Tailoring the Swelling-Shrinkable Behavior of Hydrogels for Biomedical Applications. *Advanced Science*, *10*(28), 2303326. <https://doi.org/10.1002/advs.202303326>
- Fuchs, T., Richtering, W., Burchard, W., Kajiwara, K., & Kitamura, S. (1998). Gel point in physical gels: Rheology and light scattering from thermoreversibly gelling schizophyllan. *Polymer Gels and Networks*, *5*(6), 541–559. [https://doi.org/10.1016/S0966-7822\(97\)00027-0](https://doi.org/10.1016/S0966-7822(97)00027-0)
- Gámiz-González, M. A., Piskin, A. E., Pandis, C., Chatzimanolis-Moustakas, C., Kyritsis, A., Marí, B., Ribelles, J. L. G., & Vidaurre, A. (2015). Determining the influence of *N*-acetylation on water sorption in chitosan films. *Carbohydrate Polymers*, *133*, 110–116. <https://doi.org/10.1016/j.carbpol.2015.07.020>
- Grange, C., Aigle, A., Ehrlich, V., Salazar Ariza, J. F., Brichtart, T., Da Cruz-Boisson, F., David, L., Lux, F., & Tillement, O. (2023). Design of a water-soluble chitosan-based polymer with antioxidant and chelating properties for labile iron extraction. *Scientific Reports*, *13*(1), Article 1. <https://doi.org/10.1038/s41598-023-34251-3>
- Gréa, T., Jacquot, G., Durand, A., Mathieu, C., Gasser, A., Zhu, C., Banerjee, M., Hucteau, E., Mallard, J., Lopez Navarro, P., Popescu, B. V., Thomas, E., Kryza, D., Sidi-Boumedine, J., Ferrauto, G., Gianolio, E., Fleith, G., Combet, J., Brun, S., ... Detappe, A. (2024). Subcutaneous Administration of a Zwitterionic Chitosan-Based Hydrogel for Controlled Spatiotemporal Release of Monoclonal Antibodies. *Advanced Materials*, *36*(13), 2308738. <https://doi.org/10.1002/adma.202308738>
- Hirai, A., Odani, H., & Nakajima, A. (1991). Determination of degree of deacetylation of chitosan by ¹H NMR spectroscopy. *Polymer Bulletin*, *26*(1), 87–94. <https://doi.org/10.1007/BF00299352>
- Isogai, A., & Atalla, R. H. (1998). Dissolution of Cellulose in Aqueous NaOH Solutions. *Cellulose*, *5*(4), 309–319. <https://doi.org/10.1023/A:1009272632367>
- Jayakumar, R., Selvamurugan, N., Nair, S. V., Tokura, S., & Tamura, H. (2008). Preparative methods of phosphorylated chitin and chitosan—An overview. *International Journal of Biological Macromolecules*, *43*(3), 221–225. <https://doi.org/10.1016/j.ijbiomac.2008.07.004>

- Jin, R., & Dijkstra, P. J. (2010). Hydrogels for Tissue Engineering Applications. In R. M. Ottenbrite, K. Park, & T. Okano (Eds.), *Biomedical Applications of Hydrogels Handbook* (pp. 203–225). Springer. https://doi.org/10.1007/978-1-4419-5919-5_11
- Jung, J. P., Jones, J. L., Cronier, S. A., & Collier, J. H. (2008). Modulating the mechanical properties of self-assembled peptide hydrogels via native chemical ligation. *Biomaterials*, 29(13), 2143–2151. <https://doi.org/10.1016/j.biomaterials.2008.01.008>
- Kantak, M. N., & Bharate, S. S. (2022). Analysis of clinical trials on biomaterial and therapeutic applications of chitosan: A review. *Carbohydrate Polymers*, 278, 118999. <https://doi.org/10.1016/j.carbpol.2021.118999>
- Kean, T., & Thanou, M. (2010). Biodegradation, biodistribution and toxicity of chitosan. *Advanced Drug Delivery Reviews*, 62(1), 3–11. <https://doi.org/10.1016/j.addr.2009.09.004>
- Ladet, S., David, L., & Domard, A. (2008). Multi-membrane hydrogels. *Nature*, 452(7183), 76–79. <https://doi.org/10.1038/nature06619>
- Laftah, W. A., Hashim, S., & Ibrahim, A. N. (2011). Polymer Hydrogels: A Review. *Polymer-Plastics Technology and Engineering*, 50(14), 1475–1486. <https://doi.org/10.1080/03602559.2011.593082>
- Leduc, J.-F., Leduc, R., & Cabana, H. (2014). Phosphate Adsorption onto Chitosan-Based Hydrogel Microspheres. *Adsorption Science & Technology*, 32(7), 557–569. <https://doi.org/10.1260/0263-6174.32.7.557>
- Li, J., & Mooney, D. J. (2016). Designing hydrogels for controlled drug delivery. *Nature Reviews. Materials*, 1(12), 16071. <https://doi.org/10.1038/natrevmats.2016.71>
- Matica, M. A., Aachmann, F. L., Tøndervik, A., Sletta, H., & Ostafe, V. (2019). Chitosan as a Wound Dressing Starting Material: Antimicrobial Properties and Mode of Action. *International Journal of Molecular Sciences*, 20(23), Article 23. <https://doi.org/10.3390/ijms20235889>
- Metters, A., & Hubbell, J. (2005). Network Formation and Degradation Behavior of Hydrogels Formed by Michael-Type Addition Reactions. *Biomacromolecules*, 6(1), 290–301. <https://doi.org/10.1021/bm049607o>
- Minh, N. C., Cuong, H. N., Phuong, P. T. D., Schwarz, S., Stevens, W. F., Van Hoa, N., & Trung, T. S. (2017). Swelling-assisted reduction of chitosan molecular weight in the solid state using hydrogen peroxide. *Polymer Bulletin*, 74(8), 3077–3087. <https://doi.org/10.1007/s00289-016-1880-3>
- Mogoşanu, G. D., & Grumezescu, A. M. (2014). Natural and synthetic polymers for wounds and burns dressing. *International Journal of Pharmaceutics*, 463(2), 127–136. <https://doi.org/10.1016/j.ijpharm.2013.12.015>
- Montembault, A., Viton, C., & Domard, A. (2005a). Physico-chemical studies of the gelation of chitosan in a hydroalcoholic medium. *Biomaterials*, 26(8), 933–943. <https://doi.org/10.1016/j.biomaterials.2004.03.033>
- Montembault, A., Viton, C., & Domard, A. (2005b). Rheometric Study of the Gelation of Chitosan in Aqueous Solution without Cross-Linking Agent. *Biomacromolecules*, 6(2), 653–662. <https://doi.org/10.1021/bm049593m>
- Natuzzi, M., Grange, C., Gréa, T., Brichart, T., Aigle, A., Bechet, D., Hautefeuille, B., Thomas, E., Ayoub, J.-Y., Bonnet, J.-M., Louzier, V., Allaouchiche, B., Couturier, A.,

- Montembault, A., de Oliveira, P. N., David, L., Lux, F., & Tillement, O. (2021). Feasibility study and direct extraction of endogenous free metallic cations combining hemodialysis and chelating polymer. *Scientific Reports*, *11*(1), Article 1. <https://doi.org/10.1038/s41598-021-99462-y>
- Noishiki, Y., Takami, H., Nishiyama, Y., Wada, M., Okada, S., & Kuga, S. (2003). Alkali-Induced Conversion of β -Chitin to α -Chitin. *Biomacromolecules*, *4*(4), 896–899. <https://doi.org/10.1021/bm0257513>
- Omidian, H., & Park, K. (2010). Introduction to Hydrogels. In R. M. Ottenbrite, K. Park, & T. Okano (Eds.), *Biomedical Applications of Hydrogels Handbook* (pp. 1–16). Springer. https://doi.org/10.1007/978-1-4419-5919-5_1
- Osorio-Madrado, A., David, L., Trombotto, S., Lucas, J.-M., Peniche-Covas, C., & Domard, A. (2010). Kinetics Study of the Solid-State Acid Hydrolysis of Chitosan: Evolution of the Crystallinity and Macromolecular Structure. *Biomacromolecules*, *11*(5), 1376–1386. <https://doi.org/10.1021/bm1001685>
- Peers, S., Montembault, A., & Ladavière, C. (2020). Chitosan hydrogels for sustained drug delivery. *Journal of Controlled Release*, *326*, 150–163. <https://doi.org/10.1016/j.jconrel.2020.06.012>
- Pierog, M., Gierszewska, M., & Ostrowska-Czubenko, J. (2009). Effect of ionic crosslinking agents on swelling behavior of chitosan hydrogel membranes. Progress on Chemistry and Application of Chitin and its Derivatives. *Polish Chitin Society, Łódź*, 75.
- Pita-López, M. L., Fletes-Vargas, G., Espinosa-Andrews, H., & Rodríguez-Rodríguez, R. (2021). Physically cross-linked chitosan-based hydrogels for tissue engineering applications: A state-of-the-art review. *European Polymer Journal*, *145*, 110176. <https://doi.org/10.1016/j.eurpolymj.2020.110176>
- Rami, L., Malaise, S., Delmond, S., Fricain, J.-C., Siadous, R., Schlaubitz, S., Laurichesse, E., Amédée, J., Montembault, A., David, L., & Bordenave, L. (2014). Physicochemical modulation of chitosan-based hydrogels induces different biological responses: Interest for tissue engineering. *Journal of Biomedical Materials Research Part A*, *102*(10), 3666–3676. <https://doi.org/10.1002/jbm.a.35035>
- Salazar Ariza, J. F., Lux, F., Da Cruz-Boisson, F., Resende de Azevedo, J., Vera, R., Tillement, O., Montembault, A., & David, L. (2025). Chitosan based hydrogel for iron (III) chelation in biological conditions. *Carbohydrate Polymers*, *347*, 122670. <https://doi.org/10.1016/j.carbpol.2024.122670>
- Shariatnia, Z. (2018). Carboxymethyl chitosan: Properties and biomedical applications. *International Journal of Biological Macromolecules*, *120*, 1406–1419. <https://doi.org/10.1016/j.ijbiomac.2018.09.131>
- Tamo, A. K., Tran, T. A., Doench, I., Jahangir, S., Lall, A., David, L., Peniche-Covas, C., Walther, A., & Osorio-Madrado, A. (2022). 3D Printing of Cellulase-Laden Cellulose Nanofiber/Chitosan Hydrogel Composites: Towards Tissue Engineering Functional Biomaterials with Enzyme-Mediated Biodegradation. *Materials*, *15*(17), Article 17. <https://doi.org/10.3390/ma15176039>
- Toporivska, Y., & Gumienna-Kontecka, E. (2019). The solution thermodynamic stability of desferrioxamine B (DFO) with Zr(IV). *Journal of Inorganic Biochemistry*, *198*, 110753. <https://doi.org/10.1016/j.jinorgbio.2019.110753>

- Tsai, S.-P., Hsieh, C.-Y., Hsieh, C.-Y., Wang, D.-M., Huang, L. L.-H., Lai, J.-Y., & Hsieh, H.-J. (2007). Preparation and cell compatibility evaluation of chitosan/collagen composite scaffolds using amino acids as crosslinking bridges. *Journal of Applied Polymer Science*, *105*(4), 1774–1785. <https://doi.org/10.1002/app.26157>
- Uliniuc, A., Popa, M., Hamaide, T., & Dobromir, M. (2012). New approaches in hydrogel synthesis -- Click chemistry: A review. *Cellulose Chemistry and Technology*, *46*.
- Vachoud, L., Zydowicz, N., & Domard, A. (1997). Formation and characterisation of a physical chitin gel. *Carbohydrate Research*, *302*(3), 169–177. [https://doi.org/10.1016/S0008-6215\(97\)00126-2](https://doi.org/10.1016/S0008-6215(97)00126-2)
- Wang, W., Meng, Q., Li, Q., Liu, J., Zhou, M., Jin, Z., & Zhao, K. (2020). Chitosan Derivatives and Their Application in Biomedicine. *International Journal of Molecular Sciences*, *21*(2), Article 2. <https://doi.org/10.3390/ijms21020487>
- Xu, Y., Han, J., & Lin, H. (2017). Fabrication and characterization of a self-crosslinking chitosan hydrogel under mild conditions without the use of strong bases. *Carbohydrate Polymers*, *156*, 372–379. <https://doi.org/10.1016/j.carbpol.2016.09.046>

3.4. Conclusion

The association between low DA chitosan (DA₆) and the functionalized chitosans presented in Chapter II enabled the formation of physical hydrogels through a pH-dependent gelation mechanism.

In this chapter, it was demonstrated that chitosan hydrogels can extract metals from solution through two mechanisms: direct chelation by the hydrogel and indirect extraction via electrostatic interactions between chelated metals and chitosan. This electrostatic interaction between chitosan's protonated amines and the negatively charged complex can be hindered by adding negatively charged moieties that replace the anionic metal complexes bonded to chitosan. For example, the addition of salts like Na₂SO₄ reduced the interactions between chitosan and anionic metal complexes by causing the protonated amine groups of chitosan to interact with sulphate anions (SO₄²⁻), thereby preventing the anionic complexes from binding to the chitosan. Conversely, the addition of salts did not affect the metals chelated by the chelator grafted onto the hydrogel.

This highlights the importance of using functionalized chitosans for metal extraction, especially in biological environments where various charged species may interact with chitosan. To achieve controlled chelation in such conditions, functionalized chelating chitosans are the optimal choice.

Furthermore, the properties of the resulting hydrogel can be tuned by modifying the species grafted onto the chitosan and adjusting its DA. For instance, grafting hydrophilic moieties such as DOTAGA increases the hydrophilicity and DA of deprotonated chitosan, resulting in higher swelling capacity, which can be highly advantageous for drug delivery applications. On the other hand, grafting hydrophobic moieties like p-Bz-DFO decreases the polymer's hydrophilicity, thus reducing the hydrogel's swelling.

Chapter IV: Application for localized chelation for the treatment of brain pathologies

The development of chelating polymers and materials in this work aims to propose various strategies for achieving localized chelation within the brain. Two approaches are explored in this chapter: the use of microdialysis and the use of hydrogels as chelating biodegradable implants.

4.1. Microdialysis:

The rationale for using microdialysis is similar to the MEXBRAIN technology presented in Chapter II. Small molecules bound with metal ions can be transported across the membrane into the dialysate through diffusion. By grafting the chelator to a polymer with a sufficiently high molecular weight, it can be retained within the microdialysis system, preventing its passage through the membrane (Figure 38). This enables the chelator to capture metals without reaching diffusion equilibrium, potentially extracting more metals than simple microdialysis.

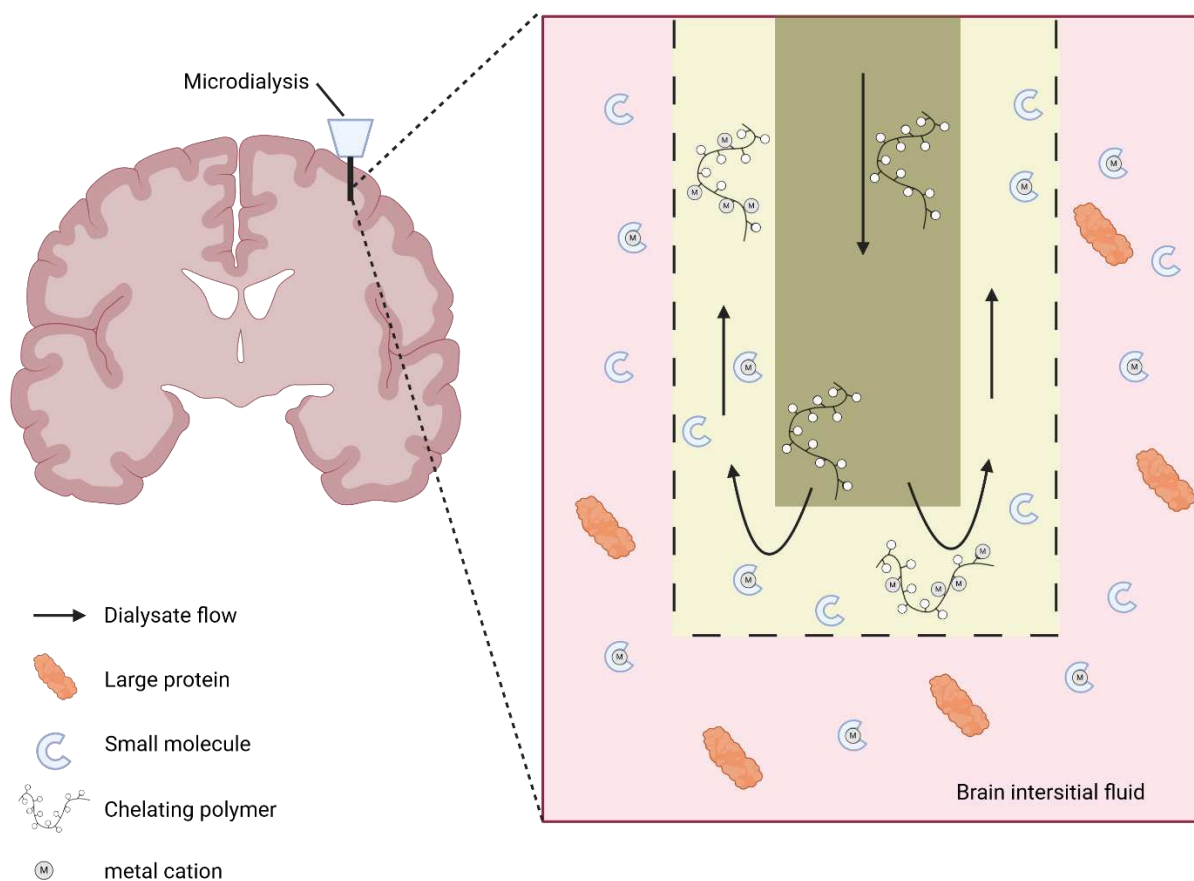


Figure 38. Representation of metal extraction in the brain by microdialysis with a chelating polymer.

Additionally, since the chelator remains within the dialysate, there is a reduced risk of chelator-related toxicity. The use of this technology would need a surgical intervention, the idea is to perform this procedure at the same time as other surgical procedures that are already use for

treating neurodegenerative diseases, for instance this could be done after patients go through DBS with the goal of limiting surgical interventions.

Two polymers were evaluated for the application of brain chelation by microdialysis, 8-arm PEG@DFO and chitosan DA₂₉@DOTAGA₉ due to their solubility in physiological media.

4.1.1. Microdialysis with 8-arm-PEG@DFO

The following experiments were performed by the team of Pr Philippe De Deurwaerdere at Institut de Neurosciences Cognitives et Intégratives d'Aquitaine, (INICIA) university of Bordeaux

In vitro measurements.

Material and methods Two microdialysis probes (CMA 12 Elite, $\phi = 0.5$ mm, L = 4 mm, membrane cut-off 20 kDa; PAES, Phymep) were submerged 1.5 mm apart in a 10 μ M iron(II) solution prepared in artificial cerebrospinal fluid (aCSF) (NaCl 147 mM, KCl 2.7 mM, CaCl₂ 1.2 mM, MgCl₂ 0.85 mM, Phymep, Paris, France). The iron source was iron (II) ammonium sulfate hexahydrate from Sigma-Aldrich. One probe served as the perfusion probe, where either 8-arm-PEG@DFO at a concentration of 10 μ M in aCSF or aCSF alone (control) was perfused at a flow rate of 3 μ L/min (Figure 39A). The second probe was the measurement probe, with a flow rate of 1 μ L/min. The perfusion of the iron (II) solution by both the experimental and measuring probe was conducted for 4 hours, and samples from the measurement probe were collected every 30 minutes to determine iron concentration using spectrophotometry with bathophenanthroline.

Results and discussion Despite the lower complexation constant of DFO with iron (II) compared to its complexation constant with iron (III) (Table 1), perfusion with 8-arm-PEG@DFO resulted in significantly higher iron clearance compared to perfusion with aCSF alone (Figure 39B). This increased clearance can be attributed to the chelation of iron(II) by 8-arm-PEG@DFO, which facilitated the diffusion of iron (II) into the microdialysis probe, enhancing its extraction.

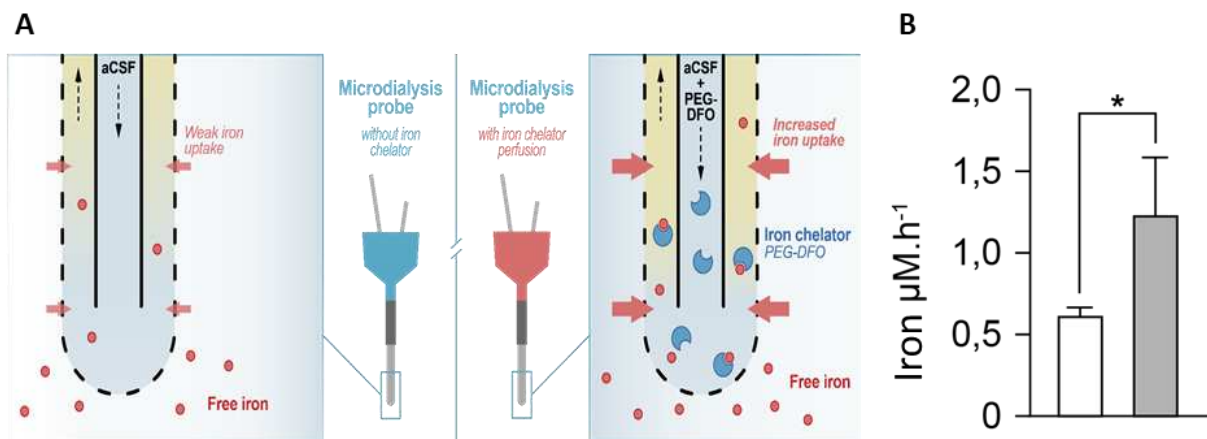


Figure 39. A: Comparison of iron extraction by microdialysis without 8-arm-PEG@DFO (Left) and with PEG@DFO (right) **B:** *in vitro* iron(II) clearance measured in the measurement

probe for the control experiment aCSF (white) compared to 8-arm-PEG@DFO at 10 μ M in aCSF (grey) during 4 hours of perfusion (n = 3) p < 0,05 ; Mann-Whitney's test.

In vivo measurements

As discussed in Chapter One, the increase in metal ions not tightly bound to proteins can induce ROS production through Fenton and Haber-Weiss reactions. To investigate this *in vivo*, a simple rat model of PD was used by administering 6-hydroxydopamine (6-OHDA) to the rat brains. 6-OHDA was chosen because it has been shown to elevate extracellular iron (II/III) levels and increase ROS production in rat brains [244,245]. The Fe(II)/Fe(III) ratio in solution is governed by the redox state of the medium [245]. Therefore, while 8-arm-PEG@DFO primarily chelates iron (III), the decrease in iron (III) levels may indirectly decrease the amount of iron (II) in the medium as well as reducing the total extracellular iron. This study aims to evaluate whether the use of microdialysis combined with the macrochelator 8-arm-PEG@DFO can reduce extracellular iron (II) concentrations in the rat brain following 6-OHDA administration. Two microdialysis probes are implanted in the rat brain: one for perfusing 8-arm-PEG@DFO and the other for collecting samples. To assess extracellular iron (II) levels, bathophenanthroline is used based on the method developed by Freinbichler *et al.* (2020) [245]. Bathophenanthroline forms a complex with iron (II), which has a characteristic absorbance at 535 nm, allowing iron (II) quantification via HPLC.

Material and methods Sprague-Dawley male rats (n=10) (10 weeks old, weighting 320-380g) purchased from the Janvier laboratory (Le Genest-Saint-Isle, France). They were maintained under standard housing conditions (12-hour light-dark cycles) with standard rodent food and water available *ad libitum*. The study protocol was approved by the local animal protection committee (University of Bordeaux) and complied with EU guidelines (86/609/EEC). Rats were anesthetized with isoflurane (3%) before being placed in a stereotaxic frame to implant the microdialysis probes. Rats were anesthetized during the whole experiment with 1.5% isoflurane. Sterile surgical procedures were used to implant the CMA 12 microdialysis cannulas (CMA Microdialysis AB, Solna, Sweden). The cannulas were stereotactically inserted into the left striatum of the rats at a distance between each other of 1.5mm (Figure 40).

As in the *in vitro* experiments, one probe served as the measurement probe for sample collection (flow rate of 1 μ L/min), while the other was the perfusion probe, where either 8-arm-PEG@DFO at a concentration of 10 μ M in aCSF or aCSF alone (control) was perfused at a flow rate of 3 μ L/min. Rats were perfused for a total of 6 hours, including a 2-hour stabilization period, a 2-hour basal measurement period, a 30-minute perfusion of 6-hydroxydopamine (6-OHDA) 200 μ M at a flow rate of 1 μ L/ min, and a final 1.5-hour measurement period post-6-OHDA. 6-OHDA was diluted in 0.05% (w/w) ascorbic acid to prevent oxidation. 6-OHDA was administered through the measurement probe (Figure 40B). Samples from the measurement probe were collected every 30 minutes for iron (II) concentration measurement using spectrophotometry with bathophenanthroline. Additionally, dopamine, its metabolite 3,4-dihydroxyphenylacetic acid (DOPAC), and the serotonin metabolite 5-hydroxyindoleacetic acid (5-HIAA) were measured in the collected samples

during the basal measurement period using a HPLC system coupled with coulometric detection (5014 analytical cell at 175 mV connected to a Coulochem 2 detector). These measurements were done in order to evaluate the effect of 8-arm-PEG@DFO perfusion on neurotransmitters in healthy rats.

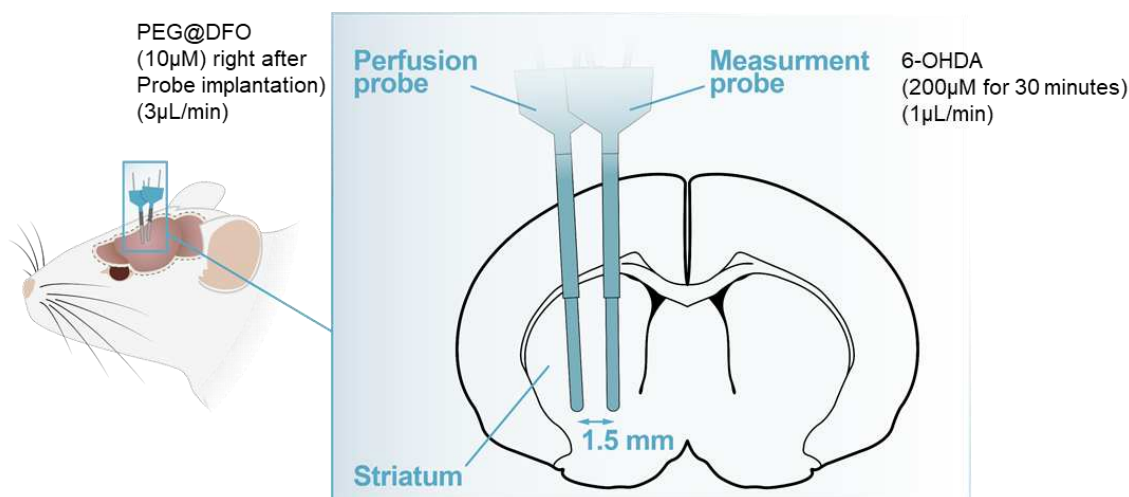


Figure 40. Schematic representation of the microdialysis probe placement: **Perfusion probe:** Located in the striatum, perfused with either 8-arm-PEG@DFO (10 μM in aCSF) or aCSF alone (control) at a flow rate of 3 $\mu\text{L}/\text{min}$. **Measurement probe:** Located adjacent (1.5mm) to the perfusion probe, used for sample collection and analysis. 6-OHDA (200 μM) was administered through this probe for 30 minutes.

Results and discussion During the stabilization period and basal level measurements, there were no significant differences in the baseline levels of the observed biochemical markers (dopamine, DOPAC, 5-HIAA) between the control group and the group treated with 10 μM 8-arm-PEG@DFO (Figure 41). Furthermore, the use of 8-arm-PEG@DFO did not alter the basal levels of extracellular iron(II) compared to the control group treated with aCSF alone (Figure 42). These findings suggest that the use of 8-arm-PEG@DFO in microdialysis does not negatively affect the brain of rats compared to microdialysis with aCSF alone.

Following 6-OHDA administration (t120-150 min in Figure 42), extracellular iron (II) levels increased significantly, rising from $0.77 \pm 0.24 \mu\text{M}$ to $5.23 \pm 1.77 \mu\text{M}$ in the control group, and from $0.80 \pm 0.42 \mu\text{M}$ to $3.60 \pm 1.06 \mu\text{M}$ in the 8-arm-PEG@DFO group. However, no significant difference was observed between the two groups. Extracellular iron (II) levels remained elevated for 30 minutes post-6-OHDA administration, and after 60 minutes, iron (II) levels decreased to baseline values (Figure 42). Despite the increased extraction of iron (II) *in vitro* with 8-arm-PEG@DFO, it did not enhance iron (II) extraction *in vivo* after 6-OHDA administration.

These findings suggest that iron chelation by 8-arm-PEG@DFO in the microdialysis cannula has minimal impact on distant iron (II) equilibria in the striatum (1.5 to 2 mm away). This lack of effect could be attributed to the short duration of perfusion. *In vitro* data indicate that a

noticeable reduction in iron (II) concentration occurs only after 3 hours of perfusion, whereas the increase in extracellular iron (II) *in vivo* is limited to 90 minutes. This may not provide sufficient time for 8-arm-PEG@DFO to significantly affect iron (II) levels in the surrounding tissue. Additionally, 8-arm-PEG@DFO may primarily chelate iron (III) and not iron (II). As a result, the chelation of iron (III) by DFO may be insufficient to significantly alter the iron(II)/iron(III) equilibrium, leading to a lack of reduction in extracellular iron (II) levels near the measurement probe. Measuring total extracellular iron (iron (II) and iron (III)) could provide a more comprehensive understanding of the effectiveness of macrochelators in intracranial microdialysis for iron extraction.

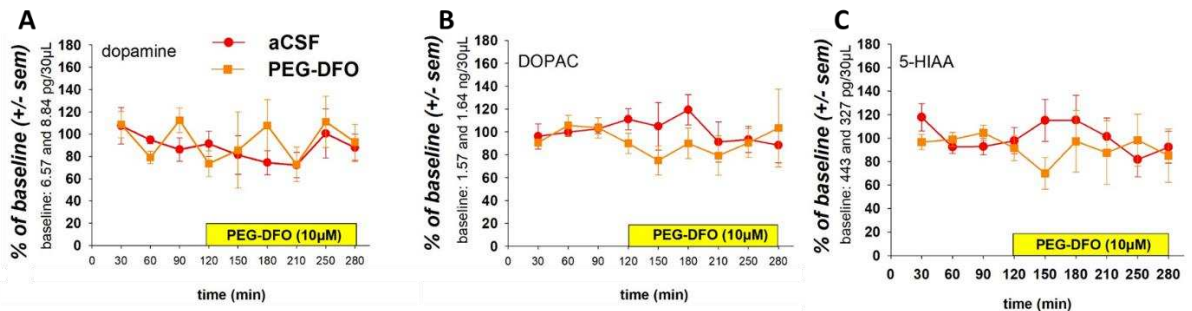


Figure 41: Evolution of the extra cellular levels of neurotransmitters (A: dopamine) and neurotransmitters metabolites (B: DOPAC C: 5-HIAA) during 4 hours (stabilization and baseline period) of microdialysis compared to baseline values. Quantification of dopamine, DOPAC and 5-HIAA done by HPLC system coupled to coulometric detection.

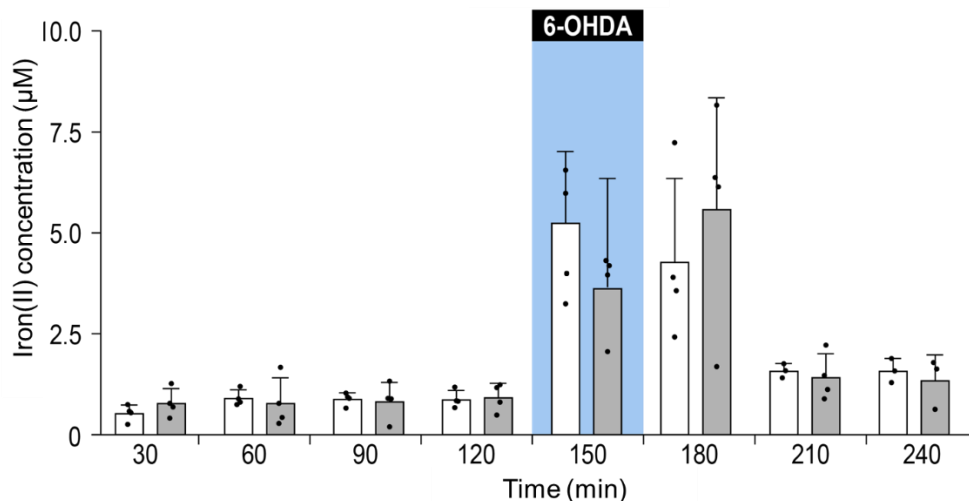


Figure 42: Evolution of the extra cellular levels of iron(II) measured from the samples retrieved from the measurement probe position at 1.5 mm from the perfusion probe (n=4). Measurements done by HPLC. 8-arm-PEG@DFO in grey and aCSF in white.

4.1.2. Microdialysis with DA₂₉@DOTAGA₉

Given the known neurotoxicity of manganese (Manganism and possible involment in AD and other neuro degenerative diseases as explained in the first chapter), this series of experiments involved intravenously administering manganese(II) to rats. The primary objective of this study

was to evaluate the metal extraction capabilities of DA₂₉@DOTAGA₉ using microdialysis *in vivo*.

The following experiments were performed by the team of Dr. Yannick Cremilieux at Institut des Sciences Moléculaires, (ISM) university of Bordeaux with the participation of Noel Pinaud and Dr. Imhad Benkhaled.

Material and methods 12 female rats of the Wistar strain (10 weeks old, 240-260 g) used for *in vivo* experiments were purchased from the Janvier laboratory (Le Genest-Saint-Isle, France). They were maintained under standard housing conditions (12-hour light-dark cycles) with standard rodent food and water available ad libitum. The study protocol was approved by the local animal protection committee (University of Bordeaux) and complied with EU guidelines (Directive 2010/63/EU).

Sterile surgical procedures were used to implant the CMA 7 microdialysis cannulas (CMA Microdialysis AB, Solna, Sweden). The cannulas were stereotactically inserted into the right hippocampus of the rats. The probe shaft has a diameter of 0.4 mm and a length of 7 mm. The microdialysis membrane has a molecular cut-off of 6 Daltons, an outer diameter of 0.24 mm, and a length of 2 mm. The CMA 7 microdialysis membrane is specifically designed for use in small areas of the brain or spinal cord of small animals (<https://microdialysis.com/cma-7-microdialysis-probes.html>). During the surgery, the rats were anesthetized with 2.5% isoflurane in an air/O₂ mixture (70:30) via a face mask and placed in a stereotaxic frame.

The head was shaved and the skull skin was incised in the coronal plane between the ears, along the interaural line. Three small holes were drilled in the skull; two holes with a 1 mm drill bit (for placement of the two cannulas above the hippocampus (in one probe DA₂₉@DOTAGA₉ is perfused at 1%w/w the other cannula is perfused by aCSF (control)), hole1 (coordinates AP = -3.9 mm, ML = 1.7 mm right, DV = -2 mm) and hole2 (coordinates AP = -3.9 mm, ML = 3.7 mm right, DV = -2 mm). The two cannulas were spaced 2 mm apart (Figure 43 A). Another hole with a 1.3 mm drill bit (3 mm close to the previous holes) for the placement of a plastic screw. Two cannula guides were positioned in the smaller holes, located above the hippocampus. A plastic screw was inserted into the larger hole. The screw and cannulas were fixed to the skull with dental cement (Dentalon Plus, Kulzer, Hanau, Germany) on the skull surface, then the muscles and skin were sutured. After surgery, the animals were individually housed and dosed with 0.05 mg/kg buprenorphine every 12 hours for 48 hours.

The manganese chloride solution was prepared according to the weight of the animals. A dose of 80 mg/kg of MnCl₂ was chosen, which is lower than the LD₅₀ (the lethal dose that causes 50% mortality) of manganese chloride, which is 92.6 mg/kg via intravenous injection in rats. The solution, composed of physiological saline and MnCl₂, has a concentration in manganese (II) of 165 mM for a 260 g rat. An intravenous injection of 400 µl of this solution is administered using a LEGATO 110 Pump from KD Scientific (USA) and a 2.5 ml syringe from Terumo (Japan) at a rate of 7 µl/min over 57 minutes and 14 seconds.

The CMA 402 Syringe Pump from CMA Microdialysis AB (Sweden) with a 1 ml EXMIRE syringe (Shizuoka, Japan) and a 1 m FEP Tubing from CMA Microdialysis AB is used for the

perfusion of microdialysis membranes. The perfusion of the microdialysis membranes starts 20 minutes after the beginning of the MnCl_2 injection, at a rate of $0.4 \mu\text{L}/\text{min}$ for two hours. The first membrane is perfused with aCSF, while the second is perfused with $\text{DA}_{29}\text{@DOTAGA}_9$ at $10 \text{ g}/\text{L}$ (Figure 43). The volumes of dialysate collected after 2 hours are $48 \mu\text{l}$ for each membrane. Dialysates were analyzed at the ILM by diluting them in HNO_3 1% (w/w) and measuring the metal concentration by ICP-MS using the KED mode.

MRI measurements were performed on a 7-T Bruker BioSpec 70/20 MRI system (Bruker BioSpin, Ettlingen, Germany). Images were acquired using a T1-weighted Flash sequence with the following parameters: repetition time $\text{TR} = 323.738$, echo time $\text{TE} = 3.09 \text{ ms}$, 15 slices of 0.8 mm thickness with a FOV of $35 \times 35 \text{ mm}^2$, flip angle = 40° Image size = $384 \times 384 \times 15$. Acquisition time was 11 min 03 s. An initial acquisition was performed before the MnCl_2 injection, followed by a series of acquisitions starting 20 minutes after the injection, with 30-minute intervals between acquisitions, up to two hours after the manganese injection (Figure 43 D).

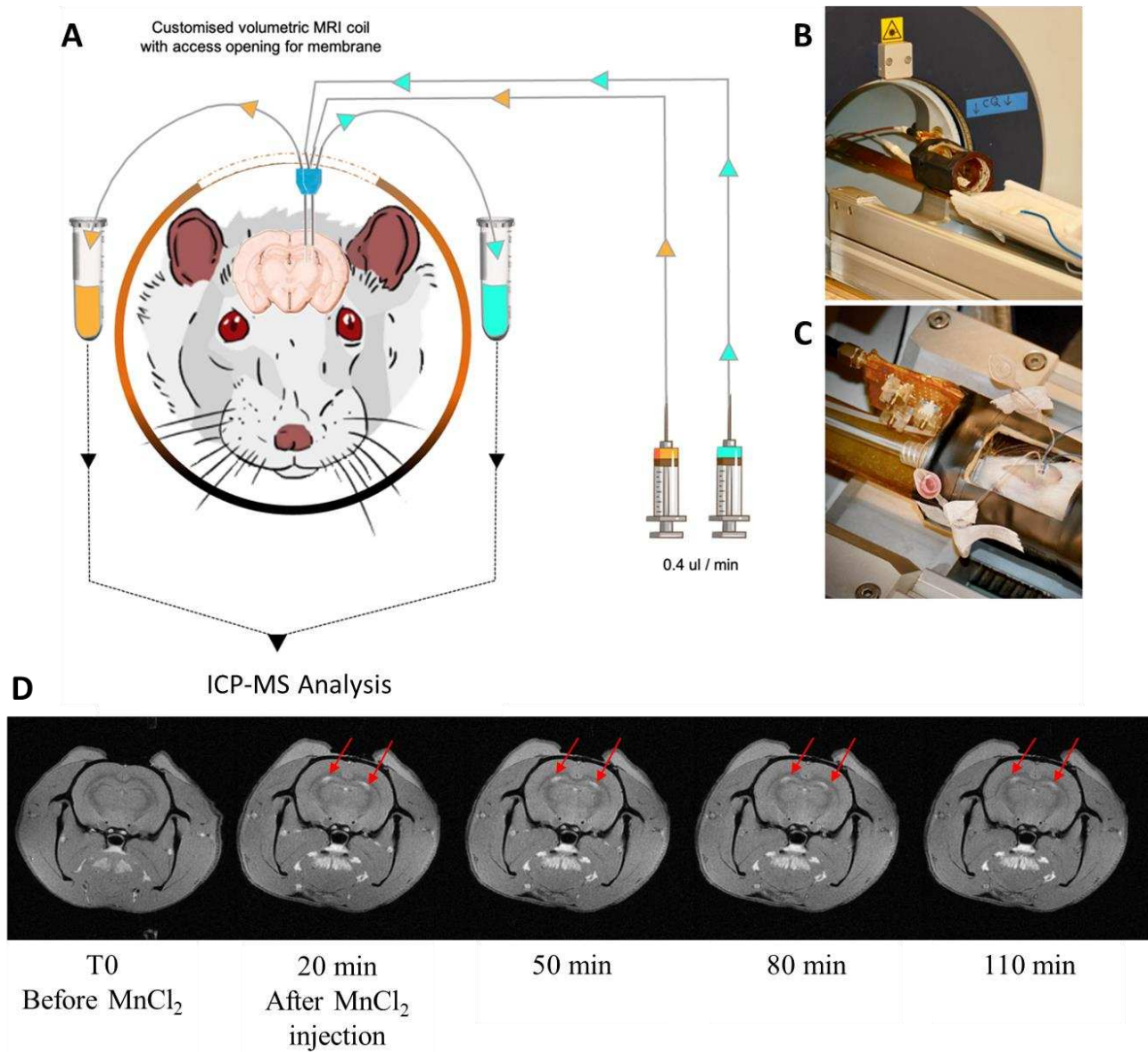


Figure 43. A: Schematic representation of the experimental set-up for the *in vivo* microdialysis experiments with DA₂₉@DOTAGA₉ 10 g/L (blue) and aCSF control (orange). The perfusion rate for both solutions was set at 0.4 μ L/min for 2 hours. **B:** Experimental set-up for simultaneous microdialysis and MRI without the animal. **C:** Experimental set-up for simultaneous microdialysis and MRI with the animal. **D:** MRI scans of a rat’s brain before and after injection of 400 μ L of MnCl₂ solution at different time intervals (20 min, 50 min, 80 min, and 110 min) after manganese (II) injections, no microdialysis probe was implanted in this rat. Red arrows shown the apparition of hyperintensities due to manganese (II) deposition.

Results and discussion Following intravenous injection of manganese (II), hyperintensities were observed in the rat’s brain after 20 minutes due to the presence of manganese (II) (Figure 43 D). ICP-MS measurements of manganese in the dialysates (control and DA₂₉@DOTAGA₉) revealed no significant difference in manganese concentrations between the two dialysates (p-value: 0.7071) although DA₂₉@DOTAGA₉ samples showed higher mean manganese concentrations ($3.9 \pm 6.1 \mu$ M for the DA₂₉@DOTAGA₉ samples and $3.0 \pm 5.6 \mu$ M for the

control samples). In both control and DA₂₉@DOTAGA₉ group there is a high standard deviation, indicating substantial variability in manganese concentrations in the rats' brain (Figure 44).

One possible explanation for the lack of significant manganese extraction by DA₂₉@DOTAGA₉ could be the adherence of the polymer to the membrane, which might underestimate the actual metal extraction. Additionally, the DA₂₉@DOTAGA₉ itself contains a non-negligible concentration of metals which could explain the higher concentration of copper and iron in the dialysates. While this concentration is known (Table 10) and can be subtracted from the total metal concentration in the dialysate to obtain the true metal extraction, determining the amount of polymer adhering to the membrane is necessary to accurately calculate the actual metal extraction.

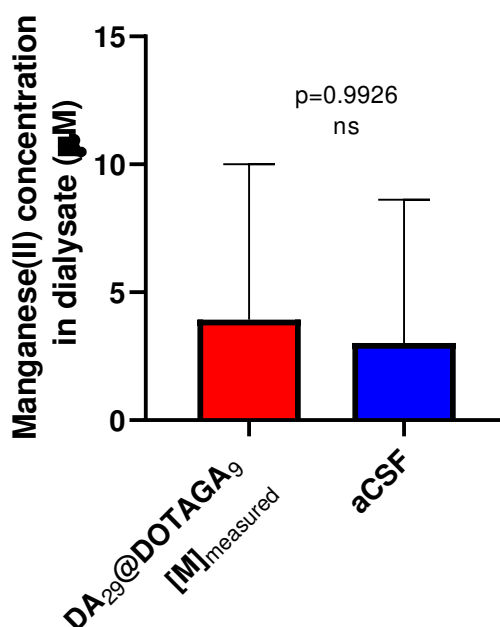


Figure 44. Manganese (II) concentration measured after 2 hours of microdialysis in rats' brain at a flow rate of 0.4 µL/min in the dialysate with DA₂₉@DOTAGA₉ in red and aCSF (control) in blue (n=12), p-values calculated by unpaired t test .

Quantification of DA₂₉@DOTAGA₉ in dialysate

In order to test the hypothesis of the polymer sticking to the membrane and assess the amount of polymer retrieved in the dialysate, as well as evaluate the manganese (II) chelation ability of DA₂₉@DOTAGA₉ a manganese (II) solution (5mM) was perfused by DA₂₉@DOTAGA₉ with the same parameter as the *in vivo* experiments.

Material and methods A single metallic solution (manganese (II) 5 mM) was prepared in HEPES 10mM pH 7.4 in a total volume of 2.5 mL. The metallic sources is a standard manganese (II) solution in 5 % HNO₃ provided by SCP-Science (ICP Standard 1000 µg.mL⁻¹,

reference: 140-052-250). By using the same microdialysis membranes as in the *in vivo* experiments the manganese (II) solution is perfused at the same rate as in the *in vivo* experiments 0.4 $\mu\text{L}/\text{min}$ for 2 hours by DA₂₉@DOTAGA₉ at 10 g/L or HEPES 10 Mm pH 7.4 (control). The resulting dialysates are analysed by ICP-MS using the same condition as the samples from the *in vivo* experiment. Each experiment was done in triplicates.

To determine the amount of DA₂₉@DOTAGA₉ retained in the membrane, the compound was quantified using the standard addition method. This study was conducted by Lise Picquoin. Briefly, this method involves preparing several DA₂₉@DOTAGA₉ solutions at known concentrations (0–0.5 g/L) in an acetate buffer (0.1 M ammonium acetate/0.1 M acetic acid, pH 4.5). A 10 μL of dialysate is added to each solution. NaNO₂ is then added in large excess (1:1000 ratio of glucosamine to NaNO₂) to depolymerize the polymer (Figure 45) [246]. The samples are stirred for 2 hours. GdCl₃ is added in a threefold excess relative to the theoretical DOTAGA concentration in each sample, and the mixtures are stirred at 60°C for 48 hours to allow gadolinium (III) chelation by DOTAGA ($\log\beta_{\text{L-Gd(III)}}: 24.7$ [247]). The samples are analyzed at the ILM using a Perkin Elmer NexION 2000 ICP-MS coupled to a Perkin Elmer Flexar LC. Separation is performed using a size exclusion column (Polysep 4000) at a flow rate of 0.4 mL/min with an acetate buffer (0.1 M ammonium acetate/0.1 M acetic acid, pH 4.5) as the eluent. The peak area corresponding to depolymerized DA₂₉@DOTAGA₉ is plotted against the known DA₂₉@DOTAGA₉ concentrations (Figure 46 B). By calculating the ratio of the y-axis intercept to the slope, and multiplying by 100 (dilution factor), the concentration of DA₂₉@DOTAGA₉ in the dialysate can be determined. The metal concentration of the initial DA₂₉@DOTAGA₉ solution used for the microdialysis experiments $[M]_{10}$ was measured by diluting a DA₂₉@DOTAGA₉ 10 g/L solution by a factor of ten in HNO₃ 1%(w/w) the resulting solution was then analysed by ICP-MS in KED mode (Table 10).

Results and discussion After measuring the metal concentrations in the dialysates from the *in vitro* experiments, it appears that the control (1.28±0.02 manganese (II) mM) extracts more metal than DA₂₉@DOTAGA₉ (0.60±0.07 manganese (II) mM) (Figure 46). This result is inconsistent with previous work, which demonstrated the polymer's ability to extract metals from solution. A likely explanation is that the polymer adheres to the membrane, leading to an underestimation of its metal-extracting capabilities.

The standard addition method was employed to quantify the amount of polymer adhering to the membrane. This method begins with the depolymerization of chitosan, achieved by cleaving the glycosidic bonds between the N-glucosamine and the other polymer units (N-acetylglucosamine or glucosamine grafted with DOTAGA) (Figure 45). Depolymerizing the polymer reduces its interactions with proteins in the dialysate, as protein-chitosan interactions can affect the polymer's retention time during HPLC-SEC analysis. Additionally, lowering the molecular weight enhances ionization, making the molecules more easily detectable by ICP-MS.

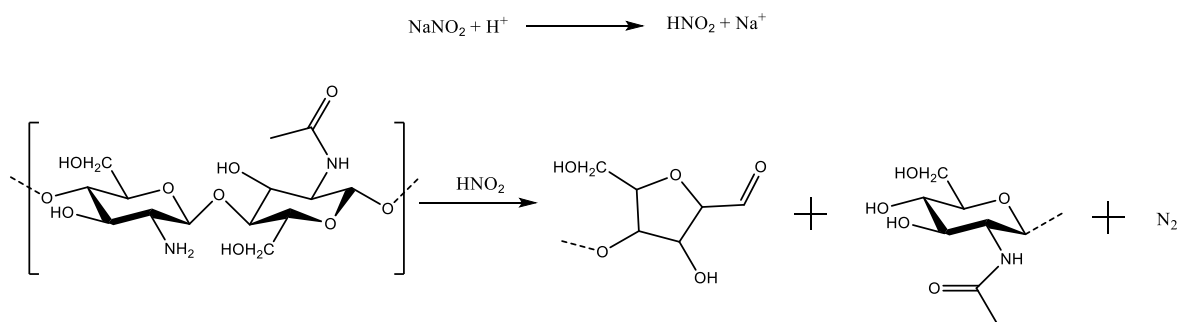


Figure 45. Chitosan depolymerization reaction induced by HNO_2 produced by NaNO_2 in acidic media [246].

The second step involves the complexation of gadolinium (III) with the DOTAGA moieties. This step marks the polymer units containing DOTAGA with an element not typically found in biological systems, allowing for the quantification of the DOTAGA-gadolinium (III) complex in solution using HPLC-SEC coupled with ICP-MS (Figure 46 A).

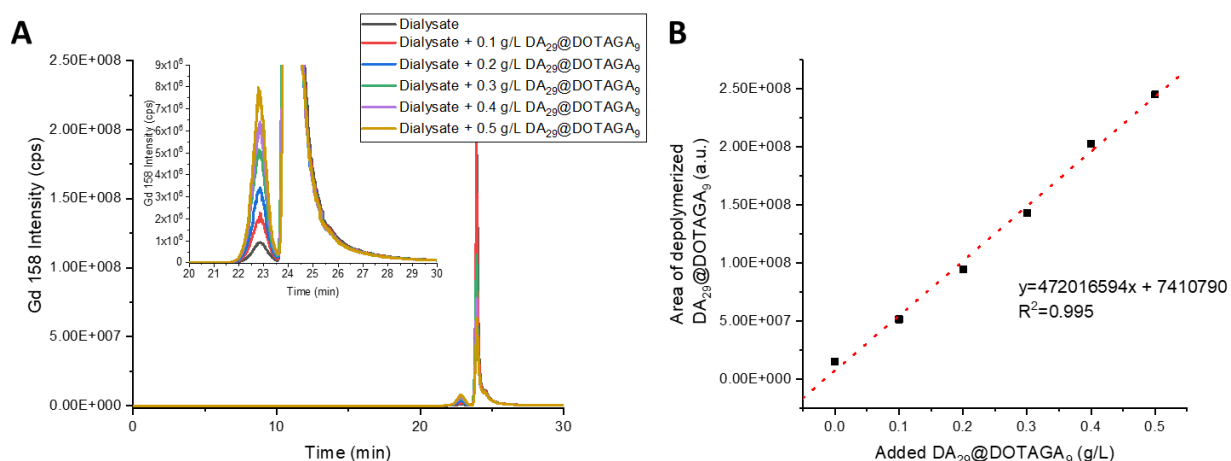


Figure 46. A: HPLC-SEC-ICPMS chromatogram of the analysed samples of the dialysate with growing concentration after depolymerization $\text{DA}_{29}@\text{DOTAGA}_9$ and complexation with gadolinium (III). The peak centred at 22.9 minutes correspond to the depolymerized $\text{DA}_{29}@\text{DOTAGA}_9$ complexed with gadolinium (III) and the peak from 23.5 min to 28 min the excess gadolinium (III). **B:** red dotted curve represents de linear regression of the area of the peak corresponding to depolymerized $\text{DA}_{29}@\text{DOTAGA}_9$ against known $\text{DA}_{29}@\text{DOTAGA}_9$ concentrations.

This method yielded the following equation for the plot of peak area corresponding to depolymerized $\text{DA}_{29}@\text{DOTAGA}_9$ against known $\text{DA}_{29}@\text{DOTAGA}_9$ concentrations: $y = 472016594x + 7410790$ (Figure 46 B). From this, the concentration of $\text{DA}_{29}@\text{DOTAGA}_9$ in the dialysate was determined to be 1.57 g/L, indicating that 84.3% of the polymer adheres to the membrane.

By knowing the percentage of polymer that remains on the membrane, we can adjust the measured values in the dialysate accordingly. It is assumed that the polymer found in the dialysate has the same complexation rate as the polymer adhering to the membrane. To estimate the metal concentration without polymer loss $[M]_{corrected}$, the metal concentrations measured in the dialysate samples $[M]_{measured}$ were divided by the percentage of polymer in the dialysate $\%_{polymer}$ (15.7%). Subtracting the metal concentrations in the polymer prior to microdialysis $[M]_{t0}$ (Table 10) yields the actual concentration of metals extracted $[M]_{extracted}$.

$$[M]_{corrected} = \frac{[M]_{measured}}{\%_{polymer}} \text{ and } [M]_{extracted} = [M]_{corrected} - [M]_{t0}$$

After this correction it is clear that the microdialysis with DA₂₉@DOTAGA₉ microdialysis (3.85±0.46 manganese (II) mM) increases significantly the metallic extraction compared to simple microdialysis (Figure 47).

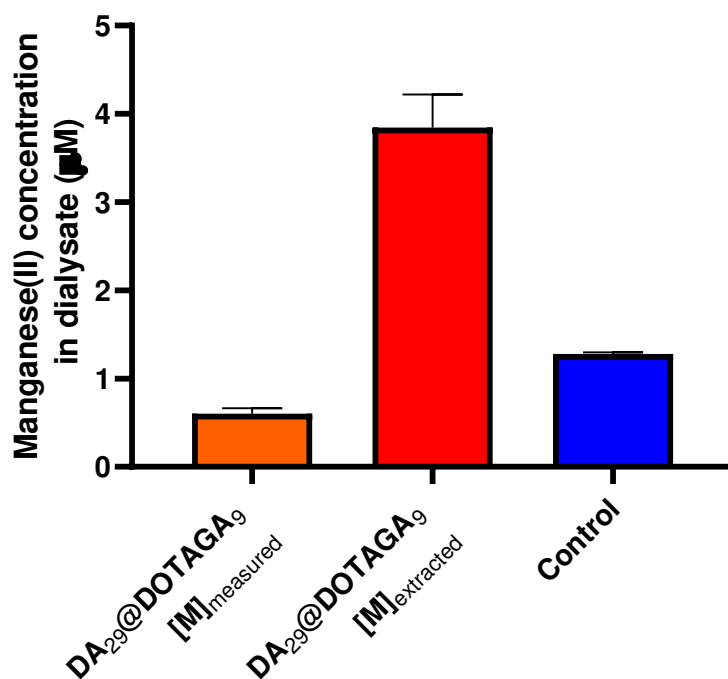


Figure 47. Concentrations of measured manganese (II) in the dialysates samples after 2 hours of microdialysis at a flow rate of 0.4 µL/min in a manganese (II) solution 5 mM in HEPES 10 Mm pH 7.4. In orange concentration measured by ICP-MS in the retrieved dialysates with DA₂₉@DOTAGA₉ ($[M]_{measured}$). In red concentration considering the portion of DA₂₉@DOTAGA₉ that is adhered to the membrane and the initial metal concentration of the DA₂₉@DOTAGA₉ 10 g/L solution ($[M]_{extracted}$). In blue concentrations measured by ICP-MS in the dialysates without polymer (control) (n=3).

Table 10. Metal (Mn, Fe, Cu, Zn) concentration (µM) in the DA₂₉@DOTAGA₉ 10g/L solution used for the microdialysis experiments, measured by ICPMS in KED mode. Results are represented as mean ± standard deviation (n=3).

Mn (μM)	Fe (μM)	Cu (μM)	Zn (μM)
0.30 ± 0.01	10.20 ± 0.40	0.06 ± 0.01	1.50 ± 0.01

Assuming that the interactions between the microdialysis membrane and the polymer in the *in vivo* experiment are similar to those *in vitro*, where only 15.7% of the initial polymer remains in the dialysate. It is then possible to calculate the concentration of metals in the dialysate if no polymer adhered to the membrane ($[M]_{\text{extracted}}$) using the same equation as in the previous experiment.

Similar to the *in vitro* results, the correction increases substantially the mean concentration of manganese (II) from $3.9 \pm 6.1 \mu\text{M}$ for the DA₂₉@DOTAGA₉ samples without correction to $24.7 \pm 38.7 \mu\text{M}$ for the DA₂₉@DOTAGA₉ samples with correction. However, due to the high standard deviation in the initial measurements, the increase in manganese (II) extraction by microdialysis using the chelating polymer was not statistically significant (p value <0.05) (Figure 48). It is likely that increasing the number of animals studied could result in statistically significant findings. Despite the current lack of significance, the use of a chelating polymer in microdialysis appears to be a viable research option for extracting neurotoxic metals from the brain, such as manganese (II).

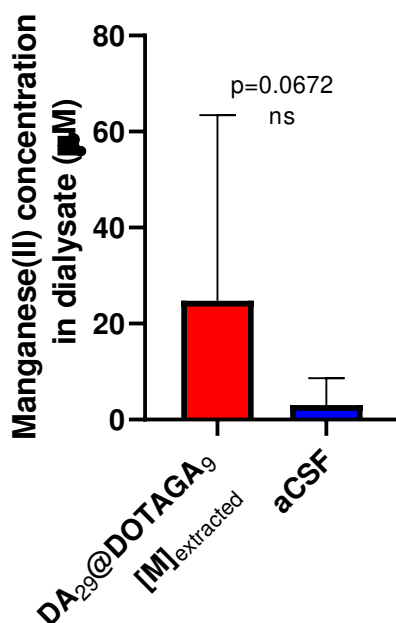


Figure 48. Concentrations of measured manganese (II) in the dialysates samples after 2 hours of microdialysis at a flow rate of $0.4 \mu\text{L}/\text{min}$ *in vivo* ($n=12$). In red concentration considering the portion of DA₂₉@DOTAGA₉ that is adhered to the membrane and subtracting the initial metal concentration of the DA₂₉@DOTAGA₉ 10 g/L solution ($[M]_{\text{extracted}}$). In blue concentrations measured by ICP-MS in the dialysates without polymer (control) with unpaired t test p-values.

4.1.3. Conclusion

While the combination of chelating polymers with microdialysis demonstrated promising results for metal extraction *in vitro*, these findings did not fully translate to *in vivo* experiments.

Microdialysis has several limitations that affect its efficacy. One of the most critical parameters is the flow rate. The flow rate must be slow enough to allow metal ions from the brain to diffuse into the microdialysis probe and be chelated by the polymer. For instance, a flow rate of zero would enable over time complete saturation of the chelating polymer.

Another limitation is the small exchange surface of the membrane, therefore increasing the exchange surface and keeping a flow rate of zero can be compared to a direct intracranial injection. However, injection could result in widespread diffusion of the chelating agent thus not achieving long-term localized chelation, moreover the chelating agent can be metabolized or degraded more rapidly, reducing its long-term efficacy. For sustained and localized chelation, the chelating polymer should have very slow diffusion. This can be achieved using chelating materials that can be implanted directly into the brain. Such an approach mimics the effect of a direct injection while minimizing the diffusion of the chelating agent, ensuring a prolonged and localized treatment. Another drawback of microdialysis is that it typically serves as a short-term intervention, requiring repeated procedures for ongoing treatment. In contrast, a biodegradable implant would require only a single procedure for deposition, offering a long-term solution. In the following section, the use of the chelating materials developed in Chapter 3 for metal extraction *in vivo* is explored.

4.2. Hydrogel implants

By utilizing the same gelation principle of chitosan amines deprotonation as for the hydrogels presented in the previous chapter, it's possible to create chelating materials with various desired shapes and forms. One approach explored in this study was the fabrication of chelating fibers. Fibers offer several advantages, including ease of handling, implantation, and a large surface-to-volume ratio, which can facilitate rapid diffusion enhancing metal chelation. Previous research at the IMP has developed a method for obtaining chitosan fibers [248–252].

4.2.1. Development of chelating biodegradable fibers “proof of concept” publication

The following article ” Neurocompatible biodegradable fibers designed to extract excess free metals in the brain ” submitted to the journal *Proceedings of the National Academy of Sciences (PNAS)* presents the development of chelating fiber made out of a precursor solution with the following formulation 5% w/w DA₆ and 10% w/w DA₆@DOTAGA₁₇ (referred in the article as Chitosan 5% Chitosan@DOTAGA 10%) resulting in a xerogel fiber made out of 2/3 w/w DA₆@DOTAGA₁₇ and 1/3 w/w DA₆.

Neurocompatible biodegradable fibers designed to extract excess free metals in the brain

Tatiana Borisova,¹ Juan Felipe Salazar Ariza,^{2,3} Natalia Pozdnyakova,¹ Natalia Krisanova,¹ Artem Pastukhov,¹ Marina Dudarenko,¹ Thomas Gréa,^{2,3} Alexandra

Montembault,³ Imad Benkhaled,⁴ Noël Pinaud,⁴ Justine Deborne,⁴ Yannick Crémillieux,⁴ Philippe De Deurwaerdere,⁵ Vladimir Lysenko,² Stéphane Palfi,⁶ Olivier Tillement², Laurent David,³ Francois Lux,^{2,7,*}

1-Palladin Institute of Biochemistry National Academy of Sciences of Ukraine, 9 Leontovicha Street, Kyiv, 01054, Ukraine.

2- Institut Lumière Matière UMR 5306 CNRS, Université Claude Bernard Lyon 1, 69622, Villeurbanne, France.

3- Université Claude Bernard Lyon 1, Institut National des Sciences Appliquées, Université Jean Monnet, CNRS, UMR 5223, Ingénierie des Matériaux Polymères (IMP), 15 bd Latarjet, 69622 Villeurbanne, France.

4- Institut des Sciences Moléculaires, UMR 5255, CNRS, Université de Bordeaux, Bordeaux, France.

5- Centre National de la Recherche Scientifique, Institut des Neurosciences Intégratives et Cognitives d'Aquitaine, UMR, 5287, Bordeaux, France.

6- Department of Neurosurgery, Henri Mondor Academic Hospital, Université Paris Est Créteil, INSERM Laboratory U955 of Translational NeuroPsychiatry, Institut Mondor de Recherche Biomédicale

7- Institut Universitaire de France (IUF), Paris, France

Corresponding authors : Francois Lux, <mailto:francois.lux@univ-lyon1.fr>

Key words

Chelation, biopolymer, neurodegenerative disease, biodegradable material

Abstract

Exposure to environmental heavy metals and disruptions in physiological metal balance are significant factors contributing to neurological and neurodegenerative conditions. To address heavy metal toxicity, a biopolymer consisting of chitosan functionalized with DOTAGA ligands (Chitosan@DOTAGA) was developed. By carefully blending conventional chitosan with Chitosan@DOTAGA, biodegradable fibers with controlled diameters were processed and their mechanical properties characterized. The chelation properties of these fibers were evaluated in an aqueous medium by ICP-MS analyses for various metal ions, including Cu (II), Cd (II), Pb (II), and Fe (III). Neuroprotection was assessed *ex vivo* using nerve terminals isolated from rat brains exposed to Cu (II), Cd (II), Pb (II), and Hg (II); effectiveness was evidenced for all metals except Hg (II) testing different neurotransmitters. To validate *in vivo* feasibility of the future use of Chitosan@DOTAGA for metal chelation in the central nervous system, Gd (III)-labeled fibers were implanted into rat brains for three months, with no observable inflammatory reactions detected via MRI or histology. The biodegradability of the fibers was assessed using MRI and ICP-MS analyses.

1. Introduction

Neurological disorders are the third most common cause of disability and premature death in the EU. Their prevalence and burden increase, as underlined by the recent report of Lancet Public Health 2020 [1]. Environmental pollution by heavy metals and disturbance of proper homeostasis of essential physiological metals can significantly contribute to development of different types of neuropathologies [2]. For example, copper is critical for the central nervous system (CNS) development and function [3]. Disorders of copper metabolism, *i.e.* Menkes and Wilson's disease, exhibit complex neurodegenerative features, thereby highlighting the impact of copper dis-homeostasis [4]. Cadmium, a neurotoxic heavy metal, is widely distributed in the polluted environment, including water, air, food, and smoke. It accumulates extensively in humans due to low clearance, with a half-life of 15–30 years. The CNS is considered one of the most vulnerable targets for cadmium action, where the metal can significantly exacerbate neurodegenerative diseases, peripheral polyneuropathies, and provoke mental deficits in children [5]. Lead is also an ubiquitous environmental neurotoxic heavy metal that remains to threaten globally public health. Epidemiological studies have demonstrated harmful effects of lead at very low levels on childhood IQ [6]. Lastly, iron, despite iron's critical role in multiple biological processes such as oxygen transportation and enzymatic reactions [7], is suspected to play an important role in neurodegenerative diseases, where it appears to promote protein aggregation and oxidative damage [8], [9]. In fact, studies have demonstrated an alteration in labile iron concentration in the cerebrospinal fluid (CSF) of patients with mild cognitive impairment, at an iron concentration of $0.46 \pm 0.04 \mu\text{M}$ in comparison with $0.29 \pm 0.04 \mu\text{M}$ for control patients [10]. Moreover, several studies have associated iron accumulation with tissue damage [11-13] as indicated by ferritin and heme-oxygenase upregulation in the brain.

Novel drug targets for the abovementioned chronic disease are eagerly sought. While potentially helpful agents, such as chelators, have traditionally been largely restricted to overt acute metal poisoning, their application in a preventive and prophylactic approach is highly promising [14]. Known chelators that are used in practice include thiols such as Dimercaprol (British Anti-Lewisite, BAL), dimercaptosuccinic acid (DMSA or succimer), dimercaptopropane sulfonate (DMPS), penicillamine, CaNa₂EDTA... Combined administration of these chelators is also recommended [14]. Wilson's disease is an example of a genetic disease treated by chelation therapy; however, traditional chelation therapy is limited by secondary adverse effects, lack of compliance, and neurological worsening, as seen in some cases of Wilson's disease [15]. Moreover, access to the brain is limited for many chelates due to the presence of blood brain barrier and their elimination is fast limiting their interest for small chronic overtime accumulation. Biodegradable chelating materials could be of interest if implemented within the diseased area, for pathologies like Parkinson's disease, which has been associated with the detrimental effect of redox active metals such as iron [16]. This can be performed during surgical procedures associated to the use of active implantable neurological devices, such as deep brain simulators [17].

Due to its attractive biological properties including biocompatibility, biodegradability and antibacterial activity, chitosan is recognized has an attractive polymer for the formation of biomaterials [18]. Chitosan is industrially derived from chitin which can be found in crustacean shells, possibly as by-products of food industry [19]. It can be processed as biodegradable hydrogels for various applications, including for example wound healing and biomedical

implants, due to its favorable properties such as, but not limited to, biocompatibility, antioxidant activity, and antibacterial effects [20-24]. Our team has recently shown the interest of functionalizing chitosan by chelating molecules like DOTAGA or DFO in combination with hemodialysis for the removal of copper or iron [25], [26]. It has led to two clinical trials currently recruiting for the treatment of Wilson disease (NCT05917327) and acute on chronic liver failure (ACLF) (NCT06340269). Interestingly, Ficiara *et al.* have developed nanobubble formulations comprising glycol chitosan functionalized with DFO to bind iron for neurological applications and have shown its impact on A β misfolding [27]. Our team has also shown that chitosan coupled to DFO or DOTAGA mixed with conventional chitosan can lead to chelating hydrogels that can be used also for drug delivery [28], [29] and that conventional chitosan can be shaped into fibers whose dimensions and mechanical properties can be finely tuned [30].

Integrating Chitosan@DOTAGA in the filaments could lead to biodegradable fibers capable of removing metals from the implanted zone. In this work, we demonstrate the feasibility to synthesize such fibers and determine their mechanical and chelating properties on different metallic cations. One of the aims of this study was to assess the impact of the filament in isolated rat cortex nerve terminals (synaptosomes), i.e.: (i) evaluating the potential neurotoxic properties of the fiber *per se* analyzing its effect on the key characteristics of glutamatergic and GABA-ergic neurotransmission; (ii) evidencing a capability of copper, mercury, cadmium and lead to influence the extracellular level of excitatory neurotransmitter L-[¹⁴C]glutamate and inhibitory one [³H]GABA at the presynaptic site; (iii) evidencing the ability of the fiber to mitigate a heavy metal-induced increase in the extracellular level of L-[¹⁴C]glutamate and [³H]GABA in nerve terminals. In view of future applications of chelating fibers in neuro-diseases, a preliminary *in vivo* proof of concept was also performed: the objectives were to evaluate the feasibility of implanting the fiber in the rat brain, the relevance of using MRI to monitor the fiber in the brain, and to obtain initial information on the biocompatibility of the approach and of the biodegradability of the implanted filament.

2. Material and Methods

2.1. Chitosan@DOTAGA synthesis

2.1.1. Chemicals

Medical grade chitosan with low DA ($6\% \pm 0.5\%$, determined by ¹H NMR spectroscopy using the Hirai method [31] (See Supporting Information Figure S1) from Alaska snow crab was purchased from Matexcel (Bohemia, NY, USA, reference number NAT-0030, <https://www.matexcel.com/p/30/medical-grade-chitosan/>). This chitosan was fully characterized. The weight-average and number-average molar masses (respectively $M_w=2.600 \cdot 10^5$ g/mol and $M_n=1.300 \cdot 10^5$ g/mol) were determined by size exclusion chromatography coupled with refractive index and multi-angle laser light scattering measurements at the chromatography platform of the Chemistry Institute of Lyon (ICL, <https://www.iclyon.fr/>). DOTAGA-anhydride (1,4,7,10-tetra-azacyclododecane-1-glutaric anhydride-4,7,10-triacetic acid) was purchased in CheMatech (Dijon). GdCl₃ · 6 H₂O (CAS 13450-84-5, 99.9%) was purchased from Sigma Aldrich (Saint-Quentin-Fallavier, France).

2.1.2. Functionalization of chitosan

Functionalized chitosan Chitosan@DOTAGA was developed by MexBrain, its synthesis and characterization are described in detail in a previous paper [28] (See Supporting Information Figures S2, S3 and Table S1 for the characterization of the functionalized chitosan). Briefly, to synthesize the chelating polymer, chitosan was first solubilized in a mixture of water and propanediol (50/50 w/w), using acetic acid to protonate chitosan chains. Then, DOTAGA-anhydride (1,4,7,10-tetra-azacyclododecane-1-glutaric anhydride-4,7,10-triacetic acid) was added to the solution to functionalize the polymer. The resulting product was purified by tangential filtration (with a cut-off membrane of 100 kDa). The amount of DOTAGA grafted onto the polymer was determined by UV-Vis titration in the presence of increasing concentration of Cu (II) using the same method of copper chelation as described by Natuzzi *et al.*, (See Supporting Information Figure S4) [26]. The Chitosan@DOTAGA polymer was found to have 0.654 mmol of DOTAGA grafted per gram of polymer, corresponding to a substitution degree of $17.0 \pm 0.5\%$ (Refer to the supporting information Figure S4 for details on the DOTAGA substitution degree).

2.1.3. Labelling of Chitosan@DOTAGA by Gd³⁺

The labelling of Chitosan@DOTAGA with gadolinium for *in vivo* experiments was performed by adding 8.74 mL of a solution of 1 M gadolinium (prepared with GdCl₃, 6 H₂O) to 1 L of a Chitosan@DOTAGA solution at 7 g.L⁻¹. The solution's pH was then adjusted to 5.6 ± 0.1 with a 1 M NaOH solution, and the solution was stirred at 60 °C for 48 h. The concentration of chelated gadolinium was determined to be 70.5 mg of Gd³⁺ per gram of polymer (*i.e.* 70% of total DOTAGA) using inductively coupled plasma mass spectrometry (ICP-MS).

2.2. Fiber formation

2.2.1. Fiber synthesis

To prepare the chelating fibers, chitosan and Chitosan@DOTAGA were dispersed in ultra-pure water at concentrations of 5% and 10% by weight, respectively. Acetic acid was added to achieve stoichiometric protonation of the amine moieties of both polymers, and the blend was mechanically stirred until a homogeneous mixture was obtained. The precursor solution (dope) was then extruded using the same procedure (Figure 1) as described by Passieux *et al.* [30]. The precursor solution was extruded at a linear velocity of $V_0 = 21 \text{ mm}\cdot\text{s}^{-1}$ through a conical spinneret with a final diameter of 410 μm (Nordson EFD, smoothflow tapered tips, 7018298), by applying pressure using a piston with a compressed air dispenser (NordsonOptimus I, NordsonEFD). The resulting extrudate was introduced into a 1 L bath of 3 M NaOH aqueous solution to induce gelation. A first motorized bobbin drove the fiber into two 5 L baths of ultra-pure water for washing, while the second motorized bobbin guided it out of the washing baths and into the drying zone. The last motorized bobbin ensured winding of

the fiber. The speeds of the motorized bobbins were $21 \text{ mm}\cdot\text{s}^{-1}$, $26 \text{ mm}\cdot\text{s}^{-1}$, and $34 \text{ mm}\cdot\text{s}^{-1}$, respectively.

The fiber labelled with gadolinium was prepared by dispersing 3 polymers, namely chitosan, Chitosan@DOTAGA and Chitosan@DOTAGA-Gd in ultra-pure water at concentrations of 5%, 8%, 2% by weight, respectively. Again, acetic acid was added to achieve stoichiometric protonation of the amine moieties, solubilizing the polymers. The dope was then extruded using the same protocol as described above for the formation of the fiber without gadolinium. Thus, with this proportion of Chitosan@DOTAGA-Gd and its level of complexation, $0.70 \times 0.20 = 14\%$ of the total DOTAGA in the fiber is complexed with gadolinium.

The chelating fibers formulated above were used for *in vivo* experiments. The diameter of the dry fibers was determined after observation of the yarns with a Leica M205A stereomicroscope equipped with the Leica Application Suite v4.12 software, and image treatment using ImageJ. The titer (in dtex) was determined by weighting 2.5 m of fiber and converting it to 10000 meters.

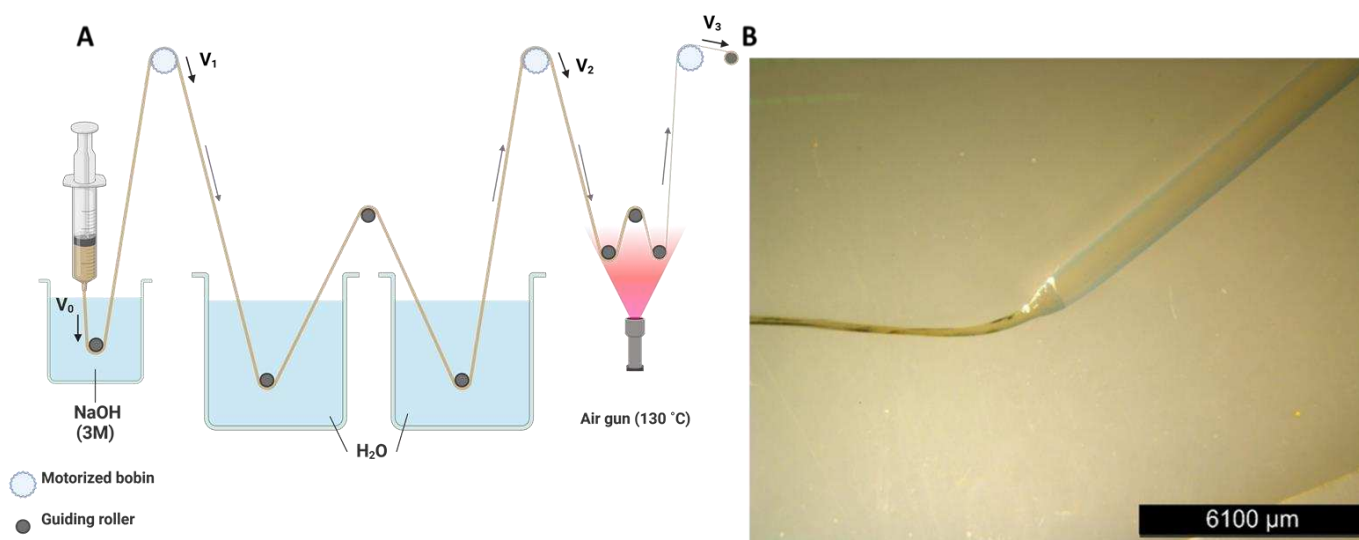


Figure 1. A: Scheme of the lab-scale wet gel spinning setup for producing chitosan fibers. It comprises a gelation bath (aqueous 3 M NaOH solution), three motorized bobbins that control the stretching rates, and an air gun for drying the fibers after they washing in two separate water baths. **B:** optical microscopy image of the fiber, with the left side showing the dry fiber (diameter $\sim 180 \mu\text{m}$) and the right side showing the rehydrated fiber in contact with a water drop ($\sim 900 \mu\text{m}$).

2.2.2. Mechanical properties of the Fibers

The tensile properties were assessed using a SHIMADZU AG-X plus device equipped with a 100 N load cell. The unidirectional tensile test was conducted at a constant speed of 10 mm/min for each sample at ambient temperature and relative humidity $\text{Rh} \sim 35\%$. The fiber was positioned between clamps establishing an effective initial length ($l_0 = 50 \text{ mm}$) and an initial deformation rate of 20%/min. The tenacity (T_e) was calculated as the ratio of the applied force

(F_b) at rupture to the yarn titer in dtex (Y_t) ($T_e = F_b/Y_t$); the nominal strain (ϵ) was expressed as the ratio of the fiber's extension to the initial length ($\epsilon_N = \Delta l/l_0 = (l - l_0)/l_0$). The Young's modulus (E), tenacity (T_e), and strain-at-break (ϵ_b) were determined from the stress-strain curves (see Figure Supporting Information Figure 5), with five measurement replicates ($n = 5$). The same test was conducted for the fibers labeled with gadolinium, and the results were similar to those of the non-labeled fibers (See Supporting Information Table S2).

Table 1. Fiber mechanical characterisation data obtained by uniaxial tensile test on 5 different samples of Chitosan 5%w/w Chitosan@DOTAGA 10% w/w fiber. The reported data are the mean of $n=5$ tensile tests.

Sample	Titer	Young's modulus ^a	Yield stress ^a	Yield strain	Tenacity ^a	Strain at rupture	Diameter ^b
	(dtex)	(cN/dtex)	(cN/dtex)	(%)	(cN/dtex)	(%)	(μ m)
Chitosan 5% Chitosan@DOTAGA 10%	391.5	0.115±0.01 4	0.288±0.01 3	2.8±0.2	0.47±0.02	19.2±2.2	192.3±14.5
Chitosan 5% Chitosan@DOTAGA 8% Chitosan@DOTAGA-Gd 2%	295	0.151±0.00 8	0.278±0.01 8	2.0±0.1	0.46±0.02	18.7±2.2	181.2±21.8

^a: The values of stress expressed in textile units cN/dTex can be converted in MPa using the estimated density of $\rho \sim 1.3 \text{g/cm}^3$ according to: $\sigma (\text{MPa}) = \sigma (\text{cN/dtex}) \rho (\text{g/cm}^3) * 100$.

^b: Values deduced from optical microscopy measurements. The apparent diameter d of the fiber can be deduced from the titer $Y_t(\text{dtex})$ with greater precision using:

$$d(\mu\text{m}) = \left(\frac{Y_t(\text{dtex}) \times 100}{\frac{\pi}{4} \times \rho (\text{g/cm}^3)} \right)^{1/2}$$

2.2.3. Characterization of metal chelation by the Fibers

Chelation experiments for each metal (Cu (II), Cd (II), Pb (II) and Fe (III)) were carried out separately. Each metallic solution was prepared in 20 mM HEPES at pH 7.4. To prevent lead precipitation, the pH of the lead solution was adjusted to 6.0. To prevent iron (III) precipitation at pH 7.4, nitrotriacetic (NTA) chelator (Log $K_{\text{Fe(III)-NTA}}$: 15.9) [32] was added to the solution at a ratio of 1.1 NTA/1 iron (III). As in previous works [28], Na_2SO_4 was also added at a concentration of 14 mM to prevent interactions between the NTA-iron (III) complex and chitosan. The metal solutions were prepared by dissolving CuSO_4 , CdCl_2 , and $\text{Pb}(\text{NO}_3)_2$ at concentrations of 50 μM for copper (II), 1 mM for cadmium (II), and 2.5 mM for lead (II) in the chelation baths. The iron solution was prepared by diluting a ferric solution (1000 $\mu\text{g.mL}^{-1}$ of Fe^{3+} in 5% HNO_3) up to desired concentration of 0.47 μM . These concentrations were chosen to be close to those used in biological experiments that have determined neuronal toxicities for the different metals. Subsequently, 5 cm of fiber were immersed into 10 ml of each metallic solution (each experiment was conducted in triplicate). The samples were stirred

at room temperature for one week. The amount of metals extracted by the fiber was determined using inductively coupled plasma mass spectrometry (ICP-MS) after the fibers were mineralized by microwave treatment with 3 ml of HNO₃ (69%). The analysis was performed using a Perkin Elmer NexION2000 equipped with Syngistix software (Perkin Elmer, Version 2.3) and ESI SC-FAST sample introduction in standard mode. The samples were prepared by dilution in an aqueous solution of 1% HNO₃ (v/v). Samples from the supernatant were also collected at different time points and analysed in the same manner as the mineralized fibers.

2.3. *Ex vivo* experiments

2.3.1. Ethical Approval

Animals (Wistar rats, males, body weight of appx 120 g) were kept in the animal facilities of the Palladin Institute of Biochemistry, National Academy of Sciences of Ukraine, housed in a temperature-controlled room (22–23°C), and provided *ad libitum* with water and standard diet using dry food pellets. The animal experiments were performed in accordance with the Guidelines of the European Community (2010/63/EU) and local laws and policies, and were approved by the Animal Care and Use Committee of the Palladin Institute (Protocol from September 21, 2020). All animal studies were reported in accordance to the ARRIVE guidelines for reporting experiments involving animals [33], [34]. The total number of rats used in the study was 48. Specifically, 48 animals were used for measuring the extracellular levels of L-[¹⁴C] glutamate and [³H] GABA in nerve terminals while 16 rats were shared for fluorimetry.

2.3.2. Materials

EGTA, EDTA, HEPES, Ficoll 400, Sigma-Fluor® High Performance LSC Cocktail, the analytical grade salts were purchased from Sigma (USA); L-[¹⁴C] glutamate and [³H] GABA (γ -[2,3-³H(N)]-aminobutyric acid) were from Perkin Elmer (Waltham, MA, USA). Rhodamine 6G were obtained from Molecular Probes (USA).

2.3.3. Statistical analysis

The experimental data were expressed as the mean \pm S.E.M. of *n* independent experiments. The difference between two groups was compared by one-way ANOVA. Differences were considered significant, when $p < 0.05$.

2.3.4. Isolation of nerve terminals (synaptosomes) from the cortex regions of the rat brains

The cortex brain region isolated from decapitated rats was rapidly removed, and then homogenized in the ice-cold solution containing 0.32 M sucrose, 5 mM HEPES-NaOH, pH 7.4, and 0.2 mM EDTA. Each synaptosome preparation was obtained from one rat, and each measurement was done in triplicate. The synaptosome preparations were obtained using differential and Ficoll-400 density gradient centrifugations of rat brain homogenate according

to previous works [35]. The synaptosome preparations were used in the experiments during 2 – 4 hours after isolation. The standard salt solution contained (in mM): NaCl 126; KCl 5; MgCl₂ 2.0; NaH₂PO₄ 1.0; HEPES 20, pH 7.4; and D-glucose 10. Total protein concentration in synaptosome preparation was examined according to Larson *et al.* [36].

2.3.5. The extracellular level of L-[¹⁴C] glutamate in the nerve terminal preparations

The synaptosome preparations were diluted in the standard salt solution to reach a concentration of 2 mg of total protein/ml, and after pre-incubation at 37 °C for 10 min were loaded with L-[¹⁴C] glutamate (2.81 μM, 1 μCi/ml) in the standard salt solution at 37 °C for 10 min. After such loading procedure, the synaptosome suspensions were washed with 10 volumes of ice-cold standard salt solution and centrifuged; the pellets were re-suspended in the standard salt solution to reach a final concentration of 1 mg of total protein/ml. Synaptosome suspensions (125 μl; 0.5 mg of total protein/ml) were pre-incubated at 37°C for 10 min; then pieces of the chitosan fiber were added and incubated with synaptosomes for 10 min, and then sedimented using a microcentrifuge (20 s at 10 000 g). The extracellular level of L-[¹⁴C] glutamate was recorded in the aliquots of supernatants (100 μl) and pellets using liquid scintillation counting with Sigma-Fluor® High Performance LSC Cocktail (1.5 ml), and the values were expressed as the percentage of total accumulated synaptosome L-[¹⁴C] glutamate [37], [38]. L-[¹⁴C] glutamate release data were collected in triplicate from several independent experiments performed with different synaptosome preparations.

2.3.6. The extracellular level of [³H] GABA in the nerve terminal preparations

The synaptosome preparations were diluted in the standard salt solution up to 2 mg of total protein/ml, and after their pre-incubation at 37°C for 10 min were loaded with [³H] GABA (50 nM, 4.7 μCi/ml) in the standard salt solution for 10 min. GABA transaminase inhibitor aminooxyacetic acid at a concentration of 100 μM was used in the experiments of [³H] GABA loading and release to minimize the formation of GABA metabolites. After loading, the synaptosome suspensions were washed with 10 volumes of ice-cold standard salt solution. The pellets were re-suspended in the standard salt solution to reach a protein concentration of 1 mg of total protein/ml. Synaptosome suspensions (120 μl) were pre-incubated at 37 °C for 10 min, then the pieces of the chitosan fibers were added and incubated for 10 min, and sedimented using a microcentrifuge (20 s at 10,000 g). [³H] GABA radioactivity was measured in the aliquots of supernatants (90 μl) by liquid scintillation counting with Sigma-Fluor® High Performance LSC Cocktail (1.5 ml), and the values were expressed as the percentage of total accumulated synaptosome [³H] GABA [39]. [³H] GABA release data were collected in triplicate from several independent experiments performed with different synaptosome preparations.

2.3.7. The plasma membrane potential (E_m) in nerve terminals

The membrane potential was measured using a potentiometric fluorescent dye rhodamine 6G (0.5 μM) based on its potential-dependent binding to the plasma membrane [38], [40], [41].

After preincubation at 37 °C for 10 min, the suspension of synaptosomes (0.2 mg of total protein/ml) was added to stirred thermostated cuvette. In order to estimate changes in the plasma membrane potential the ratio (F) as an index of membrane potential was calculated according to: $F = F_t/F_0$, where F_0 and F_t are fluorescence intensities of a fluorescent dye in the absence and presence of the synaptosomes, respectively. F_0 was calculated by extrapolation of exponential decay function to $t = 0$. Fluorescence measurements with rhodamine 6G were carried using a Hitachi 650-10 S spectrofluorimeter or a QuantaMasterTM 40 (PTI, Inc., Canada) spectrofluorimeter at 528 nm (excitation) and 551 nm (emission) wavelengths (slit bands 5 nm each).

2.4. *In vivo* feasibility study

2.4.1. Animals

Three female rats of Wistar strain (9 weeks old, 190 g) were used for *in vivo* experiments. Animals were procured from Janvier Laboratory (Le Genest-Saint-Isle, France). They were kept in standard housing conditions (12 h light-dark cycles) with a standard rodent chow and water available *ad libitum*.

2.4.2. Ethical approval

All animal procedures were performed in accordance with the rules of the European Committee Council Directive 2010/63/ EU after validation by our local ethical committee and authorization from the French Ministry of Research (University of Bordeaux, reference number 39329-2022033111368258).

2.4.3. Implantation of the fiber in the brain of rodents

During surgery, rats were anesthetized with 2.5% isoflurane in a mixture of air/O₂ (70/30) via a facial mask and fixed in a stereotaxic frame. After incision of the skull skin, a small hole was drilled in the skull using a 1 mm diameter drill bit for the insertion of the Gd-labeled chitosan chelating fiber. The hole was positioned +3 mm medio/lateral right hemisphere relative to bregma according to the atlas of the rat brain [42] for the implantation of the fiber in the right striatum. The device used for the implantation of the chelating fiber is shown in Figure 2. It consists of a polyimide cannula (with inner/outer diameter 190 μm/220 μm) glued to a support of sufficient size to be held by a stereotaxic device clamp. Once the cannula positioned in the center of the hole drilled in skull, the chelating fiber (3 mm long and ~180-μm diameter) was introduced into the cannula and pushed into the brain with a microwire (150-μm diameter) of insulated copper. Once the fiber positioned in the striatum, the cannula and copper wire were removed and the skin of the animal was stitched up.

Sterile surgical procedures were used for the implantation of the fiber, including moist heat sterilization of the cannula, copper wire and fiber itself. After surgery, the rats were housed individually and received doses of buprenorphine 0.05 mg/kg every 12 h for 48 h. The three

animals were then housed in the same cage. The weight of the animals was controlled every week.

2.4.4. MRI following of the degradation of the Gd-labeled chitosan fiber implanted in the brain

MRI experiments were performed on a preclinical 4.7-T Bruker BioSpec 47/20 MRI (Bruker BioSpin, Ettlingen, Germany) running under Paravision 6.0.1. A quadrature birdcage coil with inner diameter of 86 mm was used for RF excitation and a phased array surface coil dedicated to rat head for RF detection (Bruker, Ettlingen, Germany). One implanted animal was imaged at day 0, 3, 7 and then once a week up to 8 weeks. The follow-up MRI protocol included three MRI acquisitions with T_1 weighting (FLASH sequence, TE 3.5 ms, TR 200 ms, flip angle 60° , slice thickness 0.5 mm, in plane resolution 0.1×0.1 mm), T_2 weighting (TSE sequence, TE 36 ms, TR 2200 ms, slice thickness 0.5 mm, in plane resolution 0.14×0.14 mm) and T_2^* parametric imaging (MGE sequence, 12 echoes, TE 2.2 ms, TR 200 ms, slice thickness 0.5 mm, in plane resolution 0.14×0.14 mm). At each imaging session, the diameter and length of the implanted fiber was measured on the T_1 -weighted images. The SNR (signal-to-noise ratio) were measured in two regions of interest (ROIs) corresponding to the fiber and to brain tissue adjacent to the fiber. The T_2^* values (mean and standard deviation) were measured as well in these two ROIs. The CNRs (contrast-to-noise ratio) for T_1 and T_2 weighted acquisitions were computed as the difference between the SNRs of the fiber and brain tissue.

2.4.5. Histology of brain after sacrifice of the animals

All animals were euthanized past 3 months post implantation of the Gd-labeled chitosan fiber and their brain were collected for later analysis. In order to determine the amount of Gd in the brain and estimate the degradation of the fiber, one rat brain was divided into two hemispheres (left hemisphere and right hemisphere containing the fiber). Each hemisphere was mineralized using microwave treatment with 3 ml of HNO_3 (69%). The samples were prepared by dilution in an aqueous solution of 1% HNO_3 (v/v) and analysed by ICP-MS (samples were prepared and analysed in triplicates). In order to confirm resorption through the evolution of the size of the fiber and verify the integrity of the tissue, another brain was frozen and processed for histological staining. The forebrain was cut at $60 \mu\text{m}$ on a cryostat (-20°C ; CM1800, Leica, Paris France) in the coronal plane. Slices were directly placed on slides and stained with cresyl violet after progressive dehydration in baths of ascending concentration of alcohol. The striatum was observed under light microscope to evaluate the presence of gliosis surrounding the fiber and calculate the diameter of the fiber.

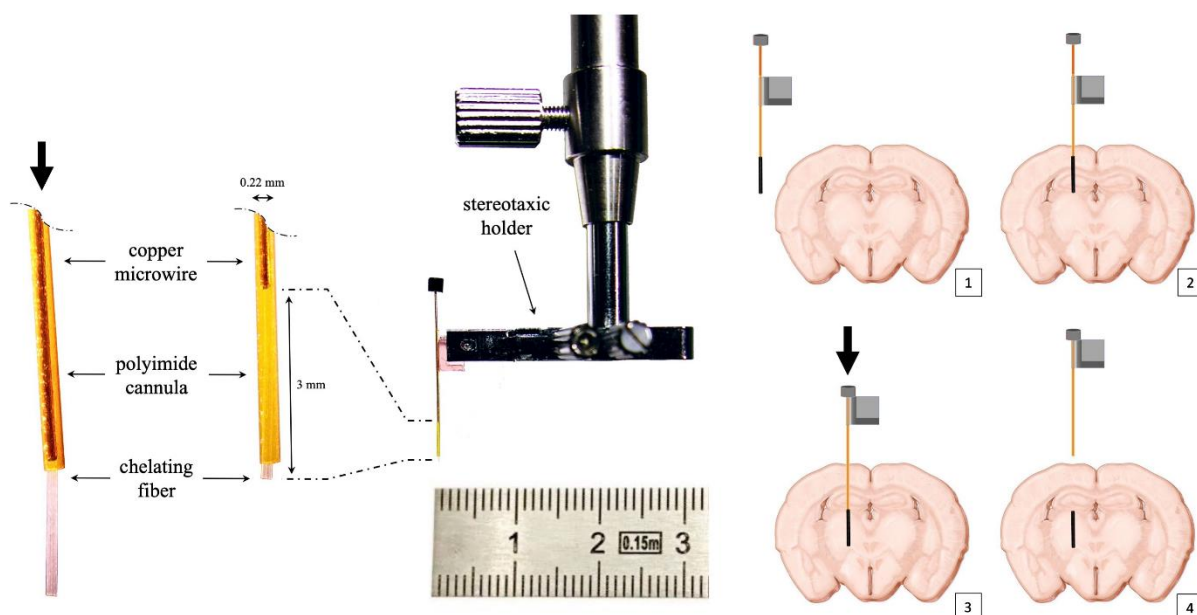


Figure 2. Photograph of the chelating fiber insertion device, in the center of the figure, with enlarged views of the cannula, fiber and copper microwire before and after insertion of the fiber. On the right side of the figure, the insertion procedure before implantation (1), after insertion of the cannula (2), after pushing the copper microwire (3), and after removal of the cannula from the brain (4).

3. Results

3.1. Formation of fibers and characterization of their chelating capacities

Chitosan@DOTAGA was obtained by direct functionalization of a low DA chitosan by DOTAGA anhydride in hydro-alcoholic media. The grafting ratio of $17.0 \pm 0.5\%$ was the higher ratio obtained by varying DOTAGA anhydride amounts in the reaction medium (data not shown). It was possible to obtain fibers from a dope consisting in a mixture of chitosan and Chitosan@DOTAGA with tunable diameters by varying conical spinneret diameters and velocities of the motorized bobbins on a lab-scale homemade apparatus (Figure 1). As previously highlighted, copper (II), cadmium (II), lead (II) and iron (III) are known to be neurotoxic. To assess the chelation efficacy of the fiber for these distinct metals, the fiber underwent exposure to $\sim 50 \mu\text{M}$ of CuSO_4 , $\sim 1 \text{ mM}$ of CdCl_2 , $\sim 2.5 \text{ mM}$ of $\text{Pb}(\text{NO}_3)_2$, and $0.47 \mu\text{M}$ of iron (III) in aqueous media, as illustrated in Figure 3A. Concentrations of metals have been chosen in order to be in line with the relevant concentrations used in the biological experiments

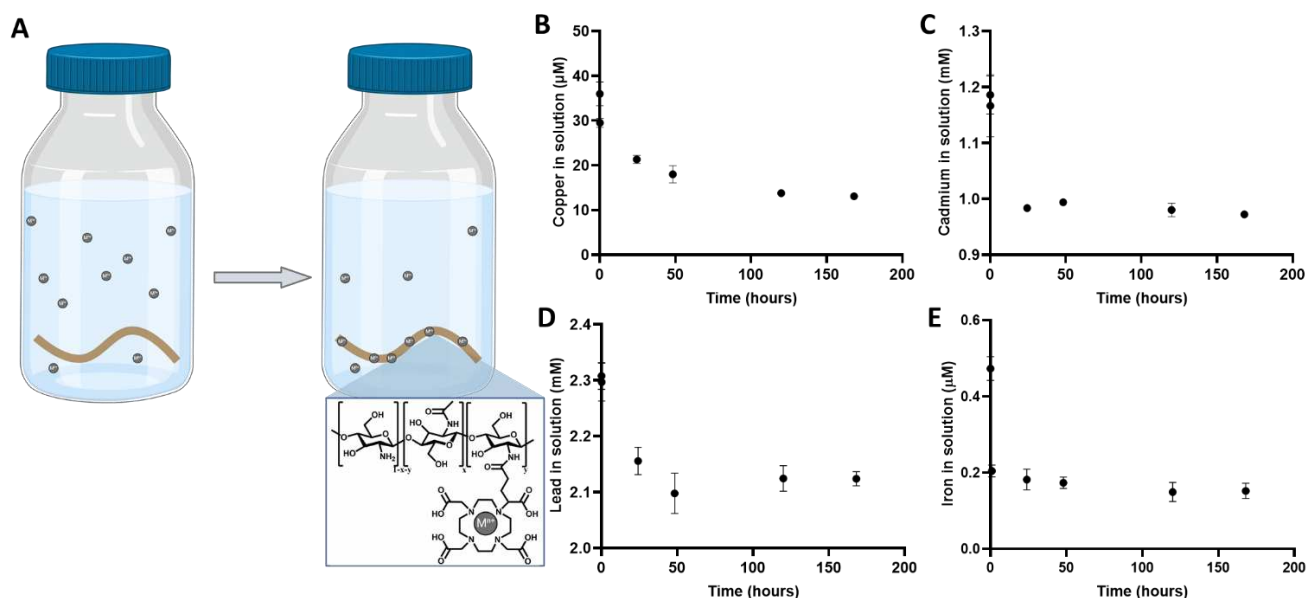


Figure 3. A representation of the chelation of metals by 5 cm of fiber in a metallic solution. Evolution **B** of copper (II) (CuSO_4 50 μM), **C** Cadmium (II) (CdCl_2 1 mM), **D** of Lead (II) ($\text{Pb}(\text{NO}_3)_2$ 2.5mM) and **E** of iron (III) (Fe-NTA 0.5 μM) concentrations over time in the presence of 5 cm of fiber in 10 ml of HEPES 20 mM pH 7.4 determined by ICP-MS. The solution containing lead (II) was at a lower pH (5.5) to avoid its precipitation.

Cadmium (II) ($11.86 \pm 0.34 \mu\text{mol}$) and lead (II) ($23.08 \pm 0.24 \mu\text{mol}$) are in large excess compared to the calculated amount of DOTAGA in 5 cm of fiber ($0.64 \mu\text{mol}$). However, in the case of the copper (II) solution ($0.36 \pm 0.03 \mu\text{mol}$), there is a slight excess of DOTAGA and in the case of the iron (III) solution, the DOTAGA present in the fibers is in large excess compared to the iron (III) ($4.7 \pm 0.3 \text{ nmol}$) in solution. Consequently, the ratios of $\text{M}^{n+}/\text{DOTAGA}$ varied to 18.6, 36, 0.6 and 0.007 for cadmium, lead, copper, and iron respectively. DOTA exhibits a strong complexation constant for the different studied metals as shown by the different complexation constants: $\text{Log}\beta_{\text{Pb II}} = 22.69$ [43], $\text{Log}\beta_{\text{Cd II}} = 21.3$ [44], $\text{Log}\beta_{\text{Cu II}} = 22.44$ [43] and $\text{Log}\beta_{\text{Fe III}} = 29.4$ [43].

By monitoring the metal concentrations in the supernatant over time using ICP-MS, it becomes apparent that the fiber extracts copper (II), cadmium (II), lead (II) and iron (III) from the solutions. Furthermore, the extraction equilibrium was achieved after 2 days for cadmium (II) and lead (II) (Figure 2B, D), whereas for copper (II) (Figure 2C), equilibrium was reached no earlier than the fifth day. The metallic extraction of the fiber was calculated from the ICP-MS analysis of the fibers by the following equation 1:

$$\text{Metallic extraction} = M^{n+} \text{ fiber}_f - M^{n+} \text{ fiber}_i \quad (1)$$

where $M^{n+} \text{ fiber}_f$ corresponds to the amount of metallic ion in the fiber at the end of the experiment, $M^{n+} \text{ fiber}_i$ the amount of metallic ion measured in the control fiber unexposed to metallic solution. The metallic extraction by the 5 cm fibers is as follows: $2.88 \pm 0.04 \mu\text{mol}$ for cadmium (II), $1.80 \pm 0.05 \mu\text{mol}$ for lead (II), $0.25 \pm 0.01 \mu\text{mol}$ for copper (II) and $3.3 \pm 0.2 \text{ nmol}$ for iron (III). Which represents $24.3 \pm 0.4\%$, $7.8 \pm 0.2\%$, $65.3 \pm 0.5\%$, and $70.7 \pm 5.1\%$ of extracted cadmium (II), lead (II), copper (II) and iron (III) respectively. The amount of metals

extracted for cadmium and lead exceeds the amount of DOTAGA present in the fiber (0.64 μmol). This suggests that not all metallic cations are chelated by DOTAGA, and some of the metals interact with chitosan. In fact, chitosan is well known to possess chelating properties [45], which are dependent on the nature of the cation as well as other species surrounding the cation, such as its counterion. This problem was previously addressed in the iron chelation experiment by introducing Na_2SO_4 [29], which is known to interact with chitosan by complexing with the amines moieties [46], [47]. This interaction prevents the NTA-Fe complex from interacting with chitosan. Therefore, in this experiment, iron (III) is effectively chelated by the DOTAGA present within the fiber. To account for the effect of the counterion on chitosan's chelation properties, future work should be conducted under conditions where the same counterion is used. No mercury chelation experiment was made due to the weak affinity of the DOTA chelator towards Hg(II) as shown by Randhawa *et al.* [48], although chitosan was reported to exhibit some mercury absorption capacity [49].

3.2. Assessment of neuro compatibility of the fiber using brain nerve terminals

The extracellular level of neurotransmitters in the nerve terminal preparations represents a dynamic balance of transporter-mediated uptake and release as well as unstimulated leakage of these neurotransmitters. This parameter is very sensitive to energy status of nerve terminals and plasma membrane integrity [50], [51].

In the first series of the experiments, the effects of the fiber together with its constituent DOTAGA on the extracellular level of neurotransmitters L- ^{14}C glutamate and ^3H GABA were assessed in the nerve terminal preparations. Two fiber lengths were analyzed (based on drafting DOTAGA chelating capability), i.e. 0.5 cm and 5 cm (with a fiber diameter close to 192 μm). It was shown that the fiber did not change the extracellular level of neither L- ^{14}C glutamate nor ^3H GABA (Table 2A). Whereas, DOTAGA starting from a concentration of 1.25 mM increased the extracellular level of L- ^{14}C glutamate and ^3H GABA in nerve terminal preparations (Table 2B).

Table. 2 The extracellular level of excitatory and inhibitory neurotransmitters L- ^{14}C glutamate and ^3H GABA, respectively, in the nerve terminal preparations in the presence of the fiber (A) and its constituent DOTAGA (B). Data are the mean \pm SEM. ***, $p < 0.001$; n.s., no significant differences as compared to the appropriate control.

Samples	The extracellular level of L- ^{14}C glutamate in the nerve terminal preparations, % of total accumulated label	The extracellular level of ^3H GABA in the nerve terminal preparations, % of total accumulated label
Control	17.91 \pm 0.59 %	18.84 \pm 0.51 %
Chitosan 5% Chitosan@DOTAGA 10%. Fiber length: 0.5 cm	17.46 \pm 0.53 %; n.s. [F _(1,94) = 0.34; p = 0.55; n = 48]	18.53 \pm 0.42 %; n.s. [F _(1,94) = 0.22; p = 0.63; n = 48]

Chitosan 5% Chitosan@DOTAGA 10% Fiber size 5 cm	18.37 ± 0.62 %; n.s. [F _(1,94) = 0.28; p = 0.59; n = 48]	18.41 ± 0.43 %; n.s. [F _(1,94) = 0.42; p = 0.51; n = 48]
---	--	--

B

Samples	The extracellular level of L-[¹⁴ C] glutamate in the nerve terminal preparations, % of total accumulated label	The extracellular level of [³ H] GABA in the nerve terminal preparations, % of total accumulated label
Control	19.34 ± 0.46 %	17.11 ± 0.54 %
DOTAGA (0.5 mM)	18.65 ± 0.73 %; n.s. [F _(1,60) = 0.67; p = 0.41; n = 16]	17.64 ± 0.67 %; n.s. [F _(1,60) = 0.39; p = 0.53; n = 16]
DOTAGA (1.25 mM)	29.90 ± 1.17% *** [F _(1,60) = 75.32; p < 0.001; n = 16]	26.02 ± 0.71%*** [F _(1,60) = 106.81 p < 0.001; n = 16]
DOTAGA (5 mM)	90.25 ± 1.13% *** [F _(1,60) = 3582.97; p < 0.001; n = 16]	91.59 ± 1.27%*** [F _(1,60) = 3103.76 p < 0.001; n = 16]

The membrane potential was monitored using the potential-sensitive fluorescent dye rhodamine 6G. F_{st} , the membrane potential index at the steady state level, was first achieved after 5 min, and it was set as 100% in statistical calculations. In such fluorometric experiments, shown in Figure 4 A and B, it can be concluded that the fiber did not change the membrane potential of nerve terminals and, therefore, so did not depolarize their plasma membrane. On the contrary, DOTAGA molecule starting from a concentration of 1.25 mM depolarized the plasma membrane of nerve terminals (Figure 4B).

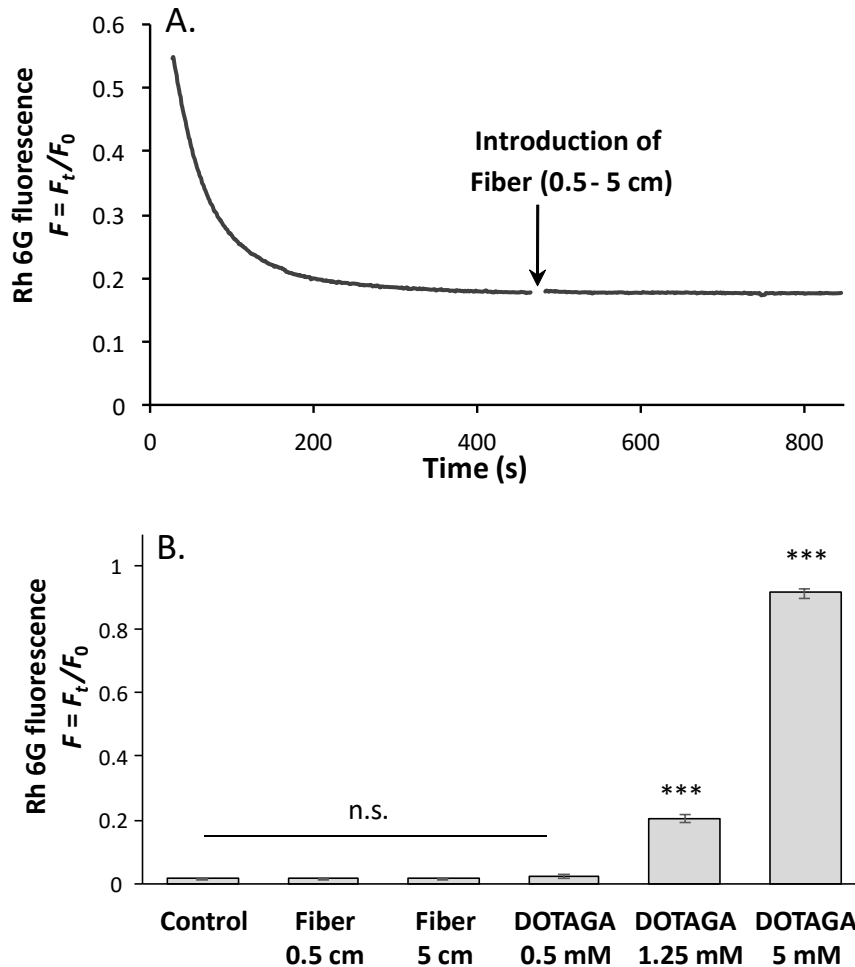


Figure 4. Fluorescence experiments: The membrane potential of nerve terminals in the presence of the fiber (0.5 - 5 cm) (**A**, **B**) and DOTAGA alone (**B**). **A** – The suspensions of synaptosomes were equilibrated with potential-sensitive dye rhodamine 6G (0.5 mM). When the steady level of the dye fluorescence had been reached, the fiber was added to synaptosomes (marked by arrows). Traces are typical and represent 16 experiments performed with different synaptosome preparations. **B** – An increase in the fluorescence signal of rhodamine 6G in response to application of water (control), the Chitosan 5% Chitosan@DOTAGA 10% fibers (0.5 - 5 cm), DOTAGA (0.5 – 5 mM). Data are the mean \pm SEM. ***, $p < 0.001$ as compared to the control; n.s., no significant differences; $n = 16$.

Consequently, the fiber did not have any effects on the extracellular level of the neurotransmitters and the membrane potential of nerve terminals, whereas its constituent DOTAGA starting from a concentration of 1 mM increased this level and depolarized the plasma membrane of nerve terminals. Therefore, the grafted macromolecular structure of chitosan@DOTAGA and the fiber microstructure overcome the neurotoxic features of its exhibited by free DOTAGA.

3.3. Capability of the Chitosan 5% Chitosan@DOTAGA 10% fiber to mitigate the extracellular level of L-[¹⁴C] glutamate induced by copper, mercury, cadmium, and lead in nerve terminal preparations

All experimental data were analyzed by two-way ANOVA followed by Tukey's post hoc test using the fiber and CuSO₄/HgCl₂/CdCl₂/PbAc presence as the independent factors. As shown in Figure 5, different concentrations of metals are necessary to induce significant increase of the extracellular level of L-[¹⁴C] glutamate in nerve terminal preparations ranging from 8 μM for HgCl₂ to 2.5 mM for PbAc. Interestingly, these concentrations are in the μM range for HgCl₂ and CuSO₄ and in the mM range for CdCl₂ and PbAc. The fiber mitigated Cu (II) (Figure 5A), Cd (II) (Figure 5C) and Pb (II) (Figure 5D)-induced increase in the extracellular level of L-[¹⁴C] glutamate in nerve terminal preparation in a dose-dependent manner, contrary to Hg (II) where no significant change is observed for the two fibers (Figure 5B).

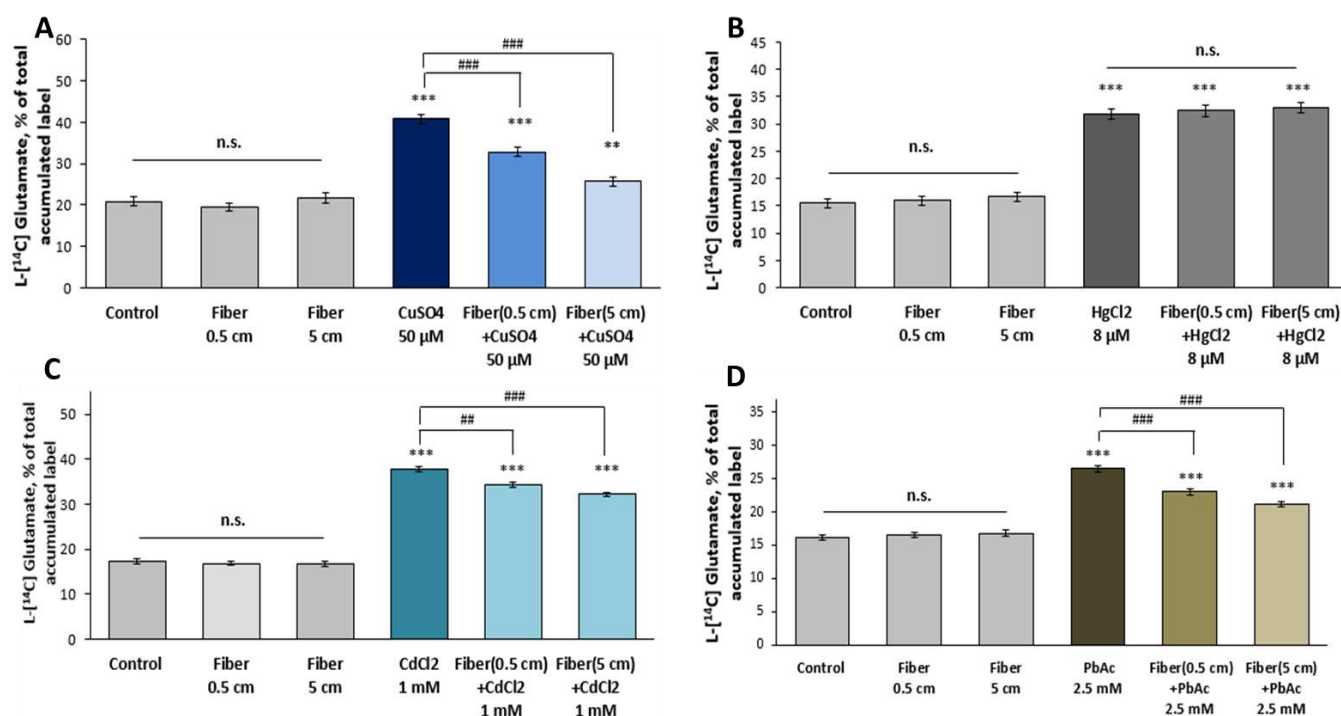


Figure 5. The extracellular level of L-[¹⁴C] glutamate in the nerve terminal preparations in the control and in the presence of the fiber (0.5 and 5 cm) and CuSO₄ (50 μM) (A); HgCl₂ (8 μM) (B); CdCl₂ (1 mM) (C); PbAc (2.5 mM) (D). Data are the mean ± SEM. ***, $p < 0.001$; **, $p < 0.01$ as compared to the appropriate control; ###, $p < 0.001$; ##, $p < 0.01$ as compared to the appropriate metal; n.s., no significant differences; $n = 16$.

3.4. Capability of the Chitosan 5% Chitosan@DOTAGA 10% fiber to mitigate changes in the extracellular level of [³H] GABA induced by copper, mercury, cadmium, and lead in nerve terminal preparations

All experimental data were also analyzed by two-way ANOVA followed by Tukey's post hoc test using the fiber and CuSO₄/HgCl₂/CdCl₂/PbAc as the independent factors in these experiments. Interestingly, the same concentrations of metallic cations also induce significant increase of the extracellular level of [³H] GABA in nerve terminal preparation (Figure 6). Similarly, a mitigation of the effect of the metals is also observed in a dose dependent manner

for Cu (II) (Figure 6A), Cd (II) (Figure 6C) and Pb (II) (Figure 6D) while no mitigation is observed for Hg (II) (Figure 6B).

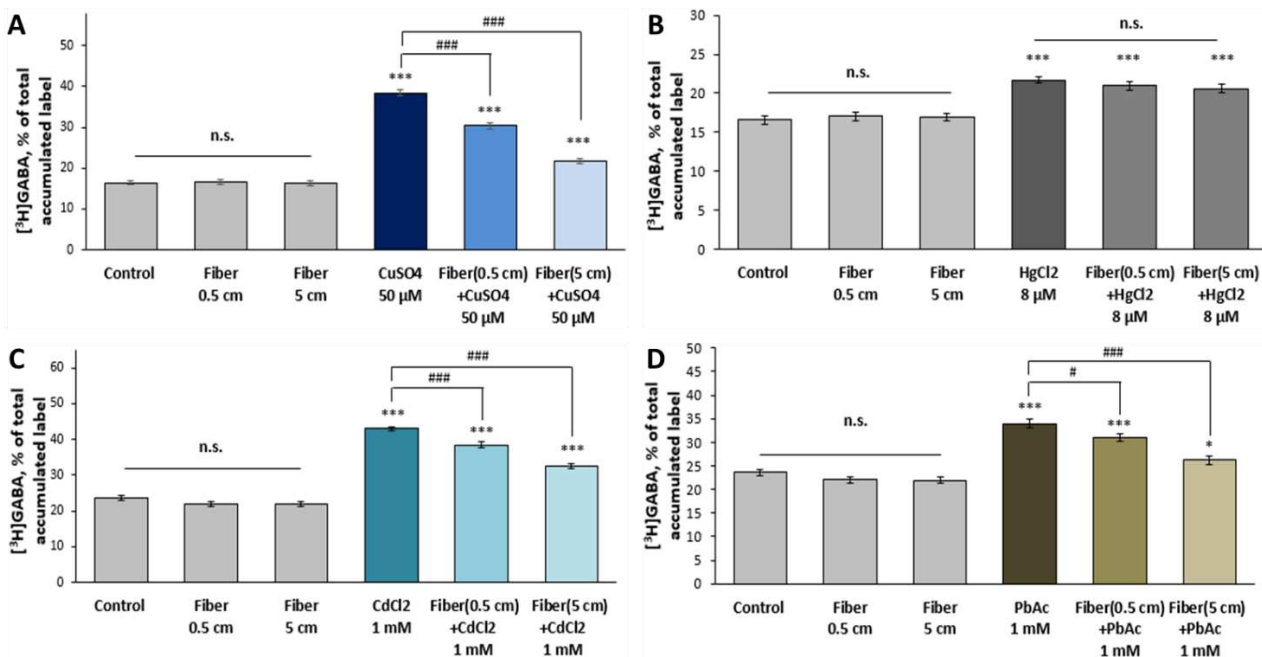


Figure 6. The extracellular level of [³H]GABA in the nerve terminal preparations in the control and in the presence of the fiber (0.5 and 5 cm) and CuSO₄ (50 μM) (A); HgCl₂ (5 μM) (B); CdCl₂ (1 mM) (C); PbAc (1 mM) (D). Data are the mean ± SEM. ***, *p* < 0.001; *, *p* < 0.05 as compared to the appropriate control; ###, *p* < 0.001; #, *p* < 0.05 as compared to the appropriate metal; n.s., no significant differences; *n* = 16.

3.5. Assessment of biocompatibility of the fiber and biodegradability

3.5.1. *In vivo* studies and MRI following of the biodegradability

If one except the first day following the surgery, the animals did not show signs of physical suffering, discomfort and abnormal behavior during the three months post-fiber implantation. Their weight increased in average from 190 to 300 g during these three months.

A selection of MRI images acquired post implantation of the fiber are shown in Figure 7.A-D3. A slice of a T₁-weighted MRI coronal acquisition acquired at J0 is shown in Figure 7 A; the white spot pointed by the red arrow corresponding to the implanted fiber. T₁-weighted sagittal images featuring the fiber acquired at J0, J21 and J49 are presented in Figure 7 B1-3. The corresponding T₂-weighted images and T₂^{*} maps are shown respectively in Figure 7 C1-3 and D1-3.

After 3 hours of implantation, the length of the implanted Chitosan 5% Chitosan@DOTAGA 8% Chitosan@DOTAGA-Gd 2% fiber, as assessed on sagittal T₁-weighted images, were measured to be close to the initial length before implantation (*i.e.* *L*=3mm). However, the diameter of the fiber increased from 180 μm before implantation to a value ranging between 300 and 400 μm due to high (anisotropic) swelling properties of the material in aqueous medium as illustrated in Figure 1.B. The length and diameter of the

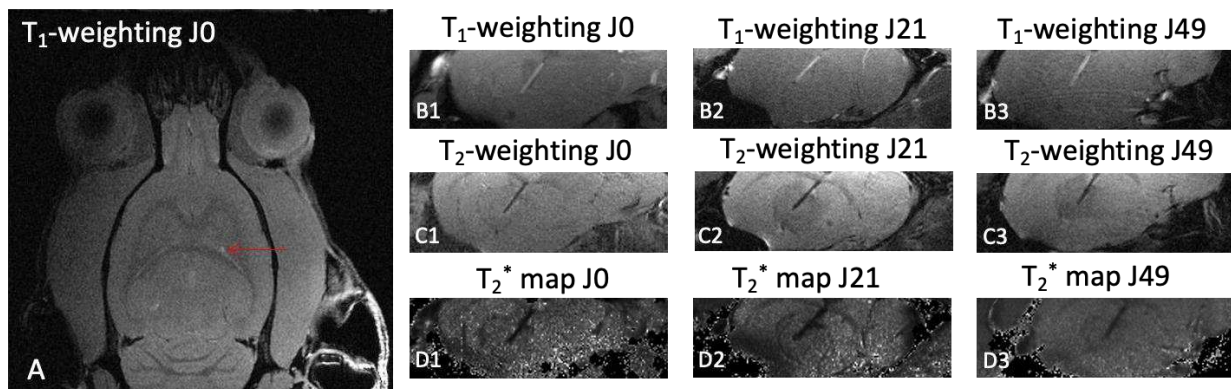
implanted fiber did not exhibit significant changes during the first 7 weeks of follow-up. However, after the 13th week, a notable difference was observed when measuring the fiber section, i.e. the fiber area in the transverse plane. We observed a decrease in the fiber area from $1.15 \pm 0.29 \text{ mm}^2$ after 3 hours of implantation to $0.69 \pm 0.23 \text{ mm}^2$ at the conclusion of the experiment (17th week). This corresponds to a $40.6 \pm 5.1\%$ degradation of the fiber (figure 7 E-F) assessing the biodegradable properties of the implanted materials. Conversely, ICP-MS analysis of one of the brains reveals that 46% of the total Gd is undetected within the fiber's zone, confirming that approximately half of the fiber has degraded after 17 weeks of implantation in the rat's brain.

The Contrast to Noise Ratio (CNR) between the fiber and the adjacent brain tissue for the T₁-weighted acquisition ranged from 5.5 to 11 (initial value equal to 8 and typical standard deviation value equal to 2). These positive values reflect the hyperintense MRI intensities in the fiber, presumably due to the presence of the chelated gadolinium ion acting as positive contrast agent, permanently chelated with DOTAGA grafts.

The CNR between the fiber and the adjacent brain tissue for the T₂-weighted acquisition ranged from -5.4 to -9.5 (similar initial and final values and typical standard deviation value equal to 3). These negative values reflect the hypointense MRI intensities in the fiber, again presumably due to the presence of the chelated gadolinium ion acting as negative contrast agent and to numerous labile relaxing protons from hydroxyl and amine groups in the chitosan polymer.

The T₂^{*} values measured in the fiber ranged from 16 ms to 19.7 ms with typical standard deviation equal to 5 ms. These values were lower to those obtained in adjacent brain tissue (35 to 51 ms) and are probably related to the presence of the chelated gadolinium ions.

No trend in the temporal evolution of CNR and T₂^{*} values could be evidenced with certainty. The corresponding graphs are available in supplementary information file (See Supporting Information Figure S6).



E

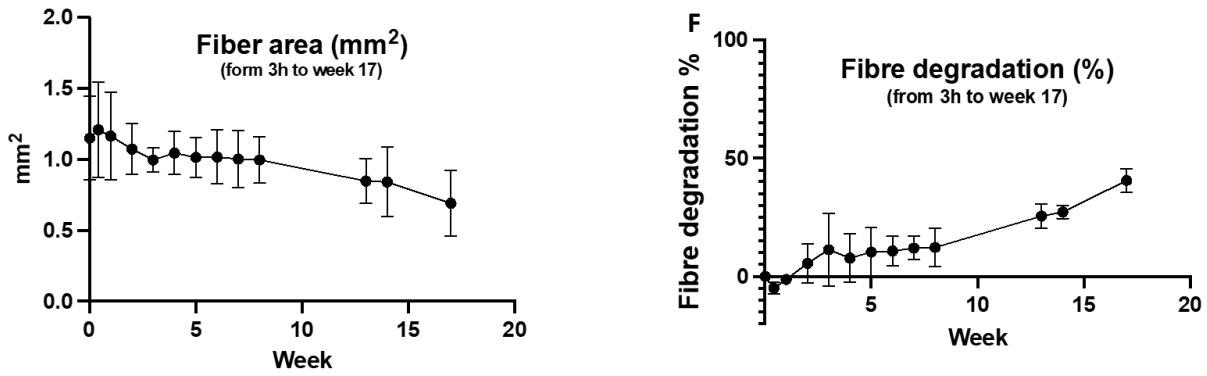


Figure 7. A-D) MRI slices including the chelating fiber acquired with different MRI contrast (T_1 and T_2 weighting and quantitative T_2^* map) at three time points (J0, J21 and J49). E) Variation of the area of the fiber measured by MRI over time in the transverse plane. F) Degradation of the fiber depicted by the decrease of the fiber area over time, as determined from MRI images (transverse plane).

3.5.2. Histology after sacrifice of the rodents

The histological analysis confirmed the presence of the fiber in the striatum (Figure 8A). It was observed on three adjacent cuts of 60 μm width. Correspondingly, its thickness was calculated at higher magnification and was close to 130 μm (Figure 8B), evidencing again bioresorption with a decrease in diameter in comparison with the initial fibers (182 μm). The histological analysis of these slices revealed absence of gliosis in the tissue surrounding the fiber (Figure 8A/B).

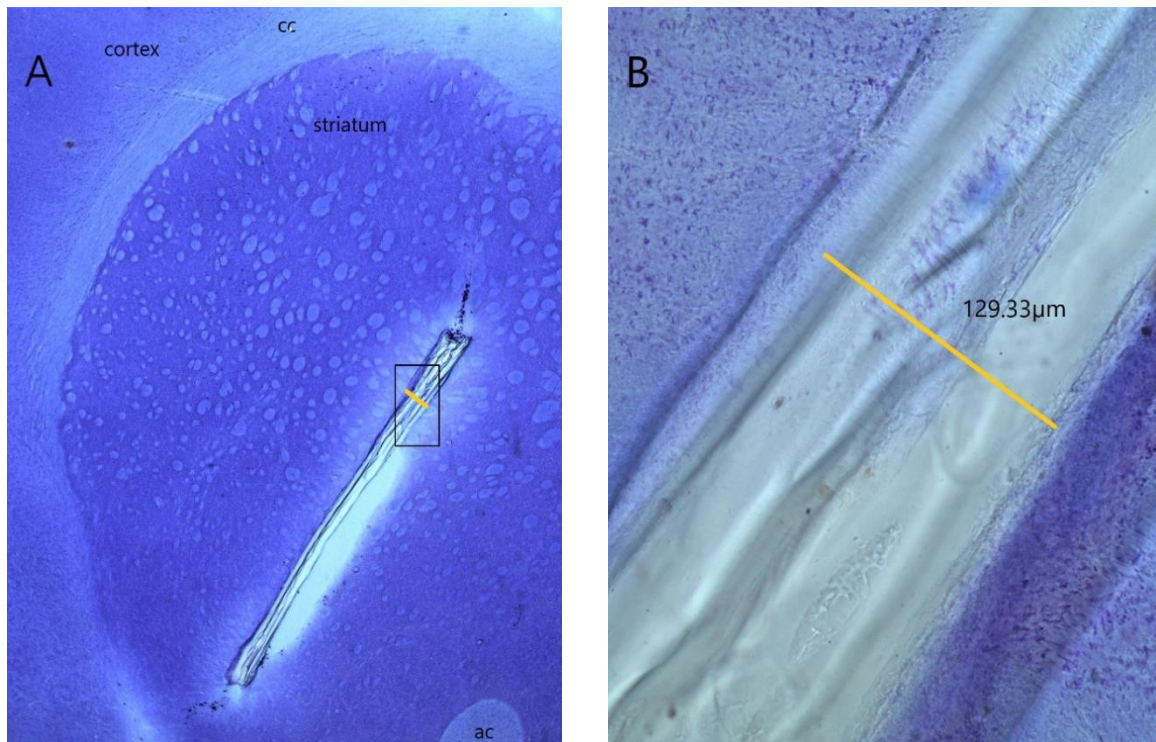


Figure 8. Histological analysis of the fiber in the striatum at low (A) or high (B) magnification. The yellow line corresponds to the thickness of the fiber (130 μm). No sign of gliosis was observed at low and high magnification. cc, corpus callosum; ac, anterior commissure.

4. Discussion

Polluted environmental metal overloads and endogenous metallic deregulation were more and more positively correlated with etiology neurological diseases, e.g. Wilson disease, neurodegeneration with brain iron accumulation, Alzheimer's disease, Parkinson's disease [52]. We hereby report the safety and efficacy of fibers prepared from metal chelator-grafted chitosan, *ex vivo* on rat brain synaptosomes and *in vivo* in the rat striatum. Our data showed that the fiber attenuates the effects of most heavy metals application on both glutamate and GABA extracellular levels, while its presence in the brain was stable for several weeks without any sign of tissue alteration, and displays quantifiable biodegradability. The strategy of such experimental developments is to further implant the fiber in specific brain regions in neurological diseases where the accumulation of heavy metals is supposed to be toxic.

Here, we demonstrated that copper, mercury, cadmium, and lead increased the extracellular level of L-[^{14}C]glutamate and [^3H]GABA in nerve terminals with different potency and efficiency (Fig. 5 and 6). Notably, the addition of 50 μM Cu(II) to the nerve terminals induced a two-fold increase in the extracellular levels of L-[^{14}C]glutamate and even more in the extracellular levels of [^3H]GABA. 8 μM Hg(II) was sufficient to enhance the extracellular levels of both neurotransmitters, but the efficacy was similar compared to Cu(II) for glutamate, and weaker for GABA. The effects produced by Cd(II) application (1 mM) were similar for both neurotransmitters (approximately doubled), whereas lead application (2.5 mM) was slightly less efficacious with similar efficacy on both neurotransmitters. The distinct actions of these metals in terms of potency and/or efficacy towards glutamatergic versus GABAergic nerve terminals suggested the contribution of various the mechanisms triggered by heavy metals on these terminals. The mechanisms are likely complex as the measured transmitters are related to a dynamic balance of neurotransmitter uptake and tonic unstimulated release [50], [51]. The reported increase is therefore not necessarily related to an increase in the Ca(II)-dependent, vesicular exocytosis as evidenced with Cd(II) which is a non-selective blocker of Ca(II) channels [53].

One of the important findings of the study was the fact that the fiber by itself did not have any effects on the extracellular levels of neurotransmitters and the membrane potential of nerve terminals. Meanwhile, its constituent DOTAGA alone induced a concentration-dependent increase in both glutamate and GABA extracellular levels and depolarized the plasma membrane of nerve terminals. Therefore, the chemical grafting of DOTAGA on chitosan and chitosan association (co-crystallization) in the fiber prevents its potential neurotoxic features. These data are in agreement with our recent data regarding the action of DOTAGA alone and as a constituent of gadolinium-based AGuIX nanoparticles for brain metastases treatment: the constituents DOTAGA and mixture DOTAGA/Gd(III) significantly affected synaptic neurotransmission at high concentrations, whereas AGuIX own structure suppressed neurotoxic features of their constituents [54]. This important experimental observation is crucial in the perspective of building new therapeutic avenues aimed at chelating

iron in Parkinson's disease using deferiprone. Oral deferiprone actually worsened the clinical picture of patients in a double-blind controlled study [55], an effect that could be attributed to its own direct activity in neurotransmitters. Even if it is difficult to compare the number of DOTAGA molecules free in solution or grafted on chitosan in our study, the attachment of DOTAGA on the fiber preserved any toxic action within cells at local and distal locations while keeping the efficacy to chelate several metal ions.

The fiber was able to mitigate metal-induced increase in the extracellular level of L- $[^{14}\text{C}]$ glutamate and $[^3\text{H}]$ GABA in nerve terminals with the highest efficiency against the effects induced by Cu(II) and Pb(II), followed by Cd(II). The beneficial effect of the fiber was attributed to the chelation properties of the grafted chelator DOTAGA acknowledging that a variety of metal ions could competitively bind the chelator. The identity of the metal predominantly bound by a chelating agent depends on factors such as the accessibility of the chelator to the tissues, the strength of the metal's existing binding in the tissues, the affinity of the metal for the chelator, and to some extent, the relative quantities of various ions [14]. As evidenced by the ICP-MS analysis of the chelation experiment, the fiber demonstrated the ability to chelate copper (II), cadmium (II), and lead (II) in a physiological solution. Furthermore, the mitigation of the increased extracellular release of both excitatory and inhibitory neurotransmitters was dependent on the length of the fiber, with greater effectiveness observed with longer fiber sizes. The efficacy of the fiber could also be due to antioxidant properties of Chitosan@DOTAGA previously shown in another study [23]. Nevertheless, the fiber was unable to diminish Hg(II)-induced increases in the extracellular levels of both neurotransmitters in nerve terminals. Several studies have reported that mercury increased glutamate concentration at the synaptic cleft [56] and could raise the oxidative metabolism. Since chelation of Hg(II) by the fibers were not significant, it suggests that the antioxidant properties of Chitosan@DOTAGA fiber are perhaps not sufficient to counteract Hg(II) noxious effects. Therefore, the lack of effect of the fiber against Hg(II)-induced increases in the extracellular levels of glutamate and GABA was presumably due to the stronger interaction of Hg(II) with synaptosome membrane components and the weak affinity of DOTAGA towards Hg(II) [48], [56], [57]. Moreover, based on the lack of effect of the fiber on the extracellular levels of neurotransmitters whatever its length (0.5 or 5 cm), it could be suggested that the fiber did not have critical effects on the concentrations of physiological metal ions essential for neurotransmission such as Ca(II) or Mg(II).

The feasibility of inserting the fiber into the brain of animal models to study their behavior over weeks are fundamental steps toward any potential clinical application. The present results showed that the implantation of chelating fibers in the rat striatum could be well tolerated up to 17 weeks. Magnetic resonance imaging showed that the chelating fiber can be accurately inserted into the striatum under stereotactic conditions. It was observed that the fiber did not overextend once implanted into the brain. Instead, it was found that its initial area measured the day of implantation was stable during 7 weeks and then progressively shrank to reach 60% of its initial area at the completion of the experiment (17 weeks). The incorporation of gadolinium ions in a fraction of the DOTAGA chelates proved to be useful to improve the MRI contrast between the chelating fiber and the surrounding brain tissue. In line with the thickness reduction of the fiber at completion of the experiment, ICP-MS analysis of the brain hemispheres reveals that 46% of the total Gd was lost within the fiber's zone (right hemisphere).

These findings strongly suggested that the fiber was biodegradable, DOTAGA-M complexes being stage and eliminated by the kidneys. Moreover, no acute or subchronic inflammatory reaction due to the presence of the fiber could be observed in any type of MRI image *in vivo* as well as under subsequent histological examination of the tissue *ex vivo*. These findings were in agreement with the known good biocompatibility of the chitosan polymer, and its application for the design of neuro-regenerative implants in the central nervous system [20], [58].

5. Conclusion

In summary, the present study demonstrated that the fiber was neuro compatible in contrast to its isolated DOTAGA constituent. The functionalization of the DOTAGA on the polymer seems to eliminate neurotoxic features of the DOTAGA constituent. The fiber was effective in decreasing the damaging effects of copper, cadmium and lead (but not mercury) on key parameters of the synaptic neurotransmission in nerve terminals. A first *in vivo* proof of concept has shown that the fiber can be safely implanted in the brain of rodents with no sign of neurotoxicity. Interestingly, biodegradability of the fiber has been proven by investigating fiber features using MRI and ICP-MS. All these data pave the way of further preclinical experiments on appropriate animal models of neurological disorders known to be related with metallic dis-homeostasis.

Declarations

Competing interests: The authors declare no financial and non-financial competing interests exist.

Authors' contributions: TB, VL, YC, LD, FL, OT – conceptualisation; AP – isolation of synaptosomes; AP, NK, NP – L-[¹⁴C] glutamate measurements and fluorimetry; NP, MD, NK – [³H] GABA measurements; NP, NK, TB, LD, FL – data analysis; JFAS, NP, LD, YC, FL – figure preparation; TB– the design of the neurochemical study; TB, JFAS LD, FL - draft manuscript writing; NP, JD, IB and YC - the design, implementation, execution and analysis of the *in vivo* and MRI study. The manuscript was edited by TB, JPSA, PD, FL, LD, OT. All authors read and approved the final manuscript.

Acknowledgements: This work was supported by the National Research Foundation of Ukraine, Project #2021.01/0061 (AP, MD, TB - neurochemistry study using Hg, Cd and Pb), Project of Polish Academy of Sciences within the “Long-term program to support Ukrainian research teams” PAN.BFB.S.BWZ.380.022.2023 (NK, TB - neurochemistry study using Cu), and EU Horizon 2020 Research and Innovation Staff Exchange Programme (RISE) under Marie Skłodowska-Curie Action (project 101008159 “UNAT”). The work was supported by French Agence Nationale de la Recherche ANR (ANR SEMB ANR-20-CE19-0011). The authors acknowledge MexBrain company for furnishing chitosan based polymer.

References

[1] G. Deuschl, E. Beghi, F. Fazekas, T. Varga, K. A. Christoforidi, E. Sipido, C. L. Bassetti, T. Vos, V. L. Feigin, The burden of neurological diseases in Europe: An analysis for the Global Burden of Disease Study 2017. *The Lancet. Public Health*, **5**, e551–e567 (2020)

- [2] C. Alquezar, J. B. Felix, E. McCandlish, B. T. Buckley, D. Caparros-Lefebvre, C. M. Karch, L. I. Golbe, A. W. Kao, Heavy metals contaminating the environment of a progressive supranuclear palsy cluster induce tau accumulation and cell death in cultured neurons. *Scientific Reports*, **10**, 569 (2020).
- [3] C. M. Opazo, M. A. Greenough, A. I. Bush, Copper: From neurotransmission to neuroproteostasis. *Frontiers in Aging Neuroscience*, **6**, 143 (2014).
- [4] Z. Tümer, L. B. Møller, Menkes disease. *European Journal of Human Genetics*, **18**, 5 (2010).
- [5] J. J. V.Branca, C. Fiorillo, D. Carrino, F. Paternostro, N. Taddei, M. Gulisano, A. Pacini, M. Becatti, Cadmium-Induced Oxidative Stress: Focus on the Central Nervous System. *Antioxidants*, **9**, 492 (2020).
- [6] D. Ramírez Ortega, D. F. González Esquivel, T. Blanco Ayala, B. Pineda, S. Gómez Manzo, J. Marcial Quino, P. Carrillo Mora, V. Pérez de la Cruz, Cognitive Impairment Induced by Lead Exposure during Lifespan: Mechanisms of Lead Neurotoxicity. *Toxics*, **9**, 23 (2021).
- [7] J. Emerit, C. Beaumont, F. Trivin, Iron metabolism, free radicals, and oxidative injury. *Biomedicine & Pharmacotherapy*, **55**, 333–339 (2001).
- [8] S. Apostolakis, A. M. Kypraiou, Iron in neurodegenerative disorders: Being in the wrong place at the wrong time? *Reviews in the Neurosciences*, **28**, 893–911 (2017).
- [9] C. Moreau, J. A. Duce, O. Rascol, J. C. Devedjian, D. Berg, D. Dexter, Z. I. Cabantchik, A. I. Bush, D. Devos, D., FAIRPARK-II study group, Iron as a therapeutic target for Parkinson's disease. *Movement Disorders: Official Journal of the Movement Disorder Society*, **33**, 568–574 (2018).
- [10] M. Lavados, M. Guillón, M. C. Mujica, L. E. Rojo, P. Fuentes, R. B. Maccioni, Mild Cognitive Impairment and Alzheimer Patients Display Different Levels of Redox-Active CSF Iron. *Journal of Alzheimer's Disease*, **13**, 225–232 (2008).
- [11] Z. Chen, C. Gao, Y. Hua, R. F. Keep, K. Muraszko, K., G. Xi, Role of Iron in Brain Injury After Intraventricular Hemorrhage. *Stroke*, **42**, 465–470 (2011).
- [12] J. Wu, Y. Hua, R. F. Keep, T. Nakamura, J. T. Hoff, J. G. Xi, Iron and Iron-Handling Proteins in the Brain After Intracerebral Hemorrhage. *Stroke*, **34**, 2964–2969 (2003).
- [13] M. Zhang, W. Li, T. Wang, Q. Zhang, Association Between Baseline Serum Ferritin and Short-term Outcome of Intracerebral Hemorrhage: A Meta-Analysis. *Journal of Stroke and Cerebrovascular Diseases*, **28**, 1799–1805 (2019).
- [14] M. E. Sears, Chelation: Harnessing and Enhancing Heavy Metal Detoxification—A Review. *The Scientific World Journal*, e219840 (2013).
- [15] P. Hedera, Clinical management of Wilson disease. *Annals of Translational Medicine*, **9**, Suppl 2 (2019).
- [16] P. B. Foley, D. J. Hare, K. L. Double, A brief history of brain iron accumulation in Parkinson disease and related disorders. *Journal of Neural Transmission*, **129**, 505–520 (2022).
- [17] T. Hyakumura, U. Aregueta-Robles, W. Duan, J. Villalobos, W. K. Adams, L. Poole-Warren, J. B. Fallon, Improving Deep Brain Stimulation Electrode Performance in vivo Through Use of Conductive Hydrogel Coatings. *Frontiers in Neuroscience*, **15**, 761525 (2021).
- [18] O. Kapusta, A. Jarosz, K. Stadnik, D. A. Giannakoudakis, B. Barczyński, M. Barczak, Antimicrobial Natural Hydrogels in Biomedicine: Properties, Applications, and Challenges—A Concise Review. *International Journal of Molecular Sciences*, **24**, 2191 (2023).

- [19] H. Amiri, M. Aghbashlo, M. Sharma, J. Gaffey, L. Manning, S. M. Moosavi Basri, J. F. Kennedy, V. K. Gupta, M. Tabatabaei, Chitin and chitosan derived from crustacean waste valorization streams can support food systems and the UN Sustainable Development Goals. *Nature Food*, **3**, 822–828 (2022).
- [20] J. Chedly, S. Soares, A. Montembault, Y. von Boxberg, M. Veron-Ravaille, C. Mouffle, M. N. Benassy, J. Taxi, L. David, F. Nothias, Physical chitosan microhydrogels as scaffolds for spinal cord injury restoration and axon regeneration. *Biomaterials*, **138**, 91–107 (2017).
- [21] Y. Iqbal, I. Ahmed, M. F. Irfan, S. A. S. Chatha, M. Zubair, A. Ullah, Recent advances in chitosan-based materials; The synthesis, modifications and biomedical applications. *Carbohydrate Polymers*, **321**, 121318 (2023).
- [22] A. Montembault, C. Viton, A. Domard, Rheometric Study of the Gelation of Chitosan in Aqueous Solution without Cross-Linking Agent. *Biomacromolecules*, **6**, 653–662 (2005).
- [23] A. Montembault, K. Tahiri, C. Korwin-Zmijowska, X. Chevalier, M. T. Corvol, A. Domard, A material decoy of biological media based on chitosan physical hydrogels: Application to cartilage tissue engineering. *Biochimie*, **88**, 551–564 (2006).
- [24] S. Peers, A. Montembault, C. Ladavière, Chitosan hydrogels for sustained drug delivery. *Journal of Controlled Release*, **326**, 150–163 (2020).
- [25] C. Grange, A. Aigle, V. Ehrlich, J. Salazar Ariza, T. Brichtart, F. Da Cruz-Boisson, L. David, F. Lux, O. Tillement, Design of a water-soluble chitosan-based polymer with antioxidant and chelating properties for labile iron extraction, *Sci. Rep.*, **13**, 7920 (2023).
- [26] M. Natuzzi, C. Grange, T. Gréa, T. Brichtart, A. Aigle, D. Bechet, B. Hautefeuille, E. Thomas, J.-Y. Ayoub, J.-M. Bonnet, V. Louzier, B. Allaouchiche, A. Couturier, A. Montembault, P. Nunes de Oliveira, L. David, F. Lux, O. Tillement, Feasibility study and direct extraction of endogenous free metallic cations combining hemodialysis and chelating polymer, *Sci. Rep.*, **11**, 11948 (2021).
- [27] E. Ficiarà, C. Molinar, S. Gazzin, S. Jayanti, M. Argenziano, L. Nasi, F. Casoli, F., Albertini, S. A. Ansari, A. Marcantoni, G. Tomagra, V. Carabelli, C. Guiot, F. D'Agata, R. Cavalli, Developing Iron Nanochelating Agents: Preliminary Investigation of Effectiveness and Safety for Central Nervous System Applications, *International Journal of Molecular Sciences*, **25**, 729 (2024).
- [28] T. Gréa, G. Jacquot, A. Durand, C. Mathieu, A. Gasser, C. Zhu, M. Banerjee, E. Hucteau, J. Mallard, P. Lopez Navarro, B. V. Popescu, E. Thomas, D. Kryza, J. Sidi-Boumedine, G. Ferrauto, E. Gionalio, G. Fleith, J. Combet, S. Brun, S. Erb, S. Cianferani, L. J. Charbonnière, L. Fellmann, C. Mirjolet, L. David, O. Tillement, F. Lux, S. Harlepp, X. Pivot, A. Detappe. Subcutaneous administration of a zwitterionic chitosan-based hydrogel for controlled spatiotemporal release of monoclonal antibodies. *Adv Mat.*, **36**, 2308738 (2023).
- [29] J. F. Salazar Ariza, F. Lux, F. Da Cruz-Boisson, J. Resende de Azevedo, R. Vera, O. Tillement, A. Montembault, L. David, Chitosan based hydrogel for iron (III) chelation in biological conditions, *Carbohydr. Polym.*, **347**, 122670 (2024).
- [30] R. Passieux, G. Sudre, A. Montembault, M. Renard, A. Hagege, P. Alcouffe, A. Haddane, M. Vandesteene, N. Boucard, L. Bordenave, L. David, Cytocompatibility / Antibacterial Activity Trade-off for Knittable Wet-Spun Chitosan Monofilaments Functionalized by the In Situ Incorporation of Cu²⁺ and Zn²⁺. *ACS Biomaterials Science & Engineering*, **8**, 1735–1748 (2022).

- [31] A. Hirai, H. Odani, A. Nakajima, Determination of degree of deacetylation of chitosan by ¹H NMR spectroscopy. *Polymer Bulletin*, **26**, 87–94 (1991).
- [32] R. J. Motekaitis, A. E. Martell, THE IRON(III) AND IRON(II) COMPLEXES OF NITRILOTRIACETIC ACID. *Journal of Coordination Chemistry*, 67-78 (1994).
- [33] C. Kilkenny, W. Browne, I. C. Cuthill, M. Emerson, D. G. Altman, NC3Rs Reporting Guidelines Working Group. (2010). Animal research: Reporting in vivo experiments: The ARRIVE guidelines. *British Journal of Pharmacology*, **160**, 1577–1579 (2010).
- [34] J. C. McGrath, G. B. Drummond, E. M. McLachlan, C. Kilkenny, C. L. Wainwright, Guidelines for reporting experiments involving animals: The ARRIVE guidelines. *British Journal of Pharmacology*, **160**, 1573–1576 (2010).
- [35] C. W. Cotman, Isolation of synaptosomal and synaptic plasma membrane fractions. *Methods in Enzymology*, **31**, 445–452 (1974).
- [36] E. Larson, B. Howlett, A. Jagendorf, Artificial reductant enhancement of the Lowry method for protein determination. *Analytical Biochemistry*, **155**, 243–248 (1986).
- [37] T. Borisova, Nervous System Injury in Response to Contact With Environmental, Engineered and Planetary Micro- and Nano-Sized Particles. *Frontiers in Physiology*, **9**, 728 (2018)
- [38] T. Borisova, Express assessment of neurotoxicity of particles of planetary and interstellar dust, *Npj Microgravity*, **5**, 2 (2019).
- [39] N. Krisanova, N. Pozdnyakova, A. Pastukhov, M. Dudarenko, O. Maksymchuk, P. Parkhomets, R. Sivko, T. Borisova, Vitamin D3 deficiency in puberty rats causes presynaptic malfunctioning through alterations in exocytotic release and uptake of glutamate/GABA and expression of EAAC-1/GAT-3 transporters, *Food Chem. Toxicol.*, **123**, 142-150 (2019).
- [40] A. Borysov, N. Krisanova, O. Chunihin, L. Ostapchenko, N. Pozdnyakova, T. Borisova, A comparative study of neurotoxic potential of synthesized polysaccharide-coated and native ferritin-based magnetic nanoparticles, *Croatian Medical Journal*, **55**, 195–205 (2014).
- [41] N. Pozdnyakova, A. Pastukhov, M. Dudarenko, M. Galkin, A. Borysov, T. Borisova, Neuroactivity of detonation nanodiamonds: Dose-dependent changes in transporter-mediated uptake and ambient level of excitatory/inhibitory neurotransmitters in brain nerve terminals. *Journal of Nanobiotechnology*, **14**, 25 (2016).
- [42] G. Paxinos, C. Watson, *The Rat Brain in Stereotaxic Coordinates—The New Coronal Set* (5th ed.), Academic Press (2004).
- [43] M. Asti, M. Tegoni, D. Farioli, M. Iori, C. Guidotti, C. S. Cutler, P. Mayer, A. Versari, D. Salvo, Influence of cations on the complexation yield of DOTATATE with yttrium and lutetium: A perspective study for enhancing the ⁹⁰Y and ¹⁷⁷Lu labeling conditions. *Nuclear Medicine and Biology*, **39**, 509–517 (2012).
- [44] G. Anderegg, F. Arnaud-Neu, R. Delgado, J. Felcman, K. Popov, Critical evaluation of stability constants of metal complexes of complexones for biomedical and environmental applications (IUPAC Technical Report): *Pure and Applied Chemistry*, **77**, 1445–1495 (2005).
- [45] G. Farinelli, A. Di Luca, V. R. I. Kaila, M. J. MacLachlan, A. Tiraferri, Fe-chitosan complexes for oxidative degradation of emerging contaminants in water: Structure, activity, and reaction mechanism. *Journal of Hazardous Materials*, **408**, 124662 (2021).

- [46] M. Hamdine, M. C. Heuzey, A. Bégin, Effect of organic and inorganic acids on concentrated chitosan solutions and gels. *International Journal of Biological Macromolecules*, **37**, 134–142 (2005).
- [47] M. Vakili, S. Deng, G. Cagnetta, W. Wang, P. Meng, D. Liu, G. Yu, Regeneration of chitosan-based adsorbents used in heavy metal adsorption: A review. *Separation and Purification Technology*, **224**, 373–387 (2019).
- [48] P. Randhawa, K. L. Gower-Fry, C. M. K. Stienstra, M. Tosato, S. Chen, Y. Gao, A. W. McDonagh, V. Di Marco, V. Radchenko, G. Schreckenbach, C. F. Ramogida, Selective Chelation of the Exotic Meitner-Auger Emitter Mercury-197 m/g with Sulfur-Rich Macrocyclic Ligands: Towards the Future of Theranostic Radiopharmaceuticals, *Chem. Eur. J.*, **29**, e202203815 (2023).
- [49] P. Miretzky, A. F. Cirelli, Hg(II) removal from water by chitosan and chitosan derivatives: A review. *Journal of Hazardous Materials*, **167**, 10–23 (2009).
- [50] T. Borisova, Permanent dynamic transporter-mediated turnover of glutamate across the plasma membrane of presynaptic nerve terminals: Arguments in favor and against. *Reviews in the Neurosciences*, **27**, 71–81 (2016).
- [51] T. Borisova, A. Borysov, Putative duality of presynaptic events, *Reviews in the Neurosciences*, **27**, 377-383 (2016).
- [52] S. Pfaender, A. M. Grabrucker, Characterization of biometal profiles in neurological disorders. *Metallomics*, **6**, 960–977 (2014).
- [53] A. N. Tsentsevitsky, G. F. Zakyrjanova, A. M. Petrov, Cadmium desynchronizes neurotransmitter release in the neuromuscular junction: Key role of ROS. *Free Radic. Biol. Med.*, **155**, 19-28 (2020).
- [54] T. Borisova, N. Pozdnyakova, N. Krisanova, A. Pastukhov, M. Dudarenko, K. Paliienko, V. Grytsaenko, F. Lux, V. Lysenko, P. Rocchi, S. Komisarenko, O. Tillement, Unique features of brain metastases-targeted AGuIX nanoparticles vs their constituents: A focus on glutamate-/GABA-ergic neurotransmission in cortex nerve terminals. *Food Chem. Toxicol.*, **149**, 112004 (2021).
- [55] D. Devos, J. Labreuche, O. Rascol, J. C. Corvol, A. Duhamel, P. Guyon Delannoy, W. Poewe, Y. Compta, N. Pavese, E. Růžička, P. Dušek, B. Post, B. R. Bloem, D. Berg, W. Maetzler, M. Otto, M. O. Habert, S/ Lehericy, J. Ferreira, R. Dodel, C. Tranchant, A. Eusebio, S. Thobois, A. R. Marques, G. Wassilios, M. D. Meissner, F. Ory-Magne, U. Walter, R. M. A. De Bie, M. Gago, D. Vilas, J. Kulisevsky, C. Januario, M. V. S. Coelho, S. Behnke, P. Worth, K. Seppi, T. Ouk, C. Potey, C. Leclerq, R. Viard, G. Kuchcinski, R. Lopes, J. P. Pruvo, P. Pigny, G. Garçon, O. Simonin, J. Carpentier, A. S. Rolland, D. Nyholm, C. Scherfler, J. F. Mangin, M. Chupin, R. Bordet, D. T. Dexter, C. Fradette, M. Spino, F. Tricta, S. Ayton, A. I. Bush, J. C. Devedjian, J. A. Duce, I. Cabantchik, L. Defebvre, D. Deplanque, C. Moreau, Trial of Deferiprone in Parkinson's Disease. *New England Journal of Medicine*, **387**, 2045–2055 (2022).
- [56] F. Xu, S. Farkas, S. Kortbeek, F. Zhang, L. Chen, G. Zamponi, N. Syed, Mercury-induced toxicity of rat cortical neurons is mediated through N-Methyl-D-Aspartate receptors. *Molecular Brain*, **5**, 30 (2012).
- [57] L. Ferraro, M. C. Tomasini, S. Tanganelli, R. Mazza, A. Coluccia, M. R. Carratù, S. Gaetani, V. Cuomo, T. Antonelli, Developmental exposure to methylmercury elicits early cell

death in the cerebral cortex and long-term memory deficits in the rat. *International Journal of Developmental Neuroscience*, **27**, 165–174 (2009).

[58] Z. Yang, A. Zhang, H. Duan, S. Zhang, P. Hao, K. Ye, Y. E. Sun, X. Li, NT3-chitosan elicits robust endogenous neurogenesis to enable functional recovery after spinal cord injury. *PNAS*, **112**, 13354–13359 (2015).

4.2.2. Synthesis of a chelating fiber for implantation in PD monkey model

The promising results from the previous study, which demonstrated the biocompatibility, biodegradability, *in vitro* chelation, and *ex vivo* efficacy of the fibers in reducing extracellular neurotransmitter release induced by metals such as copper(II), cadmium(II), and lead(II), led to the implantation of chelating fibers in a macaque model of Parkinson's disease. For successful implantation in the brain, the fibers needed to have a diameter of 0.6 mm, and their diameter should not increase by more than two-fold to avoid damaging the surrounding brain tissue, as advised by neurosurgeon Dr. Stéphane Palfi from Henri Mondor Hospital in Paris.

To obtain a fiber with the required characteristics, the experimental setup from Figure 1 of the article "Neurocompatible Biodegradable Fibers Designed to Extract Excess Free Metals in the Brain" was slightly modified (Figure 49 A). Adjustments were made to the internal radius of the extrusion tip, the concentration and ratio of the functionalized polymer and chitosan, as well as the drying protocol. The following section will discuss the selection of the optimal parameters for fiber synthesis.

For all tests, the precursor solution was extruded at a linear velocity of $V_0 = 21$ mm/s through a conical spinneret with a final diameter of 1.28 ± 0.02 mm, 1.70 ± 0.02 mm, or 1.98 ± 0.02 mm. Pressure was applied using a piston with a compressed air dispenser (Nordson Optimus I, Nordson EFD). The resulting extrudate was immersed in a 1 L bath of 3 M NaOH aqueous solution to induce gelation. A first motorized bobbin guided the fiber into two 5 L baths of ultrapure water for washing. A second motorized bobbin directed it out of the washing baths and into the enrolling zone, while a third motorized bobbin ensured the fiber was wound onto the spool. The speeds of the motorized bobbins remained consistent with the original setup ($V_0 = V_1 = 21$ mm/s, $V_2 = 26$ mm/s, and $V_3 = 34$ mm/s).

The drying step in the original setup was removed because the resulting fibers were too thick to be totally dried in the short pathway. Instead, drying was carried out using a custom "drying rack" setup at room temperature (25°C) for 24 hours, keeping the fiber under tension. The resulting straight, dry, thick fibers were then cut to the desired length (Figure 49 B).

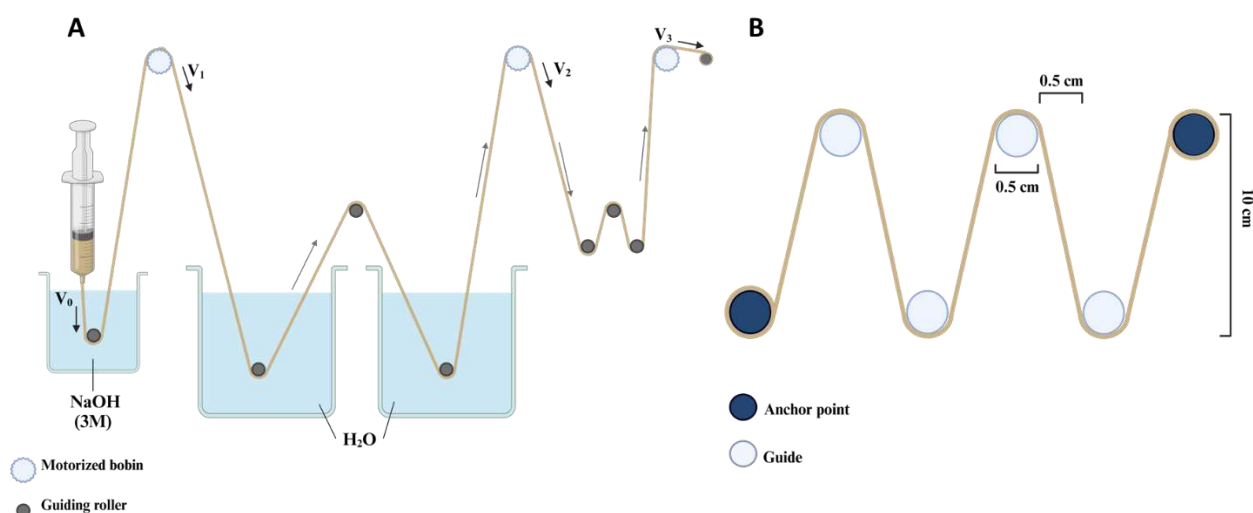


Figure 49. A: Scheme of the lab-scale wet gel spinning set-up used for producing chitosan based fibers. It comprises the gelation bath (3M NaOH solution), three motorized bobbins with tuneable speed ($V_1 = 21$ mm/s, $V_2 = 26$ mm/s, and $V_3 = 34$ mm/s). **B:** Scheme of the “drying rack” set up, with two anchor points that keep the whole fiber under tension during the drying process (25°C for 24 hours).

The same precursor solution (5% w/w DA₆ and 10% w/w DA₆@DOTAGA₁₇) from the article “Neurocompatible Biodegradable Fibers Designed to Extract Excess Free Metals in the Brain” was not suitable for this experiment due to two primary reasons. First, the 2:1 ratio of DA₆@DOTAGA₁₇ to DA₆ resulted in a fiber diameter increase of approximately five-fold when hydrated, as reported in Figure 1 of the same article. This exceeds the desired maximum diameter increase of two-fold. Second, the high polymer concentration of 15% w/w combined with the extrudate thickness and limited exposure time in the gelation bath hindered fiber formation. The high polymer concentration and thick extrudate limited the diffusion of NaOH into the fiber, leading to breakage before reaching the final bobbin.

The main parameter driving the swelling of the fiber is the amount of DOTAGA in the dry fiber as previously demonstrated in the article “Development of chitosan-based hydrogels with tailored hydrophilicity and swelling characteristics” in chapter 3, therefore the DA₆@DOTAGA₁₇ to DA₆ ratio was adjusted to 1:1. To increase the diffusion of NaOH into the fiber the precursor solution was reduced to 10% w/w, resulting in a formulation for the precursor solution as follows: 5% w/w DA₆ and 5% w/w DA₆@DOTAGA₁₇. The precursor solution was prepared following the same protocol presented in Chapter 3, with adjustments for the new polymer proportions.

Using the new precursor solution formulation, it was possible to produce continuous thick fibers from the gelation bath up to the winding bobbin, regardless of the spinneret tip size (1.28 ± 0.02 mm, 1.70 ± 0.02 mm, or 1.98 ± 0.02 mm). However, when cutting the final fibers, it was observed that gelation was only partial, with the centre of the fibers remaining in a solution state. This incomplete gelation was likely due to the thickness of the fibers and insufficient

time in the initial gelation bath. To address this, the resulting fibers were immersed in a second 3M NaOH gelation bath for 30 minutes after wet gel spinning, followed by rinsing with water and washing in 1 L of 10 mM phosphate buffer (Na₂HPO₄ 7.5 mM, KH₂PO₄ 2.5 mM, pH 7.4) for 24 hours to obtain fibers at physiological pH. The fibers were then dried using the "drying rack" setup at room temperature (25 °C) for 24 hours (Figure 49 B). The tip that produced the desired fiber diameter was approximately 1.98 mm, as shown in Table 11.

Table 11. Evolution of the diameter of the produced fibers for the three conical spinneret tips used with different diameter. Measurements with a calliper on the wet and dry fiber were done in three different zones of the fiber.

Internal diameter of the conical spinneret ± 0.02 mm	Fiber after phosphate buffer washing ± 0.1 mm	Diameter of the dried fiber ± 0.05 mm
1.28	0.7	0.30
1.70	1.0	0.50
1.98	1.2	0.60

4.2.3. Swelling of the chosen fiber in physiological saline

Material and methods The selected fibers were cut into three pieces, and each piece was immersed in physiological saline (NaCl at 0.9% w/w pH 7.4) to simulate physiological conditions for four hours. The length of both the dried and hydrated fiber segments was measured using a calliper, while the diameter was determined using an optical microscope (Leica M205A, with assistance from Jun Zhou at the IMP).

Results and discussion The dry fiber had a diameter of $515.9 \pm 12.1 \mu\text{m}$, which increased to $1039.6 \pm 36.8 \mu\text{m}$ after hydration, resulting in a 2.02-fold diameter increase. Interestingly, the length increased by only 1.13-fold, indicating anisotropic swelling primarily in the width of the fiber rather than the length. The resulting fiber produced from the precursor solution 5% w/w DA₆ and 5% w/w DA₆@DOTAGA₁₇, extruded through a tip with an internal diameter of 1.98 mm meets the necessary criteria for the implantation in the brain of a monkey.

The titer (in dtex) was determined by weighting six fiber portions (of around 10 cm each) resulting in a total length of 63.5 cm and a total mass of 425.8 mg (Table 12). By considering the density of the fiber $\rho \sim 1.3\text{g/cm}^3$ the diameter can be calculated with the same formula shown in table 1 of the previous paper, resulting in $514.6 \mu\text{m}$ a value very close to the one measured by optical microscopy.

As shown in Figure 50, the fiber exhibits two distinct zones separated by an internal diameter. This separation is likely attributed to the two-step gelation process, with the exterior ring forming during the first gelation bath and the interior zone forming during the second gelation bath.

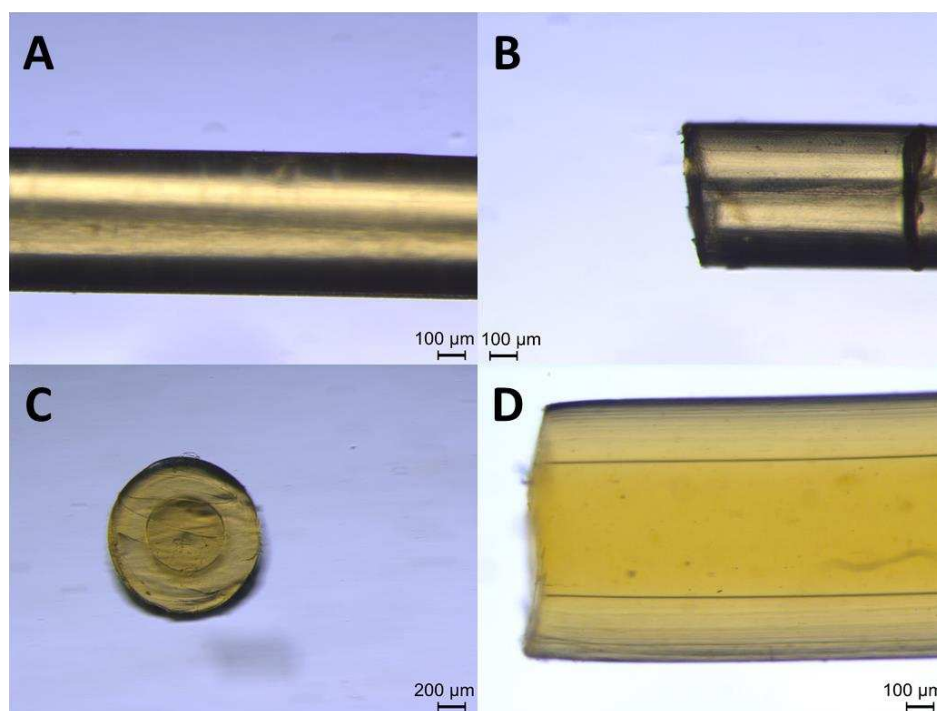


Figure 50: Optical microscopic images of **A:** Longitudinal view of the middle section of the dried fiber. **B:** Longitudinal view of the dried fiber with a transverse cut. **C:** Transverse section of the re-hydrated fiber after immersion in physiological serum for four hours. **D:** Longitudinal view of the re-hydrated fiber after immersion in physiological serum for four hours. In images C and D, two distinct zones can be observed, likely due to the two-step gelation process.

4.2.4. Mechanical properties of the chosen fiber

Material and methods The tensile properties of the thick fiber were assessed performing a unidirectional tensile test using a SHIMADZU AG-X plus device equipped with a 100 N load cell, following the same protocol and under the same conditions as for the unidirectional tensile test present in the previous paper " Neurocompatible biodegradable fibers designed to extract excess free metals in the brain ". The fiber was positioned between clamps establishing an effective initial length ($l_0 = 50$ mm) and an initial deformation rate of 20%/min. The tenacity (T_e) was calculated as the ratio of the applied force (F_b) at rupture to the yarn titer in dtex (Y_t) ($T_e = F_b/Y_t$); the nominal strain (ϵ) was expressed as the ratio of the fiber's extension to the initial length ($\epsilon_N = \Delta l/l_0 = (l - l_0)/l_0$). The Young's modulus (E), tenacity (T_e), and strain-at-break (ϵ_b) were determined from the stress-strain curves with five measurements replicates ($n=5$) (Figure 51).

Results and discussion By comparing the results of the unidirectional tensile tests on fibers made from the precursor solutions of 5% w/w DA₆ and 5% w/w DA₆@DOTAGA₁₇ (Table 12 Figure 51), and those reported in the previous paper Table 1 (5% w/w DA₆ and 10% w/w DA₆@DOTAGA₁₇), it is clear that the fiber with a higher ratio of non-functionalized chitosan is stiffer, as demonstrated by the higher Young's modulus. A lower proportion of DOTAGA in the fiber increases its crystallinity, which in turn raises the stiffness of the material. As expected, the thicker fiber exhibits higher tenacity than the fiber with a smaller cross-sectional area.

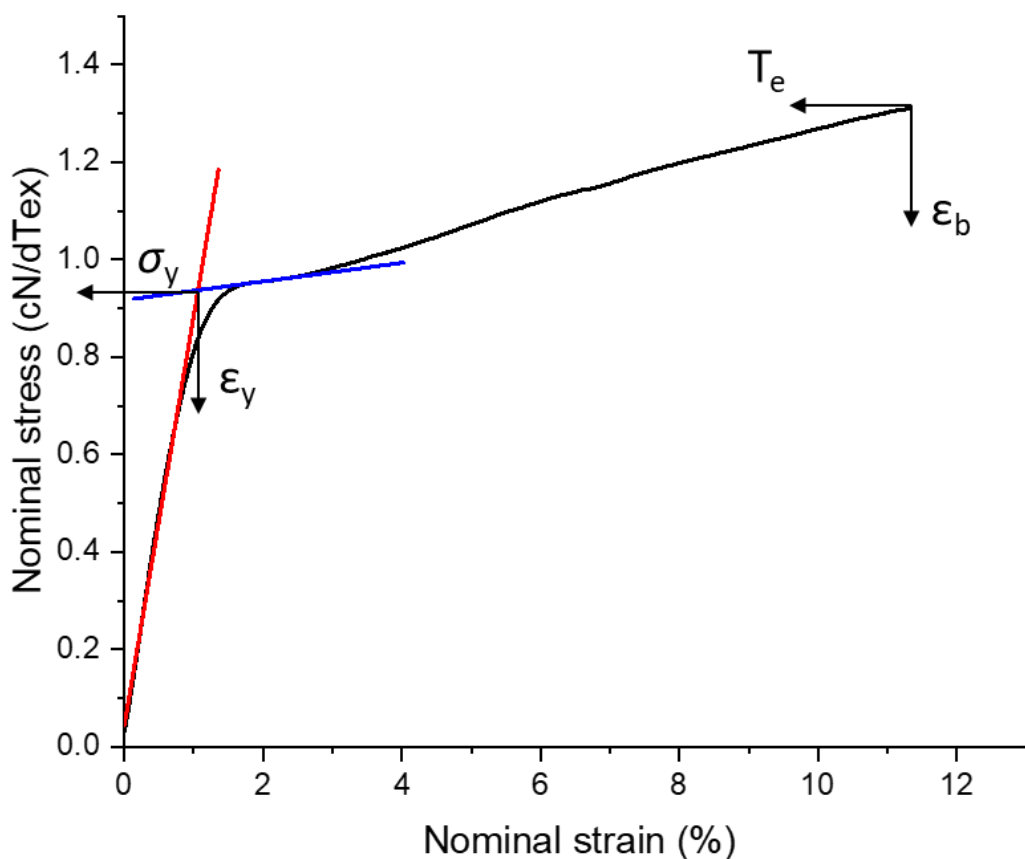


Figure 51. Example of stress-strain curve of the % w/w DA₆ and 5% w/w DA₆@DOTAGA₁₇ fiber, obtained by uniaxial tensile test (solid black line). Slope corresponding to the linear elastic region of the fiber (red line) enable the determination of the Young's modulus. The intersect between the linear elastic and plastic regimes is the yield point.

Table 12. Fiber mechanical characterisation data obtained by uniaxial tensile test on 5 different samples of the chosen fiber made out of the precursor solution 5% w/w DA₆ and 5% w/w DA₆@DOTAGA₁₇. Results are presented as the mean ± standard deviation of the 5 studied samples.

Titer	Young's modulus	Yield stress	Yield strain	Tenacity	Strain at rupture	Diameter
(dtex)	(cN/dtex)	(cN/dtex)	(%)	(cN/dtex)	(%)	(µm)
2704	0.79 ± 0.03	0.94 ± 0.09	1.21 ± 0.42	1.26 ± 0.17	11.04 ± 1.70	514.6

4.3. Conclusion

Using polymeric chelating agents in microdialysis for metal extraction offers several advantages, such as avoiding direct interaction between the chelating agent and the patient's

CNS, showing no adverse effects on CNS health, and partially improving metal extraction in an in vivo rat model. However, the approach still has drawbacks related to the microdialysis technology itself. These include the need for prolonged exposure times and multiple therapy sessions, which can place a significant burden on the patient.

To address these limitations, the use of biodegradable implants was proposed as an alternative. Unlike microdialysis, implants require only a single therapeutic session for implantation. Additionally, they allow for a concentrated amount of chelating agent to be available for metal extraction over time. Since the chelator is grafted onto the hydrogel structure, the implant remains capable of chelating metals as long as it remains in the tissue and is not fully saturated. To optimize the surface-to-volume ratio, hydrogel fibers were developed. These fibers, made from DA₆@DOTAGA₁₇, demonstrated the ability to extract heavy metals such as lead (II) and cadmium (II), as well as metals like iron (III) and copper (II), which are suspected to play a role in neurodegeneration.

The chelating properties of the fibers helped mitigate metal-induced neurotransmitter imbalances, such as excessive release of neurotransmitters caused by copper (II), lead (II), and cadmium(II). Furthermore, by tagging the DOTAGA in the fiber with gadolinium(III), its biodegradability could be monitored using MRI. The results showed that a xerogel fiber composed of 1/3 w/w DA₆ and 2/3 w/w DA₆DOTAGA₁₇ degraded by approximately 50% after 17 weeks of implantation without negatively affecting the rat's health.

The production of chitosan-based hydrogels and xerogels through amine deprotonation is a versatile method for generating hydrogels/xerogels in various shapes, adaptable to different applications. As demonstrated in this work, by using the same raw materials with minimal modifications to the production setup, adjusting the concentration and polymer proportions in the precursor solution, and varying the diameter of the extruded fibers, it is then possible to tailor the swelling and size of the final fiber to meet specific requirements.

V General conclusion and outlook

The goal of the ANR-SEMB project and this work was to develop multiple chelating materials capable of performing localized chelation to extract metal ions, particularly iron, from the central nervous system. The two approaches discussed for localized metal chelation were the use of microdialysis and chelating implants. To achieve this, aminated polymers were used as backbones for grafting small chelating agents anhydride derivatives, ensuring the resulting macromolecular chelators were large enough to prevent crossing the microdialysis membrane, but also to create chelating polymers capable of forming hydrogels. The second chapter discusses the functionalization of two systems, 8-arm-PEG and chitosan, with the DFO derivative p-NCS-Bz-DFO. DFO was chosen as the chelator due to its high (specific) affinity towards iron (III) and due its ability of completely saturating the coordination sphere of iron (III) by forming a 1 to 1 ligand to metal complex, thus hindering iron (III) participation in redox reactions.

The functionalisation of 8-arm-PEG in DMSO by p-NCS-Bz-DFO resulted in the polymer 8-arm-PEG@DFO who had on average, 3.4 out of its 8 arms grafted with DFO, and presented total solubility in physiological conditions making it ideal for microdialysis applications.

On the other hand, chitosan was functionalized with p-NCS-Bz-DFO through a two-step process. First, the DA was increased to 40% to address the solubility issues observed with low DA chitosan. The second step involved functionalization in a mixture of water, 1,2-propanediol, and DMSO (52%, 30%, and 18%, respectively) at pH 6.0 ± 0.5 . The resulting polymer with DA₄₀@DFO₄ showed better iron(III) extraction in solution in the presence of strong the strong iron(III) chelator deferiprone than chitosan grafted with the chelator DOTAGA (DA₂₉@DOTAGA₉). Although not soluble under physiological conditions, DA₄₀@DFO₄ was suitable for the development of chelating hydrogels.

The third chapter of this work focused on the development of chelating hydrogels by blending low-DA non-grafted chitosan with functionalized chitosan. Physical hydrogels were successfully produced through basic neutralization of the chitosan mixtures, without the need for additional crosslinking agents. It was demonstrated that non-grafted chitosan hydrogels can extract metal cations from solution *via* two distinct mechanisms: the first involves direct chelation between the amine groups and the metal cations, while the second relies on electrostatic interactions between protonated amines and anionic metal complexes. However, the presence of various salts in solution can interfere with chitosan's metal extraction capabilities.

To address this, functionalized chitosan with chelating agents enhanced the hydrogels' metal extraction efficiency, as the chelators grafted onto the polymer were less affected by salt addition. Additionally, it was found that the hydrogel's swelling behaviour depends on multiple factors, including the system's crystallinity and hydrophilicity, parameters that can be tuned by the type of grafted molecule used in the hydrogel's structure.

The final chapter presented *in vitro* and *in vivo* examples of using microdialysis and hydrogel implants for localized metal extraction. *In vivo*, microdialysis yielded mixed results: 8-arm-PEG@DFO did not enhance iron extraction in a PD 6-OHDA mouse model, and while DA₂₉DOTAGA₉ appeared to increase manganese(II) extraction in a mouse model injected intravenously with MnCl₂, the difference was not statistically significant. However, both polymers showed promising results *in vitro*.

Fiber-shaped hydrogels demonstrated the ability to remove metals such as lead (II), cadmium (II), iron (III), and copper (II), potentially helping to mitigate neurodegenerative effects. Additionally, their biodegradability and biocompatibility were confirmed in rats, where gadolinium (III) tagged fibers were monitored via MRI, showing safe degradation.

In conclusion, the development of chelating polymers offers a versatile tool that can be tailored to specific applications. The material properties can be fine-tuned at the molecular level by adjusting hydrophilicity or functionalizing with different chelators, and at the macroscopic level by varying the formulation, size and shape of the material.

Further work is needed to assess the *in vivo* chelating performance of biodegradable implants for metal extraction. As observed with microdialysis, promising *in vitro* results do not always translate to similar outcomes *in vivo*. While the developed hydrogels have been found to be biocompatible and biodegradable, there is limited understanding of their degradation mechanisms and pathways *in vivo*. Therefore, it would be valuable to study the biodistribution of the degraded hydrogel.

Moreover, since oxidative stress is one of the main drivers of tissue damage in neurodegeneration, functionalizing hydrogels with antioxidant compounds, such as thiol or phenolic moieties, could provide an additional strategy for combating oxidative stress, complementing metal chelation.

Lastly, the application of chelating hydrogels could extend to other pathologies where metals contribute to oxidative damage, such as wound healing an area where hydrogels are already being investigated.

Annexes

Annexe 1. Supporting information of the article “Chitosan based hydrogel for iron (III) chelation in biological conditions.”

Chitosan based hydrogel for iron (III) chelation in biological conditions.

Juan Felipe Salazar Ariza,^{1,2} François Lux,^{1,3} Fernande Da Cruz-Boisson,² Jacqueline Resende de Azevedo,⁴ Ruben Vera,⁵ Olivier Tillement,¹ Alexandra Montembault,² Laurent David*²

¹ Université Claude Bernard Lyon 1, CNRS, Institut Lumière-Matière (ILM), UMR 5306, 2 rue Victor Grignard, F-69622 Villeurbanne Cedex, France.

² Université Claude Bernard Lyon 1, INSA de Lyon, Université Jean Monnet, CNRS, Ingénierie des Matériaux Polymères (IMP), UMR 5223, 15 bd Latarjet, F-69622 Villeurbanne, France.

³ Institut Universitaire de France (IUF), 75231 Paris, France.

⁴ Université Claude Bernard Lyon 1, CNRS, Laboratoire d'Automatique, de Génie des Procédés et de Génie Pharmaceutique (LAGEPP), UMR5007, 3, rue Victor Grignard, Bâtiment CPE, F-69100 Villeurbanne Cedex, France

⁵ Université Claude Bernard Lyon 1, Centre de Diffractométrie Henri Longchambon, 5 rue de La Doua, F-69100 Villeurbanne, France.

* Correspondence and requests for materials should be addressed to Pr Laurent David (email: laurent.david@univ-lyon1.fr)

NMR Characterization of DA₄₀@DFO

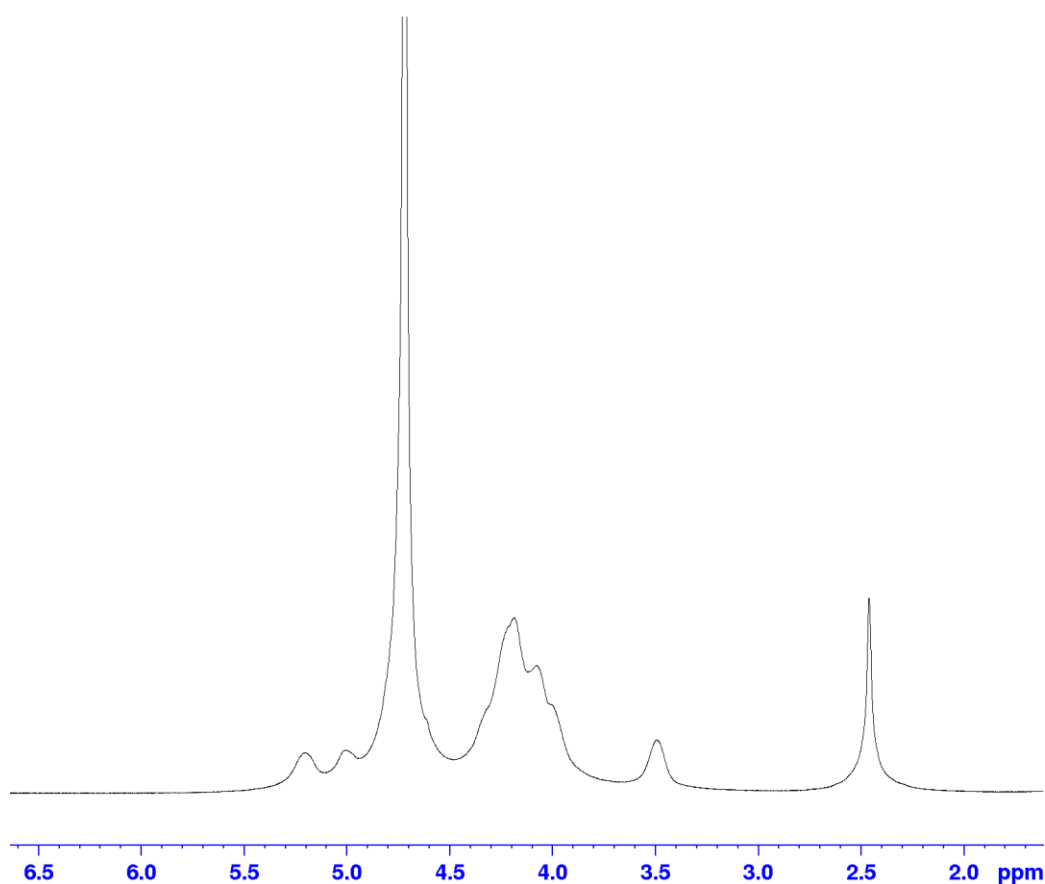


Fig. S1. ¹H NMR spectrum of re-acetylated chitosan (DA₄₀) in D₂O at 0.5% w/w. at 70 °C.

$$\frac{Area_{3.00-4.55\text{ ppm}}}{Area_{2.45\text{ ppm}}} = \frac{6}{3x} = \frac{2}{x}$$

By using the Hirai method (previous equation) $x = 40 \pm 0.5\%$

Calculation of parameter y from iron (III) titration by UV data

The mass fraction of DFO-grafted repeat unit, w , is defined as

$$w = \frac{n_{DFO} \cdot M_y}{m_{Chitosan}} = \frac{y \cdot M_y}{x \cdot M_x + y \cdot M_y + gluc \cdot M_{gluc}}$$

Where n_{DFO} is the mole number of DFO-grafted repeat unit, $m_{Chitosan}$ is the (dry) mass of dissolved Chitosan-DA₄₀@DFO in solution, x is the molar fraction of N-acetyl glucosamine repeat units, $y = n_{DFO}/n_{TOT}$ is the molar fraction of the DFO-grafted repeat units and a is the molar fraction of the glucosamine repeat units. Accordingly, M_x is defined as the molar mass of N-acetyl repeat units, M_y is the molar mass of DFO-grafted repeat units and M_{gluc} the molar mass of glucosamine residue.

Since $gluc = 1 - x - y$ the equation above becomes

$$w = \frac{y \cdot M_y}{x \cdot (M_x - M_{gluc}) + y \cdot (M_y - M_{gluc}) + M_{gluc}}$$

Therefore

$$y = \frac{w \cdot (x \cdot (M_x - M_{gluc}) + M_{gluc})}{M_y - w \cdot (M_y - M_{gluc})}$$

By computation,

$$M_x = 203.19 \text{ g} \cdot \text{mol}^{-1}, M_y = 914.06 \text{ g} \cdot \text{mol}^{-1}, M_{gluc} = 161.16 \text{ g} \cdot \text{mol}^{-1}$$

Using $m_{TOT} = 1 \text{ g}$ of hydrated Chitosan-DA₄₀@DFO dissolved in solution, from the UV titration with Fe (III), we find:

$$\frac{C_{DFO}}{m_{TOT}} = n_{DFO} = 0.135 \text{ mmol}$$

In order to evaluate the mass fraction w , we evaluated a water content of $wc = 8.2\%$ (w/w) in the lyophilized Chitosan-DA₄₀@DFO powder by thermogravimetric analysis, measuring the mass loss between 25 and 200°C under helium flow. Then,

$$w = \frac{n_{DFO} \cdot M_y}{m_{TOT} \cdot (1 - wc)}$$

Hence, the final equation is:

$$y = \frac{C_{DFO} \cdot (x \cdot (M_x - M_{gluc}) + M_{gluc})}{(1 - wc) - C_{DFO} \cdot (M_y - M_{gluc})}$$

From ¹H-NMR, $x = 40\%$

This results in $y = 3\%$

Computation of parameter x (DA, degree of acetylation) and y (DFO degree of substitution) from ¹H NMR of DA₄₀@DFO

DFO-grafting rate (y) can be obtained by ¹H NMR though the ratio between the area of the peak at 7.8 ppm (attributed to aromatic protons H_n and H_{n'} from p-NCS-BZ-DFO, see Figure S6 and Table S1) over the area in the region 3.3-4.6 ppm following the equations respectively:

$$\frac{Area_{3.5-4.5}}{Area_{7.8}} = \frac{6+12y}{4y}$$

$$\frac{Area_{3.5-4.5}}{Area_{1.6-2.2}} = \frac{6+12y}{18y}$$

From ¹H-NMR of Chitosan-DA₄₀@DFO (Figure 4), $y = 3.8\%$ for the first equation and the second equation gives $y = 3.9\%$.

The slight difference on the value y between the two equations can be explained by the integration accuracy of the peaks between 1.6-2.2 ppm and the pic at 7.8 ppm.

By considering the protons from DFO into the Hirai method the equation becomes:

$$\frac{\text{Area}_{3.5-4.5 \text{ ppm}}}{\text{Area}_{2.3-2.6}} = \frac{6+12y}{3(y+x)}$$

From $^1\text{H-NMR}$ of $\text{DA}_{40}\text{@DFO}$ $y = 3.8 \pm 0.2\%$ thus $x = 40 \pm 0.5\%$.

Table S1 Attribution of $^1\text{H NMR}$ signals of $\text{DA}_{40}\text{@DFO}$ (x : acetylation degree, y : DFO grafting)

Chemical shift (ppm)	Integration	Attribution
7.8	4y	H_n et $\text{H}_{n'}$ (in green)
4.9-5.5	1	H_1 (in black)
4.5-3.5	6 + 12y	$\text{H}_2, \text{H}_3, \text{H}_4, \text{H}_5, \text{H}_{6,7}, \text{H}_a, \text{H}_e, \text{H}_i, \text{H}_h$ (in orange)
3.2	4y	H_f (in cyan)
2.9	4y	H_g (in cyan)
2.3-2.6	3y + 3x	$\text{H}_{ac}, \text{H}_m$ (in pink)
1.6-2.2	18y	$\text{H}_b, \text{H}_c, \text{H}_d, \text{H}_k, \text{H}_j, \text{H}_i, \text{H}_j$ (in red)

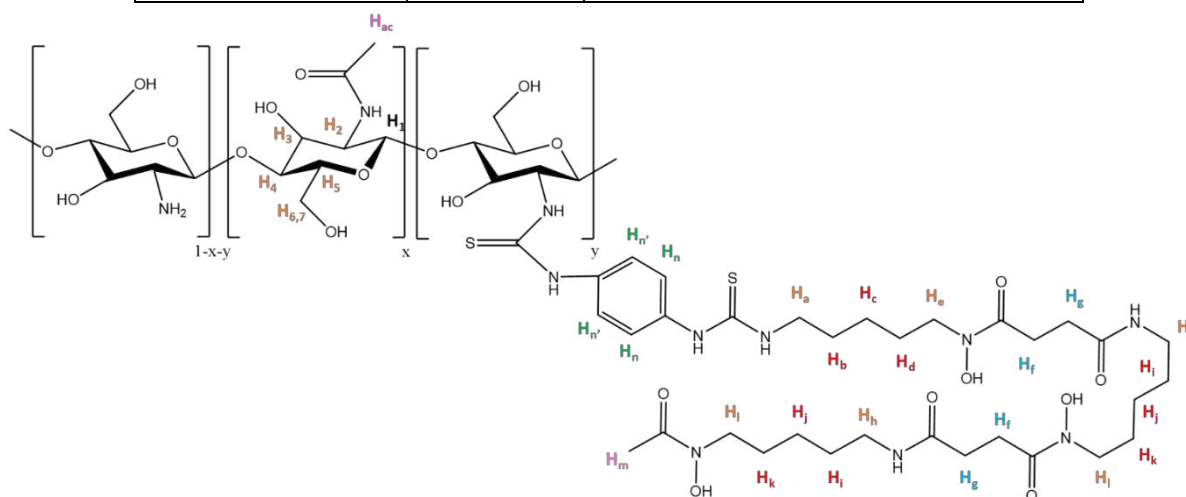


Fig. S2. Labelling for attribution of $^1\text{H NMR}$ signal of $\text{DA}_{40}\text{@DFO}$

Table S2 Dimensions of the hydrogels and xerogels used for the different experiments.

Experiment Formulation	Chelation		Swelling	
	Precursor Hydrogels disks	Xerogels disks	Precursor Hydrogels disks	Xerogels disks
14% DA ₆ 1% DA ₄₀	$\text{Ø: } 10.0 \pm 0.2 \text{ mm}$ Thickness: $2.1 \pm 0.1 \text{ mm}$ mass: $\approx 180 \text{ mg}$	$\text{Ø: } 5.8 \pm 0.2 \text{ mm}$ Thickness: $1.0 \pm 0.1 \text{ mm}$ Mass $\approx 27 \text{ mg}$	$\text{Ø: } 25.0 \pm 0.2 \text{ mm}$ Thickness: $3.0 \pm 0.1 \text{ mm}$ Mass $\approx 1270 \text{ mg}$	$\text{Ø: } 17.0 \pm 0.2 \text{ mm}$ Thickness: $1.4 \pm 0.1 \text{ mm}$ Mass $\approx 190 \text{ mg}$
13% DA ₆ 2% DA ₄₀				
10% DA ₆ 5% DA ₄₀				
15% DA ₆				
5% DA ₆ 5% DA ₄₀	$\text{Ø: } 10.0 \pm 0.2 \text{ mm}$ Thickness: $2.10 \pm 0.1 \text{ mm}$ mass: $\approx 180 \text{ mg}$	$\text{Ø: } 5.8 \pm 0.2 \text{ mm}$ Thickness: $0.5 \pm 0.1 \text{ mm}$ Mass $\approx 18 \text{ mg}$	$\text{Ø: } 25.0 \pm 0.2 \text{ mm}$ Thickness: $3.0 \pm 0.1 \text{ mm}$ Mass $\approx 1270 \text{ mg}$	$\text{Ø: } 14.0 \pm 0.2 \text{ mm}$ Thickness: $0.7 \pm 0.1 \text{ mm}$ Mass $\approx 127 \text{ mg}$
14% DA ₆ 1% DA ₄₀ @DFO	$\text{Ø: } 10.0 \pm 0.2 \text{ mm}$ Thickness: $2.1 \pm 0.1 \text{ mm}$ mass: $\approx 180 \text{ mg}$	$\text{Ø: } 5.8 \pm 0.2 \text{ mm}$ Thickness: $1.0 \pm 0.1 \text{ mm}$ Mass $\approx 27 \text{ mg}$	$\text{Ø: } 25.0 \pm 0.2 \text{ mm}$ Thickness: $3.0 \pm 0.1 \text{ mm}$ Mass $\approx 1270 \text{ mg}$	$\text{Ø: } 17.0 \pm 0.2 \text{ mm}$ Thickness: $1.4 \pm 0.1 \text{ mm}$ Mass $\approx 190 \text{ mg}$
13% DA ₆ 2% DA ₄₀ @DFO				
10% DA ₆ 5% DA ₄₀ @DFO				
5% DA ₆ 5% DA ₄₀ @DFO	$\text{Ø: } 10.00 \pm 0.2 \text{ mm}$ Thickness: $2.1 \pm 0.1 \text{ mm}$ mass: $\approx 180 \text{ mg}$	$\text{Ø: } 5.8 \pm 0.2 \text{ mm}$ Thickness: $0.5 \pm 0.1 \text{ mm}$ Mass $\approx 18 \text{ mg}$	$\text{Ø: } 25.0 \pm 0.2 \text{ mm}$ Thickness: $3.0 \pm 0.1 \text{ mm}$ Mass $\approx 1270 \text{ mg}$	$\text{Ø: } 14.0 \pm 0.2 \text{ mm}$ Thickness: $0.7 \pm 0.1 \text{ mm}$ Mass $\approx 127 \text{ mg}$

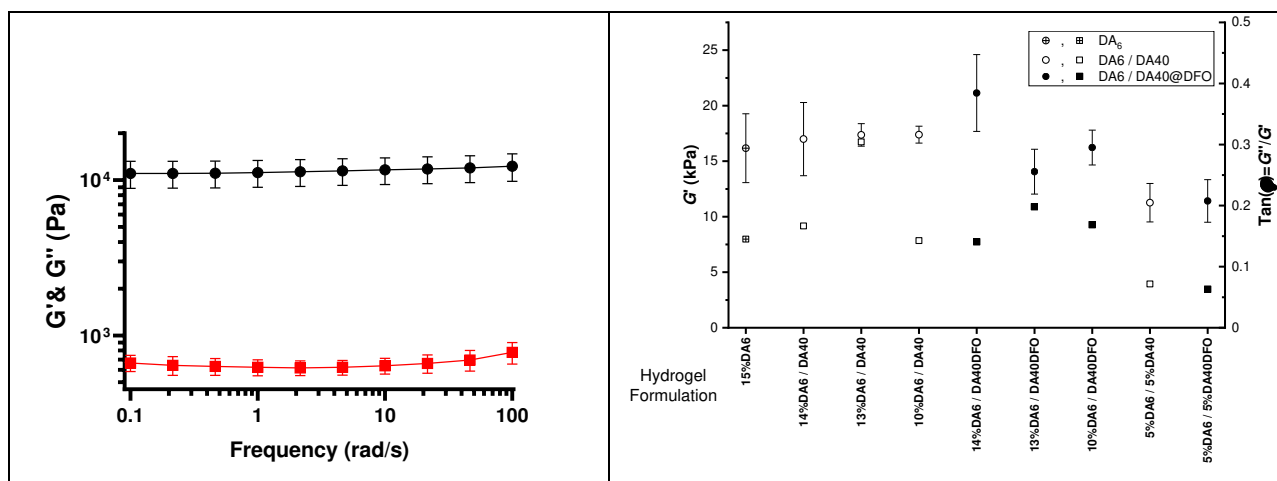


Fig. S3. (A) Example of variation of the storage ($\bullet G'$) and loss ($\blacksquare G''$) vs angular frequency of the hydrogel obtained from 5% DA₆ 5% DA₄₀@DFO formulation, after gelation in 3M NaOH aqueous solution. (B) Values of (\bullet) G' left axis and (\blacksquare) loss ratio G''/G' right axis for the different hydrogels.

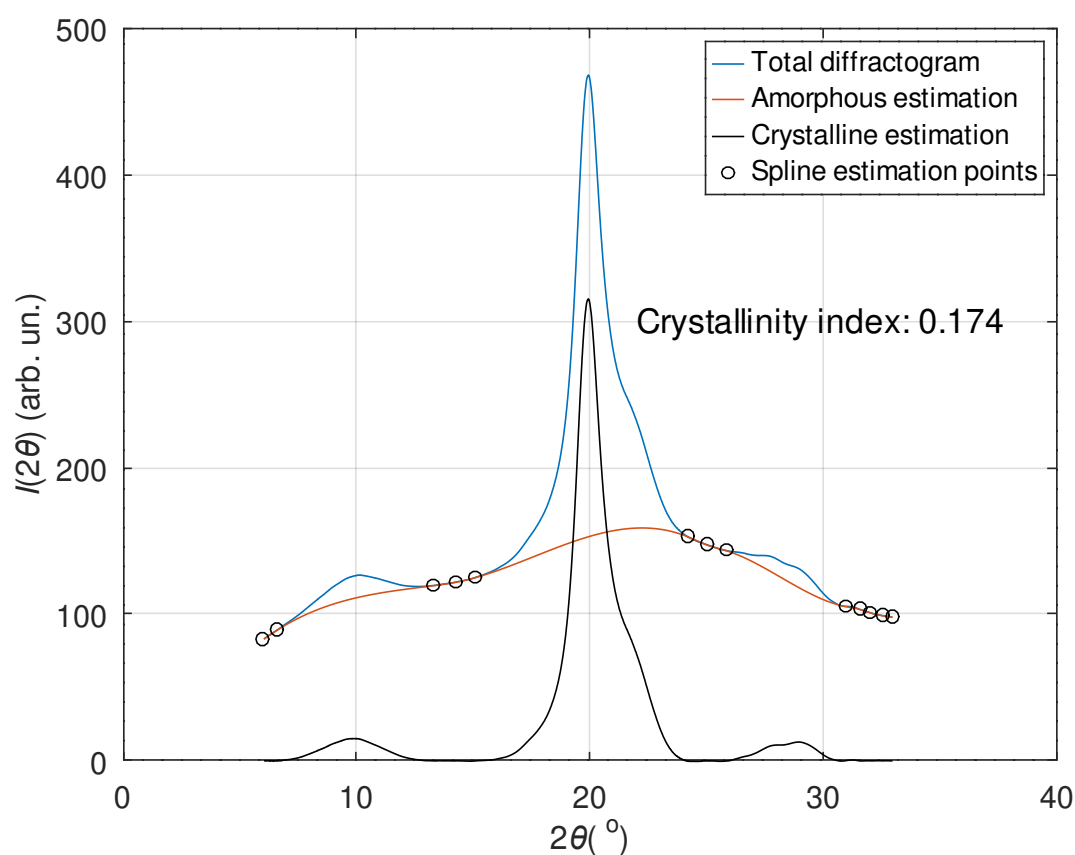


Fig. S4. Example of diffractogram treatment for the determination of the area crystallinity index for the formulation 5% DA₆ / 5% DA₄₀@DFO. The amorphous contribution is calculated as a cubic spline through the estimated points shown as empty circles (all diffractograms are treated with the same series of 2θ values to calculate the spline). From this amorphous estimation, the subtraction of the amorphous halo to the total diffractogram yields the

crystalline contribution. The crystallinity area index is calculated by integration between 6 to 33 °.

Chelation experiments

Single metal chelation

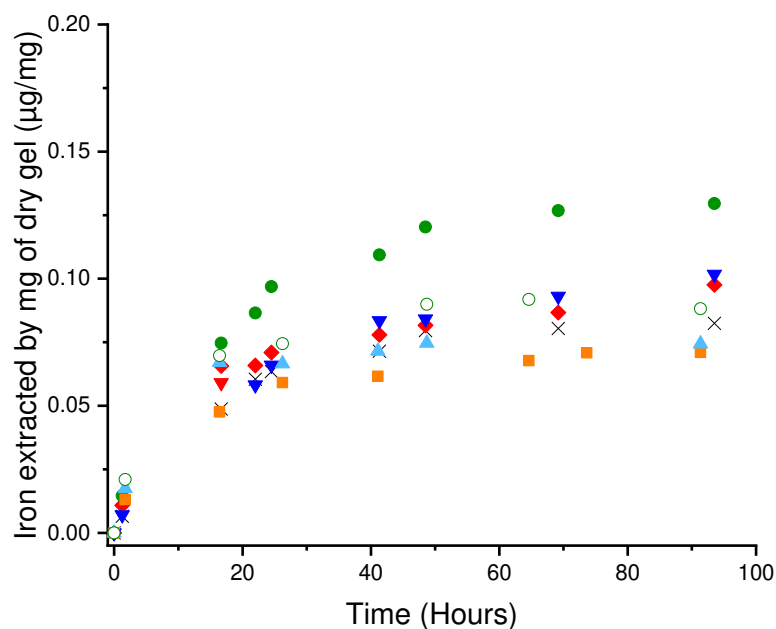


Fig. S5. Kinetics of iron (III) extraction per mg of initial xerogel in an iron (III) solution at a concentration of $3.58 \mu\text{M}$ of iron (III), $14.3 \mu\text{M}$ of deferiprone in phosphate buffer 10 mM (pH 7.4). The measurements were performed by ICP-MS. ● 10% DA₆ 5% DA₄₀@DFO, ○ 10% DA₆ 5% DA₄₀, ▼ 13% DA₆ 2% DA₄₀@DFO, ▲ 13% DA₆ 2% DA₄₀, ◆ 14% DA₆ 1% DA₄₀@DFO, ■ 14% DA₆ 1% DA₄₀, x 15% DA₆.

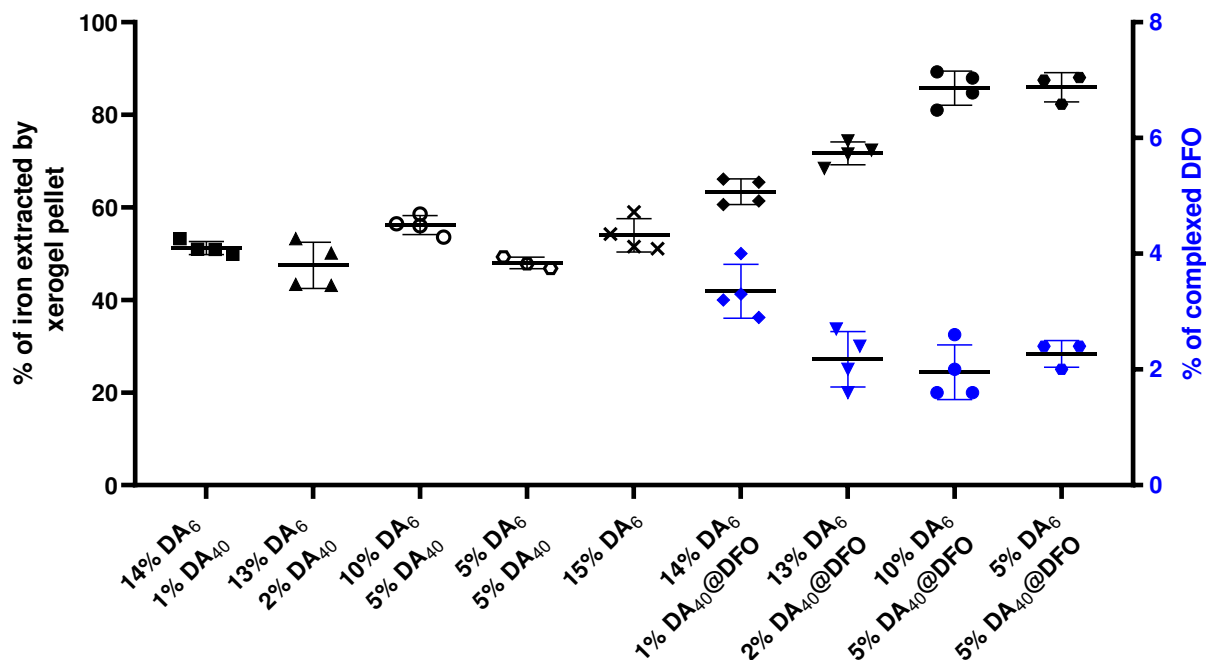


Fig. S6. Iron (III) extraction by xerogels after 90 hours in 20 ml solution with an initial concentration of 3.58 μM of $\text{Fe}(\text{NO}_3)_3$, 14.3 μM of deferiprone in phosphate buffer 10 mM (pH 7.4). The measurements were obtained using ICPMS and are given on the **black** (left) axis as % of iron extracted by xerogel pellet. **Blue** (right) axis as % of complexed DFO

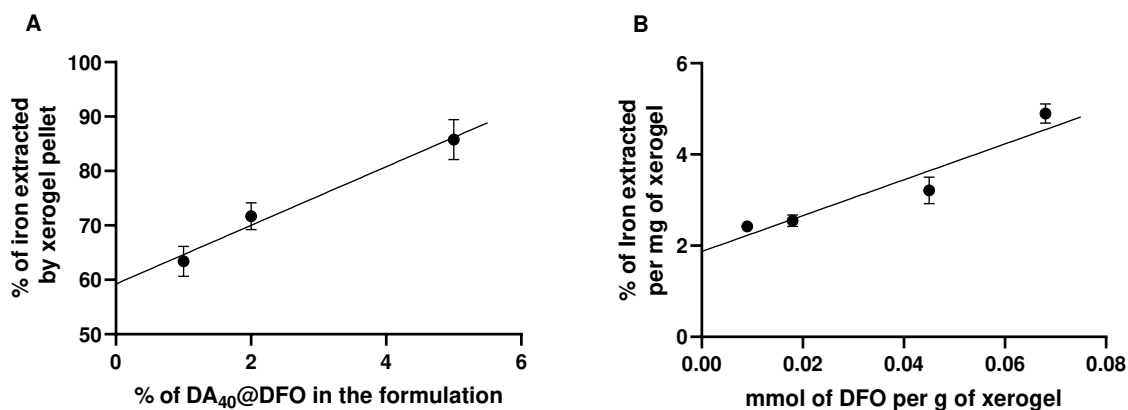


Fig. S7. A: Linear regression of the results of the % of iron (III) extraction per xerogel pellet with DA₄₀@DFO against the % of chelating polymer in the 15% w/w formulations, giving the equation $Y = 5.385 \cdot X + 59.24$ with an $R^2 = 0.909$. **B:** Linear regression of the % of iron (III) extraction per mg of xerogel against the content of mmol of DFO per g of xerogel, giving the equation $Y = 39.30 \cdot X + 1.872$ with an $R^2 = 0.874$.

Competitive multi-metal ion chelation

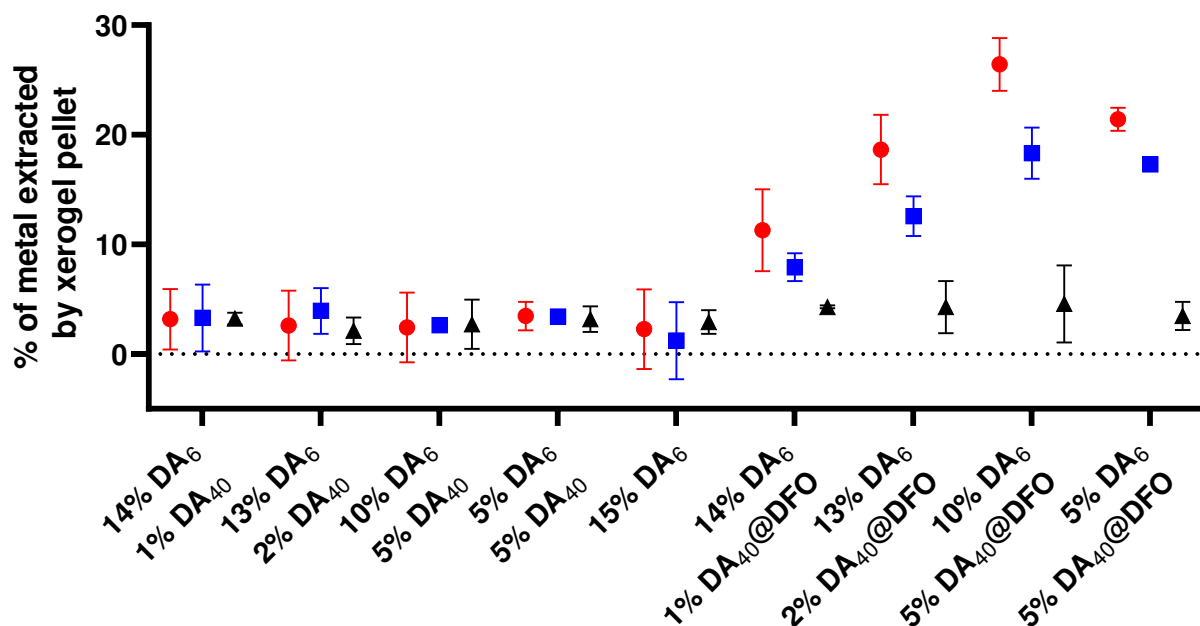


Fig. S8. Extraction of ●Iron (III), ■copper (II) and ▲zinc (II) by mg of xerogel pellet after 90 hours in 20 ml of a multi metal solution with a concentration of 3.58 for each metal, 12.9 μM of EDTA and 35 mM of Na_2SO_4 in HEPES 10 mM (pH 7.4). The molar fraction EDTA/Metal= 1.2, the molar fraction Na_2SO_4 / amine = 5. The molar fraction DFO/Metal are 1.1, 2.3 and 5.7 for the formulations containing 1%, 2%, and 5% Chitosan- DA_{40} @DFO respectively. The measurements were obtained using ICP-MS.

Table S3. Complexation constants of DFO, EDTA and Deferiprone found in literature. L stands for Ligand

Chelator	EDTA			(Desferrioxamine) (DFO)			Deferiprone (Def)
	Fe	Cu	Zn	Fe	Cu	Zn	Fe
Metal	Fe	Cu	Zn	Fe	Cu	Zn	Fe
Complex type	$\text{Fe}^{3+} + \text{EDTA}^{4-} \rightarrow (\text{FeEDTA})^-$	$\text{Cu}^{2+} + \text{EDTA}^{4-} \rightarrow (\text{CuEDTA})^{2-}$	$\text{Zn}^{2+} + \text{EDTA}^{4-} \rightarrow (\text{ZnEDTA})^{2-}$	$\text{Fe}^{3+} + \text{DFOH}^{2-} \rightarrow (\text{FeHL})^+$	$\text{Cu}^{2+} + \text{DFOH}^{2-} \rightarrow (\text{CuHL})$	$\text{Zn}^{2+} + \text{DFOH}^{2-} \rightarrow (\text{ZnHL})$	$\text{Fe}^{3+} + 3 \text{Def}^- \rightarrow \text{FeDef}_3 (\text{FeL}_3)$
Log K	25.1(Kontoghiorghes & Kontoghiorghe, 2020)	18.8(Kontoghiorghes & Kontoghiorghe, 2020)	16.5(Kontoghiorghes & Kontoghiorghe, 2020)	41.8(Toporivska & Gumienna-Kontecka, 2019)	14.0(Kontoghiorghes & Kontoghiorghe, 2020)	11.1(Kontoghiorghes & Kontoghiorghe, 2020)	36.7(Nurchi et al., 2008)

References

- Kontoghiorghes, G., & Kontoghiorghe, C. (2020). Iron and Chelation in Biochemistry and Medicine: New Approaches to Controlling Iron Metabolism and Treating Related Diseases. *Cells*, 9, 1456. <https://doi.org/10.3390/cells9061456>
- Nurchi, V. M., Crisponi, G., Pivetta, T., Donatoni, M., & Remelli, M. (2008). Potentiometric, spectrophotometric and calorimetric study on iron(III) and copper(II) complexes with 1,2-dimethyl-3-hydroxy-4-pyridinone. *Journal of Inorganic Biochemistry*, 102(4), 684–692. <https://doi.org/10.1016/j.jinorgbio.2007.10.012>
- Toporivska, Y., & Gumienna-Kontecka, E. (2019). The solution thermodynamic stability of desferrioxamine B (DFO) with Zr(IV). *Journal of Inorganic Biochemistry*, 198, 110753. <https://doi.org/10.1016/j.jinorgbio.2019.110753>

Annexe 2. Supporting information of the article “Development of chitosan-based hydrogels with tailored hydrophilicity and swelling characteristics”

Development of chitosan-based hydrogels with tailored hydrophilicity and swelling characteristics

Juan Felipe Salazar Ariza,^{1,2} François Lux,^{1,3} Olivier Tillement,¹ Alexandra Montembault,² Fabrice Gouanvé,² Laurent David^{*2}

¹ Université Claude Bernard Lyon 1, CNRS, Institut Lumière-Matière (ILM), UMR 5306, 2 rue Victor Grignard, F-69622 Villeurbanne Cedex, France.

² Université Claude Bernard Lyon 1, INSA de Lyon, Université Jean Monnet, CNRS, Ingénierie des Matériaux Polymères (IMP), UMR 5223, 15 bd Latarjet, F-69622 Villeurbanne, France.

³ Institut Universitaire de France (IUF), 75231 Paris, France.

⁴ Université Claude Bernard Lyon 1, Centre de Diffractométrie Henri Longchambon, 5 rue de La Doua, F-69100 Villeurbanne, France.

* Correspondence and requests for materials should be addressed to Pr Laurent David (email: laurent.david@univ-lyon1.fr)

5.1. Polymer characterization

1.1. ¹H-NMR of the different polymers

The DA of all polymers were determine using the Hirai method:

$$\frac{Area_{2.9-4.3\text{ ppm}}}{Area_{2.0\text{ ppm}}} = \frac{6}{3x} = \frac{2}{x}$$

The DA of DA₂₉@DOTAGA₉ and DA₂₉@DOTAGA₉@DFO₄ was determined using the intermediate, reacylated chitosan.

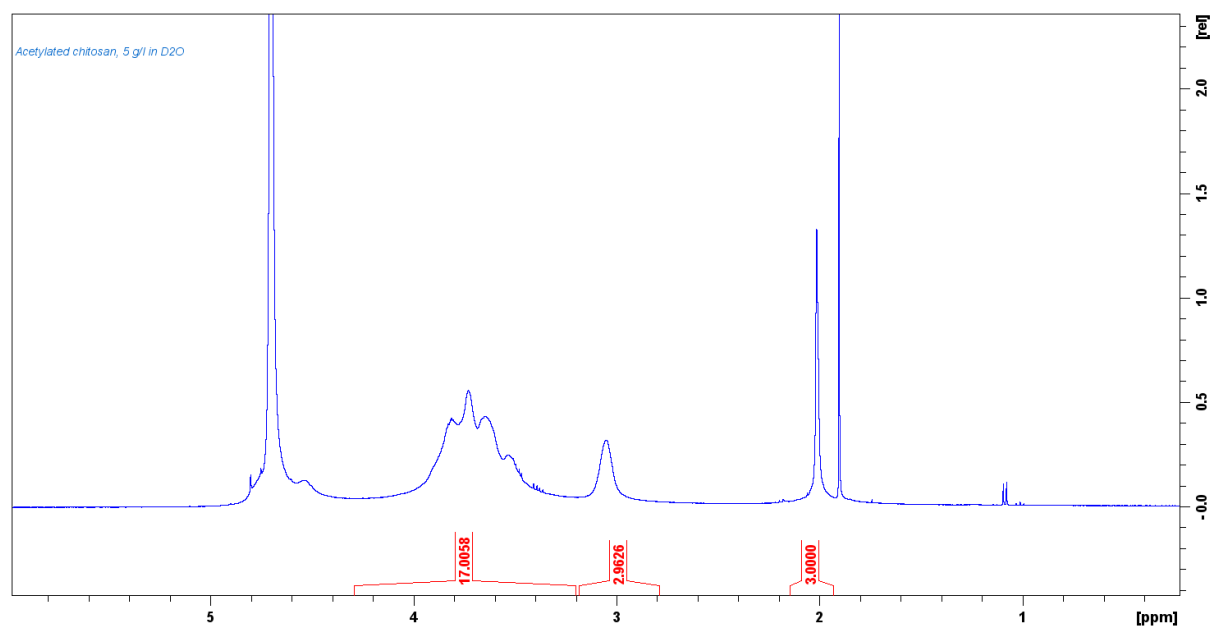


Figure S1: ¹H NMR spectrum of reacylated chitosan DA₂₉ used for the synthesis of DA₂₉@DOTAGA₉@DFO₅ in D₂O at 0.5% w/w. at 25 °C. Peak at 1.9 ppm is attributed to residual acetate group from acetic acid and doublet at 1.1 ppm corresponds to residual 1,2-propanediol.

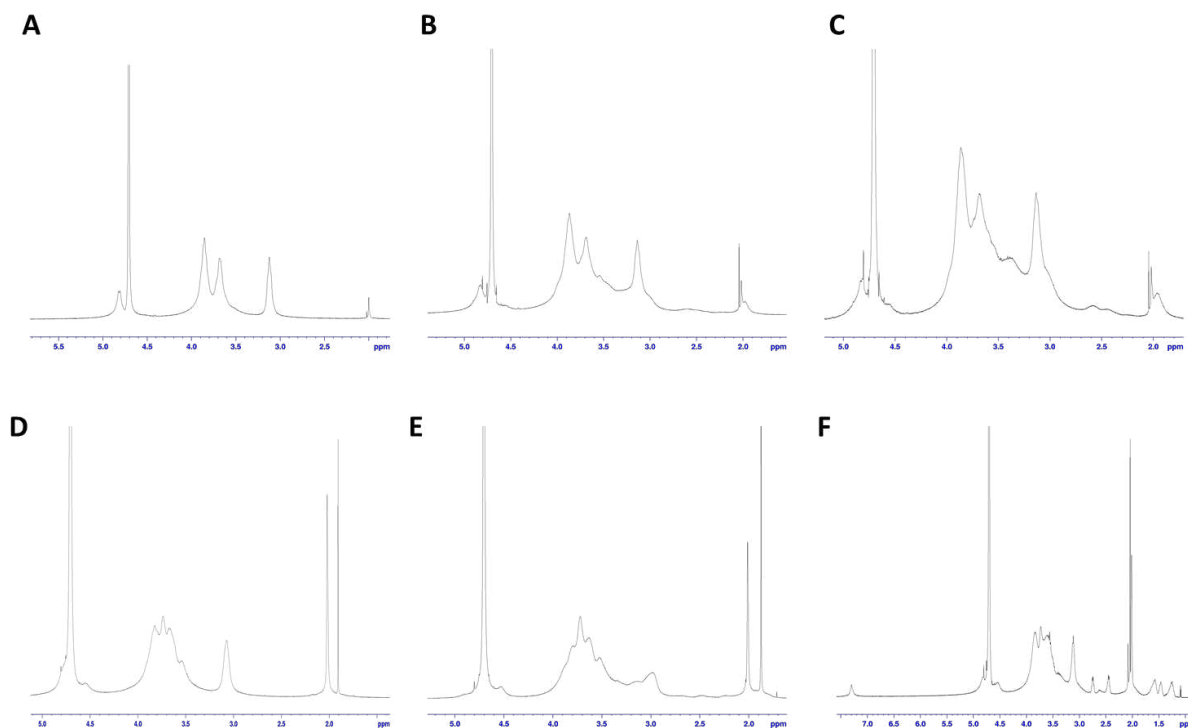


Figure S2 ¹H NMR spectrum of the studied polymers in D₂O at 0.5% w/w. at 25 °C. **A:** DA₆ in D₂O/DCl (10/1 v/v). **B:** DA₆@DOTAGA₁₁ peak at 1.9 ppm is attributed to residual acetate group from acetic acid. **C:** DA₆@DOTAGA₁₇ peak at 1.9 ppm is attributed to residual acetate

group from acetic acid. **D**: DA₂₉ peak at 1.9 ppm is attributed to residual acetate group from acetic acid. **E**: DA₂₉@DOTAGA₉ peak at 1.9 ppm is attributed to residual acetate group from acetic acid. **F**: DA₂₉@DOTAGA₉@DFO₅ Peak at 1.9 ppm is attributed to residual acetate group from acetic acid and doublet at 1.1 ppm corresponds to residual 1,2-propanediol.

1.2. Calculation of DOTAGA and DFO degree of substitution by UV data

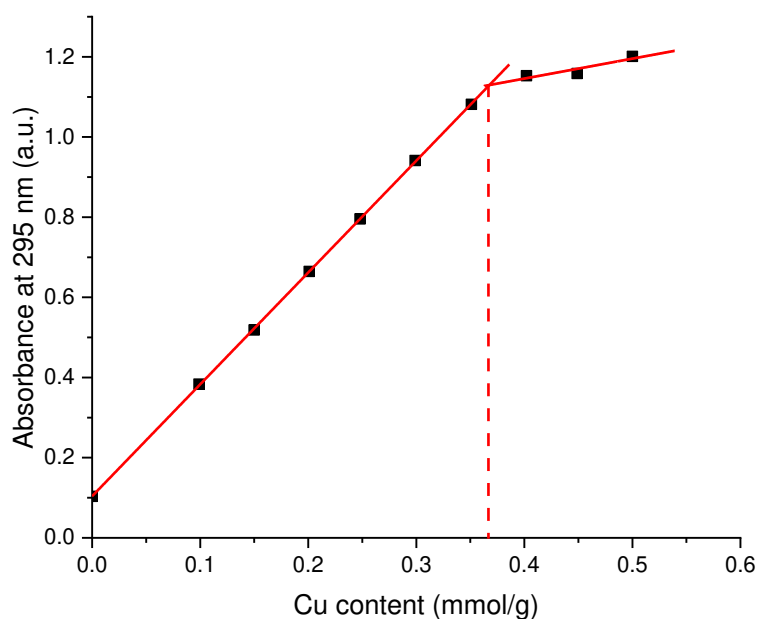


Figure S3: Absorbance at 295 nm plotted against mmol of copper per g of the intermediate chitosan acetylated with grafted DOTAGA of DA₂₉@DOTAGA₉@DFO₅ yielding 0.37 mmol of DOTAGA per g of polymer. Red lines correspond to linear regressions. The dotted line represents the crossover concentration corresponding to the saturation of DOTAGA with copper (II).

The mass fraction of DOTAGA-grafted repeat unit, w , is defined as

$$w = \frac{n_{DOTAGA} \cdot M_y}{m_{Chitosan}} = \frac{y \cdot M_y}{x \cdot M_x + y \cdot M_y + gluc \cdot M_{gluc}}$$

Where n_{DOTAGA} is the mole number of DOTAGA-grafted repeat unit, $m_{Chitosan}$ is the (dry) mass of dissolved Chitosan-DA_x@DOTAGA_y in solution, x is the molar fraction of N-acetyl glucosamine repeat units, $y = n_{DOTAGA}/n_{TOT}$ is the molar fraction of the DOTAGA-grafted repeat units and a is the molar fraction of the glucosamine repeat units. Accordingly, M_x is

defined as the molar mass of N-acetyl repeat units, M_y is the molar mass of DOTAGA-grafted repeat units and M_{gluc} the molar mass of glucosamine residue.

Since $gluc = 1 - x - y$ the equation above becomes

$$w = \frac{y \cdot M_y}{x \cdot (M_x - M_{gluc}) + y \cdot (M_y - M_{gluc}) + M_{gluc}}$$

Therefore

$$y = \frac{w \cdot (x \cdot (M_x - M_{gluc}) + M_{gluc})}{M_y - w \cdot (M_y - M_{gluc})}$$

By computation,

$$M_x = 203.19 \text{ g} \cdot \text{mol}^{-1}, M_y = 619.62 \text{ g} \cdot \text{mol}^{-1}, M_{gluc} = 161.16 \text{ g} \cdot \text{mol}^{-1}$$

Using $m_{TOT} = 1$ g of hydrated chitosan $DA_x@DOTAGA_y$ dissolved in solution, from the UV titration with Cu (III), we find:

$$\frac{C_{DOTAGA}}{m_{TOT}} = n_{DOTAGA}$$

In order to evaluate the mass fraction w , we evaluated a water content of wc (w/w) in the lyophilized polymer by thermogravimetric analysis (Table S5), measuring the mass loss between 25 and 200°C under helium flow. Then,

$$w = \frac{n_{DOTAGA} \cdot M_y}{m_{TOT} \cdot (1 - wc)}$$

Hence, the final equation is:

$$y = \frac{C_{DOTAGA} \cdot (x \cdot (M_x - M_{gluc}) + M_{gluc})}{(1 - wc) - C_{DOTAGA} \cdot (M_y - M_{gluc})}$$

The same method was used to determine the DFO degree of substitution: the mass fraction of DFO-grafted repeat unit, w' , is defined as

$$w' = \frac{n_{DFO} \cdot M_z}{m_{Chitosan}} = \frac{z \cdot M_z}{x \cdot M_x + y \cdot M_y + z \cdot M_z + gluc \cdot M_{gluc}}$$

Where n_{DFO} is the mole number of DFO-grafted repeat unit, $m_{Chitosan}$ is the (dry) mass of dissolved Chitosan DA₂₉@DOTAGA₉@DFO₅ in solution, x is the molar fraction of N-acetyl glucosamine repeat units, $z = n_{DFO}/n_{TOT}$ is the molar fraction of the DFO-grafted repeat units and a is the molar fraction of the glucosamine repeat units. Accordingly, M_x is defined as the molar mass of N-acetyl repeat units, M_z is the molar mass of DFO-grafted repeat units and M_{gluc} the molar mass of glucosamine residue.

Since $gluc = 1 - x - y - z$ the equation above becomes

$$w' = \frac{z \cdot M_z}{x \cdot (M_x - M_z) + y \cdot (M_y - M_{gluc}) + z \cdot (M_z - M_{gluc}) + M_{gluc}}$$

Therefore

$$z = \frac{w' \cdot (x \cdot (M_x - M_{gluc}) + y \cdot (M_y - M_{gluc}) + M_{gluc})}{M_z - w' \cdot (M_z - M_{gluc})}$$

By computation,

$$M_x = 203.19 \text{ g.mol}^{-1}, M_y = 619.62 \text{ g.mol}^{-1}, M_z = 914.06 \text{ g.mol}^{-1},$$

$$M_{gluc} = 161.16 \text{ g.mol}^{-1}$$

Using $m_{TOT} = 1$ g of hydrated DA₂₉@DOTAGA₉@DFO₅ dissolved in solution, from the UV titration with Fe (III), we find:

$$\frac{C_{DFO}}{m_{TOT}} = n_{DFO} = 0.16 \text{ mmol}$$

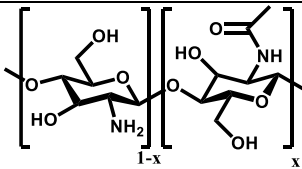
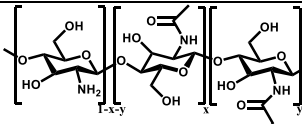
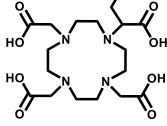
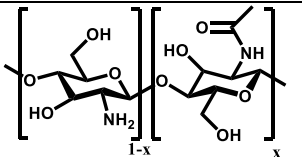
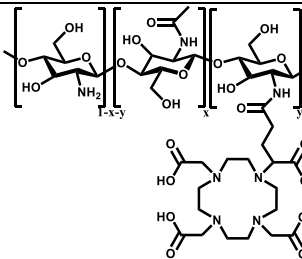
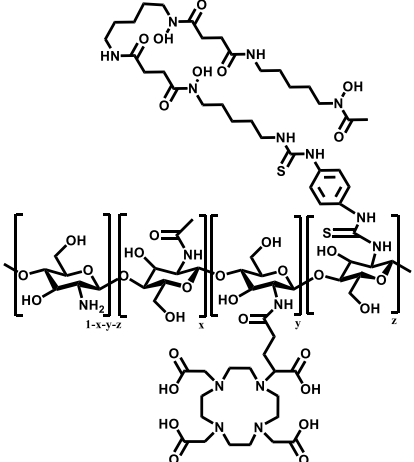
In order to evaluate the mass fraction w , we evaluated a water content of $wc = 14.6\%$ (w/w) in the lyophilized Chitosan DA₂₉@DOTAGA₉@DFO₅ powder by thermogravimetric analysis (Table S1), measuring the mass loss between 25 and 200°C under helium flow. Then,

$$w' = \frac{n_{DFO} \cdot M_z}{m_{TOT} \cdot (1 - wc)}$$

Hence, the final equation is:

$$z = \frac{C_{DFO} \cdot (x \cdot (M_x - M_{gluc}) + y \cdot (M_y - M_{gluc}) + M_{gluc})}{(1 - wc) - C_{DFO} \cdot (M_z - M_{gluc})}$$

Table S1: Parameters allowing to calculate the DS for each polymer. *DA determined by ¹H-NMR analysis of the re-acetylated intermediary. **Analysis done on the intermediate polymer only grafted with DOTAGA

Analyzed polymer	Structure	DA (x) determined by ¹ H NMR % (±1%)	n _{DOTAGA} from copper titration (mmol)	n _{DFO} from iron titration (mmol)
DA ₆		6	/	
DA ₆ @DOTAGA ₁₁		6	0.45	
DA ₆ @DOTAGA ₁₇		6	0.61	/
DA ₂₉		29	/	
DA ₂₉ @DOTAGA ₉		29*	0.35	
DA ₂₉ @DOTAGA ₉ @DFO ₅		29*	0.37**	0.16

6. Gel characterization

Table S2: Dimensions of the hydrogels and xerogels used for the different experiments.

Experiment Formulation	Drug release		Swelling	
	Precursor Hydrogels disks	Xerogels disks	Precursor Hydrogels disks	Xerogels disks
Gel DA ₆				
Gel 2/3 DA ₆ @DOTAGA ₁₁	Ø: 10.0 ± 0.2 mm Thickness: 2.10 ± 0.1 mm mass: ≈180 mg	Ø: 5.8 ± 0.2 mm Thickness: 0.5 ± 0.1 mm Mass ≈18 mg	Ø: 25.0 ± 0.2 mm Thickness: 3.0 ± 0.1 mm Mass ≈1270 mg	Ø: 14.0 ± 0.2 mm Thickness: 0.7 ± 0.1 mm Mass ≈127 mg
Gel 2/3 DA ₆ @DOTAGA ₁₇				
Gel 2/3 DA ₂₉				
Gel 2/3 DA ₂₉ @DOTAG A ₉				
Gel 2/3 DA ₂₉ @DOTAG A ₉ @DFO ₅				

Rheology

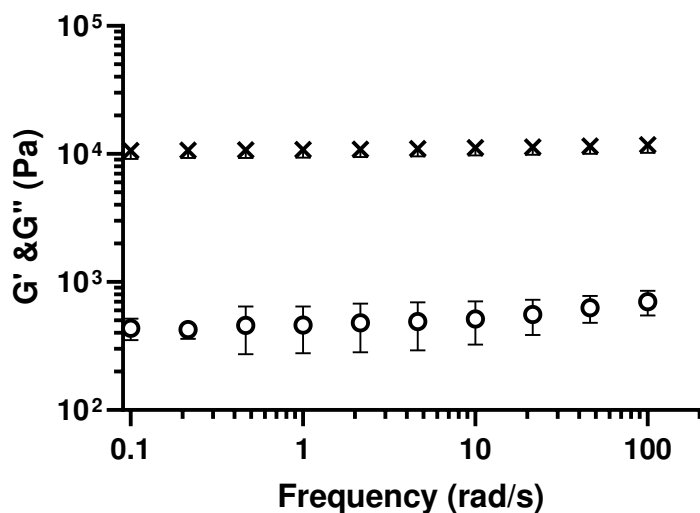


Figure S4: Example of variation of the storage (x G') and loss (o G'') vs angular frequency of the hydrogel obtained from Gel 2/3 DA₆@DOTAGA₁₇ after gelation in a 3M NaOH solution.

Table S3: G' and G'' plateau value (measured at low frequency) for each hydrogel formulation obtained after neutralization of mixed solutions in a NaOH 3M gelation bath pH>10 at room temperature (25°C) and after washing in water pH≈10 at room temperature (25°C).

Formulation's name	Measurement after gelation in 3M NaOH		Measurement after washing in water	
	G' (kPa)	G'' (kPa)	G' (kPa)	G'' (kPa)
Gel DA ₆	15.50 ± 1.84	1.30 ± 0.23	28.40 ± 2.03	4.26 ± 0.33
Gel 2/3 DA ₆ @DOTAGA ₁₁	10.00 ± 0.82	0.40 ± 0.07	6.75 ± 0.88	1.71 ± 0.18
Gel 2/3 DA ₆ @DOTAGA ₁₇	10.80 ± 1.20	0.46 ± 0.12	10.10 ± 0.78	2.14 ± 0.31
Gel 2/3 DA ₂₉	9.540 ± 1.46	1.00 ± 0.13	28.70 ± 5.40	2.96 ± 0.21
Gel 2/3 DA ₂₉ @DOTAGA ₉	12.20 ± 0.24	0.69 ± 0.09	8.62 ± 2.28	2.11 ± 0.37
Gel 2/3 DA ₂₉ @DOTAGA ₉ @DFO ₅	9.54 ± 0.56	0.58 ± 0.10	8.01 ± 0.92	2.06 ± 0.20

Table S4: Mass variation ratio between initial material and washed gel and calculated G'_{norm} after washing with water the hydrogels.

Formulation's name	R_m from gelation and after washing in water (%)	G'_{norm} (kPa) after washing in water
Gel DA ₆	-19 ± 1	35.00 ± 2.50
Gel 2/3 DA ₆ @DOTAGA ₁₁	1 ± 7	9.79 ± 2.15
Gel 2/3 DA ₆ @DOTAGA ₁₇	61 ± 10	6.27 ± 0.48
Gel 2/3 DA ₂₉	-22 ± 2	36.80 ± 6.91
Gel 2/3 DA ₂₉ @DOTAGA ₉	24 ± 5	6.92 ± 1.83
Gel 2/3 DA ₂₉ @DOTAGA ₉ @DFO ₅	22 ± 4	6.05 ± 0.69

Cristallinity analysis by XRD

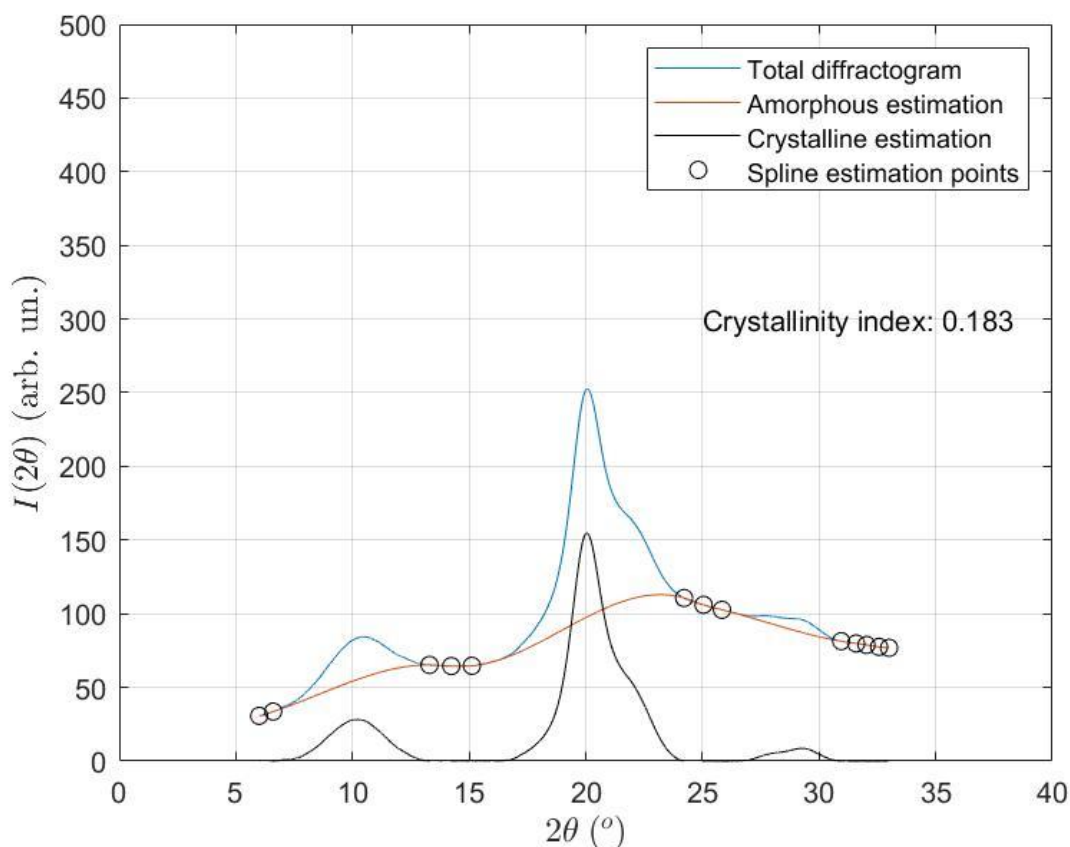


Figure S5: Example of diffractogram treatment for the determination of the area crystallinity index for the formulation Gel 2/3 DA₆@DOTAGA₁₇. The amorphous contribution is calculated as a cubic spline through the estimated points shown as empty circles (all diffractograms are treated with the same series of 2θ values to calculate the spline). From this amorphous estimation, the subtraction of the amorphous halo to the total diffractogram yields the crystalline contribution. The crystallinity area index is calculated by integration between 6 to 34 $^\circ$.

Swelling of the xerogels

Table S5: Wc measured by thermogravimetric analysis for each polymer.

Polymer	Water content measured by thermogravimetric analysis
DA ₆	12.6%
DA ₆ @DOTAGA ₁₁	13.5%
DA ₆ @DOTAGA ₁₇	14.8%
DA ₂₉	14.2%
DA ₂₉ @DOTAGA ₉	14.5%

DA₂₉@DOTAGA₉@DFO₅	14.6%
---	-------

Table S6: Wc of each xerogel formulation. *Wc was calculated using the Wc values obtained from thermogravimetric analysis (TGA) of the lyophilized polymers and the proportions of the different chitosans in each formulation.

Formulation's name	Wc calculated in xerogels %*	Maximum SR%	Mass loss after one rehydration cycle %
Gel DA₆	12.6	100±5	6.8±0.4
Gel 2/3 DA₆@DOTAGA₁₁	13.2	1345±20	7.2±0.7
Gel 2/3 DA₆@DOTAGA₁₇	14.1	1528±13	11.9±1.7
Gel 2/3 DA₂₉	13.6	226±5	8.4±0.8
Gel 2/3 DA₂₉@DOTAGA₉	13.9	1410.5±25	14.7±1.8
Gel 2/3 DA₂₉@DOTAGA₉@DFO₅	13.9	816±18	12.7±0.6

Table S7. Theoretical quantity of rhodamine 6G present in each hydrogel formulation after xerogels are submerged in 10ml of a rhodamine 6G solution for two hours. Calculation done by supposing that the rhodamine solution has a density of 1, and that there are no interactions between the hydrogel and rhodamine .

Formulation's name	Volume of rhodamine solution (µL) in hydrogel per g of initial xerogel	Theoretical mass of rhodamine (µg) inside the hydrogel per g of xerogel (Q_{th} (µg/g))
Gel DA₆	697.6 ± 48.6	17.4 ± 1.2
Gel 2/3 DA₆@DOTAGA₁₁	9962.3 ± 831.5	249.1 ± 20.8
Gel 2/3 DA₆@DOTAGA₁₇	11724.4 ± 248.4	293.1 ± 6.2
Gel 2/3 DA₂₉	1715.2 ± 45.3	42.9 ± 1.1
Gel 2/3 DA₂₉@DOTAGA₉	9457.4 ± 554.3	236.4 ± 13.9
Gel 2/3 DA₂₉@DOTAGA₉@DFO₅	3653.4 ± 105	91.3 ± 2.6

Annexe 3. Supporting information of the article “ Neurocompatible biodegradable fibers designed to extract excess free metals in the brain.”

Neurocompatible biodegradable fibers designed to extract excess free metals in the brain.

Tatiana Borisova,^{1,*} Juan Felipe Salazar Ariza,^{2,3} Natalia Pozdnyakova,¹ Natalia Krisanova,¹ Artem Pastukhov,¹ Marina Dudarenko,¹ Thomas Gréa,^{2,3} Alexandra Montembault,³ Imad Benkhaled,⁴ Noël Pinaud,⁴ Justine Deborne,⁴ Yannick Crémillieux,⁴ Philippe De Deurwaerdere,⁵ Vladimir Lysenko,¹ Stéphane Palfi,⁶ Olivier Tillement², Laurent David,³ Francois Lux,^{2,7,*}

1-Palladin Institute of Biochemistry National Academy of Sciences of Ukraine, 9 Leontovicha Street, Kyiv, 01054, Ukraine. Electronic address: tborisov@biochem.kiev.ua.

2- Institut Lumière Matière UMR 5306 CNRS, Université Claude Bernard Lyon 1, 69622, Villeurbanne, France.

3- Université Claude Bernard Lyon 1, Institut National des Sciences Appliquées, Université Jean Monnet, CNRS, UMR 5223, Ingénierie des Matériaux Polymères (IMP), 15 bd Latarjet, 69622 Villeurbanne, France.

4- Institut des Sciences Moléculaires, UMR 5255, CNRS, Université de Bordeaux, Bordeaux, France.

5- Centre National de la Recherche Scientifique, Institut des Neurosciences Intégratives et Cognitives d'Aquitaine, UMR, 5287, Bordeaux, France.

6- Henri-Mondor Hospital, University Hospital APHP, Department of Neurosurgery, 51 AV Mar de Lattre de Tassigny, 94000 Créteil, France

7- Institut Universitaire de France (IUF), Paris, France

Corresponding authors : tborisov@ukr.net, francois.lux@univ-lyon1.fr

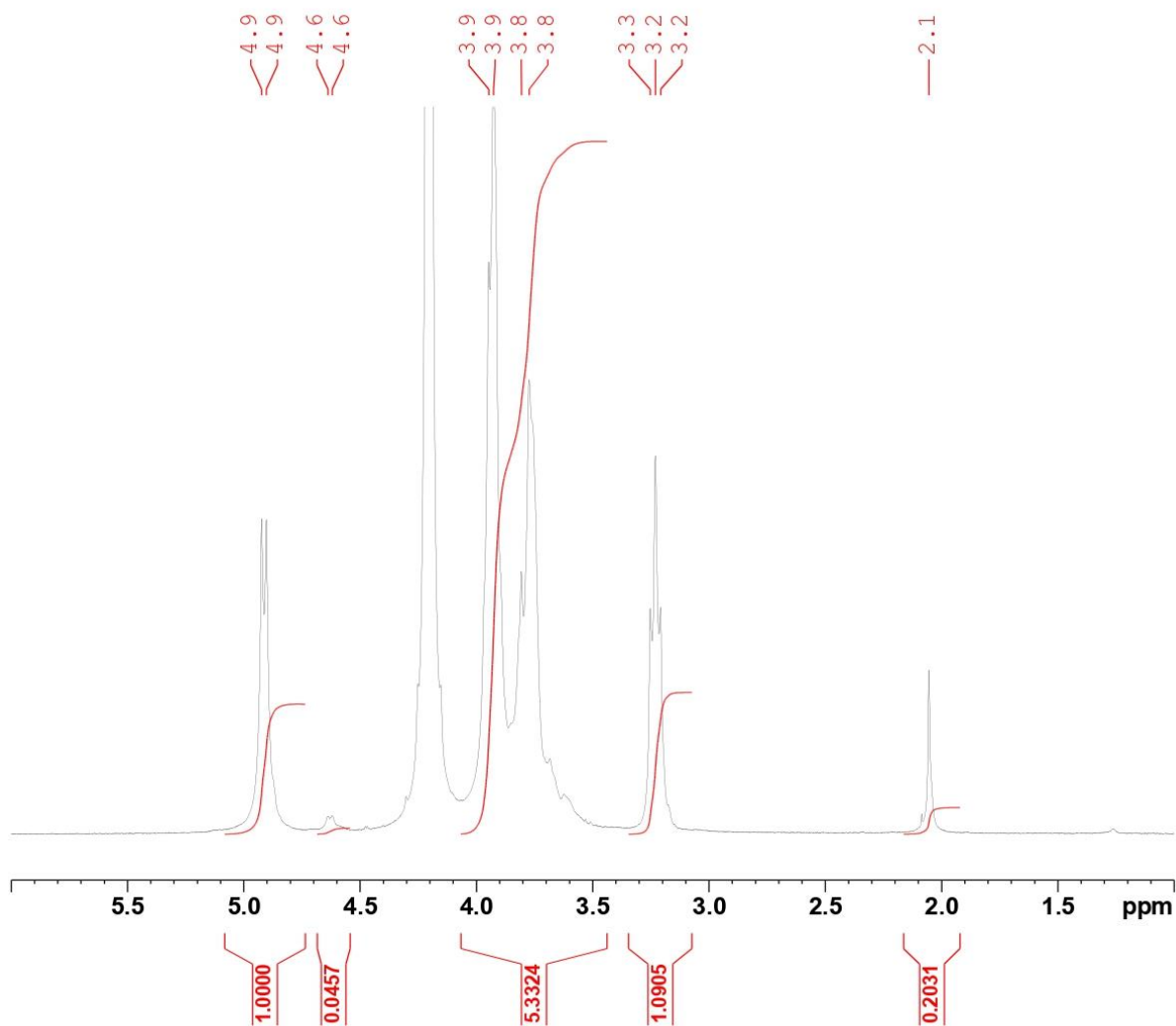


Figure S1: NMR 1H spectrum of Matexcel chitosan at 343 K in D₂O/DCl.

Determination of the DA of the raw chitosan by the Hirai method:

$$\frac{Area_{3.00-4.55 \text{ ppm}}}{Area_{2.45 \text{ ppm}}} = \frac{6}{3x} = \frac{2}{x}$$

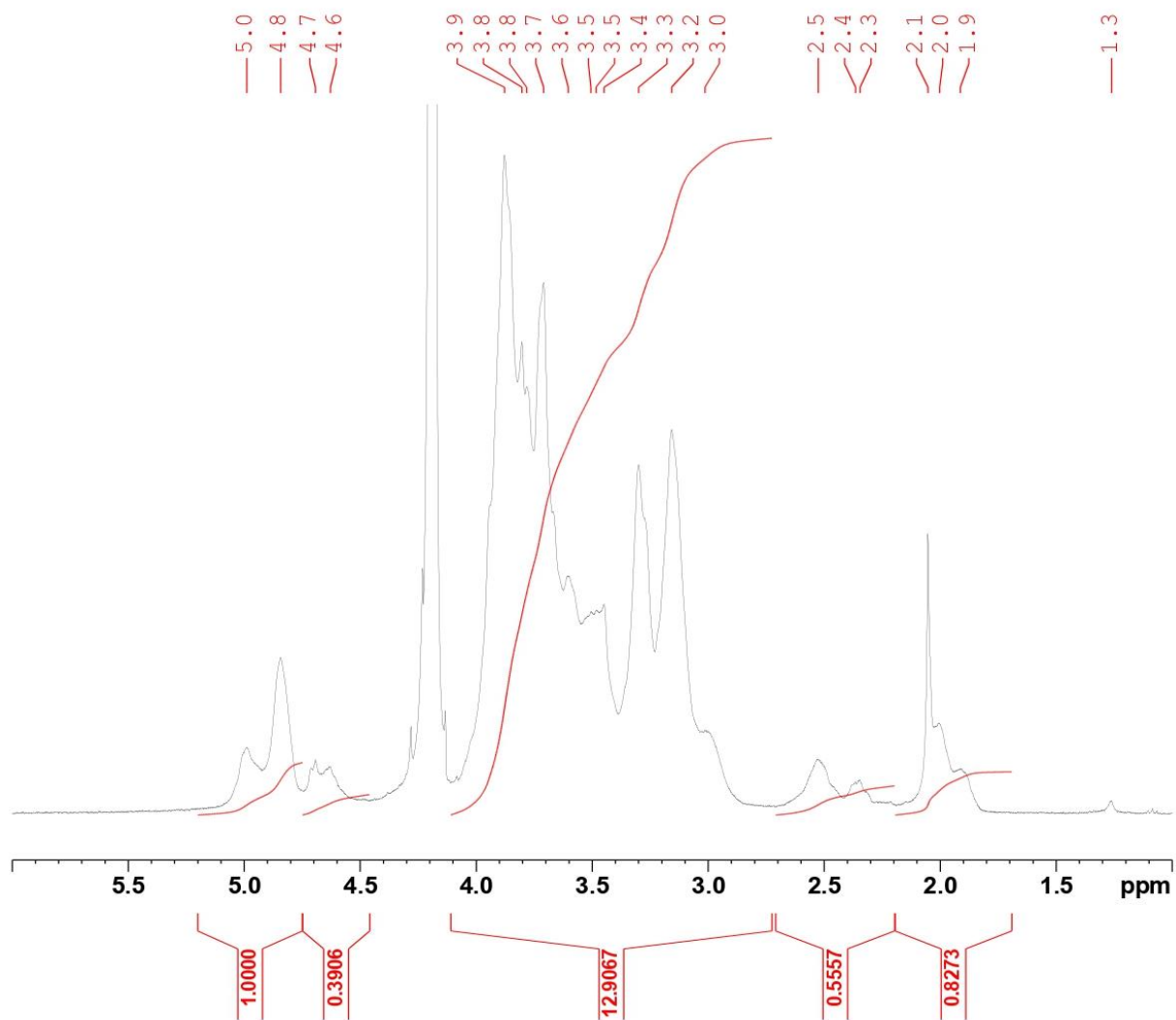


Figure S2: NMR ^1H Chitosan@DOTAGA 1%_{w/w} at 343 K in $\text{D}_2\text{O}/\text{DCI}$. Additional peaks in relation to figure S1 from 1.8-4.1 ppm correspond to the grafted DOTAGA. See Table S1 for further detail.

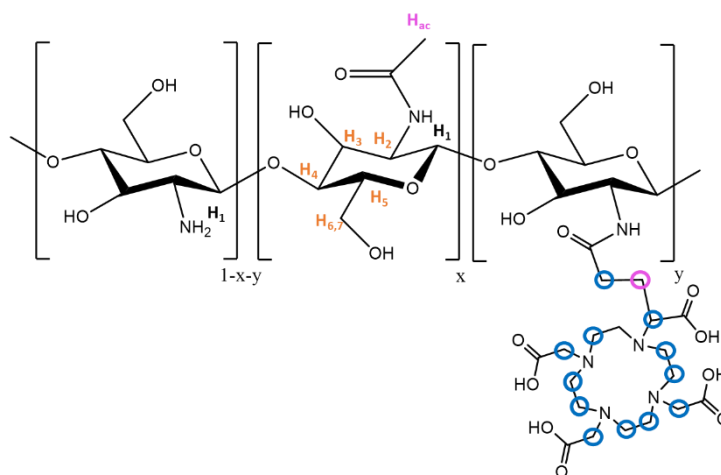


Figure S3: Labelling for attribution of ^1H NMR signal of Chitosan@DOTAGA

Chemical shift (ppm)	Integration	Attribution
4.2-5.2	1	H_1 (in black)
4.1-2.2	$6 + 25y$	$\text{H}_2, \text{H}_3, \text{H}_4, \text{H}_5, \text{H}_{6,7}$ (in orange) + 25 DOTAGA protons (in blue)
1.8-2.2	$3x + 2y$	H_{ac} , 2 DOTAGA protons (in pink)

Table S1: Attribution of ^1H NMR signals of Chitosan@DOTAGA (x: acetylation degree, y: DOTAGA grafting)

Computation of parameter y from copper (II) titration by UV data.

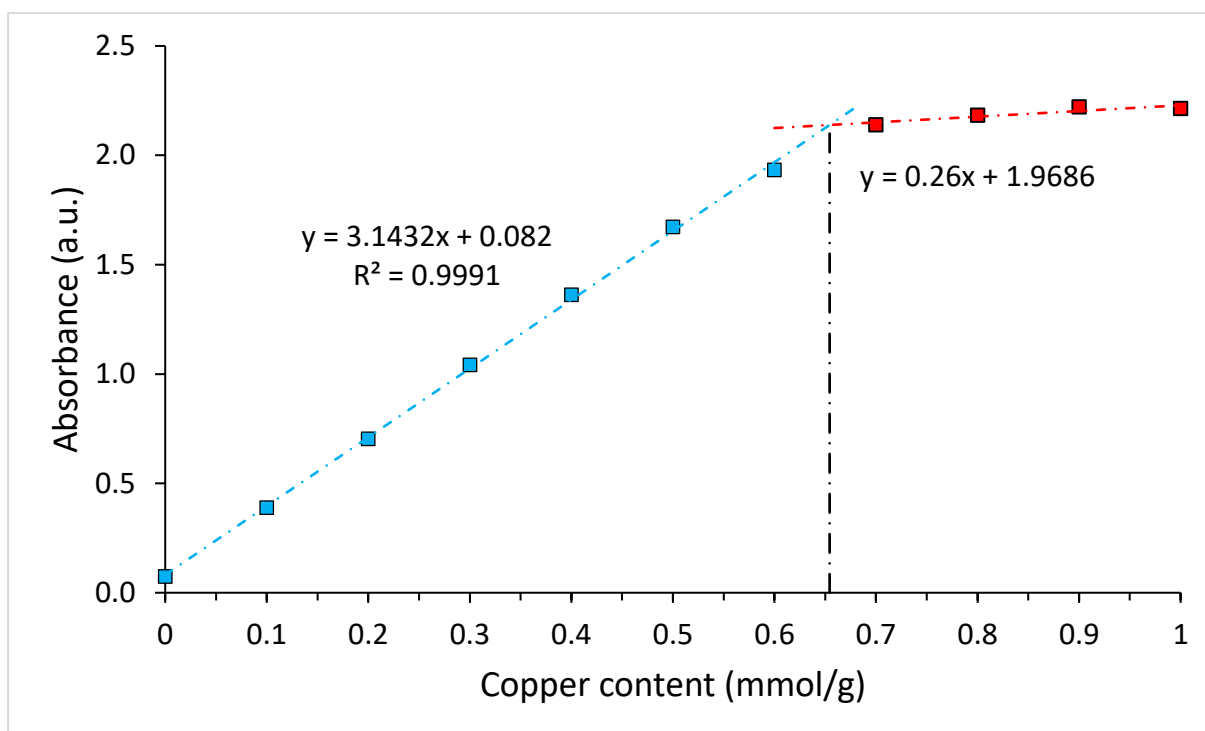


Figure S4: Absorbance at 295 nm plotted against mmol of copper per g of Chitosan@DOTAGA. Red lines correspond to the linear regression. The black dotted line represents the saturation of DOTAGA with copper corresponding to 0.654 mmol/g.

The mass fraction of DOTAGA-grafted repeat unit, w , is defined as

$$w = \frac{n_{DFO} \cdot M_y}{m_{Chitosan}} = \frac{y \cdot M_y}{x \cdot M_x + y \cdot M_y + a \cdot M_a}$$

Where n_{DFO} is the mole number of DFO-grafted repeat unit, $m_{Chitosan}$ is the (dry) mass of dissolved Chitosan@DOTAGA in solution, x is the molar fraction of N-acetyl glucosamine repeat units, $y = n_{DOTAGA}/n_{TOT}$ is the molar fraction of the DOTAGA-grafted repeat units and a is the molar fraction of the glucosamine repeat units. Accordingly, M_x is defined as the molar mass of N-acetyl repeat units, M_y is the molar mass of DOTAGA-grafted repeat units and M_a the molar mass of glucosamine residue.

Since $a = 1 - x - y$ the equation above becomes

$$w = \frac{y \cdot M_y}{x \cdot (M_x - M_z) + y \cdot (M_y - M_a) + M_a}$$

Therefore

$$y = \frac{w \cdot (x \cdot (M_x - M_a) + M_a)}{M_y - w \cdot (M_y - M_a)}$$

By computation,

$$M_x = 203.19 \text{ g.mol}^{-1}, M_y = 619.62 \text{ g.mol}^{-1}, M_a = 161.16 \text{ g.mol}^{-1}$$

Using $m_{TOT} = 1$ g of hydrated Chitosan@DOTAGA dissolved in solution, from the UV titration with copper (II), we find:

$$n_{DOTAGA} = 0.654 \text{ mmol}$$

In order to evaluate the mass fraction w , we evaluated a water content of $wc=8.2\%$ w/w in the lyophilized Chitosan-DA₄₀@DFO powder by thermogravimetric analysis, measuring the mass loss between 25 and 200°C under nitrogen flow. Then,

$$w = \frac{n_{DOTAGA} \cdot M_y}{m_{TOT} \cdot (1 - wc)} = 0.438$$

From ¹H-NMR, $x = 0.063$

This results in $y = 0.171$

As such, the estimated DS of the synthesized Chitosan@DOTAGA product is $17 \pm 0.5\%$

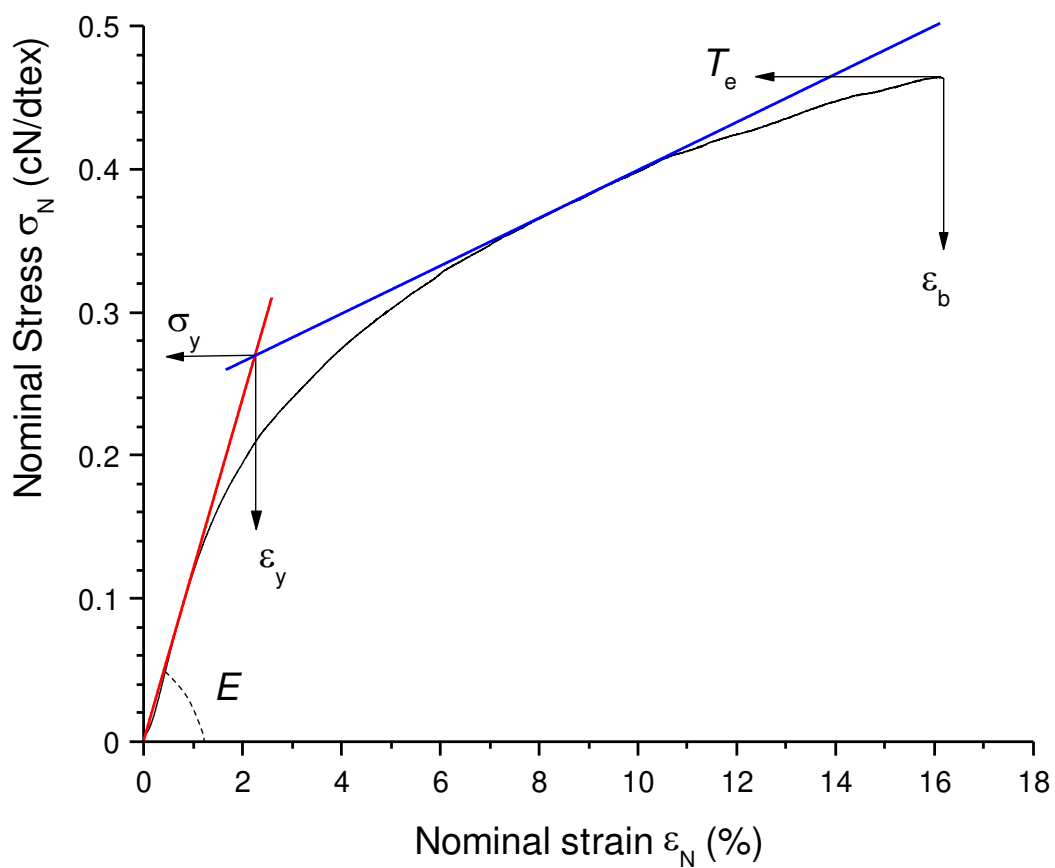
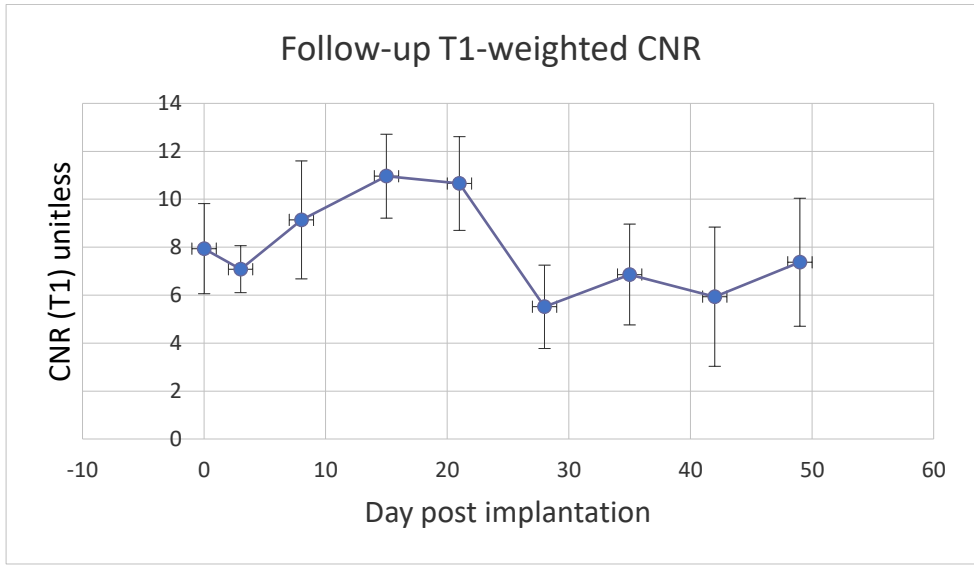
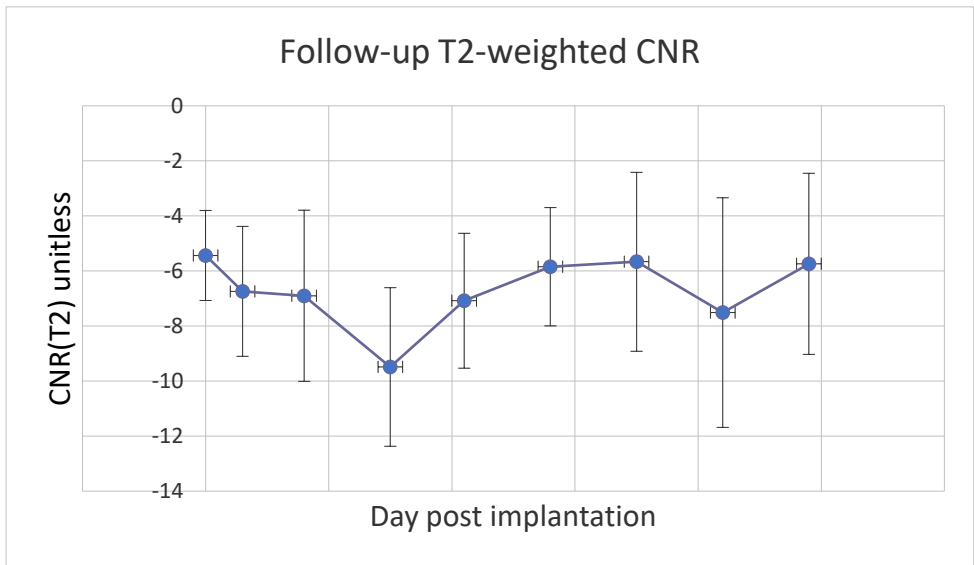


Figure S5: Example of stress-strain curve of the Chitosan 5% Chitosan@DOTAGA 10% fiber, obtained by uniaxial tensile test (solid black line). Slope corresponding to the linear elastic region of the fiber (red line) enable the determination of the Young's modulus. The intersect between the linear elastic and plastic regimes is the yield point.



A.



B.

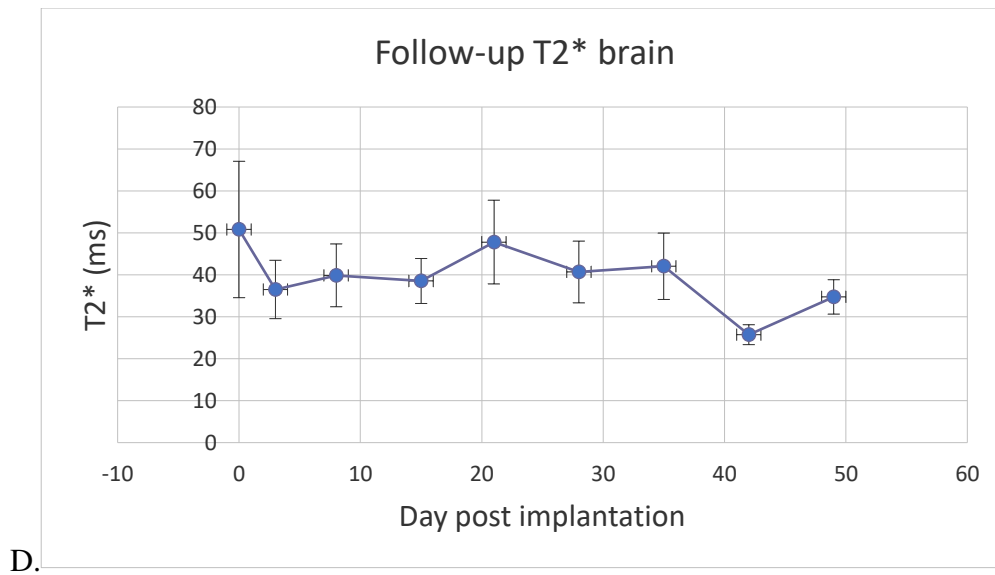
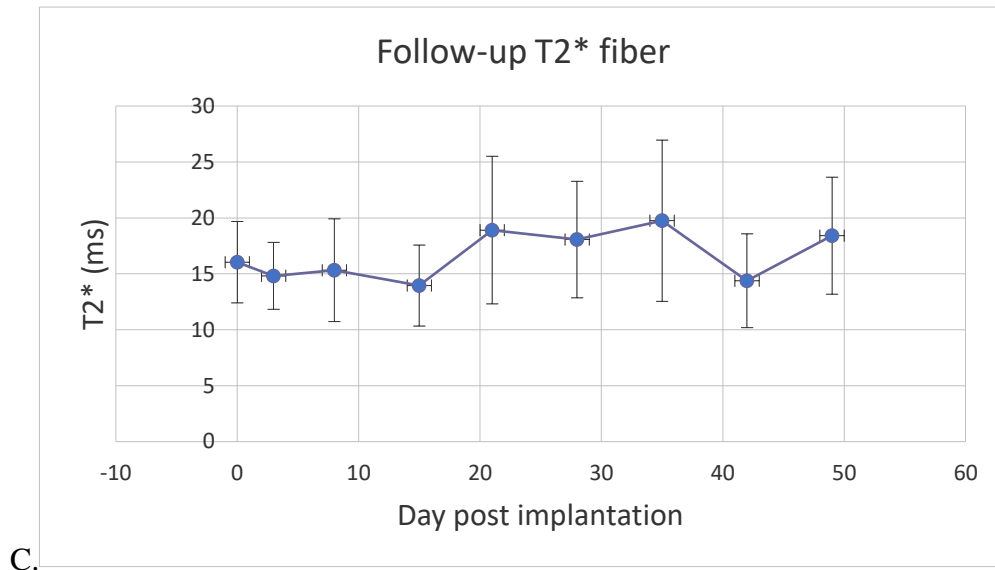


Figure S6: Follow-up graphs of (A) T1-weighted CNR, (B) T2-weighted CNR, (C) T2* value of the fiber and (D) T2* value of the brain. Error bars correspond to the standard deviation of the measurements.

VI Bibliography:

- [1] J.I. Lachowicz, V.M. Nurchi, G. Crisponi, I. Cappai, R. Cappai, M. Busato, A. Melchior, M. Tolazzi, M. Peana, E. Garribba, M.A. Zoroddu, P. Coni, G. Pichiri, J. Aaseth, para-Aminosalicylic acid in the treatment of manganese toxicity. Complexation of Mn²⁺ with 4-amino-2-hydroxybenzoic acid and its N-acetylated metabolite, *New J. Chem.* 42 (2018) 8035–8049. <https://doi.org/10.1039/C7NJ04648K>.
- [2] G. Anderegg, CRITICAL SURVEY OF STABILITY CONSTANTS OF EDTA COMPLEXES, in: G. Anderegg (Ed.), *Crit. Surv. Stab. Constants EDTA Complexes*, Pergamon, 1977: pp. 1–36. <https://doi.org/10.1016/B978-0-08-022009-3.50004-0>.
- [3] V.K. Gupta, I. Ali, Determination of stability constants of Fe(II), Co(II) and Cu(II) – nitrilotriacetate–penicillamine mixed complexes by electrophoresis, (1998).
- [4] V.M. Nurchi, G. Crisponi, M. Crespo-Alonso, J.I. Lachowicz, Z. Szewczuk, G.J.S. Cooper, Complex formation equilibria of Cu^{II} and Zn^{II} with triethylenetetramine and its mono- and di-acetyl metabolites, *Dalton Trans* 42 (2013) 6161–6170. <https://doi.org/10.1039/C2DT32252H>.
- [5] V.M. Nurchi, G. Crisponi, T. Pivetta, M. Donatoni, M. Remelli, Potentiometric, spectrophotometric and calorimetric study on iron(III) and copper(II) complexes with 1,2-dimethyl-3-hydroxy-4-pyridinone, *J. Inorg. Biochem.* 102 (2008) 684–692. <https://doi.org/10.1016/j.jinorgbio.2007.10.012>.
- [6] G. Crisponi, V.M. Nurchi, M. Crespo-Alonso, G. Sanna, M.A. Zoroddu, G. Alberti, R. Biesuz, A Speciation Study on the Perturbing Effects of Iron Chelators on the Homeostasis of Essential Metal Ions, *PLOS ONE* 10 (2015) e0133050. <https://doi.org/10.1371/journal.pone.0133050>.
- [7] A.E. Martell, R.D. Hancock, R.M. Smith, R.J. Motekaitis, Coordination of Al(III) in the environment and in biological systems, *Coord. Chem. Rev.* 149 (1996) 311–328. [https://doi.org/10.1016/S0010-8545\(96\)90034-X](https://doi.org/10.1016/S0010-8545(96)90034-X).
- [8] Y. Toporivska, E. Gumienna-Kontecka, The solution thermodynamic stability of desferrioxamine B (DFO) with Zr(IV), *J. Inorg. Biochem.* 198 (2019) 110753. <https://doi.org/10.1016/j.jinorgbio.2019.110753>.
- [9] E. Farkas, É.A. Enyedy, L. Zékány, G. Deák, Interaction between iron(II) and hydroxamic acids: oxidation of iron(II) to iron(III) by desferrioxamine B under anaerobic conditions, *J. Inorg. Biochem.* 83 (2001) 107–114. [https://doi.org/10.1016/S0162-0134\(00\)00197-5](https://doi.org/10.1016/S0162-0134(00)00197-5).
- [10] G. Kontoghiorghe, C. Kontoghiorghe, Iron and Chelation in Biochemistry and Medicine: New Approaches to Controlling Iron Metabolism and Treating Related Diseases, *Cells* 9 (2020) 1456. <https://doi.org/10.3390/cells9061456>.
- [11] K.L. Summers, G.P. Roseman, G.J. Sopasis, G.L. Millhauser, H.H. Harris, I.J. Pickering, G.N. George, Copper(II) Binding to PBT2 Differs from That of Other 8-Hydroxyquinoline Chelators: Implications for the Treatment of Neurodegenerative Protein Misfolding Diseases, *Inorg. Chem.* 59 (2020) 17519–17534. <https://doi.org/10.1021/acs.inorgchem.0c02754>.
- [12] M. Tosato, V. Di Marco, Metal Chelation Therapy and Parkinson’s Disease: A Critical Review on the Thermodynamics of Complex Formation between Relevant Metal Ions and Promising or Established Drugs, *Biomolecules* 9 (2019) 269. <https://doi.org/10.3390/biom9070269>.
- [13] G. Anderegg, F. Arnaud-Neu, R. Delgado, J. Felcman, K. Popov, Critical evaluation of stability constants of metal complexes of complexones for biomedical and environmental applications* (IUPAC Technical Report);, *Pure Appl. Chem.* 77 (2005) 1445–1495. <https://doi.org/10.1351/pac200577081445>.

- [14] E.T. Clarke, A.E. Martell, Stabilities of trivalent metal ion complexes of the tetraacetate derivatives of 12-, 13- and 14-membered tetraazamacrocycles, *Inorganica Chim. Acta* 190 (1991) 37–46. [https://doi.org/10.1016/S0020-1693\(00\)80229-7](https://doi.org/10.1016/S0020-1693(00)80229-7).
- [15] W.A. Cilley, D.A. Nicholson, An Equilibrium Model for the Nta Complexation of Metal Ions in Natural Waters, *Environ. Lett.* 2 (1971) 121–129. <https://doi.org/10.1080/00139307109435433>.
- [16] R.J. Motekaitis, A.E. Martell, THE IRON(III) AND IRON(II) COMPLEXES OF NITRILOTRIACETIC ACID, *J. Coord. Chem.* (1994). <https://doi.org/10.1080/00958979408022546>.
- [17] W.A.E. McBryde, J.L. McCourt, V. Cheam, Copper(II)-nitrilotriacetate complexes in aqueous solution, *J. Inorg. Nucl. Chem.* 35 (1973) 4193–4197. [https://doi.org/10.1016/0022-1902\(73\)80407-5](https://doi.org/10.1016/0022-1902(73)80407-5).
- [18] L.-C. Königsberger, E. Königsberger, P.M. May, G.T. Hefter, Complexation of iron(III) and iron(II) by citrate. Implications for iron speciation in blood plasma, *J. Inorg. Biochem.* 78 (2000) 175–184. [https://doi.org/10.1016/S0162-0134\(99\)00222-6](https://doi.org/10.1016/S0162-0134(99)00222-6).
- [19] W. Kaim, B. Schwederski, A. Klein, W. Kaim, Chapter 2 Some General Principles, in: *Bioinorg. Chem. Inorg. Elem. Chem. Life Introd. Guide*, 2. ed, Wiley, Chichester, 2013: pp. 7–36.
- [20] J. Aaseth, L. Gerhardsson, M.A. Skaug, J. Alexander, Chapter 1 - General Chemistry of Metal Toxicity and Basis for Metal Complexation, in: J. Aaseth, G. Crisponi, O. Andersen (Eds.), *Chelation Ther. Treat. Met. Intox.*, Academic Press, Boston, 2016: pp. 1–33. <https://doi.org/10.1016/B978-0-12-803072-1.00001-8>.
- [21] J. Emsley, J. Emsley, *Nature's Building Blocks: An A-Z Guide to the Elements*, Second Edition, Second Edition, Oxford University Press, Oxford, New York, 2011.
- [22] W. Kaim, B. Schwederski, A. Klein, W. Kaim, Chapter 17 The Bioinorganic Chemistry of the Quintessentially Toxic Metals, in: *Bioinorg. Chem. Inorg. Elem. Chem. Life Introd. Guide*, 2. ed, Wiley, Chichester, 2013.
- [23] M.T. Lorincz, Neurologic Wilson's disease, *Ann. N. Y. Acad. Sci.* 1184 (2010) 173–187. <https://doi.org/10.1111/j.1749-6632.2009.05109.x>.
- [24] S. Pfaender, A.M. Grabrucker, Characterization of biometal profiles in neurological disorders†, *Metallomics* 6 (2014) 960–977. <https://doi.org/10.1039/c4mt00008k>.
- [25] P.B. Foley, D.J. Hare, K.L. Double, A brief history of brain iron accumulation in Parkinson disease and related disorders, *J. Neural Transm.* 129 (2022) 505–520. <https://doi.org/10.1007/s00702-022-02505-5>.
- [26] A. Budimir, Metal ions, Alzheimer's disease and chelation therapy, *Acta Pharm.* 61 (2011) 1–14. <https://doi.org/10.2478/v10007-011-0006-6>.
- [27] S.J. Texel, X. Xu, S. Pin, Z.L. Harris, Neuropathology and Iron: Central Nervous System Iron Homeostasis, in: G.J. Anderson, G.D. McLaren (Eds.), *Iron Physiol. Pathophysiol. Hum.*, Humana Press, Totowa, NJ, 2012: pp. 455–476. https://doi.org/10.1007/978-1-60327-485-2_23.
- [28] S. Bolognin, D. Drago, L. Messori, P. Zatta, Chelation therapy for neurodegenerative diseases, *Med. Res. Rev.* 29 (2009) 547–570. <https://doi.org/10.1002/med.20148>.
- [29] K. Tuschl, P.B. Mills, P.T. Clayton, Chapter Twelve - Manganese and the Brain, in: K.P. Bhatia, S.A. Schneider (Eds.), *Int. Rev. Neurobiol.*, Academic Press, 2013: pp. 277–312. <https://doi.org/10.1016/B978-0-12-410502-7.00013-2>.
- [30] M. Valko, H. Morris, M.T.D. Cronin, Metals, Toxicity and Oxidative Stress, *Curr. Med. Chem.* 12 (2005) 1161–1208. <https://doi.org/10.2174/0929867053764635>.

- [31] M. Latorre, R. Troncoso, R. Uauy, Chapter 4 - Biological Aspects of Copper, in: N. Kerkar, E.A. Roberts (Eds.), *Clin. Transl. Perspect. WILSON Dis.*, Academic Press, 2019: pp. 25–31. <https://doi.org/10.1016/B978-0-12-810532-0.00004-5>.
- [32] C. Grange, F. Lux, T. Brichart, L. David, A. Couturier, D.E. Leaf, B. Allaouchiche, O. Tillement, Iron as an emerging therapeutic target in critically ill patients, *Crit. Care* 27 (2023) 475. <https://doi.org/10.1186/s13054-023-04759-1>.
- [33] O. Karcioğlu, B. Arslan, G.A. Engwa, P.U. Ferdinand, F.N. Nwalo, M.N. Unachukwu, Poisoning in the Modern World - New Tricks for an Old Dog?, in: *Poisoning Mod. World - New Tricks Old Dog*, IntechOpen, 2019. <https://doi.org/10.5772/intechopen.73906>.
- [34] A. Smith, Iron Salvage Pathways, in: G.J. Anderson, G.D. McLaren (Eds.), *Iron Physiol. Pathophysiol. Hum.*, Humana Press, Totowa, NJ, 2012: pp. 141–171. https://doi.org/10.1007/978-1-60327-485-2_8.
- [35] M.L. Hegde, P. Bharathi, A. Suram, C. Venugopal, R. Jagannathan, P. Poddar, P. Srinivas, K. Sambamurti, K.J. Rao, J. Scancar, L. Messori, L. Zecca, P. Zatta, Challenges Associated with Metal Chelation Therapy in Alzheimer's Disease, *J. Alzheimers Dis.* 17 (2009) 457–468. <https://doi.org/10.3233/JAD-2009-1068>.
- [36] D.J. Betteridge, What is oxidative stress?, *Metabolism* 49 (2000) 3–8. [https://doi.org/10.1016/S0026-0495\(00\)80077-3](https://doi.org/10.1016/S0026-0495(00)80077-3).
- [37] K. Jomova, D. Vondrakova, M. Lawson, M. Valko, Metals, oxidative stress and neurodegenerative disorders, *Mol. Cell. Biochem.* 345 (2010) 91–104. <https://doi.org/10.1007/s11010-010-0563-x>.
- [38] W. Kaim, B. Schwederski, A. Klein, W. Kaim, Chapter 6 Catalysis through Hemoproteins: Electron Transfer, Oxygen Activation and Metabolism of Inorganic Intermediates, in: *Bioinorg. Chem. Inorg. Elem. Chem. Life Introd. Guide*, 2. ed, Wiley, Chichester, 2013: pp. 99–116.
- [39] R.G. Ruddell, G.A. Ramm, Hepatic Pathobiology of Iron Overload, in: G.J. Anderson, G.D. McLaren (Eds.), *Iron Physiol. Pathophysiol. Hum.*, Humana Press, Totowa, NJ, 2012: pp. 357–383. https://doi.org/10.1007/978-1-60327-485-2_18.
- [40] S.V. Verstraeten, L. Aimo, P.I. Oteiza, Aluminium and lead: molecular mechanisms of brain toxicity, *Arch. Toxicol.* 82 (2008) 789–802. <https://doi.org/10.1007/s00204-008-0345-3>.
- [41] H. Milnerowicz, M. Ściskalska, M. Dul, Pro-inflammatory effects of metals in persons and animals exposed to tobacco smoke, *J. Trace Elem. Med. Biol.* 29 (2015) 1–10. <https://doi.org/10.1016/j.jtemb.2014.04.008>.
- [42] M. Worwood, Estimation of Body Iron Stores, in: G.J. Anderson, G.D. McLaren (Eds.), *Iron Physiol. Pathophysiol. Hum.*, Humana Press, Totowa, NJ, 2012: pp. 499–528. https://doi.org/10.1007/978-1-60327-485-2_25.
- [43] S.K. Srail, P. Sharp, Proteins of Iron Homeostasis, in: G.J. Anderson, G.D. McLaren (Eds.), *Iron Physiol. Pathophysiol. Hum.*, Humana Press, Totowa, NJ, 2012: pp. 3–25. https://doi.org/10.1007/978-1-60327-485-2_1.
- [44] R.M. Graham, A.C.G. Chua, D. Trinder, Plasma Iron and Iron Delivery to the Tissues, in: G.J. Anderson, G.D. McLaren (Eds.), *Iron Physiol. Pathophysiol. Hum.*, Humana Press, Totowa, NJ, 2012: pp. 117–139. https://doi.org/10.1007/978-1-60327-485-2_7.
- [45] S.J. Dixon, J.A. Olzmann, The cell biology of ferroptosis, *Nat. Rev. Mol. Cell Biol.* 25 (2024) 424–442. <https://doi.org/10.1038/s41580-024-00703-5>.

- [46] Y. Xia, Y. Li, X. Wu, Q. Zhang, S. Chen, X. Ma, M. Yu, Ironing Out the Details: How Iron Orchestrates Macrophage Polarization, *Front. Immunol.* 12 (2021). <https://doi.org/10.3389/fimmu.2021.669566>.
- [47] B. Brüne, N. Dehne, N. Grossmann, M. Jung, D. Namgaladze, T. Schmid, A. von Knethen, A. Weigert, Redox Control of Inflammation in Macrophages, *Antioxid. Redox Signal.* 19 (2013) 595–637. <https://doi.org/10.1089/ars.2012.4785>.
- [48] M.I. Martínez-Hernández, L.C. Acosta-Saavedra, L.C. Hernández-Kelly, J. Loaeza-Loaeza, A. Ortega, Microglial Activation in Metal Neurotoxicity: Impact in Neurodegenerative Diseases, *BioMed Res. Int.* 2023 (2023) 7389508. <https://doi.org/10.1155/2023/7389508>.
- [49] M.B. Virgolini, M. Aschner, Chapter Five - Molecular mechanisms of lead neurotoxicity, in: M. Aschner, L.G. Costa (Eds.), *Adv. Neurotoxicology*, Academic Press, 2021: pp. 159–213. <https://doi.org/10.1016/bs.ant.2020.11.002>.
- [50] H.-O. Hellström, K. Michaëlsson, H. Mallmin, B. Mjöberg, The aluminium content of bone, and mortality risk, *Age Ageing* 37 (2008) 217–220. <https://doi.org/10.1093/ageing/afm152>.
- [51] W. Kaim, B. Schwederski, A. Klein, W. Kaim, Chapter 12 Zinc: Structural and Gene-regulatory Functions and the Enzymatic Catalysis of Hydrolysis and Condensation Reactions, in: *Bioinorg. Chem. Inorg. Elem. Chem. Life Introd. Guide*, 2. ed, Wiley, Chichester, 2013.
- [52] A. Hartwig, M. Asmuss, H. Blessing, S. Hoffmann, G. Jahnke, S. Khandelwal, A. Pelzer, A. Bürkle, Interference by toxic metal ions with zinc-dependent proteins involved in maintaining genomic stability, *Food Chem. Toxicol.* 40 (2002) 1179–1184. [https://doi.org/10.1016/S0278-6915\(02\)00043-1](https://doi.org/10.1016/S0278-6915(02)00043-1).
- [53] A. Mudipalli, Cadmium Carcinogenesis and Mechanistic Insights, in: A. Mudipalli, J.T. Zelikoff (Eds.), *Essent. Non-Essent. Met. Carcinog. Prev. Cancer Ther.*, Springer International Publishing, Cham, 2017: pp. 113–142. https://doi.org/10.1007/978-3-319-55448-8_6.
- [54] J.T. Brosnan, M.E. Brosnan, The Sulfur-Containing Amino Acids: An Overview, *J. Nutr.* 136 (2006) 1636S-1640S. <https://doi.org/10.1093/jn/136.6.1636S>.
- [55] R.G. Pearson, Chemical hardness and density functional theory, *J. Chem. Sci.* 117 (2005) 369–377. <https://doi.org/10.1007/BF02708340>.
- [56] G. Crisponi, V.M. Nurchi, Chapter 2 - Chelating Agents as Therapeutic Compounds—Basic Principles, in: J. Aaseth, G. Crisponi, O. Andersen (Eds.), *Chelation Ther. Treat. Met. Intox.*, Academic Press, Boston, 2016: pp. 35–61. <https://doi.org/10.1016/B978-0-12-803072-1.00002-X>.
- [57] L. Vujisić, D.Z. Krstić, K.S. Krinulović, V.M. Vasić, Influence of transition and heavy metal ions on ATP-ases activity in rat synaptic plasma membranes, *J. Serbian Chem. Soc.* 69 (2004) 541–547.
- [58] W. Zheng, Blood-Brain Barrier and Blood-CSF Barrier in Metal-Induced Neurotoxicities, in: E.J. Massaro (Ed.), *Handb. Neurotoxicology Vol. I*, Humana Press, Totowa, NJ, 2002: pp. 161–193. https://doi.org/10.1007/978-1-59259-132-9_10.
- [59] A. Szutowicz, Aluminum Neurotoxicity, in: E.J. Massaro (Ed.), *Handb. Neurotoxicology Vol. I*, Humana Press, Totowa, NJ, 2002: pp. 211–236. https://doi.org/10.1007/978-1-59259-132-9_12.
- [60] J.J.V. Branca, C. Fiorillo, D. Carrino, F. Paternostro, N. Taddei, M. Gulisano, A. Pacini, M. Becatti, Cadmium-Induced Oxidative Stress: Focus on the Central Nervous System, *Antioxidants* 9 (2020) 492. <https://doi.org/10.3390/antiox9060492>.

- [61] M. Aschner, J.R. Connor, D.C. Dorman, E.A. Malecki, K.E. Vrana, Manganese in Health and Disease, in: E.J. Massaro (Ed.), *Handb. Neurotoxicology Vol. I*, Humana Press, Totowa, NJ, 2002: pp. 195–209. https://doi.org/10.1007/978-1-59259-132-9_11.
- [62] A.L. Wani, A. Ara, J.A. Usmani, Lead toxicity: a review, *Interdiscip. Toxicol.* 8 (2015) 55–64. <https://doi.org/10.1515/intox-2015-0009>.
- [63] M.K. Nihei, T.R. Guilarte, Molecular Mechanisms of Low-Level Pb²⁺ Neurotoxicity, in: E.J. Massaro (Ed.), *Handb. Neurotoxicology Vol. I*, Humana Press, Totowa, NJ, 2002: pp. 107–133. https://doi.org/10.1007/978-1-59259-132-9_8.
- [64] T. Borisova, N. Krisanova, R. Sivko, L. Kasatkina, A. Borysov, S. Griffin, M. Wireman, Presynaptic malfunction: The neurotoxic effects of cadmium and lead on the proton gradient of synaptic vesicles and glutamate transport, *Neurochem. Int.* 59 (2011) 272–279. <https://doi.org/10.1016/j.neuint.2011.05.014>.
- [65] A.W. Dobson, K.M. Erikson, M. Aschner, Manganese Neurotoxicity, *Ann. N. Y. Acad. Sci.* 1012 (2004) 115–128. <https://doi.org/10.1196/annals.1306.009>.
- [66] P. Dusek, J. Aaseth, Chapter 3 - Diagnosis and Evaluation of Metal Poisonings and Chelation Therapy, in: J. Aaseth, G. Crisponi, O. Andersen (Eds.), *Chelation Ther. Treat. Met. Intox.*, Academic Press, Boston, 2016: pp. 63–83. <https://doi.org/10.1016/B978-0-12-803072-1.00003-1>.
- [67] T. Kanda, Y. Nakai, S. Aoki, H. Oba, K. Toyoda, K. Kitajima, S. Furui, Contribution of metals to brain MR signal intensity: review articles, *Jpn. J. Radiol.* 34 (2016) 258–266. <https://doi.org/10.1007/s11604-016-0532-8>.
- [68] D.S. Harischandra, S. Ghaisas, G. Zenitsky, H. Jin, A. Kanthasamy, V. Anantharam, A.G. Kanthasamy, Manganese-Induced Neurotoxicity: New Insights Into the Triad of Protein Misfolding, Mitochondrial Impairment, and Neuroinflammation, *Front. Neurosci.* 13 (2019). <https://doi.org/10.3389/fnins.2019.00654>.
- [69] O. Andersen, Chapter 4 - Chelation Treatment During Acute and Chronic Metal Overexposures—Experimental and Clinical Studies, in: J. Aaseth, G. Crisponi, O. Andersen (Eds.), *Chelation Ther. Treat. Met. Intox.*, Academic Press, Boston, 2016: pp. 85–252. <https://doi.org/10.1016/B978-0-12-803072-1.00004-3>.
- [70] A. Marreilha dos Santos, V. Andrade, M. Aschner, Neuroprotective and Therapeutic Strategies for Manganese-Induced Neurotoxicity, *Clin. Pharmacol. Transl. Med.* 1 (2017) 54–62.
- [71] K.A. Jellinger, Chapter One - The Relevance of Metals in the Pathophysiology of Neurodegeneration, Pathological Considerations, in: K.P. Bhatia, S.A. Schneider (Eds.), *Int. Rev. Neurobiol.*, Academic Press, 2013: pp. 1–47. <https://doi.org/10.1016/B978-0-12-410502-7.00002-8>.
- [72] E. Herrero Hernandez, G. Discalzi, C. Valentini, F. Venturi, A. Chiò, C. Carmellino, L. Rossi, A. Sacchetti, E. Pira, Follow-up of patients affected by manganese-induced Parkinsonism after treatment with CaNa₂EDTA, *NeuroToxicology* 27 (2006) 333–339. <https://doi.org/10.1016/j.neuro.2005.09.003>.
- [73] Y.-M. Jiang, X.-A. Mo, F.-Q. Du, X. Fu, X.-Y. Zhu, H.-Y. Gao, J.-L. Xie, F.-L. Liao, E. Pira, W. Zheng, Effective Treatment of Manganese-Induced Occupational Parkinsonism With p-Aminosalicylic Acid: A Case of 17-Year Follow-Up Study, *J. Occup. Environ. Med. Am. Coll. Occup. Environ. Med.* 48 (2006) 644–649. <https://doi.org/10.1097/01.jom.0000204114.01893.3e>.
- [74] O. Bandmann, K.H. Weiss, S.G. Kaler, Wilson’s disease and other neurological copper disorders, *Lancet Neurol.* 14 (2015) 103–113. [https://doi.org/10.1016/S1474-4422\(14\)70190-5](https://doi.org/10.1016/S1474-4422(14)70190-5).

- [75] H. Hefter, O. Tezayak, D. Rosenthal, Long-term outcome of neurological Wilson's disease, *Parkinsonism Relat. Disord.* 49 (2018) 48–53. <https://doi.org/10.1016/j.parkreldis.2018.01.007>.
- [76] P. Dusek, J. Aaseth, Chapter 6 - Chelating Therapy in Metal Storage Diseases, in: J. Aaseth, G. Crisponi, O. Andersen (Eds.), *Chelation Ther. Treat. Met. Intox.*, Academic Press, Boston, 2016: pp. 285–311. <https://doi.org/10.1016/B978-0-12-803072-1.00006-7>.
- [77] A.H. Koeppen, J.E. Mazurkiewicz, Friedreich Ataxia: Neuropathology Revised, *J. Neuropathol. Exp. Neurol.* 72 (2013) 78–90. <https://doi.org/10.1097/NEN.0b013e31827e5762>.
- [78] G. Tai, L.A. Corben, E.M. Yiu, S.C. Milne, M.B. Delatycki, Progress in the treatment of Friedreich ataxia, *Neurol. Neurochir. Pol.* 52 (2018) 129–139. <https://doi.org/10.1016/j.pjnns.2018.02.003>.
- [79] A.H. Koeppen, Friedreich's ataxia: Pathology, pathogenesis, and molecular genetics, *J. Neurol. Sci.* 303 (2011) 1–12. <https://doi.org/10.1016/j.jns.2011.01.010>.
- [80] N. Boddaert, K.H. Le Quan Sang, A. Rötig, A. Leroy-Willig, S. Gallet, F. Brunelle, D. Sidi, J.-C. Thalabard, A. Munnich, Z.I. Cabantchik, Selective iron chelation in Friedreich ataxia: biologic and clinical implications, *Blood* 110 (2007) 401–408. <https://doi.org/10.1182/blood-2006-12-065433>.
- [81] M. Pandolfo, J. Arpa, M.B. Delatycki, K.H. Le Quan Sang, C. Mariotti, A. Munnich, I. Sanz-Gallego, G. Tai, M.A. Tarnopolsky, F. Taroni, M. Spino, F. Tricta, Deferiprone in Friedreich ataxia: A 6-Month randomized controlled trial, *Ann. Neurol.* 76 (2014) 509–521. <https://doi.org/10.1002/ana.24248>.
- [82] R. Galanello, S. Campus, Deferiprone chelation therapy for thalassemia major, *Acta Haematol.* 122 (2009) 155–164. <https://doi.org/10.1159/000243800>.
- [83] S.A. Schneider, Chapter 46 - Neurodegeneration with brain iron accumulation, in: R.N. Rosenberg, J.M. Pascual (Eds.), *Rosenb. Mol. Genet. Basis Neurol. Psychiatr. Dis. Sixth Ed.*, Academic Press, 2020: pp. 621–631. <https://doi.org/10.1016/B978-0-12-813955-4.00046-5>.
- [84] P. Santambrogio, M. Ripamonti, A. Cozzi, M. Raimondi, C. Cavestro, I. Di Meo, A. Rubio, S. Taverna, V. Tiranti, S. Levi, Massive iron accumulation in PKAN-derived neurons and astrocytes: light on the human pathological phenotype, *Cell Death Dis.* 13 (2022) 1–12. <https://doi.org/10.1038/s41419-022-04626-x>.
- [85] S.M.H. Nordlie, U. Hadziahmetovic, S. Padilla-Lopez, M.C. Kruer, Chapter 47 - Pantothenate kinase-associated neurodegeneration, in: R.N. Rosenberg, J.M. Pascual (Eds.), *Rosenb. Mol. Genet. Basis Neurol. Psychiatr. Dis. Sixth Ed.*, Academic Press, 2020: pp. 633–641. <https://doi.org/10.1016/B978-0-12-813955-4.00047-7>.
- [86] S.J. Hayflick, S.Y. Jeong, O.C.M. Sibon, PKAN pathogenesis and treatment, *Mol. Genet. Metab.* 137 (2022) 283–291. <https://doi.org/10.1016/j.ymgme.2022.09.011>.
- [87] M.A. Kurian, S.J. Hayflick, Pantothenate Kinase-Associated Neurodegeneration (PKAN) and *PLA2G6*-Associated Neurodegeneration (PLAN), in: K.P. Bhatia, S.A. Schneider (Eds.), *Int. Rev. Neurobiol.*, Academic Press, 2013: pp. 49–71. <https://doi.org/10.1016/B978-0-12-410502-7.00003-X>.
- [88] P. Hogarth, M.A. Kurian, A. Gregory, B. Csányi, T. Zagustin, T. Kmiec, P. Wood, A. Klucken, N. Scalise, F. Sofia, T. Klopstock, G. Zorzi, N. Nardocci, S.J. Hayflick, Consensus clinical management guideline for pantothenate kinase-associated neurodegeneration (PKAN), *Mol. Genet. Metab.* 120 (2017) 278–287. <https://doi.org/10.1016/j.ymgme.2016.11.004>.

- [89] G.L. Forni, M. Balocco, L. Cremonesi, G. Abbruzzese, R.C. Parodi, R. Marchese, Regression of symptoms after selective iron chelation therapy in a case of neurodegeneration with brain iron accumulation, *Mov. Disord.* 23 (2008) 904–907. <https://doi.org/10.1002/mds.22002>.
- [90] A. Kwiatkowski, G. Ryckewaert, P. Jissendi Tchofo, C. Moreau, I. Vuillaume, P.F. Chinnery, A. Destée, L. Defebvre, D. Devos, Long-term improvement under deferiprone in a case of neurodegeneration with brain iron accumulation, *Parkinsonism Relat. Disord.* 18 (2012) 110–112. <https://doi.org/10.1016/j.parkreldis.2011.06.024>.
- [91] G. Zorzi, F. Zibordi, L. Chiapparini, E. Bertini, L. Russo, A. Piga, F. Longo, B. Garavaglia, D. Aquino, M. Savoiaro, A. Solari, N. Nardocci, Iron-related MRI images in patients with pantothenate kinase-associated neurodegeneration (PKAN) treated with deferiprone: Results of a phase II pilot trial, *Mov. Disord.* 26 (2011) 1755–1759. <https://doi.org/10.1002/mds.23751>.
- [92] G. Cossu, G. Abbruzzese, G. Matta, D. Murgia, M. Melis, V. Ricchi, R. Galanello, S. Barella, R. Origa, M. Balocco, E. Pelosin, R. Marchese, U. Ruffinengo, G.L. Forni, Efficacy and safety of deferiprone for the treatment of pantothenate kinase-associated neurodegeneration (PKAN) and neurodegeneration with brain iron accumulation (NBIA): Results from a four years follow-up, *Parkinsonism Relat. Disord.* 20 (2014) 651–654. <https://doi.org/10.1016/j.parkreldis.2014.03.002>.
- [93] M. Rohani, S. Razmeh, G.A. Shahidi, M. Orooji, A pilot trial of deferiprone in pantothenate kinase-associated neurodegeneration patients, *Neurol. Int.* 9 (2018). <https://doi.org/10.4081/ni.2017.7279>.
- [94] T. Klopstock, F. Tricta, L. Neumayr, I. Karin, G. Zorzi, C. Fradette, T. Kmiec, B. Büchner, H.E. Steele, R. Horvath, P.F. Chinnery, A. Basu, C. Küpper, C. Neuhofer, B. Kálmán, P. Dušek, Z. Yapici, I. Wilson, F. Zhao, F. Zibordi, N. Nardocci, C. Aguilar, S.J. Hayflick, M. Spino, A.M. Blamire, P. Hogarth, E. Vichinsky, Safety and efficacy of deferiprone for pantothenate kinase-associated neurodegeneration: a randomised, double-blind, controlled trial and an open-label extension study, *Lancet Neurol.* 18 (2019) 631–642. [https://doi.org/10.1016/S1474-4422\(19\)30142-5](https://doi.org/10.1016/S1474-4422(19)30142-5).
- [95] M.J. Armstrong, M.S. Okun, Diagnosis and Treatment of Parkinson Disease: A Review, *JAMA* 323 (2020) 548–560. <https://doi.org/10.1001/jama.2019.22360>.
- [96] W. Poewe, K. Seppi, C.M. Tanner, G.M. Halliday, P. Brundin, J. Volkman, A.-E. Schrag, A.E. Lang, Parkinson disease, *Nat. Rev. Dis. Primer* 3 (2017) 1–21. <https://doi.org/10.1038/nrdp.2017.13>.
- [97] C. Moreau, J.A. Duce, O. Rascol, J.-C. Devedjian, D. Berg, D. Dexter, Z.I. Cabantchik, A.I. Bush, D. Devos, FAIRPARK-II study group, Iron as a therapeutic target for Parkinson’s disease, *Mov. Disord. Off. J. Mov. Disord. Soc.* 33 (2018) 568–574. <https://doi.org/10.1002/mds.27275>.
- [98] G.E.C. Thomas, L.A. Leyland, A.-E. Schrag, A.J. Lees, J. Acosta-Cabronero, R.S. Weil, Brain iron deposition is linked with cognitive severity in Parkinson’s disease, *J. Neurol. Neurosurg. Psychiatry* 91 (2020) 418–425. <https://doi.org/10.1136/jnnp-2019-322042>.
- [99] A.C. Farr, M.P. Xiong, Challenges and Opportunities of Deferoxamine Delivery for Treatment of Alzheimer’s Disease, Parkinson’s Disease, and Intracerebral Hemorrhage, *Mol. Pharm.* 18 (2021) 593–609. <https://doi.org/10.1021/acs.molpharmaceut.0c00474>.
- [100] S. Masaldan, A.I. Bush, D. Devos, A.S. Rolland, C. Moreau, Striking while the iron is hot: Iron metabolism and ferroptosis in neurodegeneration, *Free Radic. Biol. Med.* 133 (2019) 221–233. <https://doi.org/10.1016/j.freeradbiomed.2018.09.033>.

- [101] H. McDermott, *Neurobionics: Treatments for Disorders of the Central Nervous System*, in: *Neurobionics Biomed. Eng. Neural Prostheses*, John Wiley & Sons, Ltd, 2016: pp. 213–230. <https://doi.org/10.1002/9781118816028.ch8>.
- [102] J.M. Bronstein, M. Tagliati, R.L. Alterman, A.M. Lozano, J. Volkmann, A. Stefani, F.B. Horak, M.S. Okun, K.D. Foote, P. Krack, R. Pahwa, J.M. Henderson, M.I. Hariz, R.A. Bakay, A. Rezai, W.J. Marks Jr, E. Moro, J.L. Vitek, F.M. Weaver, R.E. Gross, M.R. DeLong, *Deep Brain Stimulation for Parkinson Disease: An Expert Consensus and Review of Key Issues*, *Arch. Neurol.* 68 (2011) 165. <https://doi.org/10.1001/archneurol.2010.260>.
- [103] M. Gassen, M.B.H. Youdim, *The Potential Role of Iron Chelators in the Treatment of Parkinson's Disease and Related Neurological Disorders*, *Pharmacol. Toxicol.* 80 (1997) 159–166. <https://doi.org/10.1111/j.1600-0773.1997.tb00390.x>.
- [104] D. Devos, C. Moreau, J.C. Devedjian, J. Kluza, M. Petraut, C. Laloux, A. Jonneaux, G. Ryckewaert, G. Garçon, N. Rouaix, A. Duhamel, P. Jissendi, K. Dujardin, F. Auger, L. Ravasi, L. Hopes, G. Grolez, W. Firdaus, B. Sablonnière, I. Strubi-Vuillaume, N. Zahr, A. Destée, J.-C. Corvol, D. Pörtl, M. Leist, C. Rose, L. Defebvre, P. Marchetti, Z.I. Cabantchik, R. Bordet, *Targeting Chelatable Iron as a Therapeutic Modality in Parkinson's Disease*, *Antioxid. Redox Signal.* 21 (2014) 195. <https://doi.org/10.1089/ars.2013.5593>.
- [105] A. Martin-Bastida, R.J. Ward, R. Newbould, P. Piccini, D. Sharp, C. Kabba, M.C. Patel, M. Spino, J. Connelly, F. Tricta, R.R. Crichton, D.T. Dexter, *Brain iron chelation by deferiprone in a phase 2 randomised double-blinded placebo controlled clinical trial in Parkinson's disease*, *Sci. Rep.* 7 (2017) 1398. <https://doi.org/10.1038/s41598-017-01402-2>.
- [106] D. Devos, J. Labreuche, O. Rascol, J.-C. Corvol, A. Duhamel, P. Guyon Delannoy, W. Poewe, Y. Compta, N. Pavese, E. Růžicka, P. Dušek, B. Post, B.R. Bloem, D. Berg, W. Maetzler, M. Otto, M.-O. Habert, S. Lehericy, J. Ferreira, R. Dodel, C. Tranchant, A. Eusebio, S. Thobois, A.-R. Marques, W.G. Meissner, F. Ory-Magne, U. Walter, R.M.A. de Bie, M. Gago, D. Vilas, J. Kulisevsky, C. Janeiro, M.V.S. Coelho, S. Behnke, P. Worth, K. Seppi, T. Ouk, C. Potey, C. Leclercq, R. Viard, G. Kuchcinski, R. Lopes, J.-P. Pruvo, P. Pigny, G. Garçon, O. Simonin, J. Carpentier, A.-S. Rolland, D. Nyholm, C. Scherfler, J.-F. Mangin, M. Chupin, R. Bordet, D.T. Dexter, C. Fradette, M. Spino, F. Tricta, S. Ayton, A.I. Bush, J.-C. Devedjian, J.A. Duce, I. Cabantchik, L. Defebvre, D. Deplanque, C. Moreau, *Trial of Deferiprone in Parkinson's Disease*, *N. Engl. J. Med.* 387 (2022) 2045–2055. <https://doi.org/10.1056/NEJMoa2209254>.
- [107] Z.D. Liu, R.C. Hider, *Design of iron chelators with therapeutic application*, *Coord. Chem. Rev.* 232 (2002) 151–171. [https://doi.org/10.1016/S0010-8545\(02\)00050-4](https://doi.org/10.1016/S0010-8545(02)00050-4).
- [108] J.B. Porter, *Deferoxamine pharmacokinetics*, *Semin. Hematol.* 38 (2001) 63–68. [https://doi.org/10.1016/S0037-1963\(01\)90061-7](https://doi.org/10.1016/S0037-1963(01)90061-7).
- [109] P.E. Hallaway, J.W. Eaton, S.S. Panter, B.E. Hedlund, *Modulation of deferoxamine toxicity and clearance by covalent attachment to biocompatible polymers.*, *Proc. Natl. Acad. Sci.* 86 (1989) 10108–10112. <https://doi.org/10.1073/pnas.86.24.10108>.
- [110] E. Shimoni, R. Armon, I. Neeman, *Antioxidant properties of deferoxamine*, *J. Am. Oil Chem. Soc.* 71 (1994) 641–644. <https://doi.org/10.1007/BF02540593>.
- [111] C.A. Lane, J. Hardy, J.M. Schott, *Alzheimer's disease*, *Eur. J. Neurol.* 25 (2018) 59–70. <https://doi.org/10.1111/ene.13439>.
- [112] B.T. Winslow, M.K. Onysko, C.M. Stob, K.A. Hazlewood, *Treatment of Alzheimer Disease*, *Alzheimer Dis.* 83 (2011).

- [113] R.J. Bateman, P.S. Aisen, B. De Strooper, N.C. Fox, C.A. Lemere, J.M. Ringman, S. Salloway, R.A. Sperling, M. Windisch, C. Xiong, Autosomal-dominant Alzheimer's disease: a review and proposal for the prevention of Alzheimer's disease, *Alzheimers Res. Ther.* 3 (2011) 1. <https://doi.org/10.1186/alzrt59>.
- [114] P.B. Verghese, J.M. Castellano, D.M. Holtzman, Apolipoprotein E in Alzheimer's disease and other neurological disorders, *Lancet Neurol.* 10 (2011) 241–252. [https://doi.org/10.1016/S1474-4422\(10\)70325-2](https://doi.org/10.1016/S1474-4422(10)70325-2).
- [115] M. Babić Leko, L. Langer Horvat, E. Španić Popovački, K. Zubčić, P.R. Hof, G. Šimić, Metals in Alzheimer's Disease, *Biomedicines* 11 (2023) 1161. <https://doi.org/10.3390/biomedicines11041161>.
- [116] N. Das, J. Raymick, S. Sarkar, Role of metals in Alzheimer's disease, *Metab. Brain Dis.* 36 (2021) 1627–1639. <https://doi.org/10.1007/s11011-021-00765-w>.
- [117] Y. Li, Q. Jiao, H. Xu, X. Du, L. Shi, F. Jia, H. Jiang, Biometal Dyshomeostasis and Toxic Metal Accumulations in the Development of Alzheimer's Disease, *Front. Mol. Neurosci.* 10 (2017). <https://doi.org/10.3389/fnmol.2017.00339>.
- [118] R.A. Cherny, K.J. Barnham, T. Lynch, I. Volitakis, Q.-X. Li, C.A. McLean, G. Multhaup, K. Beyreuther, R.E. Tanzi, C.L. Masters, A.I. Bush, Chelation and Intercalation: Complementary Properties in a Compound for the Treatment of Alzheimer's Disease, *J. Struct. Biol.* 130 (2000) 209–216. <https://doi.org/10.1006/jsbi.2000.4285>.
- [119] R. Marasco, Current and Evolving Treatment Strategies for the Alzheimer Disease Continuum, 26 (2020). <https://www.ajmc.com/view/current-and-evolving-treatment-strategies-for-the-alzheimer-disease-continuum> (accessed August 1, 2024).
- [120] F. Massoud, G.C. Léger, Pharmacological Treatment of Alzheimer Disease, *Can. J. Psychiatry* 56 (2011) 579–588. <https://doi.org/10.1177/070674371105601003>.
- [121] S. Chaves, K. Várnagy, M.A. Santos, Recent Multi-target Approaches on the Development of Anti- Alzheimer's Agents Integrating Metal Chelation Activity, *Curr. Med. Chem.* 28 (2021) 7247–7277. <https://doi.org/10.2174/0929867328666210218183032>.
- [122] D.R.C. McLachlan, T.P.A. Kruck, W. Kalow, D.F. Andrews, A.J. Dalton, M.Y. Bell, W.L. Smith, Intramuscular desferrioxamine in patients with Alzheimer's disease, *The Lancet* 337 (1991) 1304–1308. [https://doi.org/10.1016/0140-6736\(91\)92978-B](https://doi.org/10.1016/0140-6736(91)92978-B).
- [123] S. Ayton, M. Woodward, K.A. Ellis, Y.Y. Lim, P.T. Maruff, P.M. Desmond, O. Salvado, A. Fazlollahi, C.C. Rowe, L. Churilov, A.I. Bush, 3D Trial Investigators, Deferiprone to delay dementia (the 3D trial), *Alzheimers Dement.* 16 (2020) e044107. <https://doi.org/10.1002/alz.044107>.
- [124] C.W. Ritchie, A.I. Bush, A. Mackinnon, S. Macfarlane, M. Mastwyk, L. MacGregor, L. Kiers, R. Cherny, Q.-X. Li, A. Tammer, D. Carrington, C. Mavros, I. Volitakis, M. Xilinas, D. Ames, S. Davis, K. Beyreuther, R.E. Tanzi, C.L. Masters, Metal-Protein Attenuation With Iodochlorhydroxyquin (Clioquinol) Targeting A β Amyloid Deposition and Toxicity in Alzheimer Disease, *ARCH NEUROL* 60 (2003).
- [125] L. Lannfelt, K. Blennow, H. Zetterberg, S. Batsman, D. Ames, J. Harrison, C.L. Masters, S. Targum, A.I. Bush, R. Murdoch, J. Wilson, C.W. Ritchie, Safety, efficacy, and biomarker findings of PBT2 in targeting A β as a modifying therapy for Alzheimer's disease: a phase IIa, double-blind, randomised, placebo-controlled trial, *Lancet Neurol.* 7 (2008) 779–786. [https://doi.org/10.1016/S1474-4422\(08\)70167-4](https://doi.org/10.1016/S1474-4422(08)70167-4).

- [126] R. Ghosh, S.J. Tabrizi, Chapter 17 - Huntington disease, in: D.H. Geschwind, H.L. Paulson, C. Klein (Eds.), *Handb. Clin. Neurol.*, Elsevier, 2018: pp. 255–278. <https://doi.org/10.1016/B978-0-444-63233-3.00017-8>.
- [127] M. Muller, B.R. Leavitt, Iron dysregulation in Huntington's disease, *J. Neurochem.* 130 (2014) 328–350. <https://doi.org/10.1111/jnc.12739>.
- [128] J.H. Fox, J.A. Kama, G. Lieberman, R. Chopra, K. Dorsey, V. Chopra, I. Volitakis, R.A. Cherny, A.I. Bush, S. Hersch, Mechanisms of Copper Ion Mediated Huntington's Disease Progression, *PLOS ONE* 2 (2007) e334. <https://doi.org/10.1371/journal.pone.0000334>.
- [129] S.L. Hands, R. Mason, M.U. Sajjad, F. Giorgini, A. Wytttenbach, Metallothioneins and copper metabolism are candidate therapeutic targets in Huntington's disease, *Biochem. Soc. Trans.* 38 (2010) 552–558. <https://doi.org/10.1042/BST0380552>.
- [130] H.D. Rosas, Y.I. Chen, G. Doros, D.H. Salat, N. Chen, K.K. Kwong, A. Bush, J. Fox, S.M. Hersch, Alterations in Brain Transition Metals in Huntington Disease: An Evolving and Intricate Story, *Arch. Neurol.* 69 (2012) 887–893. <https://doi.org/10.1001/archneurol.2011.2945>.
- [131] K.T. Potkin, S.G. Potkin, New Directions in Therapeutics for Huntington Disease, *Future Neurol.* 13 (2018) 101–121. <https://doi.org/10.2217/fnl-2017-0035>.
- [132] Huntington Study Group Reach2HD Investigators, Safety, tolerability, and efficacy of PBT2 in Huntington's disease: a phase 2, randomised, double-blind, placebo-controlled trial, *Lancet Neurol.* 14 (2015) 39–47. [https://doi.org/10.1016/S1474-4422\(14\)70262-5](https://doi.org/10.1016/S1474-4422(14)70262-5).
- [133] N. Chaudhary, A.S. Pandey, X. Wang, G. Xi, Hemorrhagic stroke—Pathomechanisms of injury and therapeutic options, *CNS Neurosci. Ther.* 25 (2019) 1073–1074. <https://doi.org/10.1111/cns.13225>.
- [134] C.O. Johnson, M. Nguyen, G.A. Roth, E. Nichols, T. Alam, D. Abate, F. Abd-Allah, A. Abdelalim, H.N. Abraha, N.M. Abu-Rmeileh, O.M. Adebayo, A.M. Adeoye, G. Agarwal, S. Agrawal, A.N. Aichour, I. Aichour, M.T.E. Aichour, F. Alahdab, R. Ali, N. Alvis-Guzman, N.H. Anber, M. Anjomshoa, J. Arabloo, A. Arauz, J. Ärnlöv, A. Arora, A. Awasthi, M. Banach, M.A. Barboza, S.L. Barker-Collo, T.W. Bärnighausen, S. Basu, A.B. Belachew, Y.M. Belayneh, D.A. Bennett, I.M. Bensor, K. Bhattacharyya, B. Biadgo, A. Bijani, B. Bikbov, M.S. Bin Sayeed, Z.A. Butt, L. Cahuana-Hurtado, J.J. Carrero, F. Carvalho, C.A. Castañeda-Orjuela, F. Castro, F. Catalá-López, Y. Chaiah, P.P.-C. Chiang, J.-Y.J. Choi, H. Christensen, D.-T. Chu, M. Cortinovic, A.A.M. Damasceno, L. Dandona, R. Dandona, A. Daryani, K. Davletov, B. De Courten, V. De La Cruz-Góngora, M.G. Degefa, S.D. Dharmaratne, D. Diaz, M. Dubey, E.E. Duken, D. Edessa, M. Endres, E.J.A. Faraon, F. Farzadfar, E. Fernandes, F. Fischer, L.S. Flor, M. Ganji, A.K. Gebre, T.G. Gebremichael, B. Geta, K.E. Gezae, P.S. Gill, E.V. Gnedovskaya, H. Gómez-Dantés, A.C. Goulart, G. Grosso, Y. Guo, R. Gupta, A. Haj-Mirzaian, A. Haj-Mirzaian, S. Hamidi, G.J. Hankey, H.Y. Hassen, S.I. Hay, M.I. Hegazy, B. Heidari, N.A. Herial, M.A. Hosseini, S. Hostiuc, S.S.N. Irvani, S.M.S. Islam, N. Jahanmehr, M. Javanbakht, R.P. Jha, J.B. Jonas, J.J. Jozwiak, M. Jürisson, A. Kahsay, R. Kalani, Y. Kalkonde, T.A. Kamil, T. Kanchan, A. Karch, N. Karimi, H. Karimi-Sari, A. Kasaiean, T.D. Kassa, H. Kazemini, A.T. Kefale, Y.S. Khader, I.A. Khalil, E.A. Khan, Y.-H. Khang, J. Khubchandani, D. Kim, Y.J. Kim, A. Kisa, M. Kivimäki, A. Koyanagi, R.K. Krishnamurthi, G.A. Kumar, A. Lafranconi, S. Lewington, S. Li, W.D. Lo, A.D. Lopez, S. Lorkowski, P.A. Lotufo, M.T. Mackay, M. Majdan, R. Majdzadeh, A. Majeed, R. Malekzadeh, N. Manafi, M.A. Mansournia, M.M. Mehndiratta, V. Mehta, G. Mengistu, A. Meretoja, T.J. Meretoja, B. Miazgowski, T. Miazgowski, T.R. Miller, E.M. Mirrakhimov, B. Mohajer, Y. Mohammad, M. Mohammadoo-khorasani, S. Mohammed, F. Mohebi, A.H. Mokdad, Y. Mokhayeri, G. Moradi, L. Morawska, I.

- Moreno Velásquez, S.M. Mousavi, O.S.S. Muhammed, W. Muruet, M. Naderi, M. Naghavi, G. Naik, B.R. Nascimento, R.I. Negoi, C.T. Nguyen, L.H. Nguyen, Y.L. Nirayo, B. Norrving, J.J. Noubiap, R. Ofori-Asenso, F.A. Ogbo, A.T. Olagunju, T.O. Olagunju, M.O. Owolabi, J.D. Pandian, S. Patel, N. Perico, M.A. Piradov, S. Polinder, M.J. Postma, H. Poustchi, V. Prakash, M. Qorbani, A. Rafiei, F. Rahim, K. Rahimi, V. Rahimi-Movaghar, M. Rahman, M.A. Rahman, C. Reis, G. Remuzzi, A.M.N. Renzaho, S. Ricci, N.L.S. Roberts, S.R. Robinson, L. Roever, G. Roshandel, P. Sabbagh, H. Safari, S. Safari, S. Safiri, A. Sahebkar, S. Salehi Zahabi, A.M. Samy, P. Santalucia, I.S. Santos, J.V. Santos, M.M. Santric Milicevic, B. Sartorius, A.R. Sawant, A.E. Schutte, S.G. Sepanlou, A. Shafieesabet, M.A. Shaikh, M. Shams-Beyranvand, A. Sheikh, K.N. Sheth, K. Shibuya, M. Shigematsu, M.-J. Shin, I. Shiue, S. Siabani, B.H. Sobaih, L.A. Sposato, I. Sutradhar, P. Sylaja, C.E.I. Szoeki, B.J. Te Ao, M.-H. Temsah, O. Temsah, A.G. Thrift, M. Tonelli, R. Topor-Madry, B.X. Tran, K.B. Tran, T.C. Truelsen, A.G. Tsadik, I. Ullah, O.A. Uthman, M. Vaduganathan, P.R. Valdez, T.J. Vasankari, R. Vasanthan, N. Venketasubramanian, K. Vosoughi, G.T. Vu, Y. Waheed, E. Weiderpass, K.G. Weldegewergs, R. Westerman, C.D.A. Wolfe, D.Z. Wondafrash, G. Xu, A. Yadollahpour, T. Yamada, H. Yatsuya, E.M. Yimer, N. Yonemoto, M. Yousefifard, C. Yu, Z. Zaidi, M. Zamani, A. Zarghi, Y. Zhang, S. Zodpey, V.L. Feigin, T. Vos, C.J.L. Murray, Global, regional, and national burden of stroke, 1990–2016: a systematic analysis for the Global Burden of Disease Study 2016, *Lancet Neurol.* 18 (2019) 439–458. [https://doi.org/10.1016/S1474-4422\(19\)30034-1](https://doi.org/10.1016/S1474-4422(19)30034-1).
- [135] M.H. Selim, R.R. Ratan, The role of iron neurotoxicity in ischemic stroke, *Ageing Res. Rev.* 3 (2004) 345–353. <https://doi.org/10.1016/j.arr.2004.04.001>.
- [136] E. Chemerinski, R.G. Robinson, The Neuropsychiatry of Stroke, *Psychosomatics* 41 (2000) 5–14. [https://doi.org/10.1016/S0033-3182\(00\)71168-6](https://doi.org/10.1016/S0033-3182(00)71168-6).
- [137] U. Samadani, V. Rohde, A review of stereotaxy and lysis for intracranial hemorrhage, *Neurosurg. Rev.* 32 (2009) 15–22. <https://doi.org/10.1007/s10143-008-0175-z>.
- [138] G. Xi, R.F. Keep, J.T. Hoff, Mechanisms of brain injury after intracerebral haemorrhage, *Lancet Neurol.* 5 (2006) 53–63. [https://doi.org/10.1016/S1474-4422\(05\)70283-0](https://doi.org/10.1016/S1474-4422(05)70283-0).
- [139] C.S. Kidwell, M. Wintermark, Imaging of intracranial haemorrhage, *Lancet Neurol.* 7 (2008) 256–267. [https://doi.org/10.1016/S1474-4422\(08\)70041-3](https://doi.org/10.1016/S1474-4422(08)70041-3).
- [140] D. Bulters, B. Gastra, A. Zolnourian, S. Alexander, D. Ren, S.L. Blackburn, M. Borsody, S. Doré, J. Galea, K. Iihara, P. Nyquist, I. Galea, Haemoglobin scavenging in intracranial bleeding: biology and clinical implications, *Nat. Rev. Neurol.* 14 (2018) 416–432. <https://doi.org/10.1038/s41582-018-0020-0>.
- [141] T. Garton, R.F. Keep, Y. Hua, G. Xi, Brain iron overload following intracranial haemorrhage, *Stroke Vasc. Neurol.* 1 (2016) 172–184. <https://doi.org/10.1136/svn-2016-000042>.
- [142] N. DeGregorio-Rocasolano, O. Martí-Sistac, T. Gasull, Deciphering the Iron Side of Stroke: Neurodegeneration at the Crossroads Between Iron Dyshomeostasis, Excitotoxicity, and Ferroptosis, *Front. Neurosci.* 13 (2019). <https://www.frontiersin.org/articles/10.3389/fnins.2019.00085> (accessed April 17, 2023).
- [143] M. Zhang, W. Li, T. Wang, Q. Zhang, Association Between Baseline Serum Ferritin and Short-term Outcome of Intracerebral Hemorrhage: A Meta-Analysis, *J. Stroke Cerebrovasc. Dis.* 28 (2019) 1799–1805. <https://doi.org/10.1016/j.jstrokecerebrovasdis.2019.03.037>.
- [144] N. Kumar, A.A. Cohen-Gadol, R.A. Wright, G.M. Miller, D.G. Piepgras, J.E. Ahlskog, Superficial siderosis, *Neurology* 66 (2006) 1144–1152. <https://doi.org/10.1212/01.wnl.0000208510.76323.5b>.

- [145] A.D. Mendelow, B.A. Gregson, H.M. Fernandes, G.D. Murray, G.M. Teasdale, D.T. Hope, A. Karimi, M.D.M. Shaw, D.H. Barer, Early surgery versus initial conservative treatment in patients with spontaneous supratentorial intracerebral haematomas in the International Surgical Trial in Intracerebral Haemorrhage (STICH): a randomised trial, *The Lancet* 365 (2005) 387–397. [https://doi.org/10.1016/S0140-6736\(05\)17826-X](https://doi.org/10.1016/S0140-6736(05)17826-X).
- [146] T. Nakamura, T. Schallert, Deferoxamine-induced attenuation of brain edema and neurological deficits in a rat model of intracerebral hemorrhage, *J Neurosurg* 100 (2004).
- [147] S. Wan, Y. Hua, R.F. Keep, J.T. Hoff, G. Xi, Deferoxamine reduces CSF free iron levels following intracerebral hemorrhage, in: J.T. Hoff, R.F. Keep, G. Xi, Y. Hua (Eds.), *Brain Edema XIII*, Springer-Verlag, Vienna, 2006: pp. 199–202. https://doi.org/10.1007/3-211-30714-1_43.
- [148] M. Selim, S. Yeatts, J.N. Goldstein, J. Gomes, S. Greenberg, L.B. Morgenstern, G. Schlaug, M. Torbey, B. Waldman, G. Xi, Y. Palesch, The Deferoxamine Mesylate in Intracerebral Hemorrhage Investigators, Safety and Tolerability of Deferoxamine Mesylate in Patients With Acute Intracerebral Hemorrhage, *Stroke* 42 (2011) 3067–3074. <https://doi.org/10.1161/STROKEAHA.111.617589>.
- [149] S.D. Yeatts, Y.Y. Palesch, C.S. Moy, M. Selim, High Dose Deferoxamine in Intracerebral Hemorrhage (Hi-Def) Trial: Rationale, Design, and Methods, *Neurocrit. Care* 19 (2013) 257–266. <https://doi.org/10.1007/s12028-013-9861-y>.
- [150] M. Selim, L.D. Foster, C.S. Moy, G. Xi, M.D. Hill, L.B. Morgenstern, S.M. Greenberg, M.L. James, V. Singh, W.M. Clark, C. Norton, Y.Y. Palesch, S.D. Yeatts, M. Dolan, E. Yeh, K. Sheth, K. Kunze, S. Muehlschlegel, I. Nieto, J. Claassen, C. Faló, D. Huang, A. Beckwith, S. Messe, M. Yates, K. O’Phelan, A. Escobar, K. Becker, P. Tanzi, N. Gonzales, C. Tremont, C. Venkatasubramanian, R. Thiessen, S. Save, S. Verrault, K. Collard, M. DeGeorgia, V. Cwiklinski, B. Thompson, L. Wasilewski, C. Andrews, R. Burfeind, M. Torbey, M. Hamed, K. Butcher, L. Sivakumar, N. Varelas, K. Mays-Wilson, E. Leira, H. Olalde, S. Silliman, R. Calhoun, N. Dangayach, R. Renvill, R. Malhotra, K. Kordesch, A. Lord, T. Calahan, R. Geocadin, M. Parish, J. Frey, M. Harrigan, D. Leifer, R. Mathias, M. Schneck, T. Bernier, S. Gonzales-Arias, J. Elysee, G. Lopez, J. Volgi, R. Brown, S. Jasak, S. Phillips, J. Jarrett, J. Gomes, M. McBride, F. Aldrich, C. Aldrich, J. Kornbluth, M. Bettle, J. Goldstein, G. Tirrell, Q. Shaw, K. Jonczak, Deferoxamine mesylate in patients with intracerebral haemorrhage (i-DEF): a multicentre, randomised, placebo-controlled, double-blind phase 2 trial, *Lancet Neurol.* 18 (2019) 428–438. [https://doi.org/10.1016/S1474-4422\(19\)30069-9](https://doi.org/10.1016/S1474-4422(19)30069-9).
- [151] L. Zeng, L. Tan, H. Li, Q. Zhang, Y. Li, J. Guo, Deferoxamine therapy for intracerebral hemorrhage: A systematic review, *PLOS ONE* 13 (2018) e0193615. <https://doi.org/10.1371/journal.pone.0193615>.
- [152] J. Yu, Q. Yuan, Y. Sun, X. Wu, Z. Du, Z. Li, X. Wu, L. Zhou, G. Wu, J. Hu, Effects of Deferoxamine Mesylate on Hematoma and Perihematoma Edema after Traumatic Intracerebral Hemorrhage, *J. Neurotrauma* 34 (2017) 2753–2759. <https://doi.org/10.1089/neu.2017.5033>.
- [153] D. Grenier, M.-P. Huot, D. Mayrand, Iron-Chelating Activity of Tetracyclines and Its Impact on the Susceptibility of *Actinobacillus actinomycetemcomitans* to These Antibiotics, *Antimicrob. Agents Chemother.* 44 (2000) 763–766.
- [154] S. Dai, Y. Hua, R.F. Keep, N. Novakovic, Z. Fei, G. Xi, Minocycline attenuates brain injury and iron overload after intracerebral hemorrhage in aged female rats, *Neurobiol. Dis.* 126 (2019) 76–84. <https://doi.org/10.1016/j.nbd.2018.06.001>.

- [155] F. Zhao, Y. Hua, R.F. Keep, G. Xi, Abstract 2156: Minocycline-induced Attenuation Of Iron Overload And Brain Injury Following Experimental Intracerebral Hemorrhage, *Stroke* 43 (2012) A2156–A2156. https://doi.org/10.1161/str.43.suppl_1.A2156.
- [156] S. Cao, Y. Hua, R.F. Keep, N. Chaudhary, G. Xi, Minocycline Effects on Intracerebral Hemorrhage-Induced Iron Overload in Aged Rats, *Stroke* 49 (2018) 995–1002. <https://doi.org/10.1161/STROKEAHA.117.019860>.
- [157] E. Kohler, D.A. Prentice, T.R. Bates, G.J. Hankey, A. Claxton, J. van Heerden, D. Blacker, Intravenous minocycline in acute stroke: a randomized, controlled pilot study and meta-analysis, *Stroke* 44 (2013) 2493–2499. <https://doi.org/10.1161/STROKEAHA.113.000780>.
- [158] A.Y. Fouda, A.S. Newsome, S. Spellacy, J.L. Waller, W. Zhi, D.C. Hess, A. Ergul, D.J. Edwards, S.C. Fagan, J.A. Switzer, Minocycline in Acute Cerebral Hemorrhage: An Early Phase Randomized Trial, *Stroke* 48 (2017) 2885–2887. <https://doi.org/10.1161/STROKEAHA.117.018658>.
- [159] J.J. Chang, M. Kim-Tenser, B.A. Emanuel, G.M. Jones, K. Chapple, A. Alikhani, N. Sanossian, W.J. Mack, G. Tsivgoulis, A.V. Alexandrov, T. Pourmotabbed, Minocycline and matrix metalloproteinase inhibition in acute intracerebral hemorrhage: a pilot study, *Eur. J. Neurol.* 24 (2017) 1384–1391. <https://doi.org/10.1111/ene.13403>.
- [160] A. Datta, D. Sarmah, L. Mounica, H. Kaur, R. Kesharwani, G. Verma, P. Veeresh, V. Kotian, K. Kalia, A. Borah, X. Wang, K.R. Dave, D.R. Yavagal, P. Bhattacharya, Cell Death Pathways in Ischemic Stroke and Targeted Pharmacotherapy, *Transl. Stroke Res.* 11 (2020) 1185–1202. <https://doi.org/10.1007/s12975-020-00806-z>.
- [161] T. Carbonell, R. Rama, Iron, Oxidative Stress and Early Neurological Deterioration in Ischemic Stroke, *Curr. Med. Chem.* 14 (2007) 857–874. <https://doi.org/10.2174/092986707780363014>.
- [162] S. Patil, R. Rossi, D. Jabra, K. Doyle, Detection, Diagnosis and Treatment of Acute Ischemic Stroke: Current and Future Perspectives, *Front. Med. Technol.* 4 (2022). <https://doi.org/10.3389/fmedt.2022.748949>.
- [163] H.B. Huttner, S. Schwab, Malignant middle cerebral artery infarction: clinical characteristics, treatment strategies, and future perspectives, *Lancet Neurol.* 8 (2009) 949–958. [https://doi.org/10.1016/S1474-4422\(09\)70224-8](https://doi.org/10.1016/S1474-4422(09)70224-8).
- [164] Y.V. Li, Zinc Overload in Stroke, in: Y.V. Li, J.H. Zhang (Eds.), *Met. Ion Stroke*, Springer, New York, NY, 2012: pp. 167–189. https://doi.org/10.1007/978-1-4419-9663-3_7.
- [165] S.L. Galasso, R.H. Dyck, The Role of Zinc in Cerebral Ischemia, *Mol. Med.* 13 (2007) 380–387. <https://doi.org/10.2119/2007-00044.Galasso>.
- [166] B. Thomas, B. Julien, Treatment of Acute Ischemic Stroke, *N. Engl. J. Med.* (2000).
- [167] A. Mizuma, M.A. Yenari, Clinical perspectives on ischemic stroke, *Exp. Neurol.* 338 (2021) 113599. <https://doi.org/10.1016/j.expneurol.2021.113599>.
- [168] M. Millán, N. DeGregorio-Rocasolano, N. Pérez De La Ossa, S. Reverté, J. Costa, P. Giner, Y. Silva, T. Sobrino, M. Rodríguez-Yáñez, F. Nombela, F. Campos, J. Serena, J. Vivancos, O. Martí-Sistac, J. Cortés, A. Dávalos, T. Gasull, Targeting Pro-Oxidant Iron with Deferoxamine as a Treatment for Ischemic Stroke: Safety and Optimal Dose Selection in a Randomized Clinical Trial, *Antioxidants* 10 (2021) 1270. <https://doi.org/10.3390/antiox10081270>.
- [169] Y. Lampl, M. Boaz, R. Gilad, M. Lorberboym, R. Dabby, A. Rapoport, M. Anca-Hershkowitz, M. Sadeh, Minocycline treatment in acute stroke, *Neurology* 69 (2007) 1404–1410. <https://doi.org/10.1212/01.wnl.0000277487.04281.db>.

- [170] S.C. Fagan, J.L. Waller, F.T. Nichols, D.J. Edwards, L.C. Pettigrew, W.M. Clark, C.E. Hall, J.A. Switzer, A. Ergul, D.C. Hess, Minocycline to Improve Neurologic Outcome in Stroke (MINOS), *Stroke* 41 (2010) 2283–2287. <https://doi.org/10.1161/STROKEAHA.110.582601>.
- [171] H.-C. Diener, D. Schneider, Y. Lampl, N.M. Bornstein, A. Kozak, G. Rosenberg, DP-b99, a Membrane-Activated Metal Ion Chelator, as Neuroprotective Therapy in Ischemic Stroke, *Stroke* 39 (2008) 1774–1778. <https://doi.org/10.1161/STROKEAHA.107.506378>.
- [172] G. Rosenberg, I. Angel, A. Kozak, Clinical pharmacology of DP-b99 in healthy volunteers: first administration to humans, *Br. J. Clin. Pharmacol.* 60 (2005) 7–16. <https://doi.org/10.1111/j.1365-2125.2005.02378.x>.
- [173] K.R. Lees, N. Bornstein, H.-C. Diener, P.B. Gorelick, G. Rosenberg, A. Shuaib, for the MACSI Investigators*, Results of Membrane-activated Chelator Stroke Intervention Randomized Trial of DP-b99 in Acute Ischemic Stroke, *Stroke* 44 (2013) 580–584. <https://doi.org/10.1161/STROKEAHA.111.000013>.
- [174] A.H. Koeppen, S.C. Michael, D. Li, Z. Chen, M.J. Cusack, W.M. Gibson, S.V. Petrocine, J. Qian, The pathology of superficial siderosis of the central nervous system, *Acta Neuropathol. (Berl.)* 116 (2008) 371–382. <https://doi.org/10.1007/s00401-008-0421-z>.
- [175] N. Kumar, Superficial Siderosis: A Clinical Review, *Ann. Neurol.* 89 (2021) 1068–1079. <https://doi.org/10.1002/ana.26083>.
- [176] S. Nanda, S.G. Sharma, S. Longo, Superficial siderosis – mechanism of disease: an alternative hypothesis, *Ann. Clin. Biochem.* 47 (2010) 275–278. <https://doi.org/10.1258/acb.2010.009226>.
- [177] M. Levy, R. Llinas, Pilot Safety Trial of Deferiprone in 10 Subjects With Superficial Siderosis, *Stroke* 43 (2012) 120–124. <https://doi.org/10.1161/STROKEAHA.111.628032>.
- [178] G. Cossu, G. Abbruzzese, G.L. Forni, G. Matta, V. Pinto, U. Ruffinengo, V. Oppo, R. Marchese, Efficacy and safety of deferiprone for the treatment of superficial siderosis: results from a long-term observational study, *Neurol. Sci.* 40 (2019) 1357–1361. <https://doi.org/10.1007/s10072-019-03847-x>.
- [179] E. Derle, Iron chelation in treatment of superficial siderosis, *Iran. J. Neurol.* 17 (2018) 195–196.
- [180] G. Cummins, G. Crundwell, D. Baguley, G. Lennox, Treatment of superficial siderosis with iron chelation therapy, *BMJ Case Rep.* 2013 (2013) bcr2013009916. <https://doi.org/10.1136/bcr-2013-009916>.
- [181] R.A. Kessler, X. Li, K. Schwartz, H. Huang, M.A. Mealy, M. Levy, Two-year observational study of deferiprone in superficial siderosis, *CNS Neurosci. Ther.* 24 (2018) 187–192. <https://doi.org/10.1111/cns.12792>.
- [182] Y. Sammaraiiee, G. Banerjee, S. Farmer, B. Hylton, P. Cowley, P. Eleftheriou, J. Porter, D.J. Werring, Risks associated with oral deferiprone in the treatment of infratentorial superficial siderosis, *J. Neurol.* 267 (2020) 239–243. <https://doi.org/10.1007/s00415-019-09577-6>.
- [183] L. Gerhardsson, G. Kazantzis, Chapter 23 - Diagnosis and Treatment of Metal Poisoning: General Aspects, in: G.F. Nordberg, B.A. Fowler, M. Nordberg (Eds.), *Handb. Toxicol. Met.* Fourth Ed., Academic Press, San Diego, 2015: pp. 487–505. <https://doi.org/10.1016/B978-0-444-59453-2.00023-8>.
- [184] G. Crisponi, V.M. Nurchi, M. Crespo-Alonso, L. Toso, Chelating agents for metal intoxication, *Curr. Med. Chem.* 19 (2012) 2794–2815. <https://doi.org/10.2174/092986712800609742>.
- [185] G. Schwarzenbach, Der Chelateffekt, *Helv. Chim. Acta* 35 (1952) 2344–2359. <https://doi.org/10.1002/hlca.19520350721>.

- [186] V.M. Nurchi, G. Crisponi, M. Arca, M. Crespo-Alonso, J.I. Lachowicz, D. Mansoori, L. Toso, G. Pichiri, M. Amelia Santos, S.M. Marques, J. Niclós-Gutiérrez, J.M. González-Pérez, A. Domínguez-Martín, D. Choquesillo-Lazarte, Z. Szewczuk, M. Antonietta Zoroddu, M. Peana, A new bis-3-hydroxy-4-pyrone as a potential therapeutic iron chelating agent. Effect of connecting and side chains on the complex structures and metal ion selectivity, *J. Inorg. Biochem.* 141 (2014) 132–143. <https://doi.org/10.1016/j.jinorgbio.2014.09.002>.
- [187] M.D. Engelmann, R.T. Bobier, T. Hiatt, I.F. Cheng, Variability of the Fenton reaction characteristics of the EDTA, DTPA, and citrate complexes of iron, *Biometals* 16 (2003) 519–527. <https://doi.org/10.1023/A:1023480617038>.
- [188] J.B. Porter, E.R. Huehns, 11 The toxic effects of desferrioxamine, *Baillières Clin. Haematol.* 2 (1989) 459–474. [https://doi.org/10.1016/S0950-3536\(89\)80027-7](https://doi.org/10.1016/S0950-3536(89)80027-7).
- [189] M. Hruby, I.I.S. Martínez, H. Stephan, P. Pouckova, J. Benes, P. Stepanek, Chelators for Treatment of Iron and Copper Overload: Shift from Low-Molecular-Weight Compounds to Polymers, *Polymers* 13 (2021) 3969. <https://doi.org/10.3390/polym13223969>.
- [190] B. Yu, Y. Yang, Q. Liu, A. Zhan, Y. Yang, H. Liu, A Novel Star Like Eight-Arm Polyethylene Glycol-Deferoxamine Conjugate for Iron Overload Therapy, *Pharmaceutics* 12 (2020) 329. <https://doi.org/10.3390/pharmaceutics12040329>.
- [191] L.R. Perez, K.J. Franz, Minding metals: Tailoring multifunctional chelating agents for neurodegenerative disease, *Dalton Trans* 39 (2010) 2177–2187. <https://doi.org/10.1039/B919237A>.
- [192] H. Zheng, M.B.H. Youdim, L.M. Weiner, M. Fridkin, Novel potential neuroprotective agents with both iron chelating and amino acid-based derivatives targeting central nervous system neurons, *Biochem. Pharmacol.* 70 (2005) 1642–1652. <https://doi.org/10.1016/j.bcp.2005.09.003>.
- [193] G. Liu, M.R. Garrett, P. Men, X. Zhu, G. Perry, M.A. Smith, Nanoparticle and other metal chelation therapeutics in Alzheimer disease, *Biochim. Biophys. Acta BBA - Mol. Basis Dis.* 1741 (2005) 246–252. <https://doi.org/10.1016/j.bbadis.2005.06.006>.
- [194] L. You, J. Wang, T. Liu, Y. Zhang, X. Han, T. Wang, S. Guo, T. Dong, J. Xu, G.J. Anderson, Q. Liu, Y.-Z. Chang, X. Lou, G. Nie, Targeted Brain Delivery of Rabies Virus Glycoprotein 29-Modified Deferoxamine-Loaded Nanoparticles Reverses Functional Deficits in Parkinsonian Mice, *ACS Nano* 12 (2018) 4123–4139. <https://doi.org/10.1021/acsnano.7b08172>.
- [195] J.M. Thomas, I. Louca, F. Bolan, O.-R. Sava, S.M. Allan, C.B. Lawrence, E. Pinteaux, Regenerative Potential of Hydrogels for Intracerebral Hemorrhage: Lessons from Ischemic Stroke and Traumatic Brain Injury Research, *Adv. Healthc. Mater.* 10 (2021) 2100455. <https://doi.org/10.1002/adhm.202100455>.
- [196] B. Gong, W. Cheng, W. Ji, X. Chen, J. Chu, W. Liang, B. He, J. Zhuang, Y. Yin, J. Gao, Hydrogel: A promising new technique for treating Alzheimer's disease, *J. Transl. Intern. Med.* 10 (2022) 188–190. <https://doi.org/10.2478/jtim-2022-0008>.
- [197] Z. Mohammadi, S.-X. Xie, A.L. Golub, S.H. Gehrke, C. Berkland, Siderophore-Mimetic hydrogel for iron chelation therapy, *J. Appl. Polym. Sci.* 121 (2011) 1384–1392. <https://doi.org/10.1002/app.33562>.
- [198] M. Natuzzi, C. Grange, T. Gréa, T. Brichtart, A. Aigle, D. Bechet, B. Hautefeuille, E. Thomas, J.-Y. Ayoub, J.-M. Bonnet, V. Louzier, B. Allaouchiche, A. Couturier, A. Montembault, P.N. de Oliveira, L. David, F. Lux, O. Tillement, Feasibility study and direct extraction of endogenous

- free metallic cations combining hemodialysis and chelating polymer, *Sci. Rep.* 11 (2021) 19948. <https://doi.org/10.1038/s41598-021-99462-y>.
- [199] C. Grange, A. Aigle, V. Ehrlich, J.F. Salazar Ariza, T. Brichart, F. Da Cruz-Boisson, L. David, F. Lux, O. Tillement, Design of a water-soluble chitosan-based polymer with antioxidant and chelating properties for labile iron extraction, *Sci. Rep.* 13 (2023) 7920. <https://doi.org/10.1038/s41598-023-34251-3>.
- [200] J.A. Howard, H. Kuznietsova, N. Dziubenko, A. Aigle, M. Natuzzi, E. Thomas, V. Lysenko, L. David, T. Brichart, F. Lux, O. Tillement, Combating lead and cadmium exposure with an orally administered chitosan-based chelating polymer, *Sci. Rep.* 13 (2023) 2215. <https://doi.org/10.1038/s41598-023-28968-4>.
- [201] E. Ficiarà, C. Molinar, S. Gazzin, S. Jayanti, M. Argenziano, L. Nasi, F. Casoli, F. Albertini, S.A. Ansari, A. Marcantoni, G. Tomagra, V. Carabelli, C. Guiot, F. D'Agata, R. Cavalli, Developing Iron Nano-chelating Agents: Preliminary Investigation of Effectiveness and Safety for Central Nervous System Applications, *Int. J. Mol. Sci.* 25 (2024) 729. <https://doi.org/10.3390/ijms25020729>.
- [202] W. Feng, Z. Wang, Tailoring the Swelling-Shrinkable Behavior of Hydrogels for Biomedical Applications, *Adv. Sci.* 10 (2023) 2303326. <https://doi.org/10.1002/advs.202303326>.
- [203] M.L. Pita-López, G. Fletes-Vargas, H. Espinosa-Andrews, R. Rodríguez-Rodríguez, Physically cross-linked chitosan-based hydrogels for tissue engineering applications: A state-of-the-art review, *Eur. Polym. J.* 145 (2021) 110176. <https://doi.org/10.1016/j.eurpolymj.2020.110176>.
- [204] R. Jin, P.J. Dijkstra, Hydrogels for Tissue Engineering Applications, in: R.M. Ottenbrite, K. Park, T. Okano (Eds.), *Biomed. Appl. Hydrogels Handb.*, Springer, New York, NY, 2010: pp. 203–225. https://doi.org/10.1007/978-1-4419-5919-5_11.
- [205] P.L. Turecek, M.J. Bossard, F. Schoetens, I.A. Ivens, PEGylation of Biopharmaceuticals: A Review of Chemistry and Nonclinical Safety Information of Approved Drugs, *J. Pharm. Sci.* 105 (2016) 460–475. <https://doi.org/10.1016/j.xphs.2015.11.015>.
- [206] X. Zhao, J. Si, D. Huang, K. Li, Y. Xin, M. Sui, Application of star poly(ethylene glycol) derivatives in drug delivery and controlled release, *J. Controlled Release* 323 (2020) 565–577. <https://doi.org/10.1016/j.jconrel.2020.04.039>.
- [207] A. Kolate, D. Baradia, S. Patil, I. Vhora, G. Kore, A. Misra, PEG — A versatile conjugating ligand for drugs and drug delivery systems, *J. Controlled Release* 192 (2014) 67–81. <https://doi.org/10.1016/j.jconrel.2014.06.046>.
- [208] W. Wu, W. Wang, J. Li, Star polymers: Advances in biomedical applications, *Prog. Polym. Sci.* 46 (2015) 55–85. <https://doi.org/10.1016/j.progpolymsci.2015.02.002>.
- [209] G.D. Mogoşanu, A.M. Grumezescu, Natural and synthetic polymers for wounds and burns dressing, *Int. J. Pharm.* 463 (2014) 127–136. <https://doi.org/10.1016/j.ijpharm.2013.12.015>.
- [210] L. Rami, S. Malaise, S. Delmond, J.-C. Fricain, R. Siadous, S. Schlaubitz, E. Laurichesse, J. Amédée, A. Montembault, L. David, L. Bordenave, Physicochemical modulation of chitosan-based hydrogels induces different biological responses: Interest for tissue engineering, *J. Biomed. Mater. Res. A* 102 (2014) 3666–3676. <https://doi.org/10.1002/jbm.a.35035>.
- [211] C.K.S. Pillai, W. Paul, C.P. Sharma, Chitin and chitosan polymers: Chemistry, solubility and fiber formation, *Prog. Polym. Sci.* 34 (2009) 641–678. <https://doi.org/10.1016/j.progpolymsci.2009.04.001>.

- [212] N. Pacheco, M. Garnica-Gonzalez, M. Gimeno, E. Bárzana, S. Trombotto, L. David, K. Shirai, Structural Characterization of Chitin and Chitosan Obtained by Biological and Chemical Methods, *Biomacromolecules* 12 (2011) 3285–3290. <https://doi.org/10.1021/bm200750t>.
- [213] M. Dash, F. Chiellini, R.M. Ottenbrite, E. Chiellini, Chitosan—A versatile semi-synthetic polymer in biomedical applications, *Prog. Polym. Sci.* 36 (2011) 981–1014. <https://doi.org/10.1016/j.progpolymsci.2011.02.001>.
- [214] T. Kean, M. Thanou, Biodegradation, biodistribution and toxicity of chitosan, *Adv. Drug Deliv. Rev.* 62 (2010) 3–11. <https://doi.org/10.1016/j.addr.2009.09.004>.
- [215] M.A. Gámiz-González, A.E. Piskin, C. Pandis, C. Chatzimanolis-Moustakas, A. Kyritsis, B. Marí, J.L.G. Ribelles, A. Vidaurre, Determining the influence of *N*-acetylation on water sorption in chitosan films, *Carbohydr. Polym.* 133 (2015) 110–116. <https://doi.org/10.1016/j.carbpol.2015.07.020>.
- [216] W. Wang, Q. Meng, Q. Li, J. Liu, M. Zhou, Z. Jin, K. Zhao, Chitosan Derivatives and Their Application in Biomedicine, *Int. J. Mol. Sci.* 21 (2020) 487. <https://doi.org/10.3390/ijms21020487>.
- [217] E. Cohen, E. Poverenov, Hydrophilic Chitosan Derivatives: Synthesis and Applications, *Chem. – Eur. J.* 28 (2022) e202202156. <https://doi.org/10.1002/chem.202202156>.
- [218] P. Sorlier, A. Denuzière, C. Viton, A. Domard, Relation between the Degree of Acetylation and the Electrostatic Properties of Chitin and Chitosan, *Biomacromolecules* 2 (2001) 765–772. <https://doi.org/10.1021/bm015531+>.
- [219] A. Montembault, C. Viton, A. Domard, Rheometric Study of the Gelation of Chitosan in Aqueous Solution without Cross-Linking Agent, *Biomacromolecules* 6 (2005) 653–662. <https://doi.org/10.1021/bm049593m>.
- [220] M.A. Matica, F.L. Aachmann, A. Tøndervik, H. Sletta, V. Ostafe, Chitosan as a Wound Dressing Starting Material: Antimicrobial Properties and Mode of Action, *Int. J. Mol. Sci.* 20 (2019) 5889. <https://doi.org/10.3390/ijms20235889>.
- [221] R.B. Hernández, A.P. Franco, O.R. Yola, A. López-Delgado, J. Felcman, M.A.L. Recio, A.L.R. Mercê, Coordination study of chitosan and Fe³⁺, *J. Mol. Struct.* 877 (2008) 89–99. <https://doi.org/10.1016/j.molstruc.2007.07.024>.
- [222] R.B. Hernández, O.R. Yola, A.L.R. Mercê, Chemical equilibrium in the complexation of first transition series divalent cations Cu²⁺, Mn²⁺ and Zn²⁺ with chitosan, *J. Braz. Chem. Soc.* 18 (2007) 1388–1396. <https://doi.org/10.1590/S0103-50532007000700015>.
- [223] G. Farinelli, A. Di Luca, V.R.I. Kaila, M.J. MacLachlan, A. Tiraferri, Fe-chitosan complexes for oxidative degradation of emerging contaminants in water: Structure, activity, and reaction mechanism, *J. Hazard. Mater.* 408 (2021) 124662. <https://doi.org/10.1016/j.jhazmat.2020.124662>.
- [224] M. Chtchigrovsky, A. Primo, P. Gonzalez, K. Molvinger, M. Robitzer, F. Quignard, F. Taran, Functionalized Chitosan as a Green, Recyclable, Biopolymer-Supported Catalyst for the [3+2] Huisgen Cycloaddition, *Angew. Chem. Int. Ed.* 48 (2009) 5916–5920. <https://doi.org/10.1002/anie.200901309>.
- [225] T. Gréa, G. Jacquot, A. Durand, C. Mathieu, A. Gasser, C. Zhu, M. Banerjee, E. Hucteau, J. Mallard, P. Lopez Navarro, B.V. Popescu, E. Thomas, D. Kryza, J. Sidi-Boumedine, G. Ferrauto, E. Gianolio, G. Fleith, J. Combet, S. Brun, S. Erb, S. Cianferani, L.J. Charbonnière, L. Fellmann, C. Mirjolet, L. David, O. Tillement, F. Lux, S. Harlepp, X. Pivot, A. Detappe, Subcutaneous Administration of a Zwitterionic Chitosan-Based Hydrogel for Controlled Spatiotemporal

- Release of Monoclonal Antibodies, *Adv. Mater.* 36 (2024) 2308738.
<https://doi.org/10.1002/adma.202308738>.
- [226] G.T. Hermanson, Chapter 2 - The Chemistry of Reactive Groups, in: G.T. Hermanson (Ed.), *Bioconjugate Tech. Second Ed.*, Academic Press, New York, 2008: pp. 169–212.
<https://doi.org/10.1016/B978-0-12-370501-3.00002-3>.
- [227] A. Hirai, H. Odani, A. Nakajima, Determination of degree of deacetylation of chitosan by ¹H NMR spectroscopy, *Polym. Bull.* 26 (1991) 87–94. <https://doi.org/10.1007/BF00299352>.
- [228] M. Imran ul-haq, J.L. Hamilton, B.F.L. Lai, R.A. Shenoi, S. Horte, I. Constantinescu, H.A. Leitch, J.N. Kizhakkedathu, Design of Long Circulating Nontoxic Dendritic Polymers for the Removal of Iron in Vivo, *ACS Nano* 7 (2013) 10704–10716. <https://doi.org/10.1021/nn4035074>.
- [229] W.-C. Kan, C.-C. Chien, C.-C. Wu, S.-B. Su, J.-C. Hwang, H.-Y. Wang, Comparison of low-dose deferoxamine versus standard-dose deferoxamine for treatment of aluminium overload among haemodialysis patients, *Nephrol. Dial. Transplant.* 25 (2010) 1604–1608.
<https://doi.org/10.1093/ndt/gfp649>.
- [230] S. Anthone, C.M. Ambrus, R. Kohli, I. Min, R. Anthone, A. Stadler, I. Stadler, A. Vladutiu, Treatment of aluminum overload using a cartridge with immobilized desferrioxamine, *J. Am. Soc. Nephrol. JASN* 6 (1995) 1271–1277. <https://doi.org/10.1681/ASN.V641271>.
- [231] K. Almdal, J. Dyre, S. Hvidt, O. Kramer, Towards a phenomenological definition of the term ‘gel,’ *Polym. Gels Netw.* 1 (1993) 5–17. [https://doi.org/10.1016/0966-7822\(93\)90020-I](https://doi.org/10.1016/0966-7822(93)90020-I).
- [232] S. Peers, A. Montembault, C. Ladavière, Chitosan hydrogels for sustained drug delivery, *J. Controlled Release* 326 (2020) 150–163. <https://doi.org/10.1016/j.jconrel.2020.06.012>.
- [233] J. Li, D.J. Mooney, Designing hydrogels for controlled drug delivery, *Nat. Rev. Mater.* 1 (2016) 16071. <https://doi.org/10.1038/natrevmats.2016.71>.
- [234] A.K. Tamo, T.A. Tran, I. Doench, S. Jahangir, A. Lall, L. David, C. Peniche-Covas, A. Walther, A. Osorio-Madrado, 3D Printing of Cellulase-Laden Cellulose Nanofiber/Chitosan Hydrogel Composites: Towards Tissue Engineering Functional Biomaterials with Enzyme-Mediated Biodegradation, *Materials* 15 (2022) 6039. <https://doi.org/10.3390/ma15176039>.
- [235] V. Pertici, C. Pin-Barre, C. Rivera, C. Pellegrino, J. Laurin, D. Gignes, T. Trimaille, Degradable and Injectable Hydrogel for Drug Delivery in Soft Tissues, *Biomacromolecules* 20 (2019) 149–163. <https://doi.org/10.1021/acs.biomac.8b01242>.
- [236] S. Ladet, L. David, A. Domard, Multi-membrane hydrogels, *Nature* 452 (2008) 76–79.
<https://doi.org/10.1038/nature06619>.
- [237] A. Borzacchiello, L. Ambrosio, P.A. Netti, L. Nicolais, C. Peniche, A. Gallardo, J. San Roman, Chitosan-based hydrogels: Synthesis and characterization, *J. Mater. Sci. Mater. Med.* 12 (2001) 861–864. <https://doi.org/10.1023/A:1012851402759>.
- [238] P. Mohammadzadeh Pakdel, S.J. Peighambaroust, Review on recent progress in chitosan-based hydrogels for wastewater treatment application, *Carbohydr. Polym.* 201 (2018) 264–279. <https://doi.org/10.1016/j.carbpol.2018.08.070>.
- [239] C. Valenta, B. Christen, A. Bernkop-Schnürch, Chitosan-EDTA Conjugate: A Novel Polymer for Topical Gels, *J. Pharm. Pharmacol.* 50 (1998) 445–452. <https://doi.org/10.1111/j.2042-7158.1998.tb06184.x>.
- [240] E. Guibal, Interactions of metal ions with chitosan-based sorbents: a review, *Sep. Purif. Technol.* 38 (2004) 43–74. <https://doi.org/10.1016/j.seppur.2003.10.004>.

- [241] M. Vakili, S. Deng, G. Cagnetta, W. Wang, P. Meng, D. Liu, G. Yu, Regeneration of chitosan-based adsorbents used in heavy metal adsorption: A review, *Sep. Purif. Technol.* 224 (2019) 373–387. <https://doi.org/10.1016/j.seppur.2019.05.040>.
- [242] R. Yamaguchi, S. Hirano, Y. Arai, T. Ito, Chitosan Salt Gels Thermally Reversible Gelation of Chitosan, *Agric. Biol. Chem.* 42 (1978) 1981–1982. <https://doi.org/10.1271/bbb1961.42.1981>.
- [243] R.-L. Tseng, F.-C. Wu, R.-S. Juang, Effect of complexing agents on liquid-phase adsorption and desorption of copper(II) using chitosan, *J. Chem. Technol. Biotechnol.* 74 (1999) 533–588. [https://doi.org/10.1002/\(SICI\)1097-4660\(199906\)74:6<533::AID-JCTB79>3.0.CO;2-O](https://doi.org/10.1002/(SICI)1097-4660(199906)74:6<533::AID-JCTB79>3.0.CO;2-O).
- [244] D.T. Dexter, S.A. Statton, C. Whitmore, W. Freinbichler, P. Weinberger, K.F. Tipton, L. Della Corte, R.J. Ward, R.R. Crichton, Clinically available iron chelators induce neuroprotection in the 6-OHDA model of Parkinson's disease after peripheral administration, *J. Neural Transm. Vienna Austria* 1996 118 (2011) 223–231. <https://doi.org/10.1007/s00702-010-0531-3>.
- [245] W. Freinbichler, B. Misini, M.A. Colivicchi, W. Linert, K.F. Tipton, L. Della Corte, The application of bathophenanthroline for the determination of free iron in parallel with hROS in microdialysis samples, *J. Neurosci. Methods* 331 (2020) 108530. <https://doi.org/10.1016/j.jneumeth.2019.108530>.
- [246] D.P. Chattopadhyay, M.S. Inamdar, Aqueous Behaviour of Chitosan, *Int. J. Polym. Sci.* 2010 (2010) 939536. <https://doi.org/10.1155/2010/939536>.
- [247] Z. Baranyai, G. Tircsó, F. Rösch, The Use of the Macrocyclic Chelator DOTA in Radiochemical Separations, *Eur. J. Inorg. Chem.* 2020 (2020) 36–56. <https://doi.org/10.1002/ejic.201900706>.
- [248] R. Passieux, G. Sudre, A. Montembault, M. Renard, A. Hagege, P. Alcouffe, A. Haddane, M. Vandesteene, N. Boucard, L. Bordenave, L. David, Cytocompatibility / Antibacterial Activity Trade-off for Knittable Wet-Spun Chitosan Monofilaments Functionalized by the In Situ Incorporation of Cu²⁺ and Zn²⁺, *ACS Biomater. Sci. Eng.* 8 (2022) 1735–1748. <https://doi.org/10.1021/acsbiomaterials.2c00079>.
- [249] F.E. Bentley, R. Passieux, L. David, A. Osorio-Madrado, Pure Chitosan Biomedical Textile Fibers from Mixtures of Low- and High-Molecular Weight Bidisperse Polymer Solutions: Processing and Understanding of Microstructure–Mechanical Properties' Relationship, *Int. J. Mol. Sci.* 23 (2022) 4767. <https://doi.org/10.3390/ijms23094767>.
- [250] M. Desorme, A. Montembault, J.-M. Lucas, C. Rochas, T. Bouet, L. David, Spinning of hydroalcoholic chitosan solutions, *Carbohydr. Polym.* 98 (2013) 50–63. <https://doi.org/10.1016/j.carbpol.2013.04.070>.
- [251] M. Desorme, A. Montembault, T. Tamet, P. Maleysson, T. Bouet, L. David, Spinning of hydroalcoholic chitosan solutions: Mechanical behavior and multiscale microstructure of resulting fibers, *J. Appl. Polym. Sci.* 136 (2019) 47130. <https://doi.org/10.1002/app.47130>.
- [252] L. Notin, C. Viton, L. David, P. Alcouffe, C. Rochas, A. Domard, Morphology and mechanical properties of chitosan fibers obtained by gel-spinning: Influence of the dry-jet-stretching step and ageing, *Acta Biomater.* 2 (2006) 387–402. <https://doi.org/10.1016/j.actbio.2006.03.003>.